UNIVERSITY OF TROMSØ UIT

FACULTY OF SCIENCE AND TECHNOLOGY
DEPARTMENT OF PHYSICS AND TECHNOLOGY

# Optical Forces, Waveguides and Micro Raman Spectroscopy

**Pål Løvhaugen**

A dissertation for the degree of
Philosophiae Doctor

August 2012

... *καὶ ἐγένετο φῶς.*

Γ*ένεσις* ι ιιι

**Abstract**

Optical waveguides are used to confine propagating light. In a dielectric waveguide, a small part of the propagating light travels along and just outside the waveguide surface. This evanescent field can interact with objects on the waveguide surface. Two effects of this light-matter interaction are presented, optical forces and Raman scattering.

Optical forces are caused by changes in the momentum of radiation. The forces are exerted on objects interacting with a propagating field. The magnitude of the force is dependent on the difference in permittivity and permeability between the object and the surrounding medium. The forces can be used to trap and control micro- and nanoparticles.

In Raman scattering, the scattered field exchanges energy with the scatterer. The amount of energy that is lost or gained depends on the molecular structure of the scatterer. By collecting the spectra of the scattered light, the molecules in the scatterer can be analyzed and characterized.

Two numerical studies have been performed to simulate optical forces on a range of micrometer-sized objects trapped and propelled on a waveguide. A numerical model of a hollow glass sphere provides new insights on how the optical force depends on the glass thickness. A numerical model of a red blood cell studies the force dependence on cell shape and refractive index. A model of a real-sized cell is made.

Two experimental studies have used Raman spectroscopy to characterize and analyze objects subject to optical forces. One study looks at the viability of using Raman scattering to characterize objects trapped on waveguides. It was found that characterization with Raman spectroscopy is viable with the use of an external, focused light source, while excitation using the evanescent field is difficult. A second study investigates a new technique for proliferation measurements of non-adherent cells. A combined optical trapping - Raman spectroscopy setup is used to show that a Raman probe can be used to measure proliferation of actively replicating cells, even in a sample were the cell growth is slow or negative.

The presented studies were performed to investigate the potential of combining characterization with optical trapping on waveguides. This could be of use in an optical lab-on-a-chip for cells.

# Acknowledgements

Trying to describe nature, whether by text, pictures, numbers or other means, is a continuous process. The process can be fast or slow, depending on experience and mental acuity. My process has been long and slow. But it has also been rich, in terms of new knowledge, in terms of geographic and climatic variations and in terms of good people.

I am grateful to all the people that made my process interesting and fulfilling. Some of them should, and will, be mentioned specifically: Olav Gaute Hellesø gave me the opportunity and freedom to work on the topics described in the thesis, and was available at any time for discussions of any peculiar or ordinary ideas, always offering constructive advice. Balpreet S. Ahluwalia was an encouraging colleague, seeing possibilities and sharing good spirits at all times. Thomas Huser offered me great opportunities and advice, both in Tromsø and in Sacramento. Dmitri Petrov welcomed me into his lab for six months, where he and his team offered rewarding experiences. I am very happy I got to meet the always friendly and helpful colleagues Giovanni, Satish, Sandro and Štefan at ICFO and Deanna, Ana, Iwan and Greg at CBST. And in Tromsø, it was a pleasure to share work and space with Katarina, Ananth, Firehun, Susan, Vahid, Ding and Alexander. In addition, I would like to thank the mechanical workshop for parts to the setup, Robert Jenssen for discussions on signal analysis, Yngve Birkelund for advice on computer simulations, Iver Brevik for clarifying aspects on optical forces, and Pans Tandberg and Eivind Larsen for proofreading.

Finally, I want to thank Tone. Her patience and support have been invaluable to me. I am looking forward to our future, which is to be filled with good things!

# Contents

# List of Symbols

## General

| | |
|---|---|
| $\langle\,\rangle$ | Time average |
| $^*$ | Complex conjugate |
| $\jmath$ | Imaginary unit |
| Re{} | Real value of |
| $\mathcal{O}$ | Order of magnitude |
| $\mathbf{r}$ | Position vector |
| $t$ | Time |
| $v$ | Velocity |
| $\nu$ | Frequency |
| $\omega = 2\pi\nu$ | Angular frequency |
| $\lambda$ | Wavelength |
| $\mathrm{k} = 2\pi/\lambda$ | Angular wavenumber |
| $\bar{\nu} = 1/\lambda$ | Wavenumber |
| $S$ | Surface |
| $V$ | Volume |
| $\mathbf{n}$ | Unit normal |
| $a$ | Sphere radius |
| $T$ | Shell thickness |
| $h$ | Distance above waveguide |
| $\tau$ | Mass density |
| $C$ | Concentration |
| $\tilde{\mathrm{R}}^2$ | Unbiased coefficient of determination |

## Electromagnetic Theory

| | |
|---|---|
| $\epsilon$ | Permittivity |
| $\mu$ | Permeability |
| $\mathbf{E}$ | Electric field |
| $\mathbf{D} = \epsilon\mathbf{E}$ | Electric displacement field |
| $\mathbf{H}$ | Magnetic field |
| $\mathbf{B} = \mu\mathbf{H}$ | Magnetic displacement field |
| $\Phi$ | Electric potential |
| $\rho$ | Charge density |
| $\mathbf{J}$ | Current density |
| $c$ | Speed of light in vacuum |
| $n$ | Refractive index |
| $\Delta n$ | Refractive index difference |
| $W$ | Work |
| $U$ | Potential energy |
| $u$ | Energy density |
| $I$ | Intensity |
| $P$ | Power |
| $\mathbf{S}$ | Power flow |
| $\mathrm{k}^{\parallel}$ | Propagation constant |
| $\tilde{\mathrm{k}}^{\perp}$ | Transversal decay constant |
| $\gamma$ | Longitudinal decay constant |
| R | Reflection coefficient |
| T | Transmission coefficient |
| $\phi$ | Reflection phase shift |
| $d$ | Waveguide thickness |
| $p$ | Mode number |
| $_{\mathrm{c}}$ | Cover region |
| $_{\mathrm{g}}$ | Guiding core region |
| $_{\mathrm{s}}$ | Substrate region |
| $_{\mathrm{eff}}$ | Effective mode |
| $Q$ | Trapping efficiency |
| $w_a$ | Gaussian beam waist radius |

## Electromagnetic Theory

| | |
|---|---|
| $\mathbf{F}$ | Force |
| $\mathbf{f}$ | Volume force density |
| $\mathbf{t}$ | Surface force density |
| $\mathbf{n}$ | Surface unit normal |
| $\boldsymbol{\sigma}$ | Stress tensor |
| $\boldsymbol{P}$ | Momentum |
| $\boldsymbol{p}$ | Momentum density |
| $\mathfrak{p}$ | Dipole moment |
| $\alpha$ | Polarizability |
| $\mathfrak{s}$ | Scattering cross section |
| $\mathbf{s}$ | Displacement vector |
| $\Psi$ | Time-dependent wave function |
| $\psi$ | Time-independent wave function |
| $\mathfrak{E}_{kn}$ | Electric moment from state $k$ to $n$ |
| $h$ | Planck's constant |
| $q$ | Vibration displacement |
| $e$ | Strain component |
| $a$ | Permittivity-strain parameter |
| $b$ | Permeability-strain parameter |
| $\lambda_1$ | Lamé's first elasticity parameter |
| $\lambda_2$ | Lamé's second elasticity parameter |
| $\boldsymbol{\sigma}$ | Stress tensor |
| $_s$ | Due to internal strain |
| $_t$ | Due to inhomogeneous permittivity |
| $_e$ | Due to elastic forces (rigidity) |
| $_c$ | Due to charge |
| $_\mathrm{p}$ | Dielectric particle |

## Finite Element Method Theory

| | |
|---|---|
| $\mathcal{L}$ | Numerical operator |
| $\varphi$ | Exact solution |
| $f$ | Constraint |
| $\Omega$ | Numerical domain |
| $\Gamma$ | Numerical boundary |
| $e$ | Element |
| $\widetilde{\varphi}$ | Exact solution in element |
| $j$ | Global node number |
| $j^e$ | Local node number |
| $\widetilde{\varphi^e}$ | Test function in element |
| $C_j$ | Test function coefficient of node $j$ |
| $\zeta_j$ | Test function shape function of node $j$ |
| $r^e$ | Residual error in element |
| $w$ | Weighting function |
| $R^e_{j^e}$ | Weighted residual error in node of element |
| $\boldsymbol{R}^e$ | Total weighted residual error of element |
| $\mathbb{K}^e$ | Stiffness matrix |
| $\boldsymbol{b}^e$ | Constraint vector |
| $\boldsymbol{C}^e$ | Coefficient vector |
| $\mathbb{L}$ | Lower triangular matrix |
| $\mathbb{U}$ | Upper triangular matrix |
| $\mathbf{T}$ | Stress vector |
| $^{\mathrm{out}}$ | Outer surface |

# Chapter 1

# Introduction

### Background

Light has been a subject of studies for a long time, reaching back to the philosophers in ancient Greece discussing the properties of sight. The development of light as a science accelerated in the Islamic world around 1000 AD, and continued in Europe with the resurgence of science, philosophy and art during the renaissance. In the 17th century, systematic studies of optical phenomena lead to the development of the wave and particle theories of Huygens and Newton. By the end of the 19th century, optics had been found to be electromagnetic radiation, and with Maxwell's equations, the observable optical phenomena of the time could be explained. However, the development of optical sciences continued when the insights from quantum physics were introduced in the 20th century, and studies of light-matter interactions contribute to the understanding of optical processes up to this day.

A range of optics based applications surfaced with the invention of the laser in the late 1950's. The most influential of these is probably optical signal transmission, which combined with new communication and information technology has been connecting the world for the last 20 years. The transmission of optical signals is done by guiding electromagnetic fields in passive structures. The common name for these structures is optical waveguides. The best known is the silica optical fibre, but light is guided using other designs and materials. Embedded waveguides are researched in sensing, laser, and integrated circuit and processor technologies. These developments would bring the guiding of light to microchips.

A different application of waveguides is optical trapping. The evanescent field outside a dielectric waveguide core allows controlled propulsion of micro- and nanoparticles. Transportation with optical forces could potentially be used in lab-on-a-chip devices, contributing to studies and analyses of chemical and biochemical processes. The starting point for the work presented in this thesis was to study characterization of microparticle trapped on optical waveguides. Combined with waveguide switches and junctions, this could lead to particle sorting in lab-on-a-chip-devices.

With characterization on waveguides as the starting point, Raman spectroscopy and optical forces in evanescent fields became the two main topics of the thesis. In the following chapters, four different studies are presented, two focused on optical forces and two focused on Raman spectroscopy.

Numerical simulations are used to study the forces exerted on microparticles trapped by the evanescent field of a waveguide. Two kinds of microparticles are examined, hollow glass microspheres and red blood cells. The studies on hollow spheres look at how the thickness of the glass shell and the diameter of the sphere influenceds the forces (chapter 4). The studies of red blood cells look at how small refractive index changes and the shape of the cell influence the forces (chapter 5)

The Raman studies involve two different setups. One microscope setup is modified to combine Raman spectroscopy studies with waveguide trapping. This is used in experiments involving different waveguide designs and different Raman excitation sources. The aim of these studies is to analyze microspheres propelling on the waveguide (chapter 8). The second microscope setup is specifically designed for cell trapping. This is used to investigate a recently proposed method to measure cell proliferation (chapter 7).

**Structure**

Throughout the thesis, chapters presenting results are preceded with chapters presenting a brief theoretical background. The theory chapters are meant to give a brief and unified introduction, sufficient to give an understanding of the topical subject. This leads to the following structure of the thesis:

Chapter 2 introduces waveguides and optical forces. The chapter starts with a presentation of basic electromagnetic theory, which is followed by a theoretical section on slab waveguides. The chapter continues with a description of channel waveg-

uides, and the topic of waveguide theory is concluded with sections on the fabrication process and the properties of the waveguides used in the experiments of later chapters. The last sections of the chapter introduces the principles behind optical trapping. First, the origins of the optical force are described, and then details on trapping of dielectric particles in strongly focused and evanescent electromagnetic fields are given.

Chapter 3 presents the numerical model used in the simulations. To begin with, the principles behind the finite element method are outlined. This is followed by a description of the numerical model, including the calculation procedure, the implementation of the physics and the model geometry. In the last section, the validity of the model is discussed.

Chapter 4 presents results from the hollow microsphere force simulations. The chapter starts with a description of hollow microspheres and their properties, and continues with the results from the simulations. A simple mathematical model is then introduced to explain some of the results, and the simulations are compared with experimental results.

Chapter 5 presents results from the red blood cell simulations. The chapter starts with a description of the red blood cell properties that are of interest for waveguide trapping, and looks at earlier optical studies of such cells. After this, details of the numerical model are described, and simulation results are presented and discussed. Finally, experimental velocities are compared to the simulation results.

Chapter 6 gives a brief presentation of the principles of Raman scattering. A semi-classical approach is used to explain how the properties of the target material influence the Raman signal, and how this gives each material a unique signature.

Chapter 7 presents results from the Raman based cell proliferation study. The first section describes cell replication and presents different methods used to measure cell proliferation. This is followed by a description of the measurement procedure, the experimental setup, and the data analysis. A separate section then describes the results from the experiment, which in the last section are analyzed and discussed.

Chapter 8 presents results from the study using Raman scattering to characterize microspheres on top of waveguides. The chapter begins with a description of the experimental setups and the waveguide designs. The following section describes the experimental procedures and presents the resulting spectra from each setup configuration. Finally, the possibilities and limitations of each experiment is discussed, and setup improvements are suggested.

Chapter 9 concludes the thesis. The main aim and the main results of the work are summed up, and future possibilities are discussed.

**Published results**

Some of the results in the thesis have been presented at conferences, some have been a part of peer reviewed publications, and some have not yet been published. It is not yet decided which parts will be edited for further publishing. The following list includes publications the author has been contributing to during the work with the thesis. An asterisk denotes publications which include work that is described in the thesis. The reason some of the publications is not described is due to the topic being out of the scope of the thesis. This applies to the work of Rao et al., which focuses on surfaced-enhanced Raman spectroscopy, the work of Gastinger et al., which focuses on low coherence speckle interferometri, and the latest work of Ahluwalia et al., which focuses on waveguide loop simulations.

- Balpreet Singh Ahluwalia, Olav Gaute Hellesø, Pål Løvhaugen, Ananth Z. Subramanian, and James S. Wilkinson. Surface transport and stable trapping of particles and cells by an optical waveguide loop. *Lab on a Chip*, 2012
- *Balpreet Singh Ahluwalia, Pål Løvhaugen, and Olav Gaute Hellesø. Waveguide trapping of hollow glass spheres. *Optics Letters*, 36(17), 2011
- *Pål Løvhaugen, Balpreet Singh Ahluwalia, Thomas R. Huser, Peter McCourt, and Olav Gaute Hellesø. Optical trapping forces on biological cells on a waveguide surface. In *Proceedings of SPIE*, volume 7902, 2011
- *Pål Løvhaugen, Balpreet Singh Ahluwalia, and Olav Gaute Hellesø. Optical waveguide trapping forces on hollow glass spheres. In *Proceedings of SPIE*, volume 7950, 2011
- Satish Rao, Štefan Bálint, Pål Løvhaugen, Mark Kreuzer, and Dmitri Petrov. Measurement of mechanical forces acting on optically trapped dielectric spheres induced by surface-enhanced raman scattering. *Physical Review Letters*, 102:087401, 2009
- Kay Gastinger, Pål Løvhaugen, and Ola Hunderi. Numerical simulations of interferometrical deformation measurements in multi-layered objects. In *Proceedings of SPIE*, volume 6995, 2008

# Chapter 2

# Optical Waveguides and Optical Forces

## 2.1 Introduction

This chapter is meant to provide the reader an understanding of the principles behind the experimental and numerical work presented in the thesis. Background theory on two topics are presented in the chapter; optical waveguides (confinement of the optical field) and optical forces (trapping by the optical field)[1]. Some of the theory described here will also be used in chapter 6 on Raman scattering.

The chapter starts with presenting some basic electromagnetic theory in section 2.2. Section 2.3 gives an overview of fundamental waveguide theory, describing how the field propagates in an optical waveguide. Section 2.4 introduces waveguide production methods and presents materials, dimensions and loss properties of the waveguides used in the experiments described in chapter 8. Section 2.5 presents a general background on how a field exerts a force on a dielectric object and how the forces can be calculated. Finally, section 2.6 presents how optical forces are used to trap small particles, either with a Gaussian beam or on top of a waveguide. The brief descriptions of theories and methods are complemented with relevant references throughout the chapter.

[1] In this context, the term light refers to radiation in the visible, ultraviolet and infrared spectra. However, the wavelengths considered in the thesis are in the near infrared spectrum.

## 2.2 Basic Electromagnetic Theory

The theory of propagation of electromagnetic fields is well known, and described in any textbook on electromagnetic theory, e.g. Jackson [7]. Much of the theory described in the following sections follow the derivations given by Lee [8].

This section describes the parts of electromagnetic theory that are relevant for later sections and chapters. To start with, Maxwell's equations and Lorentz' force equation are stated, followed by Helmholtz' equation for monochromatic fields. Finally, reflection, refraction and polarization properties of a plane wave are presented. This provides a brief, but sufficient background for the topic of optical waveguides in section 2.3. The treatment of optical forces in section 2.5 is also based on this section, but will in addition be supplemented with some theory on electrostatic fields.

### 2.2.1 Maxwell's Equations

The behavior of electromagnetic fields are described by Maxwell's equations, derived in the nineteenth century,

$$\nabla \times \mathbf{E}(\mathbf{r}, t) = -\frac{\partial}{\partial t}\mathbf{B}(\mathbf{r}, t) \tag{2.1}$$

$$\nabla \times \mathbf{H}(\mathbf{r}, t) = \frac{\partial}{\partial t}\mathbf{D}(\mathbf{r}, t) + \mathbf{J}(\mathbf{r}, t) \tag{2.2}$$

$$\nabla \cdot \mathbf{D}(\mathbf{r}, t) = \rho(\mathbf{r}, t) \tag{2.3}$$

$$\nabla \cdot \mathbf{B}(\mathbf{r}, t) = 0. \tag{2.4}$$

Here, **r** is the position in space and $t$ is the time. **J** is the current density and $\rho$ is the charge density in the medium. **E** and **H** are the electric and magnetic field vectors, respectively, and **D**=$\epsilon$**E** and **B**=$\mu$**H** is the electric and magnetic displacement vectors, describing the fields inside electrically and magnetically polarized media, respectively. The permittivity $\epsilon$=$\epsilon_r\epsilon_0$ is the polarization factor of the medium, and the permeability $\mu$=$\mu_r\mu_0$ is the magnetization factor of the medium, using $\epsilon_0$ as the permittivity in vacuum and $\mu_0$ as the permeability in vacuum.

### 2.2.2 Lorentz' Force Equation

The starting point for the derivations of optical forces given in section 2.5 is Lorentz' force equation

$$\mathbf{f}(\mathbf{r},t) = \rho(\mathbf{r},t)\mathbf{E}(\mathbf{r},t) + \mathbf{J}(\mathbf{r},t) \times \mathbf{B}(\mathbf{r},t). \tag{2.5}$$

This equation states how the charge density $\rho$ and current density **J** in the local electric and magnetic fields **E** and **B** relate to an applied force density **f**.

### 2.2.3 Helmholtz' Equation

When the electromagnetic field propagates as a time harmonic wave with a field amplitude $\mathbf{A}_0$, each of the magnetic and electric fields can be described by an equation

$$\mathbf{A}(\mathbf{r},t) = \mathbf{A}_0(\mathbf{r})e^{\jmath\omega t - \jmath\mathbf{kr}}, \tag{2.6}$$

where $\jmath$ is the imaginary unit, $\omega$ is the angular frequency of the field, and **k** is the wave number of the field. The wave number gives direction and velocity to the field. It is inversely proportional to the wavelength $\lambda/n$, $|\mathbf{k}|$=k=$2\pi n/\lambda$= $\omega n/c$, where c is the propagation velocity of the field in vacuum and $n$ is the refractive index of the medium.

If a time harmonic field propagates in a non-magnetic media without free currents **J** and free charges $\rho$, Maxwell's equations can be written

$$\nabla \times \mathbf{E}(\mathbf{r}) = -\jmath\omega\mathbf{B}(\mathbf{r}) \tag{2.7}$$
$$\nabla \times \mathbf{H}(\mathbf{r}) = \jmath\omega\mathbf{D}(\mathbf{r}) \tag{2.8}$$
$$\nabla \cdot \mathbf{D}(\mathbf{r}) = 0 \tag{2.9}$$
$$\nabla \cdot \mathbf{B}(\mathbf{r}) = 0. \tag{2.10}$$

Equations (2.7) and (2.8) can then be used to give [8]

$$\nabla \times \left(\frac{1}{\mu}\nabla \times \mathbf{E}(\mathbf{r})\right) = \omega^2\epsilon\mathbf{E}(\mathbf{r}) \tag{2.11}$$
$$\nabla \times \left(\frac{1}{\epsilon}\nabla \times \mathbf{H}(\mathbf{r})\right) = \omega^2\mu\mathbf{H}(\mathbf{r}). \tag{2.12}$$

For an isotropic medium, these two last equations will, by the use of the vector identity $\nabla \times \nabla \times \mathbf{X} = \nabla(\nabla \cdot \mathbf{X}) - \nabla^2\mathbf{X}$, as well as equations (2.9) and (2.10), give Helmholtz' equation for respectively the electric field

$$\nabla^2\mathbf{E}(\mathbf{r}) - \omega^2\epsilon\mu\mathbf{E}(\mathbf{r}) = 0, \tag{2.13}$$

and the magnetic field

$$\nabla^2\mathbf{H}(\mathbf{r}) - \omega^2\epsilon\mu\mathbf{H}(\mathbf{r}) = 0. \tag{2.14}$$

From here on, only discretely separated isotropic and homogeneous media are considered. In such media, the electric field component of a harmonic plane wave is described by $\mathbf{E}(\mathbf{r})$=$\mathbf{E}_0 e^{-\jmath\mathbf{kr}}$. Equation (2.13) then gives the propagation constant

$$\mathbf{k}^2 = \mathrm{k}_x^2 + \mathrm{k}_y^2 + \mathrm{k}_z^2 = \omega^2\epsilon\mu \equiv \mathrm{k}_0^2 n^2, \tag{2.15}$$

where $\mathrm{k}_0$ is defined as the wave number in vacuum, the refractive index in the medium is defined as $n = \sqrt{\epsilon_r\mu_r} = c\sqrt{\epsilon\mu}$, and the propagation speed of the field in empty space is given by $c = 1/\sqrt{\epsilon_0\mu_0}$.

Equation (2.15) is the dispersion relation in the isotropic and homogeneous medium. In general, a dispersion relation describes the dependencies between the velocity, phase and frequency of the field in a medium.

### 2.2.4 Reflection and Refraction

At the boundary between two media, a propagating field is reflected and transmitted. The polarization and direction of the field and the permittivity and permeability of the media determines the nature of the reflected and transmitted fields, as shown in the following paragraphs.

Figure 2.1 a) shows the transmitted and reflected fields of a plane wave incident on the horizontal plane between two homogeneous media with permittivities $\epsilon_1$ and $\epsilon_2$ and permeabilities $\mu_1$ and $\mu_2$. The directions of the fields are described relative to the surface normal with $\theta_\mathrm{i}$, $\theta_\mathrm{r}$ and $\theta_\mathrm{t}$, where the subscripts i, r and t indicate incident, reflected and transmitted fields, respectively. At a boundary, Maxwell's equations require the tangential component of the electric and magnetic fields to be continuous [9]. Assuming (without loss of generality) that the boundary plane is situated such that the perpendicular component $\mathbf{r}^\perp$ ($x$ in figure) is 0, only the tangential directions $\mathbf{r}^\parallel$ (parallel to the boundary, $z$ in figure) need to be considered:

$$\left[\mathbf{E}_{0\mathrm{i}} e^{-\jmath\mathbf{k}_\mathrm{i}^\parallel\mathbf{r}^\parallel} + \mathbf{E}_{0\mathrm{r}} e^{-\jmath\mathbf{k}_\mathrm{r}^\parallel\mathbf{r}^\parallel}\right]^\parallel = \left[\mathbf{E}_{0\mathrm{t}} e^{-\jmath\mathbf{k}_\mathrm{t}^\parallel\mathbf{r}^\parallel}\right]^\parallel, \tag{2.16}$$

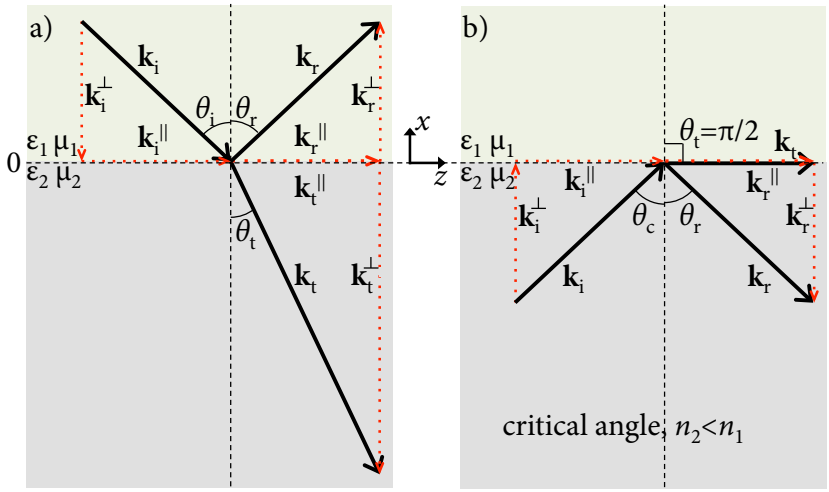


Figure 2.1: An incident field with wave vector $\mathbf{k}_i$ is refracted and reflected at the boundary between two media with permittivities $\epsilon_1<\epsilon_2$. The direction of each field is defined relative to the surface normal. The tangential wave vector components $\mathbf{k}^\parallel$ are equal for the fields.

where $\mathbf{E}_0$ indicates electric field amplitudes and $^\parallel$ indicates that the components are tangential. The relation in equation (2.16) is independent of the position $\mathbf{r}^\parallel$ where the field intersects the plane. Thus the tangential components of the wave vectors $\mathbf{k}$ must be constant and equal,

$$\mathbf{k}_i^\parallel = \mathbf{k}_r^\parallel = \mathbf{k}_t^\parallel \equiv \mathbf{k}^\parallel, \tag{2.17}$$

such that the wave numbers only depend on the medium; $|\mathbf{k}_i|=|\mathbf{k}_r|=k_1=2\pi n_1/\lambda$ in medium 1 and $|\mathbf{k}_t|=k_2=2\pi n_2/\lambda$ in medium 2.

From figure 2.1,

$$k_1 \sin\theta_i = k_1 \sin\theta_r = k_2 \sin\theta_t\,. \tag{2.18}$$

The equality implies that both the reflected and transmitted fields lie in the plane defined by the incident field. The relation also gives the directions of the reflected and transmitted fields:

$$\theta_i = \theta_r \quad \text{(reflection law)} \tag{2.19}$$

$$n_1 \sin\theta_i = n_2 \sin\theta_t \quad \text{(refraction law)}. \tag{2.20}$$

The thesis will only consider non-magnetic media. Thus, the relative permeabilities $\mu_r$ can be assumed to be equal to 1, and (from equation (2.15)) $n=\sqrt{\epsilon_r}$ in all media.

For a field propagating into a medium with lower refractive index ($n_2$<$n_1$) as in figure 2.1 b), incidence angles larger than a critical angle $\theta_c$= $\sin^{-1}(n_2/n_1)$ are undefined from the refraction law, equation (2.20). For such angles, there is total internal reflection, and no field is transmitted into medium 1. From equations (2.17) and (2.18) and figure 2.1 it can be found that

$$\mathrm{k}_\mathrm{t}^\perp = \pm\sqrt{\mathrm{k}_\mathrm{t}^2 - \mathrm{k}_\mathrm{t}^\parallel} = \pm\sqrt{\mathrm{k}_\mathrm{t}^2 - \mathrm{k}_\mathrm{r}^\parallel} = \pm\sqrt{\mathrm{k}_2^2 - \mathrm{k}_1^2 \sin^2\theta_\mathrm{r}}. \tag{2.21}$$

For $\mathrm{k}_1 \sin\theta_\mathrm{i}$ larger than $\mathrm{k}_2$ ($\theta_\mathrm{i}$> $\theta_\mathrm{c}$), the wave vector in the low-index medium $\mathrm{k}_t^\perp$ is imaginary,

$$\mathrm{k}_\mathrm{t}^\perp = \pm\jmath\sqrt{\mathrm{k}_1^2 \sin^2\theta_\mathrm{i} - \mathrm{k}_2^2} = \pm\jmath\tilde{\mathrm{k}}_\mathrm{t}^\perp = -\jmath\tilde{\mathrm{k}}_\mathrm{t}^\perp. \tag{2.22}$$

The negative value of the square root is chosen to avoid unphysical exponential growth of the transmitted field ($\mathrm{r}^\perp$> 0). The field amplitude of the transmitted field is then decaying away from the boundary plane,

$$\mathbf{E}_\mathrm{t} = \mathbf{E}_{0\mathrm{t}} e^{\jmath(\omega t - \mathbf{k}_\mathrm{t}\cdot\mathbf{r})} = \mathbf{E}_{0\mathrm{t}} e^{-\tilde{\mathrm{k}}_\mathrm{t}^\perp \mathrm{r}^\perp} e^{\jmath\left(\omega t - \mathrm{k}_\mathrm{t}^\parallel \mathrm{r}^\parallel\right)}. \tag{2.23}$$

The power flow of a field is represented by the real Poynting vector [8] $\mathbf{S} = \mathbf{E}\times\mathbf{H}^*$, where $^*$ indicates the complex conjugate. In the case of total internal reflection, and for a unity vector $\hat{\mathbf{r}}^\perp$ in the direction perpendicular to the boundary plane, the power flow in the direction out of the medium is found from the time average of $\mathbf{S}\cdot\hat{\mathbf{r}}^\perp$ in medium 2,

$$\frac{1}{2}\mathrm{Re}\left\{(\mathbf{E}_\mathrm{t}\times\mathbf{H}_\mathrm{t}^*)\cdot\hat{\mathbf{r}}^\perp\right\} \propto \mathrm{Re}\left\{\mathbf{k}_\mathrm{t}\cdot\hat{\mathbf{r}}^\perp\right\} = \mathrm{Re}\left\{\mathbf{k}_\mathrm{t}^\perp\cdot\hat{\mathbf{r}}^\perp\right\} = 0. \tag{2.24}$$

since from equation (2.22), $\mathrm{k}_\mathrm{t}^\perp$ is purely imaginary for total internal reflection. Thus, the evanescent field does not lead to power dissipating out of the medium.

### 2.2.5 Polarization and the Fresnel Equations

An electromagnetic field oscillates transversal to the propagation direction. The direction of the oscillation is called the polarization of the field. The intensity and phase changes of the field at a boundary can only be described by including the polarization. When the polarization of electric field is orthogonal to the plane of incidence (pointing out of the page, the $y$-direction in figure 2.1), the field is said to

be transverse electric (TE). When the polarization of the magnetic field is orthogonal to the plane of incidence, the field is said to be transverse magnetic (TM).

The continuity conditions at the boundary are different for TE and TM polarized fields. This leads to different relations for the coefficient R of the reflected-to-incident field ratio and the coefficient T of transmitted-to-incident field ratio, which are related by [8]

$$1 + \mathrm{R} = \mathrm{T} \tag{2.25}$$

$$1 - \mathrm{R} = \frac{\mathrm{k}_\mathrm{t}^\perp}{\mathrm{k}_\mathrm{i}^\perp}\frac{\mu_1}{\mu_2}\mathrm{T}. \tag{2.26}$$

The coefficients are described by the Fresnel equations. For TE waves the coefficients are

$$\mathrm{R}^{\mathrm{TE}} = \frac{1 - (\mu_1/\mu_2)(\mathrm{k}_\mathrm{t}^\perp/\mathrm{k}_\mathrm{i}^\perp)}{1 + (\mu_1/\mu_2)(\mathrm{k}_\mathrm{t}^\perp/\mathrm{k}_\mathrm{i}^\perp)} \tag{2.27}$$

$$\mathrm{T}^{\mathrm{TE}} = \frac{2}{1 + (\mu_1/\mu_2)(\mathrm{k}_\mathrm{t}^\perp/\mathrm{k}_\mathrm{i}^\perp)}, \tag{2.28}$$

and for TM waves the coefficients are

$$\mathrm{R}^{\mathrm{TM}} = \frac{1 - (\epsilon_1/\epsilon_2)(\mathrm{k}_\mathrm{t}^\perp/\mathrm{k}_\mathrm{i}^\perp)}{1 + (\epsilon_1/\epsilon_2)(\mathrm{k}_\mathrm{t}^\perp/\mathrm{k}_\mathrm{i}^\perp)} \tag{2.29}$$

$$\mathrm{T}^{\mathrm{TM}} = \frac{2}{1 + (\epsilon_1/\epsilon_2)(\mathrm{k}_\mathrm{t}^\perp/\mathrm{k}_\mathrm{i}^\perp)}. \tag{2.30}$$

The coefficients of reflection and transmission contain information on both amplitude and phase, and are not limited to real values.

In the case of total internal reflection ($\theta_\mathrm{i} \geq \theta_\mathrm{c}$), $\mathrm{k}_\mathrm{t}^\perp = -\jmath\tilde{\mathrm{k}}_\mathrm{t}^\perp$ is imaginary. Thus,

$$|\mathrm{R}^{\mathrm{TE}}| = |\mathrm{R}^{\mathrm{TM}}| = 1, \tag{2.31}$$

and the reflection phase shifts are found from R=|R|$e^{\jmath\phi}$ to be[2]

$$\phi^{\mathrm{TE}} = 2\tan^{-1}\left(\frac{\mu_1}{\mu_2}\frac{\tilde{\mathrm{k}}_{\mathrm{t}}^{\perp}}{\mathrm{k}_{\mathrm{i}}^{\perp}}\right) \tag{2.32}$$

and

$$\phi^{\mathrm{TM}} = 2\tan^{-1}\left(\frac{\epsilon_1}{\epsilon_2}\frac{\tilde{\mathrm{k}}_{\mathrm{t}}^{\perp}}{\mathrm{k}_{\mathrm{i}}^{\perp}}\right). \tag{2.33}$$

## 2.3 Principles of Optical Waveguides

Waveguides are passive structures where a propagating electromagnetic field follows the structure geometry. The confinement of the fields is due to total internal reflection caused by the refractive index difference between the passive structure and the surrounding regions. In the waveguide cross section transversal to the energy flow, standing wave patterns, like the ones seen in figure 2.6, arise. The pattern is determined by the wavelength, geometry and refractive indices of the structure. For a dielectric waveguide material, there is a strong real field inside the waveguide and a weaker, decaying field in the regions outside the waveguide. The decaying field is called the evanescent field.

Monochromatic and coherent laser light can be confined in sub-micrometer sized waveguides. Such structures can be used for sensing [11, 12] or propagation of micro- and nanoparticles [13, 14]. As the cross sections of such waveguides are in the wavelength range, low-loss materials and smooth surfaces are necessary to prevent significant scattering losses. In this section, the basic properties of waveguide modes in one and two dimensions are described using the properties of total internal reflection that was described in section 2.2.4.

### 2.3.1 Slab Waveguides

When the field is confined in only one direction, the guiding structure is called a slab waveguide. Figure 2.2 shows the cross section of an asymmetric slab waveguide of thickness $d$. In the waveguide, the guiding, or core, medium has a permittivity

[2] A short derivation can be found in e.g. Born & Wolf [10], section 1.5.4.

$\epsilon_g$, which is greater than the surrounding permittivities $\epsilon_s$ of the substrate medium and $\epsilon_c$ of the cover medium.

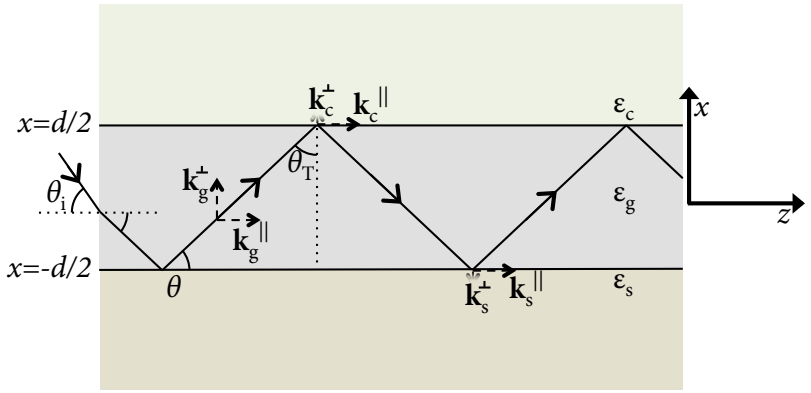


Figure 2.2: A propagating field in the $xz$-plane of a slab waveguide. The field continuity conditions at the guide-cover and guide-substrate boundaries are satisfied, such that the tangential wave vector components are equal, $k_c^{\|} = k_g^{\|} = k_s^{\|} = k^{\|}$. Total internal reflection leads to purely imaginary perpendicular wave vector components in the cover and substrate, Re$\{k_c^{\perp}, k_s^{\perp}\}$=0, and all propagating fields are bounded in the $x$-direction with transversal distributions given by standing wave patterns

At some input angles $\theta_i$, the fields create standing waves in the orthogonal direction in the guiding core medium. The spatial distribution of the field's standing wave pattern is called the waveguide mode. The mode is generated when the propagating rays combine and create a common wavefront. The field of the propagating modes can be described when the field is decaying in the cover and substrate media and the continuity conditions of the field are satisfied. Defining wave numbers $\mathbf{k}_c$, $\mathbf{k}_g$ and $\mathbf{k}_s$ in the cover, guiding core and substrate media, respectively, the calculations are described by Lee [8]. For the cross section in the $xz$-plane shown in figure 2.2, the field is

$$A_y(x,z) = A_0 \left\{ \begin{array}{l} \cos(k_g^{\perp} d/2 + \psi) e^{-\tilde{k}_c^{\perp}(x-d/2)} \\ \cos(k_g^{\perp} d/2 + \psi) \\ \cos(k_g^{\perp} d/2 - \psi) e^{+\tilde{k}_s^{\perp}(x+d/2)} \end{array} \right\} e^{-jk^{\|}z} \begin{array}{rcl} x & > & d/2 \\ |x| & \leq & d/2 \\ x & < & -d/2 \end{array} \quad (2.34)$$

where $\psi$ is a polarization dependent parameter given by

$$\left.\begin{array}{l} \mathrm{k}_{\mathrm{g}}^{\perp} d/2 + \psi = \frac{1}{2}\phi_{\mathrm{c}}^{\mathrm{TE}} \pm p\pi \\ \mathrm{k}_{\mathrm{g}}^{\perp} d/2 - \psi = \frac{1}{2}\phi_{\mathrm{s}}^{\mathrm{TE}} \pm p\pi \end{array}\right\} \quad \text{for TE polarized fields, and} \tag{2.35}$$

$$\left.\begin{array}{l} \mathrm{k}_{\mathrm{g}}^{\perp} d/2 + \psi = \frac{1}{2}\phi_{\mathrm{c}}^{\mathrm{TM}} \pm p\pi \\ \mathrm{k}_{\mathrm{g}}^{\perp} d/2 - \psi = \frac{1}{2}\phi_{\mathrm{s}}^{\mathrm{TM}} \pm p\pi \end{array}\right\} \quad \text{for TM polarized fields,} \tag{2.36}$$

with phase shifts given by

$$\phi_{\mathrm{c}}^{\mathrm{TE}} = 2\tan^{-1}\left((\mu_{\mathrm{g}}\tilde{\mathrm{k}}_{\mathrm{c}}^{\perp})/(\mu_{\mathrm{c}}\mathrm{k}_{\mathrm{g}}^{\perp})\right) \tag{2.37}$$

$$\phi_{\mathrm{s}}^{\mathrm{TE}} = 2\tan^{-1}\left((\mu_{\mathrm{g}}\tilde{\mathrm{k}}_{\mathrm{s}}^{\perp})/(\mu_{\mathrm{s}}\mathrm{k}_{\mathrm{g}}^{\perp})\right) \tag{2.38}$$

$$\phi_{\mathrm{c}}^{\mathrm{TM}} = 2\tan^{-1}\left((\epsilon_{\mathrm{g}}\tilde{\mathrm{k}}_{\mathrm{c}}^{\perp})/(\epsilon_{\mathrm{c}}\mathrm{k}_{\mathrm{g}}^{\perp})\right) \tag{2.39}$$

$$\phi_{\mathrm{s}}^{\mathrm{TM}} = 2\tan^{-1}\left((\epsilon_{\mathrm{g}}\tilde{\mathrm{k}}_{\mathrm{c}}^{\perp})/(\epsilon_{\mathrm{c}}\mathrm{k}_{\mathrm{g}}^{\perp})\right), \tag{2.40}$$

and $p$ is a positive integer called the mode number. From equations (2.35) and (2.36), the dispersion relations for mode $p$ is found to be

$$2\mathrm{k}_{\mathrm{g}}^{\perp} d - \phi_{\mathrm{c}}^{\mathrm{TE}} - \phi_{\mathrm{s}}^{\mathrm{TE}} = 2p\pi \quad \text{(TE)} \tag{2.41}$$

and

$$2\mathrm{k}_{\mathrm{g}}^{\perp} d - \phi_{\mathrm{c}}^{\mathrm{TM}} - \phi_{\mathrm{s}}^{\mathrm{TM}} = 2p\pi \quad \text{(TM)} \tag{2.42}$$

for the two polarizations.

By introducing an effective permittivity $\epsilon_{\mathrm{eff}}$, an effective refractive index $n_{\mathrm{eff}}=\sqrt{\epsilon_{\mathrm{eff}}/\epsilon_0}$ can be defined, leading to a propagation constant $\mathrm{k}^{\parallel}=\omega\sqrt{\mu\epsilon_{\mathrm{eff}}}$. From this, the dispersive relations can be written as

$$\omega d\sqrt{\mu\epsilon_0}\sqrt{\frac{\epsilon_{\mathrm{g}} - \epsilon_{\mathrm{eff},p}^{\mathrm{TE}}}{\epsilon_0}} = p\pi + \tan^{-1}\left(\sqrt{\frac{\epsilon_{\mathrm{c}}}{\epsilon_{\mathrm{g}}}}\sqrt{\frac{\epsilon_{\mathrm{eff},p}^{\mathrm{TE}}/\epsilon_{\mathrm{c}} - 1}{1 - \epsilon_{\mathrm{eff},p}^{\mathrm{TE}}/\epsilon_{\mathrm{g}}}}\right) + \tan^{-1}\left(\sqrt{\frac{\epsilon_{\mathrm{s}}}{\epsilon_{\mathrm{g}}}}\sqrt{\frac{\epsilon_{\mathrm{eff},p}^{\mathrm{TE}}/\epsilon_{\mathrm{s}} - 1}{1 - \epsilon_{\mathrm{eff},p}^{\mathrm{TE}}/\epsilon_{\mathrm{g}}}}\right) \quad \text{(TE)} \tag{2.43}$$

and

$$\omega d\sqrt{\mu\epsilon_0}\sqrt{\frac{\epsilon_{\mathrm{g}}-\epsilon_{\mathrm{eff},p}^{\mathrm{TM}}}{\epsilon_0}} = p\pi + \tan^{-1}\left(\sqrt{\frac{\epsilon_{\mathrm{g}}}{\epsilon_{\mathrm{c}}}}\sqrt{\frac{\epsilon_{\mathrm{eff},p}^{\mathrm{TM}}/\epsilon_{\mathrm{c}}-1}{1-\epsilon_{\mathrm{eff},p}^{\mathrm{TM}}/\epsilon_{\mathrm{g}}}}\right) + \tan^{-1}\left(\sqrt{\frac{\epsilon_{\mathrm{g}}}{\epsilon_{\mathrm{s}}}}\sqrt{\frac{\epsilon_{\mathrm{eff},p}^{\mathrm{TM}}/\epsilon_{\mathrm{s}}-1}{1-\epsilon_{\mathrm{eff},p}^{\mathrm{TM,}}/\epsilon_{\mathrm{g}}}}\right) \quad \text{(TM)} \quad (2.44)$$

with the help of the relations

$$\tilde{\mathrm{k}}_{\mathrm{c}}^{\perp} = \sqrt{\mathrm{k}^{\parallel 2} - \mathrm{k}_{\mathrm{c}}^2} \quad , \quad \mathrm{k}_{\mathrm{g}}^{\perp} = \sqrt{\mathrm{k}_{\mathrm{g}}^2 - \mathrm{k}^{\parallel 2}} \quad \text{and} \quad \tilde{\mathrm{k}}_{\mathrm{s}}^{\perp} = \sqrt{\mathrm{k}^{\parallel 2} - \mathrm{k}_{\mathrm{s}}^2},$$

and assuming a non-magnetic medium ($\mu_r$=1) as mentioned in section 2.2.4.

Equations (2.43) and (2.44) show that there is a unique effective permittivity for each mode number and polarization. Four other observations can also be noted.

First, an increase of the frequency $\omega$ or thickness $d$ allows solutions for larger $p$ such that a higher number of modes are possible. A single-mode waveguide is realized when only one mode exists ($p$=0). In a multi-mode waveguide, the $p$=0 mode is called the fundamental mode.

Second, solutions to the dispersion relations can only be found when the guiding core permittivity is larger than the cover and substrate permittivities. This satisfies the condition of total internal reflection. The effective permittivity of the mode always has a value between the material permittivities such that $\epsilon_{\mathrm{g}} > \epsilon_{\mathrm{eff}} > \{\epsilon_{\mathrm{c}}, \epsilon_{\mathrm{s}}\}$.

Third, if the waveguide thickness is close to the free space wavelength ($\omega d \simeq 1$), and the effective permittivity is close to the waveguide core permittivity, the differences between all the permittivities are small. This means that the field is distributed far into both the cover and substrate regions (the decay constants $\tilde{\mathrm{k}}^{\perp}$ are small). Conversely, an effective permittivity much smaller than the waveguide permittivity implies that the field is largely confined in the guiding core medium.

Finally, the arctangent arguments differs between the TE and TM dispersion relations. A large waveguide permittivity $\epsilon_{\mathrm{g}}$ leads to a small TE arctangent argument and a large TM arctangent argument. Since the waveguide permittivity also contributes to the left hand side of the equation, the TE mode requires a lower frequency than the TM mode to fulfill the equality. As such, for a specific frequency, the first allowed mode in the slab structure is a TE mode.

### 2.3.2 Channel Waveguides

By confining the field in two directions, a channel waveguide is formed. The cross section geometry of the channel waveguide determines the field distribution. The most common cross sections are the circular and the rectangular. The circle-symmetric cross section, for which an analytical solution involving Bessel functions[3] can be found, is commonly used in optical fibers. The rectangular cross section is discussed in this paragraph, and will be used in the following chapters. Other cross sections include graded-index structures, where the index transition between the media is smooth, for example due to an ion exchange process [16], and the photonic crystal cross section, which uses a periodic structure for guiding. Photonic crystal fibers can be designed for specific photonic bandgaps, and a short review by Russel is given in [17]. Figure 2.3 shows cross sections of different channel waveguide structures.

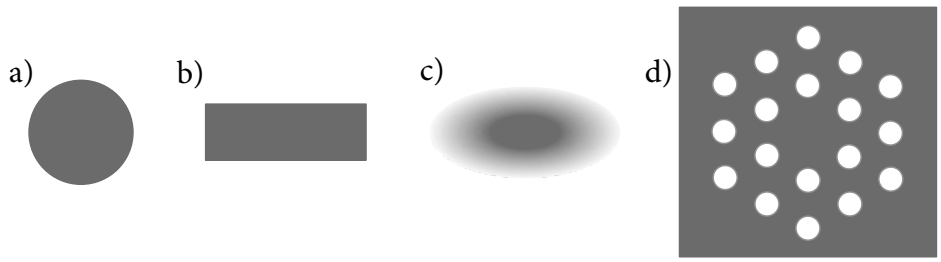


Figure 2.3: Cross sections of a) circular, b) rectangular, c) graded-index and d) periodic photonic crystal channel waveguides. Light and dark shading indicates the permittivity distribution.

#### Strip waveguides

Rectangular channel waveguides can be configured in different structures, as seen in figure 2.4. A strip waveguide structure has the channel set on top of the substrate medium such that the cover medium surrounds the guiding core medium on the top and sides. When the guiding core medium is buried in the substrate, the structure is called an embedded strip waveguide. A strip waveguide set on top of a slab waveguide confines the field in the region close to the strip, thereby forming a rib waveguide structure.

[3] See e.g. Stratton [15], section 6.4.

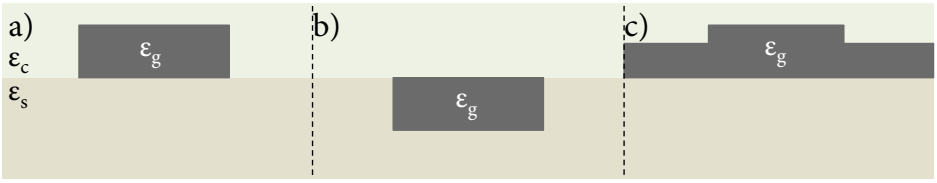


Figure 2.4: Rectangular a) strip, b) embedded strip and c) rib channel waveguides configurations.

As for the slab waveguide, the permittivity and the dimensions of the guiding medium determine how fields propagate in a channel waveguide. The modes need to be described in two dimensions, and are difficult to calculate analytically. Lee [8] describes the effective index method to approximate strip waveguide modes. This method uses the slab calculation introduced in section 2.3.1 successively in the vertical and horizontal directions, as illustrated in figure 2.5. First, a primary effective index $n'_{\text{eff,g}}$ is calculated in the vertical direction at the center of the waveguide with the use of $n_{\text{s}}$, $n_{\text{g}}$, $n_{\text{c}}$ and the thickness $d$. Then, $n'_{\text{eff,g}}$ is used with $n_{\text{c}}$ and the width $w$ in the transversal horizontal direction to calculate the final effective index of the mode, $n_{\text{eff}}$. This approximation gives good results for modes well confined inside the waveguide.

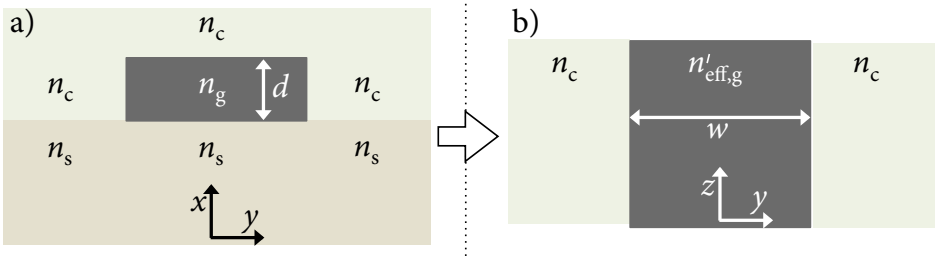


Figure 2.5: Cross sections of a strip waveguide structure illustrating the effective index method. a) A primary effective index $n'_{\text{eff,g}}$ is found in the vertical direction at the center of the waveguide with a a slab waveguide calculation (vertical cross section). b) The calculated effective index is implemented in a slab waveguide calculation in the transversal horizontal direction to find the effective index of the waveguide mode, $n_{\text{eff}}$ (horizontal cross section).

For more precise calculations and more challenging geometries, numerical solutions are necessary to find the propagating modes. Figure 2.6 shows results from a

finite element method simulation[4] where the effective index of a rectangular structure is found for a set of modes. If the electric field is tangential to the horizontal surfaces, the polarization would be transverse electric. If the electric field is tangential to the vertical surfaces, the polarization would be transverse magnetic. The fields in a rectangular waveguide are not perfectly polarized in the horizontal and vertical directions, and are therefore called TE-like and TM-like. The discontinuities and continuities described by the boundary conditions are seen in the figure.

The effective indices, and therefore the propagation constants, of the TE-like modes are seen to be higher than for the TM-like modes, confirming the statement made in section 2.3.1 that the first allowed mode in a structure is a TE mode. A different way to see why this is the case, is to consider the critical angle, which is larger for higher-index media. Therefore, TE-like modes, which have a higher effective refractive index, give total internal reflection for smaller angles than TM-like modes.

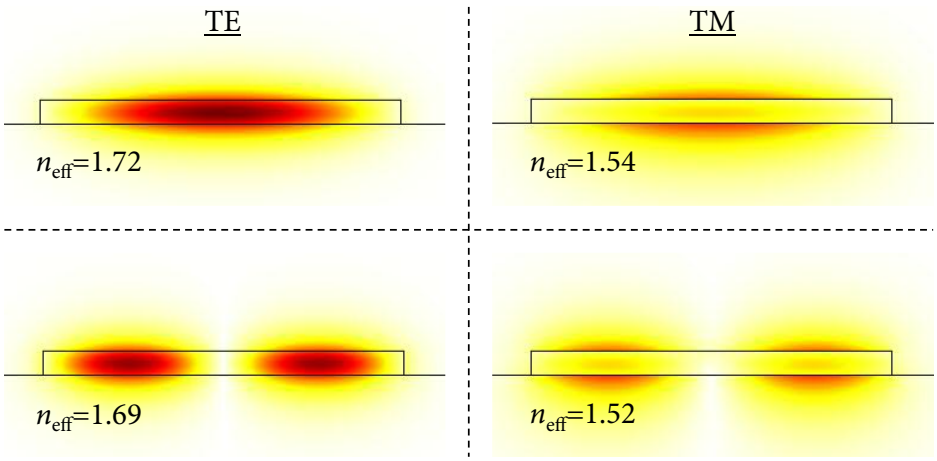


Figure 2.6: Numerical calculation of the effective index, shown with field distributions of the waveguide cross section for the first two modes ($p$=0, $p$=1) of TE and TM polarization. The materials in the structure have indices $n_g$=2.1, $n_c$=1.33, $n_s$=1.45.

[4]Properties of simulations are described in chapter 3.

## 2.4 Tantalum Pentoxide Waveguides

The experiments described in the thesis use channel waveguides of tantalum pentoxide ($Ta_2O_5$) made by Balpreet Ahluwalia and Ananth Subramanian at the Optoelectronic Research Centre (ORC) in Southampton, UK. The production and optimization process is described by Ahluwalia et al. [18]. A short overview of the waveguide production process is given in section 2.4.1. Loss measurements performed on the waveguides in the lab are described in section 2.4.2.

### 2.4.1 Waveguide Fabrication

Subsection 2.6.2 describes how particles in the evanescent field of a waveguide can be optically trapped. To increase the optical trapping forces, the evanescent field and the field gradient need to be strong. This requires strong confinement of the field as well as low waveguide losses.

$Ta_2O_5$ is a metal oxide with high refractive index ($n_{Ta_2O_5}$=2.10@1064 nm). Using this as a waveguide material on a silica substrate ($n_{SiO_2}$=1.45) results in a large refractive index difference ($\Delta n$=0.65). This allows waveguide modes for cross sections as small as 200 nm times 1 μm, and gives strong confinement of the field. $Ta_2O_5$ is also found to have a high damage threshold and low absorption at optical wavelengths. All this makes the material suitable for waveguide trapping. The production process of the waveguides is described in the following paragraphs.

**Magnetron sputtering** A tantalum pentoxide film is deposited on a 5 μm thick oxidized silicon (predominantly silica) substrate with magnetron sputtering. In the sputtering process, $Ta_2O_5$ molecules are released from a bulk sample (target) by ionized argon gas in a low-pressure chamber containing the substrate. The released molecules deposit in a thin layer on the substrate. A magnetic field controls the distribution of the ionized gas plasma to optimize the sputtering efficiency [19].

As described by Ahluwalia et al. [18], the parameters of the sputtering process were adjusted to minimize scattering losses in the waveguide. The optimal parameters are given in table 2.1, and gave losses of 0.4 dB/cm at 633 nm for the 200 nm thick slab waveguides, determined with prism coupling measurements.

Table 2.1: Sputtering parameters

| | |
|---|---|
| substrate temperature | 200 °C |
| magnetron power | 300 W |
| oxygen flow rate[5] | 5 sccm |
| argon flow rate | 20 sccm |

**Photolithography** 1-10 μm wide channel waveguides were patterned on the slab waveguide using a standard photolithography technique. A summary of the process is shown in figure 2.7. First, a layer of photoresist (a chemical sensitive to light) is distributed evenly on the slab waveguide. Then, the slab is covered with a photomask and exposed to UV light. The photoresist regions exposed to light are then removed with plasma ashing, before the exposed $Ta_2O_5$ is removed with ion beam milling, leaving $Ta_2O_5$ waveguide patterns on the silica substrate.

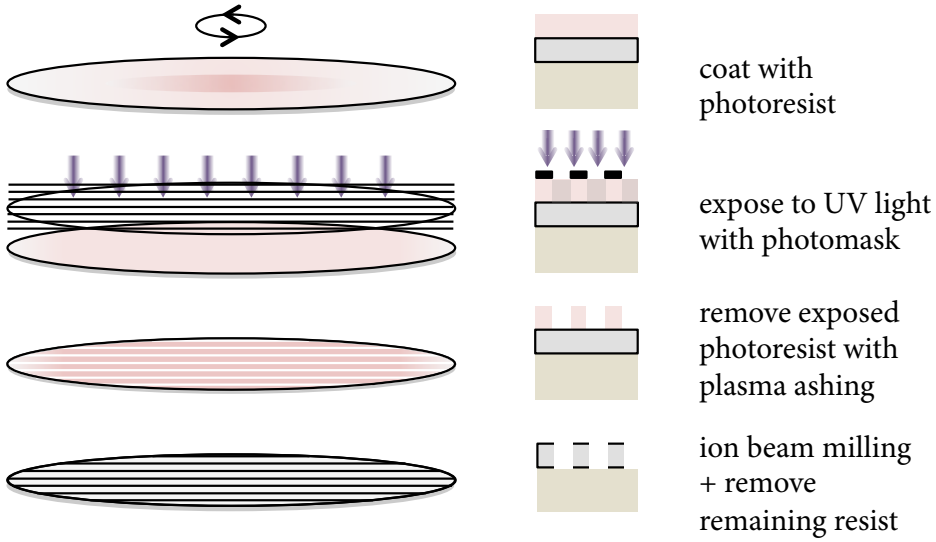


Figure 2.7: Photolithography for channel waveguide production. A thin layer of photoresist is applied to a slab waveguide and exposed to UV light under a photomask pattern. After plasma ashing and ion beam milling, only unexposed waveguide material remains, creating channel waveguides with the pattern of the photomask.

[5]the flow rate unit of the gas, sccm, is defined as cubic centimeters per minute at standard temperature (0 °C) and pressure (1 atm).

**Ion-beam milling** An argon ion beam was used to create the waveguide pattern. The waveguide material remains in the regions covered by photoresist, and thus becomes a copy of the photomask pattern. The ion beam was employed at a 45° angle with the surface to reduce the waveguides' side-wall roughness.

**Plasma ashing** Before and after ion-beam milling, plasma ashing was used to remove photoresist. In the process, reactive monatomic oxygen was introduced on the sample, oxidizing the exposed photoresist to make it easy to remove from the sample.

**Annealing** To relieve the waveguide structure from stresses that arised during the production process, the sample was heated for 5 hours. The temperature was kept at 600 °C, with heating and cooling rates of 3 °C/min. This reduced propagation losses in the channel waveguides to 1 dB/cm [18].

### 2.4.2 Waveguide Losses

Scattering, coupling and absorption reduce the power of the light propagating in the waveguide. This leads to decreased intensity of the light interacting with microparticles on the waveguide surface, and thus also decreases the efficiency of trapping and excitation. This section discusses the magnitude of losses in the waveguides used in the experiments, and compares losses for wavelengths of 785 nm and 1070 nm in one set of waveguide widths. Since only straight waveguides have been considered, bending losses have not been taken into account.

#### Absorption losses

The tantalum pentoxide waveguides used in the experiments were sensitive to heat damage for high input powers, especially for the narrowest waveguides. Absorption by hot spots randomly situated along the waveguide could also lead to permanent disruption of the power flow. To avoid destruction of waveguides and waveguide input facets, the experiments reduced the laser output in the experiments to 1.3W (out of 5 W) for the 1070 nm laser and 0.5-1W (out of 2.5 W) for the tunable 785 nm laser.

### Propagation losses

The sum of scattering and absorption losses gives the total propagation losses for straight waveguides. Earlier examinations [20–22] did not find strong propagation losses in tantalum pentoxide waveguides. However, on narrow waveguides, waveguide trapping experiments were found to be very challenging. A short study of propagation losses was performed to look into this.

Propagation losses in the experimental setup were found by imaging the intensity scattered from the waveguide with a CCD camera. Images were acquired for three different exposure times at positions 1 mm apart along the waveguide. Measurements were done for guiding of both the 785 nm and 1070 nm lasers. Figure 2.8 shows five example images of scattered light (1070 nm) from a 1 μm wide waveguide. The 785 nm laser was linearly polarized at 45 degrees, which indicates that most of the field coupled into the thin waveguide was TE-like. Propagation losses were calculated by integrating the intensity in the waveguide region in each image, and plotting this as a function of propagation length. In the integration, only intensity values close to the center of the waveguide (along the whole waveguide) were included. This was done to reduce contributions to the integral from scatterers on the substrate.

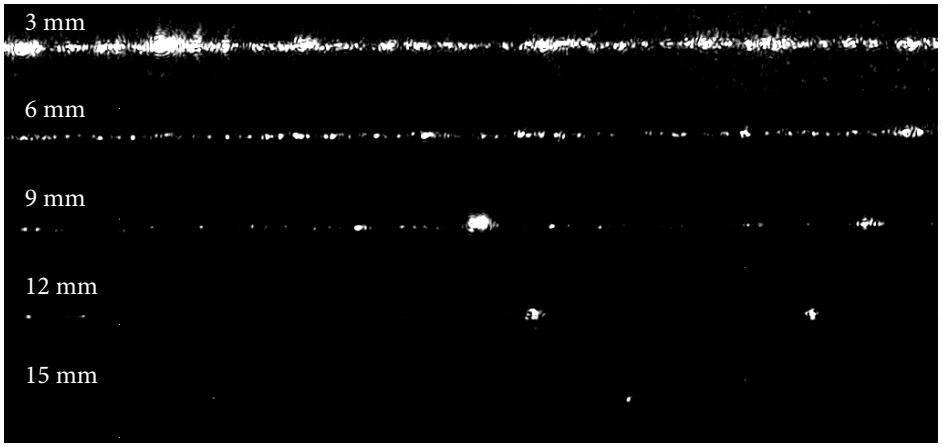


Figure 2.8: Images of 1070 nm light scattered from a 1 μm waveguide at positions 3 mm to 15 mm from the input facet. Integration of the scattered light in each image was used to estimate the propagation losses.

Relative intensity data were found by normalizing the data with the measurement

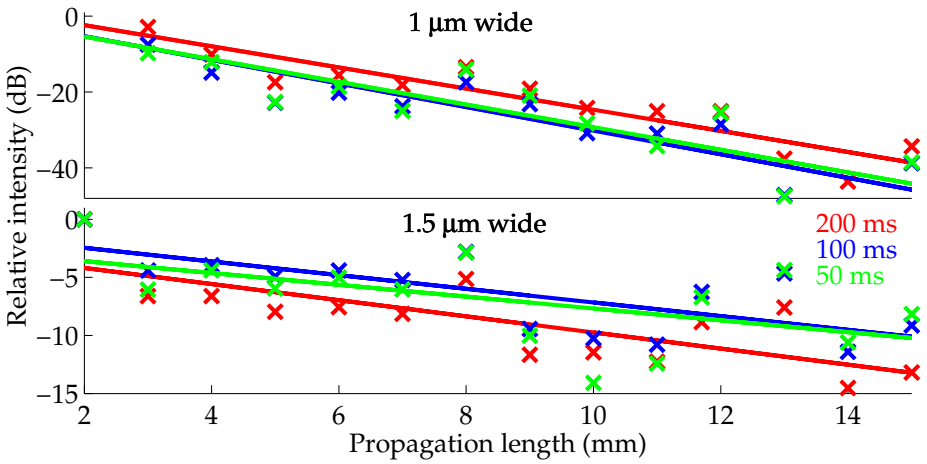


Figure 2.9: Relative scattered intensity along the waveguide for 1070 nm light. Simple linear regression at 50, 100 and 200 ms exposure times are shown for one 1 µm and one 1.5 µm wide waveguide. The average regression line slope give the propagation loss value in table 2.2.

closest to the input facet. The relative intensity data were plotted as a function of distance, as seen in figure 2.9 for 1 µm and 1.5 µm wide waveguides. Loss per unit length was found using simple linear regressions. To prevent effects from CCD saturation, the average slope from three exposure times were used to find the propagation loss values. The values are found in table 2.2. The losses in the 1 µm wide waveguide are significantly stronger than the losses in the wider waveguides. This is in line with the experience from the waveguide trapping experiments (see chapter 8), where trapping on 1 µm wide waveguides only was possible very close to the input facet.

The high losses for the narrow waveguides are probably due to the optical field distribution in the waveguide (see figure 2.6). Small scatterers on the surface of the waveguide, especially on the sidewalls, interact with a much larger part of the field compared to larger waveguides, where most of the field is confined inside the waveguide. This leads to stronger scattering, and thus higher losses.

Quantitative analysis was only performed on only one set of waveguide widths. Qualitatively, the images acquired for the analysis looked similar to images from other experiments, but standard deviations for the estimated propagation loss values have not been found. However, for the measured waveguides, the loss values seem correct for the narrow waveguides. For these, the coefficients of determi-

nation $R^2$, which describes how well the fit describes the data, are high. In table 2.2, the average $R^2$ from the three exposures are given. The $R^2$ values decrease for wider waveguides. This trend can be explained by the smaller losses. Smaller losses makes the relative intensity variation larger, and also makes the measurements more sensitive to contributions from random scatterers on the waveguides.

Table 2.2: Losses versus width and wavelength for a 200 nm thick tantalum pentoxide waveguide core

| | Width (μm) | Propagation Loss (dB/cm) | $R^2$ | Coupling Loss (dB) |
|---|---|---|---|---|
| 785 nm, | 1 | 32.1 | 0.95 | - |
| 300 mW | 1.5 | 6.5 | 0.85 | 25.7 |
| input power | 2 | 3.3 | 0.69 | 19.0 |
| 1070 nm, | 1 | 29.6 | 0.93 | - |
| 680 mW | 1.5 | 6.0 | 0.68 | 17.3 |
| input power | 2 | 2.7 | 0.24 | 10.8 |

In table 2.2, the 785 nm light is seen to have slightly larger scattering losses than the 1070 nm light. Scattering theory (see chapter 6) predicts a wavelength dependence of the fourth power, leading to 5.4 dB more scattering from the 785 nm light. The reason for the found discrepancy is not known. It is possible that the 785 nm light experience less scattering since that wavelength is more confined inside the waveguide than the 1070 nm light. This would lead to less interaction between the light and the waveguide surface, decreasing the losses.

**Coupling losses**

The total waveguide loss was found by collimating and measuring the power from the waveguide output. The power lost by coupling light into the waveguide was approximated by comparing the measured output power with the input power entering the coupling lens. The estimated propagation losses, the length of the waveguide, and the measured coupling lens losses ($\simeq$3 dB) was then used to find the coupling losses. The losses calculated from this are shown in table 2.2. The mode profile of the tunable 785 nm laser was non-Gaussian, as seen in figure 2.10. The low mode quality suggests why there is a 8 dB coupling loss difference between the two different wavelengths, and could also explain the low threshold for heat damages of the input facet (0.5 W) for this laser.

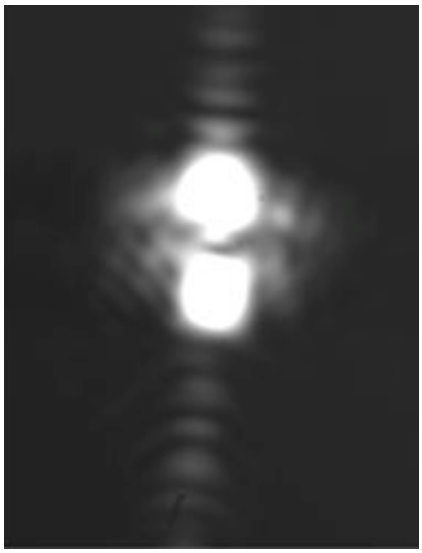

Figure 2.10: Beamprofile of the 785 nm tunable laser. Picture courtesy of Firehun Tsige Dullo [22].

**Loss summary**

Measurements of one set of waveguide widths show that propagation losses increase significantly when the waveguide width decreases down to 1 μm. An exact loss estimate is not found, but the trend agrees with experience from other waveguide experiments. Coupling losses are similarly higher for narrow waveguides, and are noticeably higher for the tunable 785 nm laser due to its a non-Gaussian mode profile.

## 2.5 Principles of Optical Forces

When a light field interacts with matter, forces are exerted on the objects in the field. In the following sections, the forces exerted on a dielectric in an optical field are described, and to a minor extent derived.

In section 2.5.1, the influence of an electrostatic field on dielectric fluids and solids is shown, and a stress tensor formulation for the force is introduced. Then, section 2.5.2 presents the equivalent formulation for magnetostatic fields. Finally, section 2.5.3 introduces forces from electromagnetic fields by considering conservation of energy and momentum. The electromagnetic stress tensor is then compared with the results from the static formulations. The derivations and order of presentation follow the more thorough derivations given by Stratton [15].

Before the theoretical treatment of sections 2.5.1, 2.5.2 and 2.5.3, though, the following two paragraphs give some physical intuition for the optical forces. Hopefully, this will provide the reader with a better understanding of the later theory.

#### Momentum view on forces

When light is incident on a scatterer, the momentum of the photons in the field changes. The change in momentum is transferred to the scatterer. In this way, forces are exerted on the scatterer. The exact change of momentum of light and scatterer is dependent on the properties of the field and the scatterer, and can only be analytically described for some cases: Forces on objects much smaller than the wavelength can be described with Rayleigh theory; forces on objects much larger than the wavelength can be described with geometrical optics; and forces on spherical objects with sizes comparable to the wavelength can be described with Mie theory. In general, a strong field gradient attracts objects when its refractive index is larger than that of the surrounding medium. A full physical description is given by Maxwell's equations.

#### Energy view on forces

As can be seen from the force law, equation (2.5), work is required to introduce a charged particle into a field. This work increases the energy in the field region. For an uncharged particle entering a field, though, it is not evident how the energy of

the system would change. The particle becomes polarized, and creates a counter-field outside its boundaries. This changes the overall field strength, and the energy in the field region changes. The polarization increases with the permittivity, as seen from the Clausius-Mossotti relation

$$\frac{\epsilon/\epsilon_0 - 1}{\epsilon/\epsilon_0 + 2} \propto \tau\alpha, \tag{2.45}$$

where $\tau$ is the mass density and $\alpha$ is the polarizability of the particle. The following paragraphs will show that the negative gradient of the permittivity is proportional to the force. Thus, an increasing permittivity gives a smaller force. Since a smaller force means that less work had to be done to move the particle, the energy in the field region decreases. Transversely, a decrease of the refractive index in the region increases the energy in the field region. In the brief derivation given here, it has been presumed (through the relation between refractive index and polarization) that the mass density in the region is unchanged. It turns out that this is not a necessary condition.

### 2.5.1 Electrostatic Fields

#### Potential energy in an electrostatic field

In a static electric field **E**, the force **F** on charge density $\rho$ of volume $V$ can be found from Lorentz' force law, equation (2.5), to be $\mathbf{F}=\int_V \rho\mathbf{E}\,\mathrm{d}v$. Since the electrostatic field is irrotational, the field can be expressend as the gradient of an electric potential $\Phi$,

$$\mathbf{E} = -\nabla\Phi. \tag{2.46}$$

The work $W$ done by moving a charge in the field a distance $r$ with force **F** is $W=\int_0^r \mathbf{F}\cdot\,\mathrm{d}\mathbf{r}'$. Thus, the acquired potential energy $U$ of the charge distribution $\int_V \rho\,\mathrm{d}v$ moving from position $0$ to $r$ can be expressed with the electric potential as

$$U(r) = -W = \int_0^r \int_V \rho\nabla\Phi\,\mathrm{d}v\cdot\,\mathrm{d}\mathbf{r}' = \int_V \rho\Phi(r)\,\mathrm{d}v, \tag{2.47}$$

where the independence of $\mathrm{d}\mathbf{r}'$ and $\mathrm{d}v$ has been used to apply the fundamental theorem of calculus in the last step.

The energy relation, equation (2.47), will be used as a basis for the force derivations for electrostatic fields described in the following paragraphs.

**Effect on the potential energy when the charge is changed**

Some work needs to be done to change the charge in a uniform medium inside the electric potential $\Phi$ with a small value $\delta\rho$. The required energy can be expressed with the electric field **E** and displacement field **D** by the using Maxwell's law for the divergence of **D**, equation (2.3),

$$\begin{aligned}\delta U &= \int_V \Phi\delta\rho \,\mathrm{d}v = \int_V \Phi\nabla\cdot(\delta\mathbf{D}) \,\mathrm{d}v = \int_V (\nabla\cdot(\Phi\delta\mathbf{D}) - \delta\mathbf{D}\cdot\nabla\Phi) \,\mathrm{d}v \\ &= \int_V (\nabla\cdot(\Phi\delta\mathbf{D}) + \delta\mathbf{D}\cdot\mathbf{E}) \,\mathrm{d}v = \int_V \mathbf{E}\cdot\delta\mathbf{D} \,\mathrm{d}v, \end{aligned} \tag{2.48}$$

where the divergence theorem is used in the last step, assuming a finite charge distribution and a very large integration surface. As the potential decreases as $r^{-1}$, the displacement decreases as $r^{-2}$, and the surface increases as $r^2$, the integral in the first term goes to zero. From equation (2.48) a change of energy *density* in the region can be defined as

$$\delta u = \mathbf{E}\cdot\delta\mathbf{D}, \tag{2.49}$$

a parameter which will be of use later.

For an isotropic and linear medium, $\mathbf{D} = \epsilon\mathbf{E}$. The total potential energy resulting from changing the charge to $\rho$ is then

$$U = \int_\rho \delta U = \int_V \int_\rho \mathbf{E}\cdot\delta(\epsilon\mathbf{E}) \,\mathrm{d}v = \frac{1}{2}\int_V \epsilon E^2 \,\mathrm{d}v, \tag{2.50}$$

which is equal to the work required to bring the charge $\rho$ into $V$. Thus, the introduced charge increases the energy by changing the electric displacement in the medium

**Effect on the potential energy when the dielectric constant is changed**

By introducing a body with dielectric constant $\epsilon_2$ and volume $V$ into an external electrostatic field **E** in an isotropic and linear medium with $\epsilon_1$, it can be shown (section 2.10 of Stratton [15]) that the change of energy is

$$\delta U = \frac{1}{2}\int_V (\epsilon_1 - \epsilon_2)\mathbf{E}\cdot\mathbf{E}' \,\mathrm{d}v, \tag{2.51}$$

where $\mathbf{E}'$ is the field after the introduction of the body. It has been assumed that the curls of both $\mathbf{E}$ and $\mathbf{E}'$ are zero (electrostatic fields), and that the distribution of the original field sources remains unchanged by the introduction of the body (such that the divergence is unchanged, $\nabla \cdot (\mathbf{D} - \mathbf{D}') = 0$. Equation (2.51) states that the energy of the system decreases by introducing higher-permittivity objects. This also implies that the energy decreases by increasing the external field. Thus, higher-permittivity bodies will move toward high field intensities and lower permittivity regions to minimize the total energy. This also means that an infinitesimal increase of permittivity in the system would change the energy by

$$\delta U = -\frac{1}{2} \int \delta\epsilon E^2 \, \mathrm{d}v, \tag{2.52}$$

since for an infinitesimal change, $\mathbf{E} \cdot \mathbf{E}' \simeq E^2$. This result is not analogous to the result in the last paragraph, where an increased charge give a higher total energy. Instead, increasing the permittivity give a lower energy, as mentioned in the *energy view* paragraph on page 26.

### Effect on the force density when a dielectric fluid is displaced

When a dielectric fluid in a constant electrostatic field is displaced at all points $\mathbf{r}$ by an infinitesimal distance $\mathbf{s}$, some work has been done, and the energy of the system is changed. If the sources of the field are kept constant, any change of energy is purely due to a change of permittivity, as seen in equation (2.52). Assuming the permittivity $\epsilon$=$\epsilon(\mathbf{r}, \tau)$ only depends on position $\mathbf{r}$ and mass density $\tau$, the displacement of a small element in the fluid leads to a change in permittivity (section 2.21 of Stratton [15])

$$\delta\epsilon = -\mathbf{s} \cdot \nabla\epsilon + \frac{\partial\epsilon}{\partial\tau}\delta\tau, \tag{2.53}$$

where the first term describes the permittivity change due to the new position of the element, and the second term describes the permittivity change due to the new mass density of the element. The mass of the element remains the same,

$$\tau_1 \, \mathrm{d}v_1 = \tau_2 \, \mathrm{d}v_2 = \tau_2(1 + \nabla \cdot \mathbf{s}) \, \mathrm{d}v_1, \tag{2.54}$$

which gives the infinitesimal change of mass density

$$\delta\tau = \tau_2 - \tau_1 = -\tau\nabla \cdot \mathbf{s}. \tag{2.55}$$

Using the product rule, this gives (from equation (2.52))

$$\begin{aligned}\delta U &= \frac{1}{2}\int_V \left(\nabla\epsilon\cdot\mathbf{s} + \tau\frac{\partial\epsilon}{\partial\tau}\nabla\cdot\mathbf{s}\right)E^2\,\mathrm{d}v \\ &= \int_V \left[\frac{1}{2}E^2\nabla\epsilon - \frac{1}{2}\nabla\left(E^2\tau\frac{\partial\epsilon}{\partial\tau}\right)\right]\cdot\mathbf{s}\,\mathrm{d}v + \frac{1}{2}\int_V \nabla\cdot\left(E^2\tau\frac{\partial\epsilon}{\partial\tau}\mathbf{s}\right)\,\mathrm{d}v.\end{aligned} \tag{2.56}$$

Applying the divergence theorem on the last integral, and letting the region of integration be much larger than the extent of the field, $E^2$ becomes zero at the surface, and only the first integral remains. For some force density $\mathbf{f}$ in a region $V$, the work done to change the energy by $\delta U$ is $\delta W = \int_V \mathbf{f}\cdot\mathbf{s}\,\mathrm{d}v$. Thus, from equation (2.56), the force density in the fluid is

$$\mathbf{f} = -\frac{1}{2}E^2\nabla\epsilon + \frac{1}{2}\nabla\left(E^2\tau\frac{\partial\epsilon}{\partial\tau}\right). \tag{2.57}$$

This means that a slight shift in the fluid position creates a force which depends on both the field strength and how the permittivity varies with space and mass density. Since the volume of the fluid is not changed, the total force on the medium is zero. Thus, mechanical forces exerted on the medium by the electric field are balanced by elastic forces within the medium.

### Effect on the force density when a dielectric solid is displaced

When a dielectric solid in an electrostatic field is displaced without a change of volume, the permittivity changes can be expressed purely by strains in the medium. Assuming the medium to be anisotropic and linear, the changes can be described with the permittivity tensor

$$\delta\epsilon_{jk} = \sum_{l=1}^{3}\sum_{m=1}^{3}\frac{\partial\epsilon_{jk}}{\partial e_{lm}}\delta e_{lm}, \tag{2.58}$$

where $e_{lm}$ are the strain components of the solid body describing the direction and magnitude of the displacement, and $j$, $k$, $l$ and $m$ each represents the three spatial dimensions[6]. From this, the energy density change given in equation (2.49), can

[6] $e_{lm}$ is defined as $\frac{\partial s_l}{\partial x_m}$ for $l$=$m$, and $\frac{1}{2}\left(\frac{\partial s_l}{\partial x_m} + \frac{\partial s_m}{\partial x_l}\right)$ for $l\neq m$, where $\mathbf{s}$ is the displacement vector and $\mathbf{x}$ is the position vector. From this it can also seen that $\nabla\cdot\mathbf{s} = e_{11} + e_{22} + e_{33}$.

be described

$$\delta u = -\frac{1}{2}\sum_{j=1}^{3}\sum_{k=1}^{3}\sum_{l=1}^{3}\sum_{m=1}^{3}\frac{\partial \epsilon_{jk}}{\partial e_{lm}} E_j E_k \, \delta e_{lm}, \tag{2.59}$$

since $\mathbf{E}\cdot\delta\mathbf{D} = \mathbf{D}\cdot\delta\mathbf{E}$ in an anisotropic linear medium. Equation (2.59) describes the change of energy density in an anisotropic solid due to strains from an electric field.

For the specific case of a solid which is isotropic with regards to both electric and elastic properties, it is possible to describe the energy change simpler than in equation (2.59). Directional and rotational invariance due to the isotropy imply that it is sufficient to describe the energy density change in equation (2.59) with only two classes of strain parameters, $a_1$ and $a_2$ (section 2.22 of Stratton [15]). When the permittivity changes due to the deformation are small, the parameters can be expressed

$$a_1 \equiv \frac{\partial \epsilon_{jj}}{\partial e_{jj}} \quad \text{and} \quad a_2 \equiv \frac{\partial \epsilon_{jj}}{\partial e_{kk}}. \tag{2.60}$$

$a_1$ corresponds to increasing permittivity due to elongations in the direction of the electric field. $a_2$ corresponds to increasing permittivity due to strains perpendicular to the electric field.

The change in electrostatic energy density due to the strain in the medium can then be derived from equations (2.59) and (2.60) to be (section 2.22 of Stratton [15])

$$\begin{aligned}\delta u_s = -\frac{1}{2}\Big[&\left(a_1E_1^2 + a_2E_2^2 + a_2E_3^2\right)\delta e_{11} + \left(a_1 - a_2\right)E_2E_3\delta e_{23} + \\ &\left(a_2E_1^2 + a_1E_2^2 + a_2E_3^2\right)\delta e_{22} + \left(a_1 - a_2\right)E_1E_3\delta e_{13} + \\ &\left(a_2E_1^2 + a_2E_2^2 + a_1E_3^2\right)\delta e_{33} + \left(a_1 - a_2\right)E_1E_2\delta e_{12}\Big],\end{aligned} \tag{2.61}$$

where $E_1$, $E_2$ and $E_3$ represent the three spatial components of the electric field.

In addition to the electrostatic energy due to strains, the electrostatic energy density in a solid changes due to small internal translations in the medium as for the dielectric fluid. From equation(2.57) this change is found to be

$$\delta u_t = \frac{1}{2}E^2\nabla\epsilon\cdot\delta\mathbf{s}. \tag{2.62}$$

For completeness, internal intermolecular forces in the medium will also be considered here. These are elastic forces that resist displacements due to the external

stress. This process increases the internal elastic energy in the medium. The change in elastic energy density due to the elastic forces is found to be (sections 2.3 and 2.22 of Stratton [15])

$$\delta u_e = (\lambda_1 \nabla \cdot \mathbf{s} + \lambda_2 e_{11})\, \delta e_{11} + (\lambda_1 \nabla \cdot \mathbf{s} + \lambda_2 e_{22})\, \delta e_{22} + (\lambda_1 \nabla \cdot \mathbf{s} + \lambda_2 e_{33})\, \delta e_{33} + \frac{\lambda_2}{2}\,(e_{12}\delta e_{12}) + \frac{\lambda_2}{2}\,(e_{23}\delta e_{23}) + \frac{\lambda_2}{2}\,(e_{13}\delta e_{13})\,, \quad (2.63)$$

where it has been assumed small elastic forces which are in an equilibrium with the stresses, and isotropic elastic properties in the medium. $\lambda_1$ and $\lambda_2$ are the Lamé parameters, elastic constants dependent on the medium, which are defined from Young's modulus[7] and Poisson's ratio[8]. $\lambda_1$ relates the bulk and shear modulus. $\lambda_2$ is the shear modulus, describing strains due to tangential stresses (nonexistent in a fluid).

A strain tensor can be constructed from the energy densities from electrostatic and elastic stresses, $u_s$ and $u_e$. Considering only the electrostatic contribution, the force density for the strain in the isotropic medium is found to be (sections 2.3 and 2.22 of Stratton [15])

$$(f_s)_i = -\frac{1}{2}\sum_{k=1}^{3} \frac{\partial}{\partial x_k}\left[(a_1 - a_2)\, E_i E_k\right] - \frac{1}{2}\frac{\partial}{\partial x_i}\left(a_2 E^2\right), \quad (2.64)$$

where $i$ and $k$ represent spatial dimensions. The equation expresses how changes of $a_1$ and $a_2$, the relations between permittivity and strain, contribute to the forces in the medium. The negative sign shows how the force works to prevent such changes. Equation (2.64) and the first term of equation (2.57) describes the total force density in a solid, uncharged and isotropic dielectric medium due to an electrostatic field. The force densities will be used in the following paragraphs to derive the stress tensor of the electrostatic field.

### Total force density for an isotropic solid in an electrostatic field

Summing up the forces acting on an isotropic dielectric from an electrostatic field, there is a contribution $\mathbf{f}_s$ due to internal strain (from equations (2.61) and (2.64)),

[7] Young's modulus describes longitudinal tension relative to elongation per unit length, i.e. how large displacement an average force induces.

[8] Poisson's ratio describes lateral contraction relative to longitudinal extension.

a contribution $\mathbf{f}_t$ due to inhomogeneous permittivity (from equations (2.62) and (2.57)), and a contribution $\mathbf{f}_c$ from electrical charges in the dielectric (from equation (2.5)), giving a total force

$$\mathbf{F}_E = \int_V \left( \rho\mathbf{E} - \frac{1}{2}E^2\nabla\epsilon + \mathbf{f}_s \right) \mathrm{d}v. \tag{2.65}$$

The force is proportional to charge density, spatial permittivity variations, and spatial variations of the permittivity-strain relations, and also depends on the electric field.

**Stress tensor formulation for an isotropic solid in an electrostatic field**

The total force acting on a closed surface in a solid isotropic dielectric medium can be found by solely considering the field values on the outside of that surface. This can be done by writing the integrand in equation (2.65) as the divergence of a tensor and applying the divergence theorem. The integral then only includes the tensor values on the surface. The tensor is called the electromagnetic stress tensor, and is expressed by

$$(\sigma_E)_{ij} = \epsilon E_i E_j - \frac{\epsilon}{2}E^2\delta_{ij} + \frac{a_2 - a_1}{2}E_i E_j - \frac{a_2}{2}E^2\delta_{ij}, \tag{2.66}$$

such that

$$\mathbf{F}_E = \oint_S \boldsymbol{\sigma}_E \cdot \mathbf{n}\, \mathrm{d}a, \tag{2.67}$$

where $\mathbf{n}$ is the unit normal pointing out of the surface $S$. To express the integrand in equation (2.65) as a divergence, $\rho = \nabla \cdot \mathbf{D}$ (equation (2.3)) was exchanged for the first term and the product rule was used on the second term. The third term was already expressed as a divergence in equation (2.64). The vector identities

$$\begin{aligned} \nabla\left(\epsilon\mathbf{E}\cdot\mathbf{E}\right) &= E^2\nabla\epsilon + \epsilon\nabla\left(\mathbf{E}\cdot\mathbf{E}\right) = \\ &E^2\nabla\epsilon + \epsilon\left[\left(\mathbf{E}\cdot\nabla\right)\mathbf{E} + \left(\mathbf{E}\cdot\nabla\right)\mathbf{E} + \mathbf{E}\times\left(\nabla\times\mathbf{E}\right) + \mathbf{E}\times\left(\nabla\times\mathbf{E}\right)\right] = \\ &E^2\nabla\epsilon + 2\epsilon\left(\mathbf{E}\cdot\nabla\right)\mathbf{E} + 2\epsilon\mathbf{E}\times\left(\nabla\times\mathbf{E}\right) \end{aligned} \tag{2.68}$$

and

$$\frac{\partial}{\partial x_1}\left(D_{x_1}\mathbf{E}\right)+\frac{\partial}{\partial x_2}\left(D_{x_2}\mathbf{E}\right)+\frac{\partial}{\partial x_3}\left(D_{x_3}\mathbf{E}\right)= D_{x_1}\left(\frac{\partial}{\partial x_1}\mathbf{E}\right)+D_{x_2}\left(\frac{\partial}{\partial x_2}\mathbf{E}\right)+D_{x_3}\left(\frac{\partial}{\partial x_3}\mathbf{E}\right)+\left(\nabla\cdot\mathbf{D}\right)\mathbf{E}= \left(\mathbf{D}\cdot\nabla\right)\mathbf{E}+\left(\nabla\cdot\mathbf{D}\right)\mathbf{E} \quad (2.69)$$

were also used in the derivation. As before, $\nabla\times\mathbf{E}$ is zero for an electrostatic field.

Equation (2.66) expresses that the total force on the closed volume can be found if the field values, the permittivity and the relation between permittivity and strain, $a_1$ and $a_2$, are known. However, it turns out that if the closed volume contains a solid body and is surrounded by a fluid, the integral can be performed on any surface $S$ in the fluid which contains the body (section 2.26 in Stratton [15]). In the fluid, shear strains are nonexistent and the only strain is along the principal axes (only $e_{jj}$ are nonzero). It can be shown (section 2.22 in Stratton [15]) that this leads to $a_1$=$a_2$=$-\tau\frac{\partial\epsilon}{\partial\tau}$. If the fluid is incompressible, it is sufficient to know the values of the first two terms of the stress tensor, and the total force on the body is given by,

$$\mathbf{F}_E=\oint_S\sum_i^3\sum_j^3\left(\epsilon E_iE_j-\frac{\epsilon}{2}E_iE_j\delta_{ij}\right)\cdot\mathbf{n}\,\mathrm{d}a, \quad (2.70)$$

only requiring knowledge of the field, the permittivity and the unit normal of the integration surface.

### 2.5.2 Magnetostatic Fields

The derivation of magnetic force densities will not be treated in this text. However, a derivation similar to that of the electric fields can be found in sections 2.14-2.18 and 2.27 in Stratton [15]. This leads to a magnetic energy

$$U_H=\frac{1}{2}\int_V\mu H^2\,\mathrm{d}v, \quad (2.71)$$

and a total force

$$\mathbf{F}_H=\int_V\left(\mu\mathbf{J}\times\mathbf{H}-\frac{1}{2}H^2\nabla\mu+\mathbf{f}_{H,s}\right)\,\mathrm{d}v. \quad (2.72)$$

The force is analogous to the electrostatic field, with $\mathbf{f}_{H,s}$ given by

$$(f_{H,s})_i = -\frac{1}{2}\sum_{k=1}^{3}\frac{\partial}{\partial x_k}\left[(b_1 - b_2)\, H_i H_k\right] - \frac{1}{2}\frac{\partial}{\partial x_i}\left[b_2 H^2\right], \tag{2.73}$$

and the dependency of the permeability on the strain given by

$$b_1 \equiv \frac{\partial \mu_{jj}}{\partial e_{jj}} \quad \text{and} \quad b_2 \equiv \frac{\partial \mu_{jj}}{\partial e_{kk}}. \tag{2.74}$$

The total force in the magnetostatic field can be expressed with a magnetic stress tensor

$$(\sigma_H)_{ij} = \mu H_i H_j - \frac{\mu}{2} H^2 \delta_{ij} + \frac{b_2 - b_1}{2} H_i H_j - \frac{b_2}{2} H^2 \delta_{ij}. \tag{2.75}$$

such that

$$\mathbf{F}_H = \oint_S \boldsymbol{\sigma}_H \cdot \mathbf{n}\, \mathrm{d}a, \tag{2.76}$$

For a solid body in an incompressible fluid, the strain-dependent terms disappear from the integrand ($b_1$=$b_2$=$-\tau\frac{\partial \mu}{\partial \tau}$), and the total force from the magnetostatic field is given by

$$\mathbf{F}_H = \oint_S \sum_i^3 \sum_j^3 \left(\mu H_i H_j - \frac{\mu}{2} H_i H_j \delta_{ij}\right) \cdot \mathbf{n}\, \mathrm{d}a, \tag{2.77}$$

only requiring knowledge of the field, the permeability and the unit normal of the integration surface.

### 2.5.3 Electromagnetic Fields

The assumptions made for electro- and magnetostatic fields being rotation-less cannot be applied for media in electromagnetic fields. However, a electromagnetic stress tensor similar to the ones found for the static fields can be devised for the case of no contributing elastic or strain properties. In the following paragraphs, energy and momentum conservation in a region with an electromagnetic field will be considered to find the energy flow, forces and stress tensor in a linear isotropic dielectric.

The Lorentz force law, equation (2.5), describe the force on a charge density distribution in an electromagnetic field. The force can also be expressed as the time

derivative of the momentum $\boldsymbol{p}$,

$$\frac{\mathrm{d}\boldsymbol{p}}{\mathrm{d}t} = \rho\mathbf{E} + \mathbf{J} \times \mathbf{B}. \tag{2.78}$$

By applying Maxwell's equations (2.2) and (2.3) to the equation, and integrating over the region of interest, the total force is given by

$$\frac{\mathrm{d}\boldsymbol{P}}{\mathrm{d}t} = \int_V \frac{\mathrm{d}\boldsymbol{p}}{\mathrm{d}t}\,\mathrm{d}v = \int_V (\nabla \cdot \mathbf{D})\,\mathbf{E} - \mathbf{B} \times \left[\nabla \times \mathbf{H} - \frac{\partial \mathbf{D}}{\partial t}\right]\,\mathrm{d}v, \tag{2.79}$$

where $\boldsymbol{P}$ is the momentum of all charge densities in the region. Rearranging the terms, and assuming the medium to be isotropic and linear, a more complex, but symmetric relation is derived,

$$\begin{aligned}&\int_V \left[\frac{\mathrm{d}\boldsymbol{p}}{\mathrm{d}t} + \frac{\partial}{\partial t}(\mathbf{D} \times \mathbf{B})\right]\,\mathrm{d}v \\ &= \int_V \left[\epsilon\mathbf{E}\,(\nabla \cdot \mathbf{E}) - \epsilon\mathbf{E} \times (\nabla \times \mathbf{E}) + \frac{1}{\mu}\mathbf{B}\,(\nabla \cdot \mathbf{B}) - \frac{1}{\mu}\mathbf{B} \times (\nabla \times \mathbf{B})\right]\,\mathrm{d}v.\end{aligned} \tag{2.80}$$

In the derivation, $\mathbf{B} \times \frac{\partial \mathbf{D}}{\partial t} = \frac{\partial}{\partial t}(\mathbf{D} \times \mathbf{B}) - \frac{\partial \mathbf{B}}{\partial t} \times \mathbf{D}$ and equation (2.1) have been used. In addition, a zero term (equation (2.4)) has been added for symmetry. The integrand to the right of the equality may be written as the divergence of a tensor $\boldsymbol{\sigma}$. According to the divergence theorem, the integral is then evaluated solely along the closed surface,

$$\frac{\mathrm{d}\boldsymbol{P}_{\text{tot}}}{\mathrm{d}t} = \int_V \nabla \cdot \boldsymbol{\sigma}\,\mathrm{d}v = \oint_S \boldsymbol{\sigma} \cdot \mathbf{n}\,\mathrm{d}a. \tag{2.81}$$

The tensor $\boldsymbol{\sigma}$ is the electromagnetic stress tensor, and is expressed by

$$\sigma_{ij} = \epsilon E_i E_j + \frac{1}{\mu} B_i B_j - \frac{1}{2}\left(\epsilon E^2 + \frac{1}{\mu} B^2\right)\delta_{ij}. \tag{2.82}$$

This can be seen by considering the $x_1$ component of the second term on the right hand side of equation (2.80),

$$\begin{aligned}&[\mathbf{E} \times (\nabla \times \mathbf{E})]_{x_1} = \\ &\qquad \frac{\partial}{\partial x_1}\left(E_1^2 - \frac{1}{2}E^2\right) + \frac{\partial}{\partial x_2}(E_2 E_1) + \frac{\partial}{\partial x_3}(E_3 E_1) - E_1 \nabla \cdot \mathbf{E},\end{aligned} \tag{2.83}$$

and performing the same expansion on all the cross products in that equation.

Equation (2.82) is similar to the sum of the electric and magnetic stress tensors in equations (2.66) and (2.75). This suggests that the total force on an isotropic, linear dielectric object in an incompressible fluid can be found by applying equation (2.81), requiring knowledge only of the permeability, permittivity and field values in a region around the object.

Two things in the previous derivation should be noted. First, $\boldsymbol{P}_{\text{tot}}$ includes the momenta of charged particles in the field, the momentum of the electromagnetic field itself, and the momentum of the medium in which the field propagates. The exact distribution of momenta between the field and the medium is not explicitly given, and there is not general consensus on this distribution in the literature. Brevik [23] has given a comprehensive review on this topic, and a more recent summary is given by Griffiths [24]. Second, strains inside the body have not been considered. The formulas derived for the electrostatic and magnetostatic fields may be applicable, but this will not be looked further into. None of these issues influence results presented in the thesis, as only the total forces on a body in an incompressible fluid are considered.

Equations (2.81) and (2.82) provide a good method to calculate the forces exerted by an electromagnetic field on an object. However, the force equations for the electro- and magnetostatic fields, (2.57), (2.65) and (2.72), describe the causes of the physical interaction better. Along with the force on charges and currents in the field directly seen from Lorentz' force equation (2.5), spatial variation in permeability and permittivity contributes to the force. This property is taken advantage of in optical trapping, an experimental technique where microscopic particles are confined to a spatial region given by the distribution of an optical field. Section 2.6 briefly considers some cases of optical trapping that can be treated analytically.

Finally, it should be mentioned that the derivations in sections 2.5.1 and 2.5.2, which lay the foundation for this theory, supposed electro*static* fields. The origins of the force for electro*dynamic* fields have not been properly explained. However, the author has not succeeded in finding more rigorous derivations of the source of the optical force in electrodynamic fields. As such, it seems like the physical origin of optical forces not yet has been properly described[9]. In practice though, the theory seems to predict experimental phenomena satisfyingly.

[9]Such theories are necessarily based on relativistic physics, which may explain why no such derivations hasn't been found.

## 2.6 Principles of Optical Trapping

Trapping of microscopic particles using an optical field have become a common technique in research laboratories in recent years. Trapping can for example be used in non-invasive studies of single cells (see chapter 7). This section describes how the optical forces can be calculated for particles in three different size regimes. The size regimes are given by the relation between the particle size and the wavelength of the field. For particles small compared to the wavelength, Rayleigh particles, a dipole approximation is used to find a solution. For spherical particles large compared to the wavelength, a geometrical approximation is used to find a solution. And finally, for a spherical particle with size comparable to the wavelength, Mie calculations are used to find a solution. These three regimes are discussed first for particles in a Gaussian beam, and then for particles in the evanescent field of an optical waveguide.

### 2.6.1 Gaussian Beam Trapping

The most commonly used optical trap is the optical tweezer, where the microparticle is held in place by a strongly focused Gaussian beam, as indicated in figure 2.11. By shifting the position of the focus spot, the position of the particle is controlled in three dimensions without the need of physical contact with the object.

#### Rayleigh particles

In the case of dielectric particles being much smaller than the wavelength of the field, Rayleigh scattering occurs, in which the particle can be described as a point dipole in a uniform electromagnetic field, with dipole moment $\mathfrak{p}$. Stenholm [25] derives the force on such a particle to be

$$\mathbf{F}_{\text{grad}} = \mathfrak{p} \cdot [\nabla \cdot (\mathbf{E} + \mathbf{v} \times \mathbf{B})] + \frac{\mathrm{d}}{\mathrm{d}t} (\mathfrak{p} \times \mathbf{B}) , \tag{2.84}$$

where $\mathbf{v}$ is the velocity of the particle. Stenholm further argues that the contribution from the last term is negligible for times longer than the periodicity of that term, and that the contribution from the second term is negligible due to the smallness of $\mathbf{B}$ compared to $\mathbf{E}$. This leads to the gradient of the field mostly contributing to the force. This means that a plane wave only would push the particle in the direction

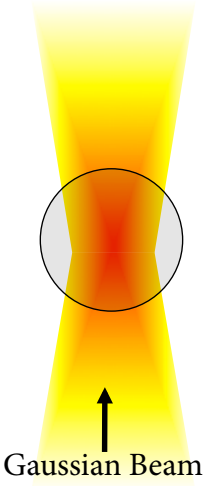


Figure 2.11: Sketch of an optical tweezer. The focus of a Gaussian beam attracts a microparticle, thereby controlling its position.

of the field, while a strong focus would attract the particle toward the focus. This force is called the gradient force.

Equation (2.84) only consider forces related to dipole scattering. In addition, there is a contribution from a scattering force. This force is proportional to the cross section $\mathfrak{s}$ of the particle, and is given by Svoboda and Block [26] to be

$$\mathbf{F}_{\text{scat}} = \frac{\mathfrak{s}\langle \mathbf{S} \rangle}{c/n_{\text{c}}}, \tag{2.85}$$

where $\langle \mathbf{S} \rangle$ is the time average of the power flow of the field, $c$ is the speed of light and $n_{\text{c}}$=$\sqrt{\epsilon_{\text{c}}}$ is the refractive index of the medium surrounding the particle. Harada et al. [27] consider the force on a homogeneous spherical Rayleigh particle with radius $a$ less than $\lambda/20$ in a weakly focused Gaussian beam. With the dipole moment proportional to the field, $\mathfrak{p}$=$\alpha\mathbf{E}$, where $\alpha$ is the polarizability of the particle, gradient and scattering forces are found to be

$$\mathbf{F}_{\text{grad}} = \alpha\mathbf{E}\cdot\nabla\mathbf{E} = \frac{\alpha}{2}\nabla\mathbf{E}(\mathbf{r},t)^2 = \pi\epsilon_0 a^3 \left(\frac{n_{\text{p}}^2 - n_{\text{c}}^2}{n_{\text{p}}^2 + 2n_{\text{c}}^2}\right) \nabla|\mathbf{E}(\mathbf{r})|^2 \tag{2.86}$$

and

$$\mathbf{F}_{\text{scat}} = \frac{n_{\text{c}}}{c}\mathfrak{s}I(\mathbf{r}) = \frac{4}{3}\pi\epsilon_0(\text{k}a)^4 a^2 \left(\frac{n_{\text{p}}^2 - n_{\text{c}}^2}{n_{\text{p}}^2 + 2n_{\text{c}}^2}\right)^2 |\mathbf{E}(\mathbf{r})|^2, \tag{2.87}$$

where $n_\mathrm{p}$ is the refractive index of the dielectric particle, $\nabla \times \mathbf{E}$ is assumed to be zero, and the intensity of the beam is given by

$$I(\mathbf{r}) = |\langle \mathbf{S}(\mathbf{r}, t) \rangle| = \frac{1}{2} n_\mathrm{c} c \epsilon_0 |\mathbf{E}(\mathbf{r})|^2. \tag{2.88}$$

The equations show that the trapping force is in the direction of the field gradient, while the scattering force is strongly dependent of the radius, and proportional to the intensity. They also reveal that a strong focus is necessary for the gradient force to exceed the scattering force.

### Large spheres

In the case of dielectric spheres being much larger than the wavelength of the field, the force calculations can be done using momentum conservation and ray optics. Figure 2.12 shows how the momentum from a focused beam attracts a sphere toward the focus.

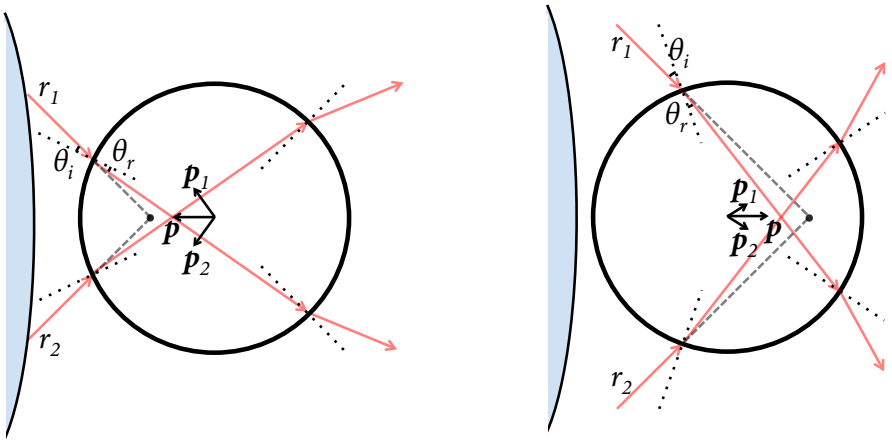


Figure 2.12: Momentum conservation for rays focused by a lens to the back and to the front of the sphere center. Rays $r_1$ and $r_2$ are focused by the lens on the left and induce the momenta $\boldsymbol{p}_1$ and $\boldsymbol{p}_2$ on the sphere, respectively.

For a sphere axially centered under a microscope lens, Ashkin [28] derives two force components, analogous to the Rayleigh regime's gradient and scattering forces.

For circularly polarized rays (averaging the polarizations parallel and perpendicular to the plane of incidence), the gradient and scattering forces for one ray are found to be

$$\mathbf{F}_{\text{grad}} = \frac{n_c P}{c}\left[R\sin 2\theta_i - \frac{T^2\left[\sin(2\theta_i - 2\theta_r) + R\sin 2\theta_i\right]}{1 + R^2 + 2R\cos 2\theta_r}\right] \tag{2.89}$$

and

$$\mathbf{F}_{\text{scat}} = \frac{n_c P}{c}\left[1 + R\cos 2\theta_i - \frac{T^2\left[\cos(2\theta_i - 2\theta_r) + R\cos 2\theta_i\right]}{1 + R^2 + 2R\cos 2\theta_r}\right], \tag{2.90}$$

where $\mathbf{F}_{\text{scat}}$ is parallel, and $\mathbf{F}_{\text{grad}}$ is perpendicular to the incident ray. $R$ and $T$ are the Fresnel reflection and transmission coefficients at the boundary of the sphere, and $\theta_i$ and $\theta_r$ are the angles of incidence and refraction relative to the surface normal at the point of incidence. Ashkin's derivation does not take into account effects for strongly focused beams. However, Gussgard et al. [29] state an error of about 15% for a beam focus diameter as small as the wavelength and sphere diameters above 30 wavelengths.

### Mie particles

In the case of particles with sizes in the range of the wavelength, the theory becomes more complex. A useful starting point has been solutions based on Mie theory [10], where the scattering of plane waves from spherical particles is described in series of spherical functions. Generalized Lorenz-Mie Theory (GLMT) has developed from solutions for spheres in Gaussian beams [30] to solutions for spheroidal particles arbitrarily located and oriented in arbitrarily shaped beams, a work mostly led by Gouesbet, Gréhan et al. [31]. This theory is similar to the Arbitrary Beam Theory (ABT) developed by Barton et al. [32]. Lock [33,34] use GLMT to derive the optical force for an axially centered sphere in the focus of a Gaussian beam in the axial direction

$$F_{\text{axial}} = \frac{n_c P}{c} Q. \tag{2.91}$$

The beam power at a plane in the center of the particle is found from

$$P \simeq \frac{n_c E_0^2}{\mu_0 c}\frac{\pi w_a^2}{2}, \tag{2.92}$$

where the focused beam has a waist radius $w_a$ and a field strength $E_0$. The trapping efficiency $Q$ is found from

$$Q = \frac{2\xi}{n_{\mathrm{c}} \mathrm{k} w_a}, \tag{2.93}$$

where $\xi$ is a series of products of beam shape coefficients and sphere scattering amplitudes expressed with spherical functions. The trapping efficiency $Q$ determines both magnitude and direction of the force in equation (2.91).

For spherical particles with diameters larger than a few wavelengths, a resonance behavior becomes evident. The behavior is sensitive to the ratio of the wavelength and the circumference of the sphere. The resonances are caused by a coupling of the incident field into the sphere. Certain wavelengths create whispering gallery modes, which are standing waves along the sphere circumference. The resonances are sharp and strong if the losses are small, and contribute significantly to the optical force. Examples of resonances can be found in the early paper of Ren et al. [35].

### 2.6.2 Waveguide Trapping

It is also possible to use the evanescent field of on optical waveguide for optical trapping. The transversally decaying part of the guided field is the source of an attractive force, while the propagating part of the field is the source of a scattering force. An object on the waveguide surface is thus pulled toward and propelled along the waveguide surface. To increase the intensity and gradient of the evanescent field, narrow, single mode waveguides with high refractive index are used. Examples of trapping of microparticles and cells on waveguides are given in chapters 4, 5 and 8.

#### Rayleigh particles

Ng et al. [36] describe the forces on Rayleigh particles interacting with the evanescent field of the fundamental TE mode of a slab waveguide. In the cover region, the field is described with refractive index $n_{\mathrm{c}}$ and wavenumber $\mathbf{k}_{\mathrm{c}}$=$\jmath\tilde{\mathrm{k}}_{\mathrm{c}}^{\perp}\hat{x} + (\mathrm{k}^{\parallel} + \jmath\gamma)\hat{z}$, where $\gamma$ is the horizontal decay constant, describing propagation losses. The forces on a dielectric Rayleigh particle can then be described similarly to the Rayleigh forces for the Gaussian beam,

$$\mathbf{F}_{\mathrm{grad}} = \alpha \mathbf{E} \cdot \nabla \mathbf{E} = -\pi \epsilon_0 a^3 \left( \frac{n_{\mathrm{p}}^2 - n_{\mathrm{c}}^2}{n_{\mathrm{p}}^2 + 2n_{\mathrm{c}}^2} \right) |\mathbf{E}(\mathbf{r})|^2 (\tilde{\mathrm{k}}_{\mathrm{c}}^{\perp}\hat{x} + \gamma\hat{z}) \tag{2.94}$$

and

$$\mathbf{F}_{\text{scat}} = \frac{n_{\text{eff}}}{c}\mathfrak{s}I(\mathbf{r}) = \frac{4\pi}{3}\frac{n_{\text{eff}}^2}{n_{\text{c}}^2}\epsilon_0(\mathrm{k}^{\parallel}a)^4a^2\left(\frac{n_{\text{p}}^2 - n_{\text{c}}^2}{n_{\text{p}}^2 + 2n_{\text{c}}^2}\right)^2|\mathbf{E}(\mathbf{r})|^2\hat{z}, \tag{2.95}$$

where the intensity of the field is given by

$$I(\mathbf{r}) = \frac{1}{2}n_{\text{eff}}c\epsilon_0|\mathbf{E}(\mathbf{r})|^2. \tag{2.96}$$

Both forces are proportional to the intensity and depend strongly on the radius $a$, as well as the ratio of refractive indices between the particle and cover medium. The gradient force is proportional to the decay constant $\tilde{\mathrm{k}}_{\text{c}}^{\perp}$ in the direction toward the waveguide surface and proportional to the much smaller decay constant $\gamma$ in the backwards direction (opposite to the field's propagation direction). The scattering force is strongly dependent on the propagation constant $\mathrm{k}^{\parallel}$ and the effective index of the mode $n_{\text{eff}}$.

### Large spheres

For a large sphere interacting with the waveguide field, equations (2.89) and (2.90) for the gradient and scattering forces derived from the ray optics approximation are still applicable. The main differences in this case are that the field distribution on the sphere is asymmetric, and that reflections between the waveguide surface and the sphere contribute to the force. Figure 2.13 shows how momentum transfer from the field to a sphere attracts the sphere toward the waveguide surface and pushes the sphere in the field propagation direction (multiple reflections are not considered). In the figure, $p_{\text{vertical}}$ corresponds to the gradient force and $p_{\text{horizontal}}$ corresponds to the scattering force from the Gaussian beam results. It should be noted that only a small portion of the sphere interacts with the evanescent field. The ray optics approximation for the evanescent field can be used with iterative methods or with ray tracing. Prieve and Walz [37,38] give some numerical results for a sphere in an evanescent field created by total internal reflection.

### Mie particles

For a spherical object with a diameter between one twentieth of a wavelength and thirty wavelengths, calculations based on Lorenz-Mie theory must be used to gain

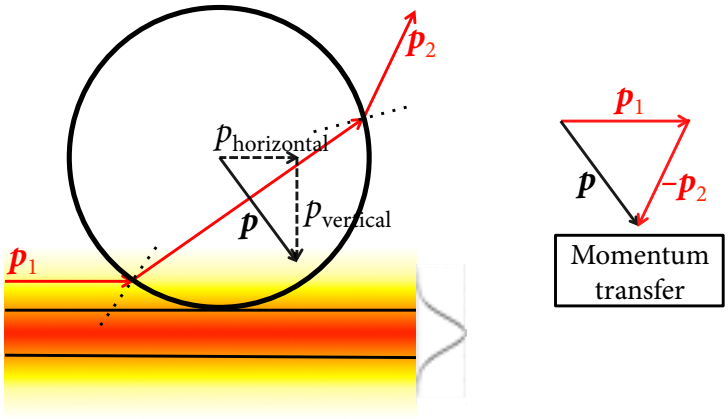


Figure 2.13: Momentum conservation for evanescent rays scattered by a particle on the waveguide surface. The figure does not consider multiple reflections, neither in the sphere or between sphere and waveguide surface.

insight in the interaction between the particle and the evanescent field. Trapping Mie particles with evanescent fields originated with Kawata's work [13, 39], and have been studied mathematically with Arbitrary Beam Theory by Jaising et al. [40, 41] in the case of evanescent fields on a waveguide surface, and Brevik et al. [42, 43] in the case of evanescent fields from total internally reflected laser beams. Both authors use the force expression derived by Barton [32], which is based on Maxwell's stress tensor equation (2.82). By integrating the product of tensor and surface normal at a spherical surface far from the object, an expression of the total force is found. The expression is a series of spherical functions representing the fields in spherical coordinates.

By considering incident evanescent fields and summing the series numerically, Jaising finds horizontal and vertical forces for both single mode TE and TM waveguide modes. Whispering gallery mode resonances become evident for sphere diameters above 4 μm for polystyrene spheres in water on a low-index waveguide, but the effects are small for spheres with diameters smaller than 8 μm.

# Chapter 3

# Numerical Modeling of Optical Forces and Waveguides

## 3.1 Introduction

Optical trapping using the evanescent field of a waveguide is described in chapters 2 and 8. Mathematical analysis of trapping on waveguides have previously been performed for spherical objects using Mie theory [40, 42, 44]. For non-spherical particles, a pure numerical treatment is necessary. The finite element method is a powerful numerical technique for solving complex physical systems, among them electromagnetic problems [45, 46]. Optical forces on nanoparticles trapped on a waveguide have previously been studied by Néel et al. [47] and Yang et al. [48].

This chapter describes a model developed with the commercial finite element method software Comsol Multiphysics[1] to find the forces on micrometer-sized objects in the evanescent field of an optical waveguide. First, section 3.2 gives a short introduction to the theory behind the finite element method. Then, section 3.3 describes the implementation and properties of the waveguide trapping model. Finally, section 3.4 analyzes and validates the model by looking at results from some basic simulations, and also compare these with results from Mie calculations.

[1] COMSOL, Stockholm, Sweden

## 3.2 Principles of the Finite Element Method

The finite element method (FEM) is a numerical method developed to solve boundary value problems. Such a problem can be described generally by the equation $\mathcal{L}\varphi = f$ inside the domain $\Omega$ with a boundary $\Gamma$. $\varphi$ is the unknown function which is to be found, the operator $\mathcal{L}$ describes the general physical conditions, and the function $f$ describes the specific physical conditions in the study. A unique solution can then be found using the boundary conditions on $\Gamma$.

A specific example of a boundary value problem is the Poisson equation, $\nabla^2\Phi = \rho/\epsilon$. This problem uses the operator $\nabla^2$ to find the electric potential $\Phi$ around charge density distribution $\rho$ in the case of a linear, isotropic, and homogeneous domain with permittivity $\epsilon$. For a large domain, it is reasonable to assume that the function $\Phi$ is zero at the boundaries, and a unique solution can be found.

Subsections 3.2.1 to 3.2.5 give a brief introduction to finite element theory and theory related to solving such problems. The description generally follows the more comprehensive derivations given by Jin [49].

### 3.2.1 Basic Theory

Boundary value problems are solved numerically with FEM by dividing the domain of interest $\Omega$ into small elements $e$, and finding approximate solutions to the many small problems $\mathcal{L}\widetilde{\varphi}=f$, where $\widetilde{\varphi}$ is the exact solution in an element. To do this, test functions $\widetilde{\varphi}^e$, representing $\widetilde{\varphi}$, are chosen for each element. To approximate a solution, the test functions are optimized such that the combined error from all elements is minimized. This turns one complex problem into a lot of simple problems which can be solved numerically. The accuracy and speed of the calculation is determined by the complexity of the test functions and the size and number of elements.

In general, two methods are used to optimize the test functions, a variational method, and a weighted residuals method. Our work, using the commercial FEM software Comsol Multiphysics, is based on *Galerkin's method*, which use weighted residuals to solve the boundary value problem.

The sketch in figure 3.1 shows a domain $\Omega$ which is divided into in total $M$ elements $e$. $N$ nodes $j$, which are positioned at $\mathbf{x}_j$, connect the elements. Each element is

connected to $n$ of the $N$ nodes, as shown in figure 3.2. These are called the *local* nodes of that element. The local nodes are denoted by $j^e$, and numbered from 1 to $n$. The approximate solution in each element is found using the local nodes. This is done by formulating the boundary value problem for that element using the test function $\widetilde{\varphi}^e$. Since neighboring elements share nodes, the formulas for all the nodes are connected, and can be implemented into one large matrix formula suitable for numerical calculation.

As the optimized $\widetilde{\varphi}^e$ does not give an exact solution, a residual error $r^e$ is introduced by each element $e$,

$$\mathcal{L}\widetilde{\varphi}^e - f = r^e \neq 0. \tag{3.1}$$

$r^e$ reaches zero when $\widetilde{\varphi}^e = \varphi(\mathbf{x}_{j^e})$ at all the element's nodes. This is the case when the element is infinitesimally small.

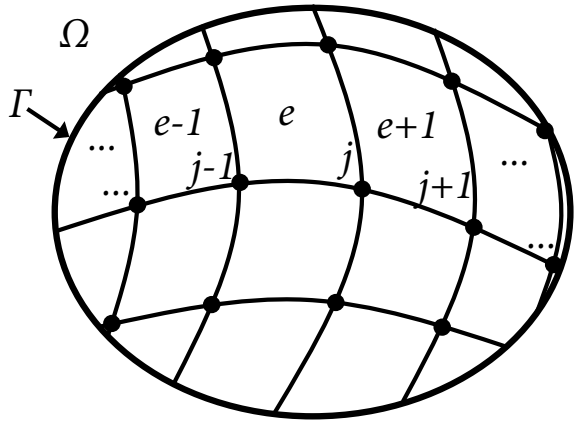


Figure 3.1: Domain $\Omega$ with boundary $\Gamma$. The domain is discretized into $M$ elements $e$ connected by in total $N$ nodes $j$. Node $j$ corresponds to the local element node $n$ in figure 3.2

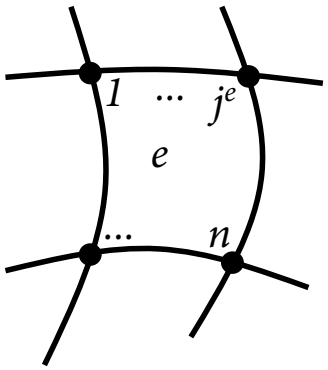


Figure 3.2: Element $e$ (subdomain $\Omega^e$) from figure 3.1 consists of $n$ out of the $N$ nodes, locally denoted $j^e$.

The test functions $\widetilde{\varphi}^e$ are composed of a sum of coefficients $C_j$ attached to shape functions (basis functions) $\zeta_j$ specific to the nodes $j$. Only the $n$ local nodes connected to an element contributes to the sum. Renaming the local nodes around element $e$ to $j^e$, the test function for element $e$ becomes

$$\widetilde{\varphi}^e = \sum_{j^e=1}^{n} C_{j^e}\zeta_{j^e} = \boldsymbol{C}^{e\mathsf{T}}\boldsymbol{\zeta}^e = \boldsymbol{\zeta}^{e\mathsf{T}}\boldsymbol{C}^e, \tag{3.2}$$

where $\mathbf{C}^e$ is the coefficient vector and $\boldsymbol{\zeta}^e$ is the basis function vector of the element's nodes. $\boldsymbol{\zeta}^e$ is only defined for element $e$, such that it is zero for all other elements $\{1, \ldots, e{-}1, e{+}1, \ldots, M\}$. This is done by requiring each shape function to be non-zero only for the node where it is defined.

The residue from an element is minimized by adjusting the values of the coefficient vector. This can be done by introducing a weighting function to each node. This function is unique to the node. It is denoted $\omega_j$ in the context of the full domain and $\omega_{j^e}$ in the context of the local element. The weighted residual from one of the nodes of the element is then

$$R^e_{j^e} = \int_{\Omega^e} \omega_{j^e} r^e \, \mathrm{d}\Omega. \tag{3.3}$$

In Galerkin's method, each weighting function $\omega_{j^e}$ is chosen equal to the shape function of the node, $\zeta_{j^e}$. Equations 3.1, 3.2 and 3.3 then give

$$\begin{aligned} R^e_{j^e} &= \int_{\Omega^e} \zeta_{j^e} \left( \mathcal{L}\widetilde{\varphi}^e - f \right) \mathrm{d}\Omega \\ &= \int_{\Omega^e} \zeta_{j^e} \mathcal{L} \left( \boldsymbol{\zeta}^{e\mathsf{T}} \mathbf{C}^e \right) \mathrm{d}\Omega - \int_{\Omega^e} \zeta_{j^e} f \, \mathrm{d}\Omega, \end{aligned} \tag{3.4}$$

and the sum of weighted residues from the nodes associated to element $e$ can then be described as a matrix equation

$$\begin{aligned} \boldsymbol{R}^e &= \sum_{j^e=1}^{n} \int_{\Omega^e} \zeta_{j^e} \mathcal{L} \left( \boldsymbol{\zeta}^{e\mathsf{T}} \mathbf{C}^e \right) \mathrm{d}\Omega - \int_{\Omega^e} \zeta_{j^e} f \, \mathrm{d}\Omega \\ &= \int_{\Omega^e} \boldsymbol{\zeta}^e \mathcal{L} \boldsymbol{\zeta}^{e\mathsf{T}} \, \mathrm{d}\Omega \, \mathbf{C}^e - \int_{\Omega^e} \boldsymbol{\zeta}^e f \, \mathrm{d}\Omega \\ &= \mathbb{K}^e \mathbf{C}^e - \boldsymbol{b}^e, \end{aligned} \tag{3.5}$$

where the $n \times 1$ vector $\boldsymbol{R}^e$ contains the residues $R^e_{j^e}$, the $n \times n$ stiffness matrix $\mathbb{K}^e$ contains elements $K_{j^e i^e} = \int_{\Omega^e} \zeta_{j^e} \mathcal{L} \zeta_{i^e} \, \mathrm{d}\Omega$, the $n \times 1$ vector $\boldsymbol{b}^e$ contains constraints $b_{j^e} = \int_{\Omega^e} \zeta_{j^e} f \, \mathrm{d}\Omega$, and the $n \times 1$ vector $\mathbf{C}^e$ contains the constant test function coefficients $C^e_{j^e}$.

By mapping the element node numbers $j^e$ back to the global node numbers $j$, the error of all nodes (the full domain) can be given by one single equation. Summing all elements, the total error becomes

$$\boldsymbol{R} = \sum_{e=1}^{M} \overline{\boldsymbol{R}^e} = \sum_{e=1}^{M} \left( \overline{\mathbb{K}^e} \, \overline{\mathbf{C}^e} - \overline{\boldsymbol{b}^e} \right), \tag{3.6}$$

where the lines above the matrices imply renumbering of the indices from local to global nodes. This converts each matrix and vector to $N$ dimensions. However, the test functions $\zeta_{i^e}^e$ are zero everywhere outside element $e$. This means that a very large part of the elements in the resulting stiffness matrix are zero, making it a sparse[2] matrix. This is important for the numerical efficiency of the finite element method solutions, as will be discussed in section 3.2.5.

By letting the error at each node go to zero (***R***=***0***) a full algebraic expression can be set up, from which the problem is solved at every node,

$$\mathbb{K}\boldsymbol{C} = \boldsymbol{b}. \tag{3.7}$$

This equation can be solved numerically to find the unknown test function parameters ***C***. To increase the solution accuracy, it is necessary to increase either the node density, at the cost of a larger matrix, or the complexity of the shape function, at the cost of a more complex equation. Sections 3.2.2 to 3.2.5 discuss different aspects regarding the process of solving the matrix problem.

### 3.2.2 Discretization Into a Mesh

Discretization of the domain into elements is critical to solve the finite element problem in an efficient way. The grid of elements is called a mesh, and gives the position of all the nodes in the domain. The optimal shape of the elements depends on the shape of the geometry in the domain. Surfaces are usually divided into rectangular or triangular elements, and volumes into tetrahedral prisms, rectangular prisms or triangular prisms. Triangular surface elements and tetrahedral volume elements are useful for discretization of curved or irregular geometries. The number of element nodes depends on the chosen shape function. This will be discussed further in section 3.2.3.

Designing the mesh to fit a specific model can greatly enhance the efficiency and accuracy of a solution. A dense mesh should be applied to domains where the solution is expected to vary fast or have large values, while a looser mesh can be applied to domains where the solution is expected to vary slowly and have small values. Also, the angles of the mesh elements should neither be too small ($\sim 0°$), nor too large ($\sim 180°$). This will lead to either poor discretization of the domain or

[2] A large number of the matrix elements are zero.

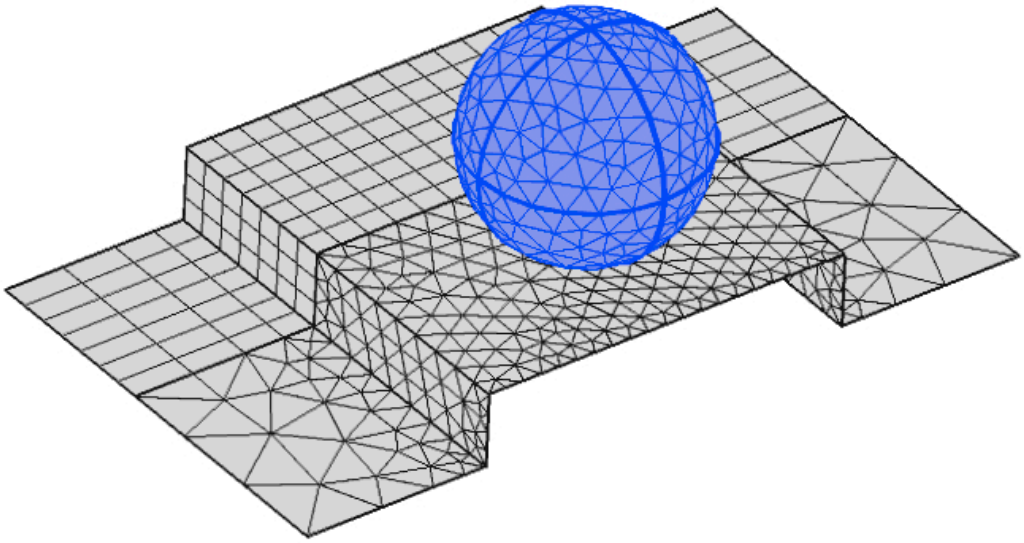

Figure 3.3: Examples of surface meshes. A rectangular and a triangular mesh are seen on the straight surfaces, while a triangular mesh is used on the spherical surface.

large magnitude differences between elements in the stiffness matrix $\mathbb{K}$, degrading the solution accuracy [50, 51].

### 3.2.3 Choice of Test Functions

The test function of an element is a superposition of shape functions from each element node, as described in section 3.2.1. The structure of the shape function is chosen by considering numerical efficiency and solution accuracy, but it also depends on the type of problem that is to be solved. The functions are usually continuous, and often also smooth. The chosen shape functions determine the name of the element in the domain, such that using a linear shape function give a system of linear elements.

A simple shape function is easy to implement and solve for, but the accuracy of the solution can be too low, and large models can converge slowly. More complex shape functions increase the accuracy and converge faster, at the cost of higher computer memory demands. The memory cost is due to the bandwidth[3] of the

[3]The bandwidth refers to matrices with non-zero elements only close to the diagonal. The max-

stiffness matrix $\mathbb{K}$. Simple test functions tend to have a narrow bandwidth, achieving close to diagonal matrices which are quick to solve. Complex test functions have wider bandwidths and fewer zero elements, and therefore require more computer memory.

The accuracy and speed of higher order functions often make these preferable. Different shape functions have specific advantages and disadvantages, and the most popular functions are Lagrange and vector shape functions.

### Lagrange functions

Lagrange functions are polynomials which are continuous across elements by demanding the polynomial to have a set value at one element node, and be zero at all other element nodes ($f(x_{j^e=i}) = a$ and $f(x_{j^e \neq i}) = 0$). The degree of the polynomial determines the shape function complexity, with linear functions being the most basic function. Examples of linear, quadratic and cubic functions for one dimension can be seen in figure 3.4. The number of nodes connected to an element is adjusted to enable the required function shape (a linear function needs two points for interpolation, a quadratic function needs three points, and so on). As the number of nodes increase, the problem complexity increases.

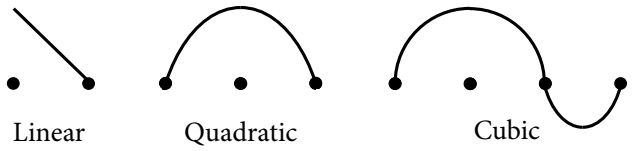


Figure 3.4: Examples of Lagrange polynomials for a one-dimensional model.

### Vector functions

When deciding the shape functions, it is convenient to keep the physics of the problem in mind. In a problem involving electromagnetic fields, the tangential electric

imum number of non-zero elements across the diagonal, along some row or column, is the matrix bandwidth.

field components should be continuous across boundaries. However, field components along the element boundaries cannot be described by singular nodes, which only would be efficient for studying scalar potentials.

By using shape functions defined from node pairs, the field along the edges of the mesh elements can be defined. These functions can be used to describe tangential field continuities, and allow perpendicular field discontinuities across elements [52]. Elements described with such vector, or edge, shape functions are called edge elements. Using vector shape functions in electromagnetic models ensures a more correct solution and avoids unphysical solutions for the waveguide modes, which tend to be a problem [53]. Higher order edge elements use higher order Lagrangian functions on the node pairs [54]. A detailed introduction to vector shape functions is given by Bossavit and Mayergoyz [52].

### 3.2.4 Removing Propagating Fields

The boundaries of physical systems describing radiation are challenging to treat numerically. When the radiation propagates out of the domain, it needs to be removed without influencing the physics inside. This requires an absorbing and non-reflecting boundary. One way to achieve this is to perfectly match the impedance of the outer surface of the domain with the outgoing fields. However, this requires calculation and implementation for all possible fields. A more efficient way is to introduce a non-reflecting absorbing *layer* outside of the physical domain, which efficiently removes radiation from the numerical domain without any previous knowledge of the field propagation.

Berenger [55] was the first to introduce such a layer, the perfectly matched layer (PML). In this outside layer, the material and field properties are slightly different from the ones on the inside domain. The changes in material are introduced by the artificial electric and magnetic conductivities. These have two functions, absorbing the radiation and matching the impedances between the physical domain and the PML. The change of the fields is done by splitting up both the electric field and the magnetic field into two transversal components, independent of radiation polarization. These changes ensures a non-reflecting boundary for radiation from all incidence angles. The PML absorbs fields in both propagating directions, such that any remaining field reflected from the outer PML boundary continues to decay until it reaches the physical domain again.

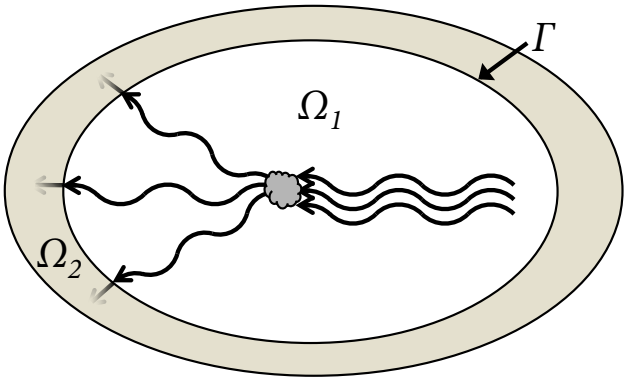


Figure 3.5: Perfectly matched layer. Radiation is absorbed without reflection in the domain $\Omega_2$ outside the boundary $\Gamma$ of the physical domain $\Omega_1$.

It can be shown that the absorption in the PML is proportional to the cosine of the incidence angle and the PML conductivity [55]. Thus, radiation incident on the PML nearly tangential with the boundary will not be efficiently absorbed. The design of the PML should take this into consideration.

A high conductivity in the PML is favorable to achieve a small numerical model. However, abrupt conductivity changes in a discretized system will lead to numerical reflections. This can be improved by letting the conductivity increase gradually in the PML.

An evanescent field is already a decaying field. The introduction of a PML (conductive medium) will not increase the field decay, but only change the propagation constant of the field in some way. If necessary, the field decay can be increased by introducing an imaginary PML conductivity, but usually, the evanescent decay in itself is sufficient to avoid boundary reflections.

The material and field property changes in a PML has been found to be equivalent to a coordinate transform in that domain [56]. A coordinate transform provides a simpler way to implement the PML in the numerical equation.

### 3.2.5 Solving the Matrix Equation

The finite element method matrix equation is linear and contains a large and sparse stiffness matrix $\mathbb{K}$. Conveniently, this means that solving does not need to involve

full Gaussian elimination. From the 1980's, much work has been done to optimize solving large, sparse and linear matrix equations numerically [57]. Several techniques have been developed, many of them suitable for parallelization. The solvers can be divided in two main groups, direct and iterative solvers.

### Direct solvers

Direct solvers solve linear matrix equations $\mathbb{K}\boldsymbol{C} = \boldsymbol{b}$ by pivoting (Gaussian elimination). In this process, the matrix elements are eliminated from the equation by subtracting rows or columns from each other. Using this technique, it is computationally demanding ($\mathcal{O}(N^3)$ operations) to find the inverse of $\mathbb{K}$, and direct solvers cannot always be used. Unless mentioned specifically, the following paragraphs regarding direct solvers are based on the work of Duff [58, 59].

**Factorization** By factorizing the matrix into its lower and upper triangular matrices $\mathbb{L}\mathbb{U}$, the equation can be solved in two less demanding steps ($\mathcal{O}(N^2)$ operations)[4], $\mathbb{L}\boldsymbol{z} = \boldsymbol{b}$ and $\mathbb{U}\boldsymbol{C} = \boldsymbol{z}$.

The factorization is most efficient if the triangular matrices keep the sparsity of the stiffness matrix. This can be done by pivoting the rows and columns with the least number of elements, and by ensuring that the pivot is not much smaller (by some set threshold factor) than the largest entry in its row or column (threshold pivoting).

**Frontal method** Some methods exploit the sparsity of the stiffness matrix by dividing the matrix into submatrices which can be independently pivoted. This requires that the matrix elements in rows and columns coinciding with a submatrix are zero. Methods using this technique are called frontal methods, and avoids assembly of the whole stiffness matrix, since coefficients belonging to only one mesh element are eliminated before the matrix is constructed.

Frontal methods save memory and are suitable for parallelization, and the concept can be expanded by letting pivoted submatrices become elements of other

[4]The $\mathbb{L}\mathbb{U}$ factorization is in principle as computationally demanding as finding the inverse, but properties of sparse matrices makes the process more efficient. Also, if the same stiffness matrix can be used to solve different problems, $\mathbb{L}\mathbb{U}$ factorization needs to be done only once for all problems.

submatrices, thus creating a nested pivoting system. Such techniques are called multifrontal methods, which are even more efficient for parallelization.

Examples of direct solvers for sparse matrices which use $\mathbb{L}\mathbb{U}$ factorization and multifrontal methods are MUMPS (MUltifrontal Massively Parallel sparse direct Solver, suitable for distributed memory computers) [60], SPOOLES (SParse Object Oriented Linear Equations Solver, suitable for symmetric or Hermitian matrices) [61], and PARDISO (suitable for computers where multiple processors share memory) [62]. The Comsol Multiphysics software has the option to use any of these solvers.

**Iterative solvers**

Iterative solvers solve a linear matrix equation $\mathbb{K}\boldsymbol{C} = \boldsymbol{b}$ by guessing an initial trial solution $\boldsymbol{C}_0$, comparing the computed and correct results, and using some method to refine the trial solution. This process is repeated until the computed trial solution are sufficiently close to the real solution (within some preset accuracy). In this way, no inversion or factorization of the stiffness matrix is necessary, and only matrix-vector calculations are performed ($\mathcal{O}(N^2)$ operations [57]). The method used to refine the trial solution determines the efficiency at each step, and therefore the convergence rate. For large equations, a fast convergence rate is necessary to achieve a solution. Unfortunately, no general methods exist which guarantee convergence for all problems. Unless stated differently, the following paragraphs regarding iterative solvers are based on the work of Golub [63].

**Stationary methods** A trial solution $\boldsymbol{C}'$ will give a residue $\boldsymbol{r}_0=\mathbb{K}\boldsymbol{C}'-\boldsymbol{b}$. This can be compensated by adjusting the trial solution, $\mathbb{K}(\boldsymbol{C}'+\delta\boldsymbol{C})=\boldsymbol{b}$. Stationary methods implement this adjustment iteratively by choosing $\boldsymbol{C}'=\boldsymbol{C}_k$ and $\delta\boldsymbol{C}=\boldsymbol{C}_k-\boldsymbol{C}_{k-1}$, where $k$ is the iteration step. This leads to the iteration formula $\boldsymbol{C}_k=\boldsymbol{C}_{k-1}+\mathbb{M}^{-1}(\boldsymbol{b}-\mathbb{K}\boldsymbol{C}_{k-1})$, where $\mathbb{M}$ is an easily invertible matrix similar to $\mathbb{K}$. Stationary iterative techniques differ in their choice of $\mathbb{M}$. These techniques include the Gauss-Seidel method and the Successive Over-Relaxation (SOR) method.

**Projection methods** For large sparse matrix equations, stationary methods are inefficient, and projection methods are commonly used. These methods optimize a trial solution in some subspace of the equation, and expand the subspace for the

next iteration, optimizing the trial solution each time. Several methods are developed using a so-called *Krylov* subspace $\mathcal{K}$ [64], which is spanned by the residual from the initial guess, and residual-matrix products; $\mathcal{K}^m(\boldsymbol{r}_0, \mathbb{K}) = \{\boldsymbol{r}_0, \mathbb{K}\boldsymbol{r}_0, \ldots, \mathbb{K}^m\boldsymbol{r}_0\}$ in $m$ dimensions.

The projection methods differ in how the solutions are optimized in each step. Some methods construct solutions which are orthogonal to the subspace (e.g. the conjugate gradients method [65]), and some methods minimize the norm of the residual in the subspace (e.g. the generalized minimal residue method (GMRES) [66]). The vectors of the Krylov subspace are often orthogonalized, thereby minimizing numerical errors which can result from using almost identical subspaces.

**Preconditioning** Improving the convergence is critical for solving many equations iteratively. Preconditioning is an essential tool to give faster convergence, and works by multiplying the stiffness matrix with a similar, but simpler, inverted matrix; $\mathbb{M}^{-1}\mathbb{K}\boldsymbol{C} = \mathbb{M}^{-1}\boldsymbol{b}$. Finding a good preconditioning matrix simplifies the equation, and increase the convergence speed. Some procedures used to find appropriate preconditioning matrices are discussed by Golub [63].

## 3.3 The Waveguide Model

The objective of the numerical waveguide model presented in the thesis is to study the magnitude of optical forces on objects close to the waveguide surface. By changing the object size, shape, and refractive index, objects ranging from plastic and glass microspheres to metal particles and cells can be studied.

This section describes how the waveguide model is implemented and solved in Comsol Multiphysics, as well as the advantages and limitations of the model. First, an overview of the procedure is given in section 3.3.1, and then the physical formulas are introduced in section 3.3.2. Finally, section 3.3.3 presents the specific properties of the model.

### 3.3.1 Procedure of the Numerical Model

The optical force on an object on a waveguide surface is found with the help of an electromagnetic stress tensor. This has been done using a three-step procedure, where the initial values at the waveguide input face are found first, the field in the three-dimensional domain is found next, and finally, the stress tensor equation is used to find the force. The fundamental TE mode is chosen as the propagating field in all simulations, since this mode would be predominant in experiments (having the largest $n_{\text{eff}}$, see section 2.3.2).

#### 1st step. Propagation constant

The field at the input face of the model and the propagation constant for the waveguide are used as initial values in the boundary value problem describing the full three-dimensional domain. These initial values are themselves found with a two-dimensional boundary value problem. For a given frequency, the propagation constants (effective refractive indices) of the waveguide are found. The fundamental mode is chosen as basis for the full field simulation step. Figure 3.6 shows the fundamental mode (TE) for a 3 μm wide and 200 nm thick waveguide,

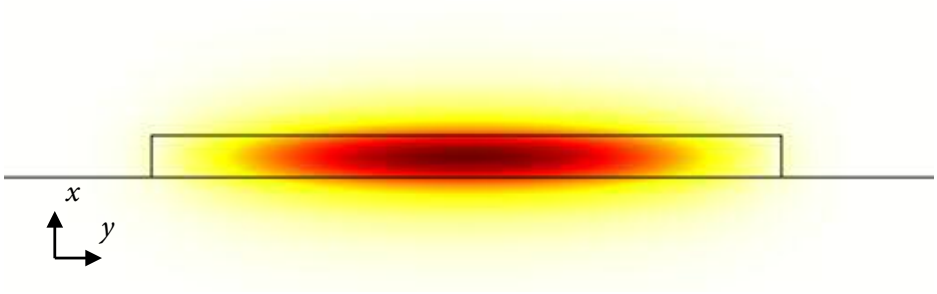


Figure 3.6: Plot of the field norm of the fundamental mode of a 3 μm wide and 200 nm high waveguide. Axis directions are indicated.

#### 2nd step. Stationary solution of the field

A new boundary value problem is solved to describe the field distribution in the whole domain. A stationary solution is found, describing the stabilized state of

the system. The three-dimensional problem is far more computationally intensive than the mode calculation, and the mesh and geometry have to be carefully chosen to allow numerical solutions to the problem. A longitudinal cross section of the waveguide is given in figure 3.7, showing how an electric field propagates along a waveguide with the evanescent field decaying above and below the waveguide and with the field being absorbed in the PML region at the right.

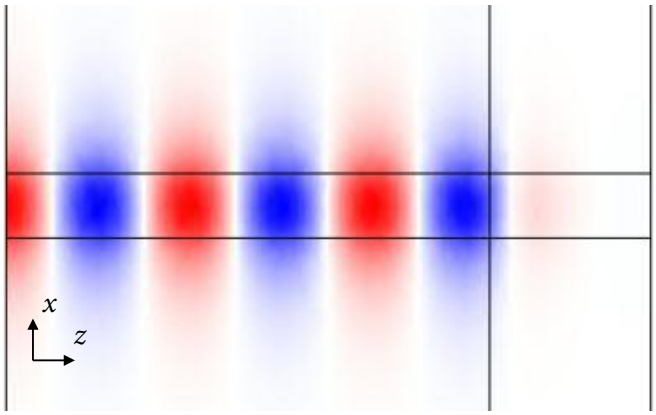


Figure 3.7: Plot of the transversal component of the electric field propagating in the positive z direction along a 3 μm wide and 200 nm high waveguide. The field is absorbed in the PML region at the end of the waveguide.Axis directions are indicated. The color code is arbitrary, and not equal to the one in figure 3.8.

**3rd step. Force calculation**

The electric field distribution from the boundary value problem is used to find Maxwell's electromagnetic stress tensor[5] values on the object of interest. The product of the tensor and the surface normal at each surface point of the object gives three stress values at each object surface point, one for each spatial direction. Summing up the stress at all surface points gives the total force on the object for each direction.

[5]See section 2.5.3 for the stress tensor derivation.

### 3.3.2 Physics of the Numerical Model

The numerical model describes a monochromatic wave propagating in a low loss dielectric medium. The wave is guided by total internal reflection, and is described by the Helmholtz equation

$$\nabla \times \frac{1}{\mu_r} (\nabla \times \mathbf{E}) - k_0^2 \left( \epsilon_r - \frac{\jmath \sigma}{\omega \epsilon_0} \right) \mathbf{E} = \mathbf{0}, \tag{3.8}$$

derived from Maxwell's equations with time-harmonic electric and magnetic fields (see section 2.2). The Helmholtz equation and the given boundary conditions lead to a second order elliptic boundary value problem. Linear elliptic equations are well suited for numerical calculations, since solutions (from a wide-ranging mathematical space) exist and are unique [67].

#### Weak formulation

The Helmholtz equation (3.8) is seen to require twice differentiable solutions **E**. A reformulation of the equation can allow solutions with less restrictive smoothness properties. This makes it easier to find numerical solutions. Such a transformation gives a so called weak formulation, for which the solution is called a weak solution. In this context, 'weak' refers to the solution not needing to be twice differentiable. The weak solution does not necessarily satisfy the original Helmholtz equation, only the weak form of it. The weak solutions are also the source of the unphysical (spurious) waveguide modes mentioned in section 3.2.3, which can be prevented by the use of vector test functions.

A weak formulation is usually found by introducing an infinitely differentiable test function $\boldsymbol{\psi}$ and integrating by parts, thereby moving the differentiability requirement from the solution to the test function. Helmholtz equation can be rewritten in weak form with the help of the triple vector product $\mathbf{a} \cdot (\mathbf{b} \times \mathbf{c}) = \mathbf{b} \cdot (\mathbf{c} \times \mathbf{a})$, the product rule for vector cross products $(\mathbf{a} \times \mathbf{b})' = \mathbf{a}' \times \mathbf{b} - \mathbf{b}' \times \mathbf{a}$, and the divergence theorem $\int_V \nabla \cdot \mathbf{F} \, \mathrm{d}V = \int_{\partial V} \mathbf{F} \cdot \, \mathrm{d}\mathbf{S}$. This gives

$$\int_V \left[ \nabla \times \boldsymbol{\psi} \cdot \frac{1}{\mu_r} \nabla \times \mathbf{E} - k_0^2 \left( \epsilon_r - \frac{\jmath \sigma}{\omega \epsilon_0} \right) \mathbf{E} \cdot \boldsymbol{\psi} \right] \mathrm{d}V = \oint_{\partial V} \frac{1}{\mu_r} (\nabla \times \mathbf{E}) \times \boldsymbol{\psi} \cdot \mathrm{d}\mathbf{S}, \tag{3.9}$$

where the test function $\psi$ satisfies the same boundary conditions as **E**. The boundary conditions of the problem determine how the surface integral is treated. If the fields at the boundary are zero, then the boundary integral will be zero, but in a radiation problem, special boundary conditions are necessary to avoid back-reflections, as discussed in section 3.2.4. The exact formulation of the boundary conditions in the Comsol software is not given, but the properties of the chosen boundary conditions are described in section 3.3.3.

### Force calculation

The field from the simulation can be used to calculate Maxwell's stress tensor $\boldsymbol{\sigma}$, which is implemented in the Comsol software as

$$\sigma_{ij} = \frac{1}{2}\mathrm{Re}\left\{\epsilon_0 n_{\text{cover}}^2 (E_i^{\text{out}})(E_j^{\text{out}})^* + \frac{1}{\mu_0}(B_i^{\text{out}})(B_j^{\text{out}})^* \right. \\ \left. -\delta_{ij}\cdot\frac{1}{2}\left(\epsilon_0 n_{\text{cover}}^2 |E^{\text{out}}|^2 \cdot \frac{|B^{\text{out}}|^2}{\mu_0}\right)\right\}, \quad (3.10)$$

where $i$ and $j$ spans the upward, lateral and propagation directions $x$, $y$ and $z$, the superscript $^{\text{out}}$ indicates that only field values from the outer object surface are included, the superscript $^*$ denotes the complex conjugate, $\delta_{ij}$ is the Kronecker delta, $n_{\text{cover}}$ is the refractive index of the medium outside the object, and Re takes the real value of the expression.

For each spatial dimension $i$, the stress $\mathbf{T}_i$ at object surface position $r$ is found from the product of the tensor components and the surface normal

$$\mathbf{T}_i(r) = \sum_{j=\{x,y,z\}} \sigma_{ij}\cdot\mathbf{n}_j(r)\,, \quad i=\{x,y,z\}. \quad (3.11)$$

A plot of the stress in each spatial direction can be seen in figure 3.8 for a 2 μm diameter glass sphere ($n$=1.5) interacting with the evanescent field from a 3 μm wide waveguide. Red values are positive, and blue values are negative. Stress is only experienced by the part of the sphere close to the waveguide. In the vertical $x$ direction, the stresses work toward the waveguide. In the lateral $y$ direction, the stresses act toward the center of the waveguide. In the horizontal $z$ directions, the stresses are pushing the front of the sphere and pulling the end of the sphere. A non-rigid sphere would thus be flattened onto the waveguide, compressed in the

lateral direction, and elongated in the horizontal direction. The figure is discussed further in section 3.4.2 in the context of numerical noise in the model.

The total force experienced by the object is found by summing up the stress around the whole object surface

$$\mathbf{F}_i = \sum_{\text{object surface}} \mathbf{T}_i(r), \quad i = \{x, y, z\}. \tag{3.12}$$

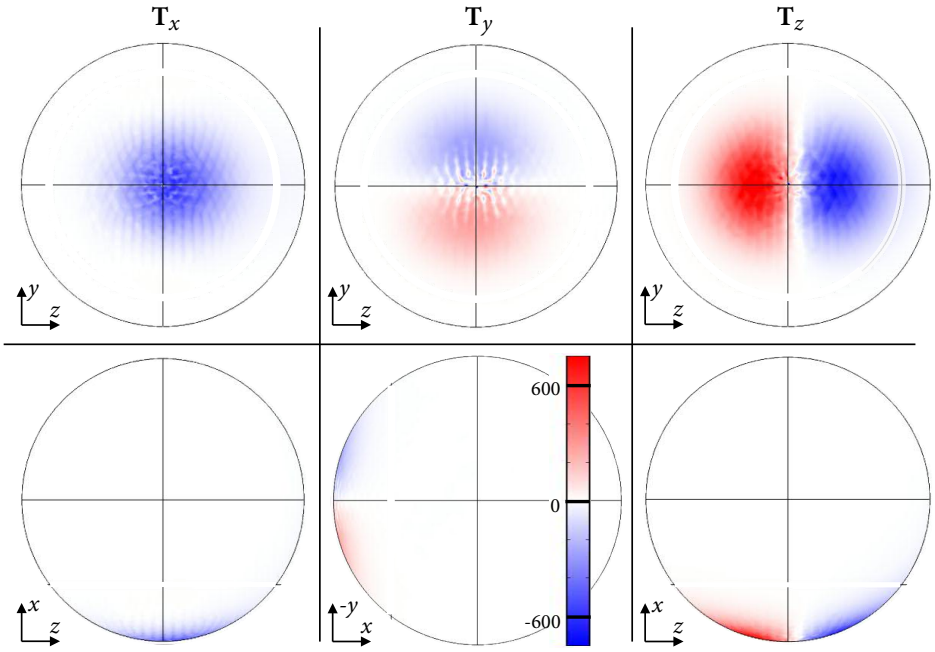


Figure 3.8: Plots showing the distribution of the stress ($\mathbf{T}_i$=$\sum_j \sigma_{ij} \cdot \mathbf{n}_j$, $i, j$=$\{x, y, z\}$) on the surface of a 2 µm diameter glass sphere ($n$=1.5) on top of a 3 µm wide waveguide, with the field propagating in the positive $z$ direction. The stress in the upward ($x$), lateral ($y$), and propagation $z$ directions are shown from left to right. In the top row, the sphere is seen from underneath. The leftmost and rightmost plot in the bottom row shows the sphere seen from the side. The center plot in the bottom row shows the sphere seen from the front. The color scale is similar for all the plots, with local stress values ranging from -700 (blue) to +700 (red) N/m$^2$

### 3.3.3 Properties of the Numerical Model

For the numerical model to give accurate results, it is necessary to properly describe the field propagating in the waveguide, the field interacting with the object, and to absorb the propagating and scattered field at the boundaries of the numerical domain. In this section, the properties of the model used in the simulations are described and discussed.

#### Symmetry

The model describes an object on the surface of a dielectric waveguide with a rectangular cross section, as shown in figure 3.9. The geometry has a symmetry plane at the lateral center of the waveguide. This is not used to halve the model size, since the field scattered off the object cannot be perfectly mirrored with a simple boundary condition. For the precision necessary for small horizontal forces, a halving introduces too big errors.

#### Domain

The numerical domain consists of several subdomains; a silica substrate, a tantalum pentoxide waveguide, a water cover region, and the object of interest. The subdomains are defined by their refractive indices. The object is placed 25 nm above the waveguide surface, centered in the lateral direction. The object is not placed closer to the surface since the mesh density between the waveguide and the object would become too high, substantially increasing the number of nodes in the numerical model. The physical domain is surrounded by absorbing PML domains at the top, bottom and end surfaces. All the domains are shown in figure 3.9. In all the subdomains, conductivities are set to zero and relative permeabilities are set to one.

#### Mesh

The substrate, cover, waveguide, and object domains are meshed with triangular elements on surfaces and tetrahedral elements in volume regions. The PML domains

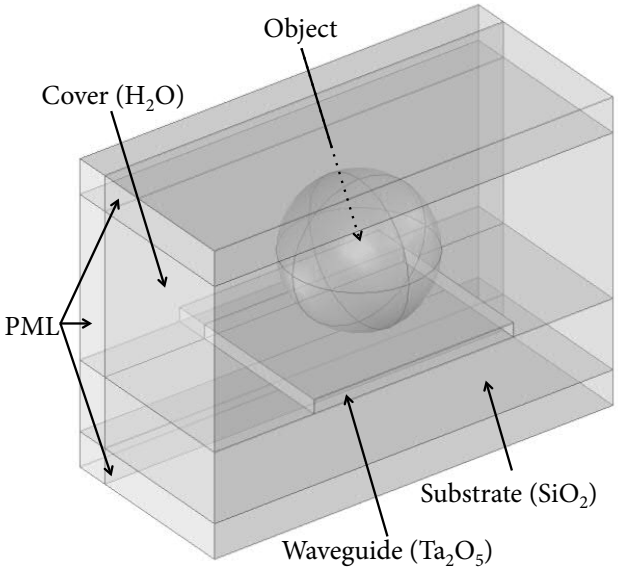


Figure 3.9: Simulation geometry. The physical domain consists of substrate, waveguide, cover, and object regions. An absorbing PML surrounds the physical domain at the top, bottom and end surfaces.

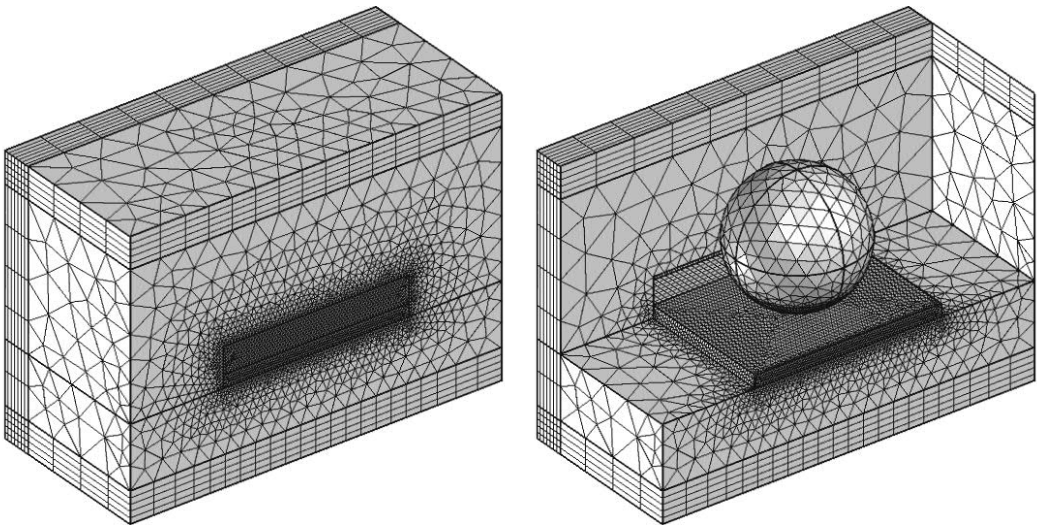

Figure 3.10: Surface meshes of the different domains in the model, seen on the outside (left) and inside (right). A triangular surface mesh is used in the physical domains, while a rectangular swept mesh is used in the PML regions. The tetrahedral elements in the volume regions are not shown.

are swept outward from the physical domain boundary with rectangular elements. Figure 3.10 shows the surface meshes in the whole domain.

The number of mesh points (nodes) determines the size of the numerical model. The mesh should reflect the field distribution in the domain, with a dense mesh where the field is strong or strongly varying. A looser mesh can be used in regions where the field is weak and slowly varying. Using quadratic shape functions, five or more mesh elements per wavelength are required for an accurate simulation of a propagating wave [68]. The relationship between the geometric size of the model and the wavelength thus determines the numerical size of a model. This means that simulating a field propagating in a long and wide waveguide will be demanding. In the waveguide trapping model, the length of the waveguide is set as small as possible. This means that it is the size of the trapped object that limits the model size. Large objects thus give considerably larger numerical models than small objects. In narrow spaces between separate domains, the mesh density should also be high, increasing model size. Thus, thin or narrow regions should as far as possible be avoided to limit the model size.

To create strong evanescent fields, tightly confined waveguide modes are preferred in the experiments. This means the field is mainly concentrated very close to the waveguide, and a dense mesh must be set in this domain. As the evanescent field quickly decay, the mesh density is set to gradually decrease moving away from the waveguide. An example of mesh densities used in the simulations can be seen in figure 3.11, which shows a cross section of the domain along the propagation direction. Since only the waveguide and its immediate surroundings experience strong and strongly varying fields, the coarsely meshed regions far from waveguide and object contribute much less to the size of the numerical model.

**Test Functions**

The default test functions in Comsol are used in the model. For electromagnetic models, this corresponds to quadratic vector shape functions. As described in section 3.2.3, vector functions ensures continuity of the tangential electric field and allows discontinuity of the normal field across elements, thereby preventing unphysical solutions.

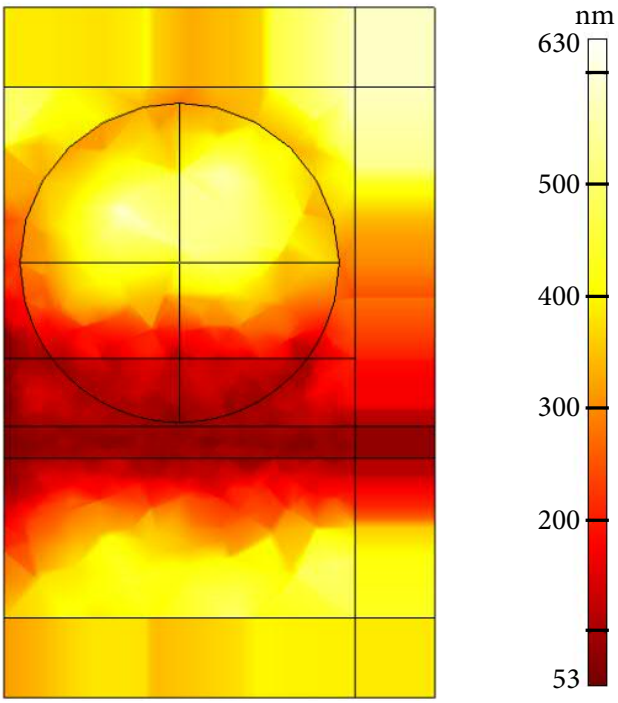


Figure 3.11: Cross section along the center of the waveguide showing the mesh density in different regions of the model. The color legend indicates the size of a mesh element in the domain.

### Boundary Values

The field distribution in the model is found using the Helmholtz equation. An accurate solution requires proper boundary conditions. For each surface, a suitable boundary condition is chosen depending on the distribution and propagation direction of the field.

**Perfectly conducting boundary** The boundaries that interact very little with propagating or scattered fields are set to be perfectly conducting for a polarization direction. The tangential components of the electric or magnetic field will be set to zero, while perpendicular components will be reflected. This boundary condition will thus only remove tangential fields. The two alternative boundary equations implemented through functions $\nabla \times \mathbf{E} = 0$ for a perfect electric conductor and $\nabla \times \mathbf{B} = 0$ for a perfect magnetic conductor.

In the two-dimensional boundary mode analysis, the boundaries are the four outer surface edges. Only the TE polarized (horizontal electric field) fundamental mode will be considered in the simulations. Thus, the top and bottom edges are set to be perfect electric conductors while the side edges are set to perfect magnetic conductors. In the three-dimensional model, the side boundaries are set to be perfect magnetic conductors. As the field decays quickly away from the waveguide, practically no field is seen by the edges and the side boundaries.

**Port boundary** The fundamental mode propagating constant and field distribution is calculated in a two-dimensional boundary mode analysis of the input boundary face. These values are used to excite the waveguide field in the full three-dimensional analysis. The coupling between the analyses is done using Comsol's 'port' boundary condition. The port boundary absorbs fields with similar propagation constant as the excited field. Field components which do not exist in the excited field will be partially reflected. Such reflections have not been observed in the waveguide simulations. S-parameters at the port give reflection ratios of around 1 part in 10 000.

**Perfectly matched layer** A boundary surface does not suffice to completely absorb propagating and scattered fields with unknown propagation constants. To

remove these fields, the perfectly matched layer domain described in section 3.2.4 is introduced at the end, at the top and at the bottom of the model

The top and bottom surface is covered with PML domains absorbing fields propagating in vertical directions. These PML domains are followed by perfect electric conductors which absorb the tangential components of the remaining field. The end surface is covered with a PML domain absorbing fields propagating in horizontal directions. This PML domain is followed by a scattering boundary surface (see next paragraph), which removes plane waves. The PML thickness is 0.5 µm, scaled to one wavelength by coordinate transformation, which is found to be sufficient to stop reflections within the required accuracy.

**Scattering boundary** The scattering boundary condition is designed to remove plane waves. This means any waves described by $\mathbf{E} = \mathbf{E}_0 \exp^{-\jmath \mathbf{k}_0 \mathbf{r}} + \mathbf{E}_{\text{scattered}} \exp^{-\jmath \mathbf{k} \mathbf{r}}$, where $\mathbf{k}$ is the propagation constant of the scattered field and $\mathbf{E}_0$ represents the initial value plane wave. Waves at normal incidence are completely removed, while other plane waves are partially reflected.

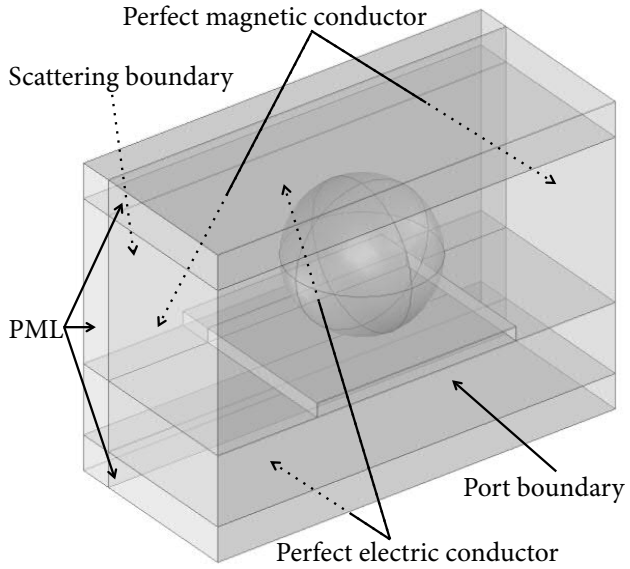


Figure 3.12: Boundary conditions on the surface of the three-dimensional model.

**Solver**

The simulations were done on two different computers. The first simulations were done with Comsol version 3.5, and used the SPOOLES solver on an 8-core, 32 GB memory computer. Random disconnections from the license server made these simulations problematic. Most of the simulations were done with Comsol version 4.2 on the computer cluster Stallo [69], mostly using 8 nodes, each with 8 cores and 16 GB memory (85.12 Gigaflop/s/node). The MUMPS solver was used due to good parallelization properties.

## 3.4 Model Validation

The numerical model was tested by simulating cases with easily verifiable results. Three tests were performed to study the force magnitude, the force direction, and to compare noise level and resolution for different model parameters. For the first test, the sphere was displaced sideways on the waveguide to confirm expected force magnitudes and directions. For the second test, a sphere with similar refractive index as the cover medium was used, such that all calculated forces should be zero. This zero-force model was used to test the mesh convergence, to relate the mesh density to the noise level, and to indicate the resolution of the simulations. For the final test, the accuracy of the model was compared with Mie calculations.

The model was found to give reliable results with a mesh density of 6 points per wavelength in the strong-field regions. This gave a resolution of around 1 pN for the horizontal force and around 4 pN for the vertical force.

### 3.4.1 Lateral Displacement

A spherical object is stably trapped laterally in the center position on a waveguide surface. By displacing the sphere laterally, an optical force would arise to attract the sphere back toward the waveguide center. By simulating the sphere at different off-center positions, a range of lateral forces are calculated. Figure 3.13 shows a cross section of the simulated geometry with a 1 μm diameter glass ($n$=1.5) sphere on top of a 1 μm wide waveguide. Relative lateral force magnitudes on the displaced sphere are shown with arrows in the figure, and the calculated forces at 8 positions to the right of the center are listed in table 3.1.

The calculated lateral forces are found to be negative at all displaced positions, confirming that the sphere is pulled toward the center position. The lateral force becomes stronger with distance from the center, with a maximum for a displacement of 300 nm. At the center position, the calculated lateral force is 1 pN, and not zero as expected. This can be attributed to numerical errors, further described in section 3.4.2. The discrepancy gives an estimate of the noise level in the lateral direction.

The results in table 3.1 show that the total force is stronger at positions near the center of the waveguide. This is to be expected, since the field gradient is stronger in the center. In addition, the field interacts with a larger region of the sphere in the center.

The results from the displacement test qualitatively validates the simulations. The displaced sphere is attracted toward the centre and toward the waveguide and pushed forward in the horizontal direction. It is also reasonable that the magnitude of the vertical force dominates the horizontal and lateral forces, considering the strong gradient and weak intensity of the evanescent field.

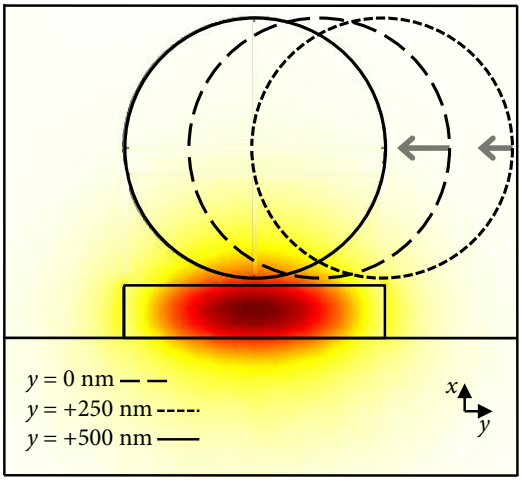


Figure 3.13: Illustration of forces on a laterally displaced 1 $\mu$m diameter glass sphere ($n$=1.5) on a 1 $\mu$m wide waveguide. The force values are found in table 3.1. The arrow length indicates lateral force magnitude

Table 3.1: Forces on a 1 μm diameter glass sphere ($n$=1.5) laterally displaced on a 1 μm wide waveguide

| Lateral Displacement (nm) | Vertical $F_x$ (pN) | Lateral $F_y$ (pN) | Horizontal $F_z$ (pN) | Total Force $\sqrt{F_x^2 + F_y^2 + F_z^2}$ |
|---|---|---|---|---|
| 0 | -203.9 | 1.0 | 19.0 | 204.8 |
| 25 | -202.8 | -7.8 | 20.6 | 204.0 |
| 50 | -205.9 | -10.7 | 24.7 | 207.7 |
| 100 | -195.2 | -16.5 | 15.1 | 196.5 |
| 200 | -168.6 | -28.2 | 12.3 | 171.4 |
| 300 | -128.6 | -32.5 | 12.6 | 133.2 |
| 400 | -88.2 | -30.6 | 8.67 | 93.8 |
| 500 | -55.5 | -21.9 | 5.86 | 60.0 |

### 3.4.2 Resolution

#### Field-dependent resolution

The uncertainty of the model results was estimated with simulations of a spherical object with the same refractive index as the surrounding medium. Without any index difference, any optical forces on the object should be absent. However, any numerical inaccuracies will result in force simulation errors. This can be understood from how the force is calculated. The total force on the object is found by summing up the stress over the object surface. The stress is found by the product of the stress tensor and the surface normals and is dependent of the field through Maxwell's stress tensor, as shown in equation (3.10). Any change the field experiences inside the object is interpreted as a scattering incident. Whether the change is the result of an inaccurate field value or the result of an actual scattering event is not taken into account. To avoid numerical errors, the mesh density must be sufficient to properly describe the propagating and scattered fields inside the object.

Figure 3.8 showed the local stress distribution for each spatial direction on the surface of a glass sphere interacting with an evanescent field. In the vertical $x$ direction, the stress adds up and the sphere experiences a strong force toward the waveguide. Thus, even if the relative noise level is low, the absolute noise levels can be be high compared to the forces in the horizontal and lateral directions. In the horizontal $z$ direction, the stress values are strong and opposite in the front and back of the sphere. Thus, the horizontal force on the sphere depends on the differ-

ence between two large numbers. This makes accurate numerical force calculations challenging, and requires a high mesh density both on the surface and inside the sphere. In the lateral $y$ direction, the stress values are weaker and opposite on the left and right side of the sphere. For a centered sphere the expected total lateral force is zero, as the stresses are symmetric. Section 3.4.1 showed a lateral noise level of around 1 pN, and most simulations show sub-piconewton lateral forces.

### Mesh-dependent resolution

Table 3.2 and figure 3.14 show results from force simulations for a 2 μm diameter sphere with refractive index equal to the cover medium ($n$=$n_c$=1.33), on a 3 μm wide waveguide. Calculations were done using Comsol's MUMPS solver on the Stallo computer cluster [69] using 8 cluster nodes, each with 8 cores and 16 GB memory. The mesh density is set to a maximum value (mesh points per wavelength) inside the waveguide and in a region reaching from the waveguide surface up to 400 nm above the surface. The same mesh density is set on the waveguide and sphere surfaces. In the surrounding regions, the mesh is set to grow slowly. The set maximum value then determines the mesh density in the whole model. These meshes are not optimized for simulation accuracy, but give a good overview of how the resolution depends on the mesh density.

Table 3.2: Force convergence for increasing mesh densities for a 2 μm diameter water sphere submerged in water. Any calculated force deviating from zero is the result of numerical inaccuracies. Simulations were performed using the direct MUMPS solver on the Stallo computer cluster using 8 nodes, each with 8 cores and 16 GB memory.

| Density ($\frac{\text{mesh points}}{\lambda}$) | Vertical (pN) | Lateral (pN) | Horizontal (pN) | Degrees of Freedom (1000) | Solver Time (s) |
|---|---|---|---|---|---|
| 2 | 293.9 | -3.9 | 43.2 | 318.3 | 168 |
| 3 | 62.5 | -4.1 | 11.7 | 432.4 | 197 |
| 4 | 31.1 | 1.8 | -3.2 | 551.5 | 286 |
| 5 | 12.8 | -0.2 | 1.3 | 772.2 | 422 |
| 6 | 4.9 | -0.3 | -0.5 | 1099.2 | 671 |
| 7 | 2.3 | -0.2 | 1.5 | 1450.2 | 4100 |
| 8 | 2.1 | 0.4 | -1.9 | 1936.3 | 1369[a] |

[a] For 8 mesh points per wavelength, the number of processors was increased from 64 (8 nodes) to 128 (16 nodes), as 64 processors was unable to solve the problem in 8 hours.

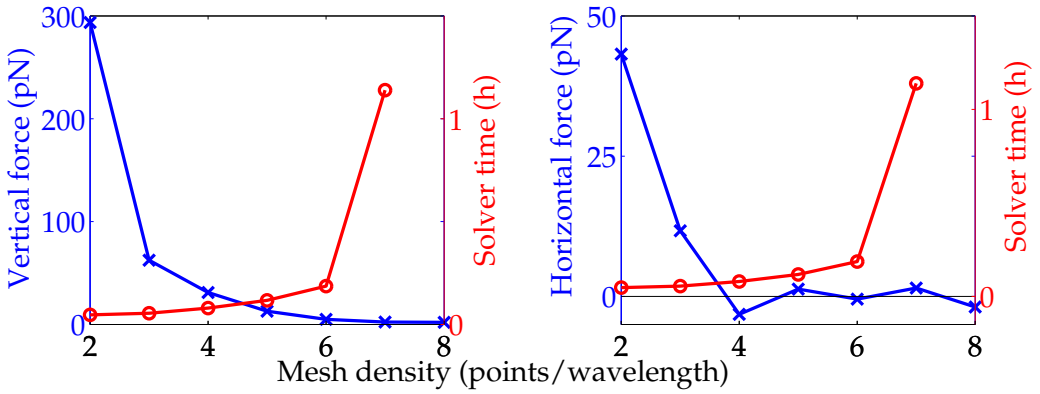


Figure 3.14: Accuracy depending on mesh-density. Forces from a 3 μm wide waveguide for different mesh densities using 2 μm diameter spheres with the same refractive index as the cover medium. Any non-zero forces result from numerical inaccuracies. Calculations were done with Comsol's MUMPS solver on the Stallo cluster computer using 8 nodes, each with 8 cores and 16 GB memory.

The sudden increase of solver time shown in table 3.2 and figure 3.14 shows how the model is easily solved with a direct solver as long as there is sufficient memory available. Each node has 16 GB available memory. The simulation slows down exponentially when the amount of memory is insufficient. By increasing the available memory, larger models can be solved. Table 3.2 does not show the solution time for the model with 1.9 million degrees of freedom. This model could not be solved in 8 hours on 8 nodes, but was solved in slightly more than 20 minutes using 16 nodes.

The results shown in the table and the figure suggest that 6 mesh points per wavelength gives a decent accuracy within a reasonable solver time. The accuracy does not increase noticeably with higher densities in the waveguide and the region above the waveguide, and the mesh can be adjusted in weak-field regions in the domain to further improve the accuracy. In the simulations in chapters 4 and 5, the meshes have been optimized by minimizing the resolution of the horizontal force using a model where the sphere and cover media have equal refractive indices. The specific mesh parameters used in each model will not be given.

**Object size-dependent resolution**

The available memory limits either the physical size or the resolution of a model. Accurate results demand a high mesh density in all regions with strong or strongly varying fields. If the field is strongly scattered, the mesh density needs to be high in a large region. This limits the size of the total region. The field distribution around a waveguide is strongly confined to the region inside and a small region surrounding the waveguide, unless the field is scattered away. Introducing an object on the waveguide surface significantly increase the mesh density requirements in the region where the field is scattered. As scattering is stronger for higher-index objects, the allowed model size also depends on object refractive index. In addition to this, the object size influences the numerical size of the model, even if only a small part of the object is close to the waveguide. The waveguide needs to be at least as long as the diameter of a spherical object. Since the waveguide has a high mesh density, this limits the allowed size of the sphere, even if the scattering is very weak (for the case of a refractive index very similar to that of the cover medium).

### 3.4.3 Comparison with Mie Calculations

Mie theory, briefly explored in sections 2.6.1 and 2.6.2, analytically describes the fields around a sphere with spherical functions expressed in series. The field expressions can be used to numerically calculate forces on the spheres. The calculations derived by Jaising et al. [40, 44] are used to compare Mie and finite element calculations for solid glass spheres and infinitely thin shells (air bubbles) on a waveguide surface. Sphere dimensions and refractive indices are identical for the calculations. In addition, the input powers were chosen such that the intensity at the centre of the waveguide surface was equal. The forces found with the two different methods are shown in figure 3.15 and figure 3.16. The figures mostly show the same general dependence between force and sphere diameter, but the force magnitudes differ.

The vertical forces are repulsive for air bubbles and attractive for glass spheres, and are 1.5 times stronger in the FEM simulations compared to the analytical Mie calculations. The horizontal forces are smaller, and the Mie simulation forces tend to be stronger than the FEM simulation forces. The horizontal force on glass spheres increases, reaching a stable value for large diameters, while the horizontal force on air bubbles reaches a maximum for diameters slightly above 1 μm diameter. A small comment on the Mie results is also given at the end of section 4.4.2.

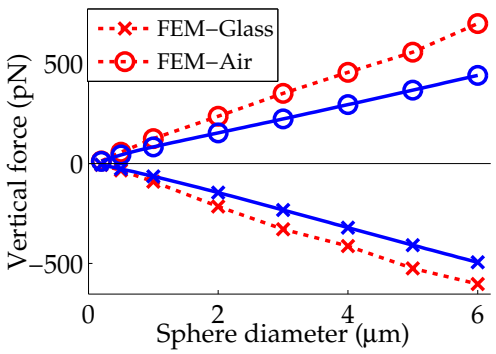


Figure 3.15: Mie-FEM comparison of vertical optical forces.

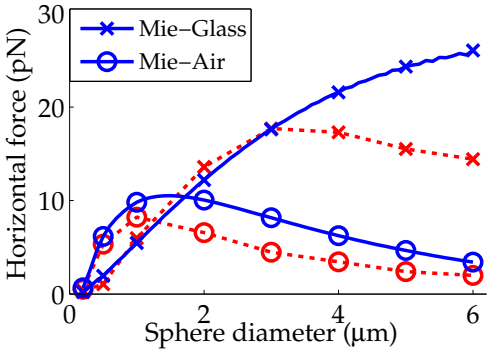


Figure 3.16: Mie-FEM comparison of horizontal optical forces.

The Mie calculations presuppose a uniform evanescent field distribution in the cover region, using the values from the center of the waveguide. This implies a stronger horizontal force in the Mie calculation, as the constant-height evanescent field gives a larger intersection area (the field does not taper off laterally). A similar reasoning explains why the vertical force is larger in the FEM simulation, as the gradient is stronger for the non-uniform evanescent field in the intersection region of the field and the sphere. These considerations account for some of the discrepancy between the models. In addition, interactions between the sphere and waveguide, such as multiple reflections, are taken into account in the FEM simulation, but not considered in the Mie calculations.

## 3.5 Conclusions

A numerical model is constructed for simulations of microparticle trapping on an optical waveguide surface. The model is implemented in the commercial software Comsol Multiphyscs, which solves the problem using the finite element method. This method is suitable for problem geometries of any shape. The simulations are run on the computer cluster Stallo using the MUMPS solver.

Lateral displacement tests and comparisons with Mie calculations provide qualitative results that validate the use of the numerical model. There is a strong dependence on mesh density and accurate field propagation to acquire accurate results. This means that each simulation geometry requires a specifically designed mesh.

The validation tests give reason to believe that models using spherical objects with more than 6 mesh points per wavelength in strong field regions are accurate to within 5 pN in the vertical direction and 2 pN in the horizontal direction. The following two chapters present calculations of optical forces for different microparticles.

# Chapter 4

# Modeling Hollow Microspheres on a Waveguide

## 4.1 Introduction

Hollow microspheres are gas-filled organic or inorganic spherical shells. They are used in biomedicine as ultrasound contrast agents [70], and has the potential to be used for drug delivery or drug targeting [71]. The shells are made from organic material or glass. Organic shells are very thin, while the shell thickness of the hollow glass microspheres is difficult to control accurately in the manufacturing process, giving a large distribution of thicknesses. Gas bubbles can be considered to be hollow spheres with infinitely thin shells, and have been studied experimentally in solution [72].

In the context of optics, hollow microspheres are interesting because of their average refractive index, which decreases due to the gas cavity inside the shell. When the refractive index is lower than that of the surrounding liquid media, the gradient force in an optical trap (see chapter 2) is repulsive. Thus, optical trapping becomes a challenge and special optical designs are necessary for trapping.

This chapter presents a numerical model of optical forces exerted on a hollow sphere by an evanescent field. A full range of glass shell thicknesses is used, from gas bubbles to solid spheres. The results are compared with two simpler models, as well as experimental results. The chapter first discusses properties of hollow spheres,

how such low-index particles can be trapped optically, and the limits of the trapping. Then, in section 4.3, trapping of hollow spheres on waveguides is described, and some experimental results are presented. In section 4.4, the computer simulations of the waveguide trapping are described. With the use of simple analytical models described in section 4.5, this gives some insights in the hollow sphere trapping properties. Finally, section 4.6 compares experimental velocities to velocities calculated from the simulations, discrepancies are discussed, and the chapter is concluded in section 4.7.

## 4.2 Hollow Sphere Properties

This section introduces a way to calculate the density and refractive index of a hollow sphere. These parameters will not be used until section 4.5, but are presented early to provide some insights in the properties of hollow spheres.

### 4.2.1 Buoyancy

For thin shells, the mass density of hollow spheres is lower than the mass density of water. Such particles would float in solution. This makes the particles challenging to trap close to surfaces covered with water. The hollow sphere density $\tau_{\text{HS}}$ can be calculated as

$$\begin{aligned}\tau_{\text{HS}} &= \frac{\tau_{\text{shell}} \cdot V_{\text{sphere}} - \tau_{\text{shell}} \cdot V_{\text{cavity}} + \tau_{\text{cavity}} \cdot V_{\text{cavity}}}{V_{\text{sphere}}} \\ &= \tau_{\text{shell}} + (\tau_{\text{cavity}} - \tau_{\text{shell}}) \frac{(a-T)^3}{a^3}, \end{aligned} \tag{4.1}$$

where $a$ is the sphere radius, $T$ is the shell thickness, $\tau_{\text{shell}}$ is the mass density of the shell, $\tau_{\text{cavity}}$ is the mass density of the cavity, and the sphere and cavity have volumes

$$V_{\text{sphere}} = \frac{4\pi}{3} a^3 \quad \text{and} \quad V_{\text{cavity}} = \frac{4\pi}{3} (a-T)^3 . \tag{4.2}$$

Another useful parameter will also be introduced at this point. This is the volume of a spherical cap, the region cut off a sphere by a planar surface. With $h$ being

the cap height (the longest distance perpendicular to the planar surface), the cap volume is given by

$$V_{\text{cap}} = \frac{\pi h^2}{3}\left(3a - h\right), \tag{4.3}$$

where $h$ is the height of the cap.

In the simulations, the chosen material for the shell is glass with a mass density $\tau_{\text{glass}} = 2.2$ g/cm, and the chosen material for the cavity is air with a mass density $\tau_{\text{air}} = 0.001$ g/cm. The mass density of water is $\tau_{\text{water}} = 0.998$ g/cm. Spheres with an average mass density lower than $\tau_{\text{water}}$ float.

### 4.2.2 Refractive Index

The total (average) refractive index of hollow spheres, $n_{\text{HS}}$, can be calculated in a similar way as its mass density. This gives

$$n_{\text{HS}} = n_{\text{shell}} + (n_{\text{cavity}} - n_{\text{shell}})\frac{(a-T)^3}{a^3}, \tag{4.4}$$

where $n_{\text{shell}}$ is the refractive index of the shell and $n_{\text{cavity}}$ is the refractive index of the cavity. In the simulations, the glass shell is chosen to have a refractive index $n_{\text{glass}} = 1.5$ and the air cavity is chosen to have a refractive index $n_{\text{air}} = 1$.

Particles with an average refractive index higher than their surrounding medium are called high-index particles, while particles with lower average refractive index than their surroundings are called low-index particles. High-index particles experience an attractive force near a field gradient, while low-index particles experience an repulsive force near a field gradient.

## 4.3 Trapping of Hollow Spheres

### 4.3.1 Trapping with a Strongly Focused Beam

Figure 4.1 shows sketches of high- and low-index spheres in focused Gaussian and non-Gaussian beams. The directions of the optical forces are indicated in the figure, and show how a low-index sphere is repelled from a Gaussian beam trap and

trapped with a non-Gaussian beam. Such beams include vortex beams [73–75], Bessel beams of different order [76, 77], and self-imaged bottle beams [78], which all contain a vortex or discontinuity point and are constructed by manipulating the wavefront of a Gaussian beam. The intensity distribution in the focal plane of such beams surrounds the low-index particle. The particle cavity is repelled away from the field gradient, while the shell is attracted toward the field gradient, locking the particle in place as suggested in the rightmost sketch in the figure. Manipulating the spatial distribution with a circularly scanning beam [79, 80] or by an interference patterns [81] also allows Gaussian beams to be used for low-index trapping. The working principle is similar to the non-Gaussian beam traps, and the techniques require precise spatial and temporal control of the field distribution.

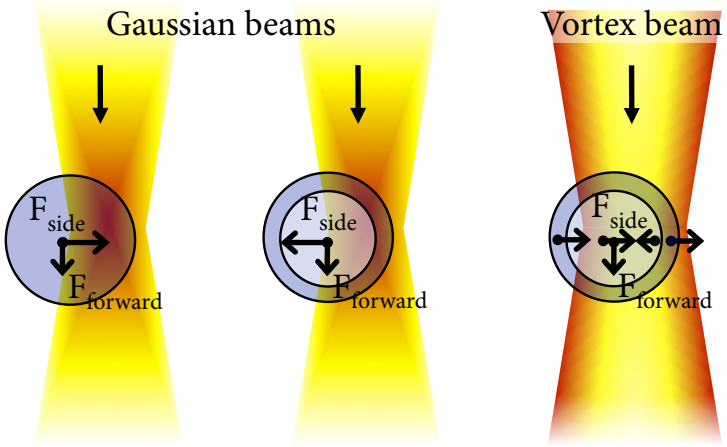


Figure 4.1: Optical forces in free space focus traps. (left) A solid high-index sphere is attracted to a Gaussian beam focus. (center) A hollow low-index sphere is repelled from a gaussian beam focus. (right) The shell and cavity of a hollow low-index sphere is respectively attracted to and repelled from the high-intensity regions in the non-Gaussian beam focus.

### 4.3.2 Trapping on a Waveguide

The methods for low-index trapping depend mostly on repulsive optical forces. These methods surround the particle with an optical field, thus creating a low-energy potential well for the particle inside the field. However, attractive optical forces can also contribute by trapping only a small high-index part of the particle.

The evanescent field above an optical waveguide would attract the shell and repel the cavity of the hollow sphere. When the attractive forces dominate, the hollow sphere is trapped by the evanescent field. The trapping force magnitude and direction depends on the waveguide field distribution, the sphere radius and the shell thickness, as well as cavity and shell refractive indices. A sketch of waveguide field distribution near a hollow sphere is shown in figure 4.2

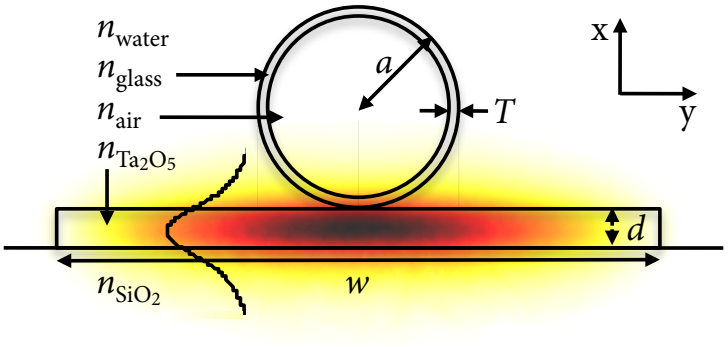


Figure 4.2: Cross section transversal to the waveguide showing a hollow glass sphere with radius $a$ and shell thickness $T$ on a Tantalum pentoxide waveguide with width $w$ and height $d$. The fundamental TE mode of the waveguide is shown with a plot of the field intensity across the waveguide.

Experiments where waveguide trapping was used to trap hollow microspheres [2] instigated the numerical study of optical force dependency on shell thickness presented in this chapter. The experiments showed that some hollow spheres where trapped while others were not. An analytical model shows how the trapping properties can be explained by the average refractive index of the sphere region experiencing the evanescent field. This chapter, expanding on previous work by Løvhaugen et al. [4], presents the simulation results, and compare them with the experimental data and the analytical analysis.

### Experiments with hollow spheres on waveguides

Experiments with hollow spheres, performed and presented by B. S. Ahluwalia et al. [2], studied velocity and shell thickness distributions of samples of hollow and solid glass spheres. Figures 4.3 and 4.4 present results from this work for spheres with diameters under 7 μm.

Figure 4.3 shows the shell thickness distribution for a number of hollow glass spheres. At one micrometer intervals, mean values and standard deviations of shell thicknesses and diameters are found. These values are plotted with error bars in the figure. A dashed blue line indicates the boundary between floating and sinking hollow spheres in water. A dotted red line indicates the boundary between high- and low-index hollow spheres. Gaussian beam trapping is only possible for the particles above the red transition line.

Most of the particles from the batch of hollow glass spheres could be trapped on waveguides. The particle velocities of solid and hollow spheres are shown in figure 4.4 as function of the particle diameter. At one micrometer intervals, the velocity means and standard deviations are plotted with error bars. The input laser power in the experiments was 1.5 W.

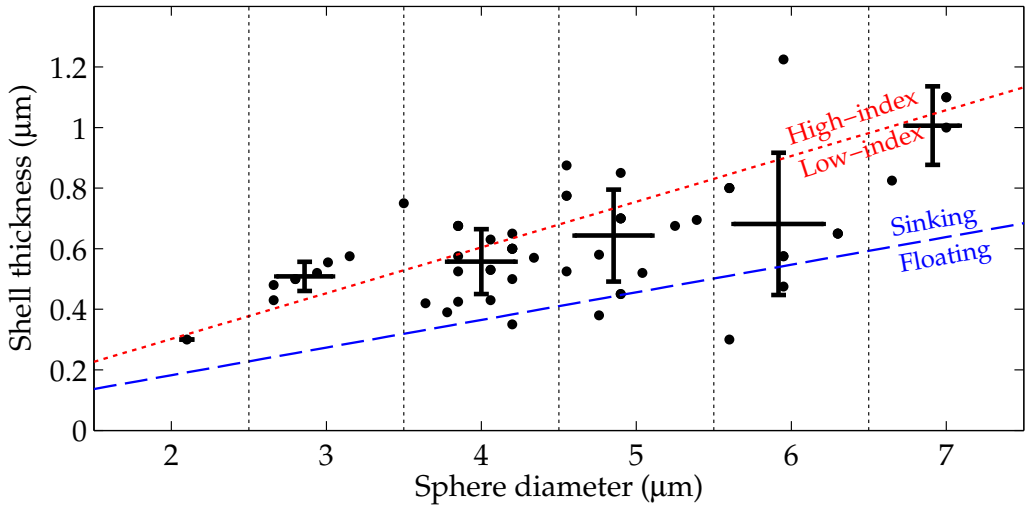


Figure 4.3: Distribution of sphere diameters and shell thicknesses in a batch of 59 hollow glass spheres. Only a small part of the spheres are floating. The large hollow spheres are mostly low-index, while the small hollow spheres are mostly high-index, as expected when the shell thicknesses are fairly constant (increase slowly) over the range of sphere diameters. Data from [2].

The exact optical properties of the hollow and solid spheres are not known. The refractive indices were not given by the manufacturer, and the surface structure of the spheres are not known. For the hollow spheres, some detergent was applied in the sample solution to allow propulsion. This suggests that some surface effect

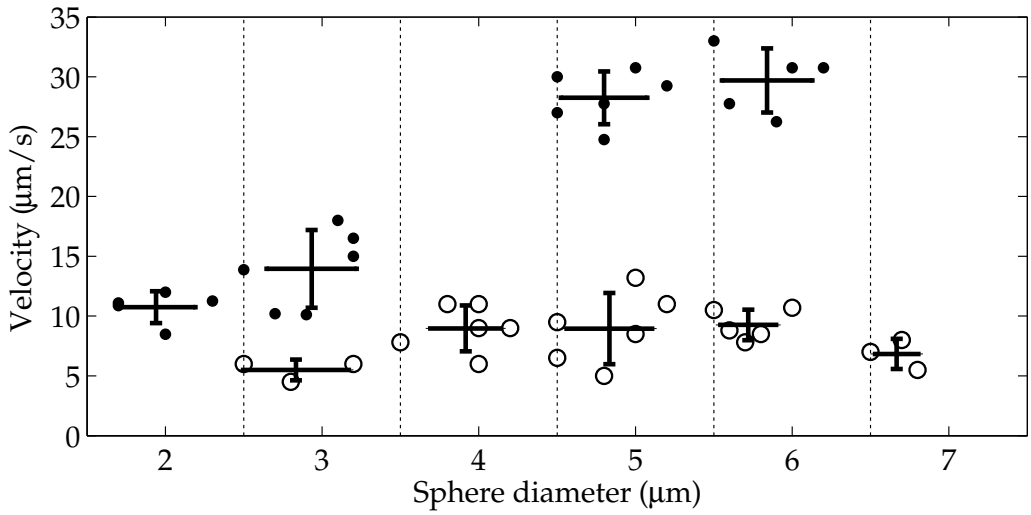


Figure 4.4: Distribution of sphere diameters and velocities for samples of 22 solid (solid rings) and 23 hollow (empty rings) glass spheres on a 3 µm wide waveguide at 1.5 W laser input power. The hollow spheres travel markedly slower than the solid spheres. At one micrometer intervals, error bars show mean and standard deviation of diameters and velocities. Data from [2].

between the spheres and the waveguide was present. This effect is not accounted for in the simulations.

## 4.4 Simulations of Hollow Spheres on Waveguides

The simulations were done using the finite element method software Comsol Multiphysics, as described in chapter 3. The model simulates a sphere on a 3 μm wide waveguide. The sphere was laterally centered on the waveguide, situated 25 nm above its surface. The small vertical gap was used to avoid very small mesh elements. Sphere diameters ranged from 0.2 to 6 μm, with thicknesses from 25 to 500 nm, and also included solid spheres and air bubbles. The length of the waveguides in the model were only slightly longer than the sphere diameter to minimize computational effort, but still allow simulations of whole spheres.

Forces in horizontal and vertical directions were found by integrating Maxwell's stress tensor over the sphere surface. The results are presented in figures 4.5-4.10. In the figures, empty ring markers indicate simulated gas bubbles, solid ring markers indicate simulated solid glass spheres, and cross markers indicate simulated hollow spheres.

It is important to note that every simulation has been optimized with zero-index difference simulations (see section 3.4.2). The offset force found from these simulations have been subtracted from the results presented here. This means the presented results have been shifted within the force resolution of the simulations; at most 2 pN for the horizontal force and 5 pN for the vertical force.

### 4.4.1 Shell thickness dependence

Figure 4.5 shows calculated forces in the vertical direction as a function of shell thickness. The origin of these forces is mainly the gradient of the field. The results are given for 8 different diameters. For larger spheres, the evanescent field interacts with more of the sphere surface than for smaller spheres. Thus, large spheres experience larger forces. For thin shell thicknesses, repulsive forces push the spheres away from the waveguide. When the shell thickness increases, the repulsive force decreases, and the force becomes attractive when the shell thickness approaches around 65 nm. The attractive forces reach a constant value for thicknesses around

250 nm. A close-up of the transition point between repulsive and attractive forces are given in figure 4.7. This shows that the transition point increases with sphere size up to 1 μm diameter, where the transition points stabilizes close to 65 nm. This has to do with the sphere and cavity surfaces as well as the range of the evanescent field, and will be further discussed in section 4.5.

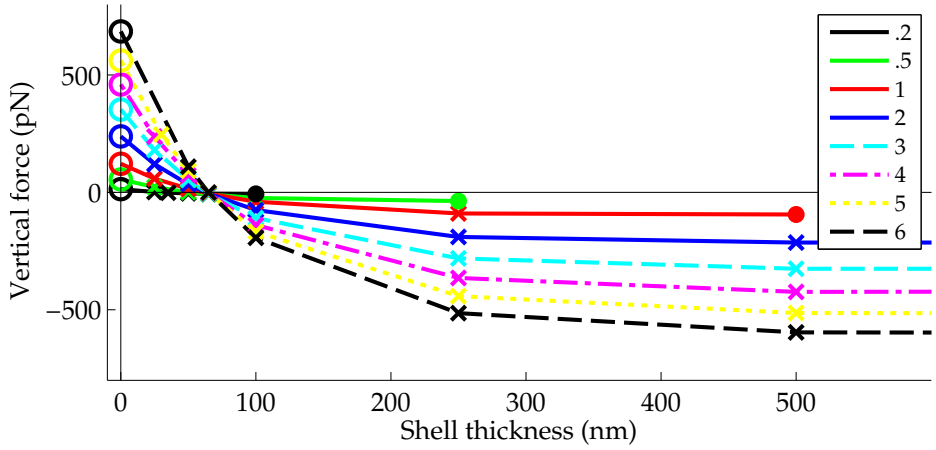


Figure 4.5: Vertical forces on hollow spheres from 0.2 to 6 μm diameter as function of shell thickness. Larger spheres experience larger forces, and the transition from repulsive to attractive forces occur close to 65 nm shell thickness. The legend indicates sphere diameters.

Figure 4.6 shows calculated forces in the horizontal direction as a function of shell thickness. The origin of the force is mainly scattering of the field. The results are given for 8 different diameters. The horizontal forces are found to be more than one order of magnitude weaker than the vertical forces. A minimum force is found close to 100 nm shell thickness for all sphere diameters. It is reasonable to relate this minimum to the zero vertical force in the same shell thickness region. Apparently, for spheres with this shell thickness, the field is only slightly perturbed, and the scattered field is very similar to the incident field.

A close-up of the horizontal force minimum is given in figure 4.8. This plot also includes results for a 0.2 μm diameter sphere. The horizontal forces near the minimum are so weak that the results are below the resolution limit of the simulations. This is particularly noticeable for thin shells and large diameters, as the mesh at some point becomes so big that the geometry of the shell region cannot be properly approximated. For the simulations of a 6 μm diameter hollow sphere, results

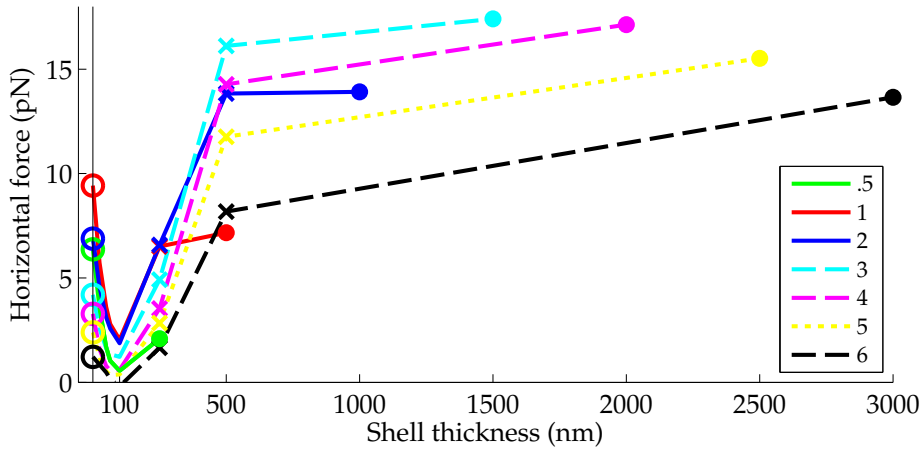


Figure 4.6: Horizontal forces on hollow spheres from 0.5 to 6 μm diameter as function of shell thickness. The force resolution is around 2 pN. A force minimum is found close to 100 nm thickness for all sphere diameters. The legend indicates sphere diameters.

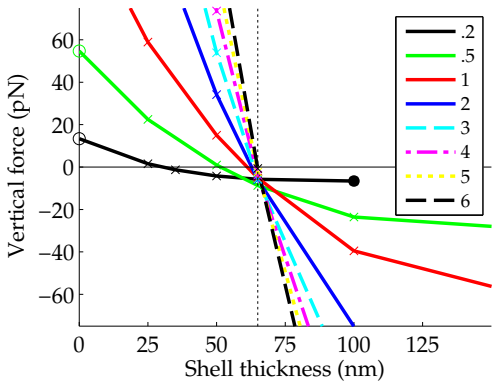


Figure 4.7: Close-up of figure 4.5, showing the transition points between repulsive and attractive gradient forces on the hollow spheres.

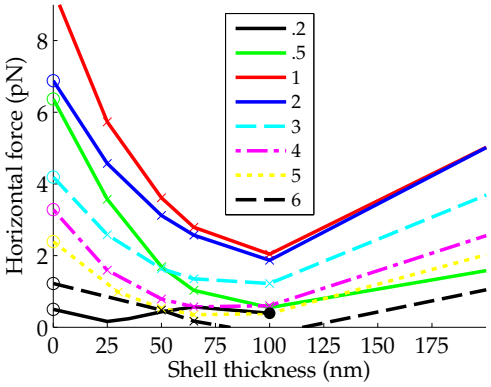


Figure 4.8: Close-up of figure 4.6, showing the minimum propagation force of the hollow spheres.

for thin shells show higher uncertainties than the other spheres. In the plot, the force offsets from the zero-index difference simulations have been subtracted, as mentioned at the start of the section. The close-up also reveals a slight shift of the force minimum toward thinner shells for smaller spheres. This is again analogous with the vertical force results, and will be discussed in section 4.5.2.

### 4.4.2 Sphere diameter dependence

Figures 4.9 and 4.10 present the force distributions as function of sphere diameter. This is just a different presentation of the data shown in figures 4.5 and 4.6. However, only results from air bubbles, 50, 100 and 250 nm thick shells and solid glass spheres are included.

The vertical force in figure 4.9 shows a linear relationship between diameter and force for all thicknesses. Air bubbles and spheres with 50 nm thick shells are repelled from the waveguide, while the remaining spheres are attracted to the waveguide. A vertical force of zero is experienced for a shell thickness between 50 and 100, found to be close to 65 nm for large spheres in figure 4.7.

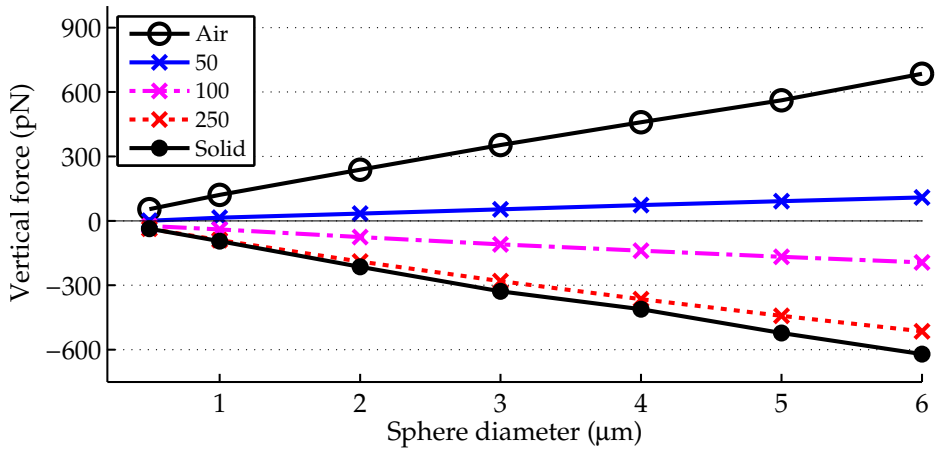


Figure 4.9: Vertical forces on solid spheres, and spheres with 0, 50, 100, 250 nm shell thickness as function of the sphere diameter. Spheres where air dominates are repelled from the waveguide. Spheres where glass dominates are attracted to the waveguide. The transition point is close to 65 nm shell thickness. The forces are linearly dependent on the diameter. The legend indicates the shell thicknesses in nanometers.

The horizontal force in figure 4.10 shows maxima close to 3 μm for the solid glass sphere and close to 1 μm for the air bubble. The hollow spheres experience least forces, with minimum forces for a 100 nm thick shell and force maxima for diameters between 1 and 2 μm. The plots provide some insights into the nature of the weak horizontal force. First, very small spheres experience very small horizontal forces as the Rayleigh force strongly depend on sphere size (section 2.6.2). Second, large spheres experience small horizontal forces as the evanescent field only interacts with a very narrow cap of the sphere. This means that the incident angle of the field is very large, close to tangential. For this reason, the incident field reflect off the surface with only a slight perturbation. Thus, very little momentum is transferred to the sphere. The sphere diameters represented in the figure are bigger than Rayleigh particles, but small enough to experience the field (as seen in figure 4.11 for a 1 μm diameter sphere). For these spheres, the field can be refracted into, or reflected back from, the sphere. Thus, momentum transfer to the sphere can occur. The reflectivity from the air bubble is larger than from the glass shell, giv-

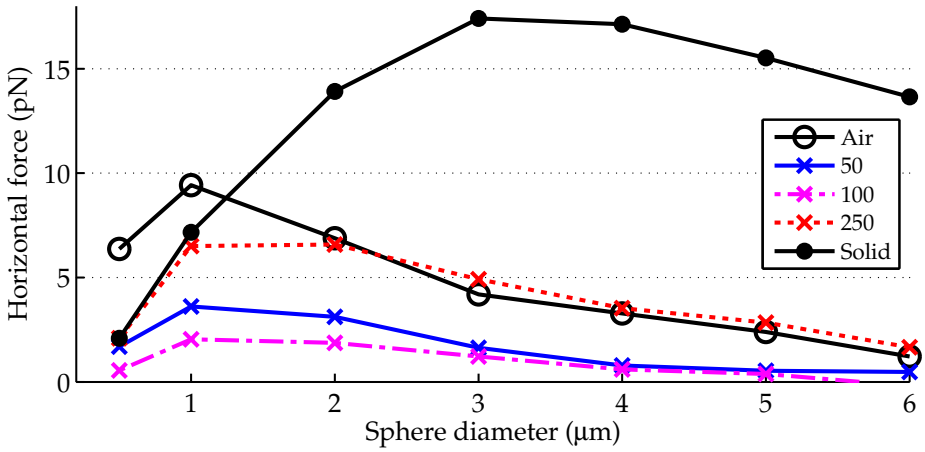


Figure 4.10: Horizontal forces on solid spheres, and spheres with 0, 50, 100 and 250 nm shell thickness as function of the sphere diameter. Solid glass spheres have a maximum force near 3 μm, air bubbles have a maximum force near 1 μm, and the hollow spheres have maxima between 1 and 3 μm. The resolution of the simulations is between 1 and 2 pN. The legend indicates the shell thicknesses in nanometers.

ing larger forces for the (more reflecting, less refracting) smaller spheres. The decreasing force for larger air bubbles and the force maximum for the 3 μm diameter sphere can be explained by looking at the gradient force. Imagining the spheres to act as a micro-lenses for the incident field, the scattered field will be converging for

the solid glass sphere and diverging for the air bubble. These fields create a small field gradient, positive for the converging and negative for the diverging field. From Gaussian field optics, it is known that the narrowest focus occurs when the incident field match the lens width. Thus, the strongest gradient force occur for the sphere best matching the 3 μm width of the waveguide. For smaller and larger spheres, the evanescent field 'overfills' or 'underfills' the sphere lens. Thus, the strongest positive horizontal gradient force is experienced for the 3 μm diameter solid glass sphere, and the strongest negative horizontal gradient force is experienced for the 3 μm diameter air bubble. No minimum is found for the air bubble though, as the force decrease with sphere size, as discussed previously in this paragraph.

The same effect can be used to explain the horizontal force discrepancy between FEM and Mie calculations shown in section 3.4.3. For forces calculated with Mie theory, the width of the incident field is set to be infinite, and the 'lens effect' described above is not seen.

For the hollow spheres, a combination of the air bubble and solid glass sphere effects takes place. Figure 4.10 shows the smallest forces for the spheres with 100 nm thick shells and force maxima between 1 and 2 μm. Surprisingly, the shell thickness needs to be much larger than the extent of the evanescent field to experience the same force as the solid spheres. Thus, field perturbations from small cavities in a sphere significantly influence the horizontal force.

## 4.5 Refractive Index Dependent Force Models

As seen in section 4.3.2, low-index spheres can be optically trapped on a waveguide surface due to the evanescent field interacting mainly with the high-index shell. This section will present two simple models which give a physical understanding of when hollow spheres are attracted to the waveguide, and when they are not. The model is based on the refractive index difference between the hollow sphere and the surrounding medium. The results will be compared to results from the full three-dimensional model.

### 4.5.1 Weighted Refractive Indices

The refractive index of a hollow sphere is described in section 4.2.2. However, if only parts of the sphere interact with a field, or if a field is non-uniform across the sphere, the total refractive index can be calculated differently to better describe the physical behavior of the sphere. By introducing a weighted refractive index, only the interaction region shared by field and sphere is included. Two different weighted effective indices will be described in the following to model a hollow sphere on a waveguide surface. The first weighted index uses a step weighting function with height $h$. This corresponds to the evanescent field being approximated by a weak, constant field with fixed height. The second weighted index uses an exponentially decaying weighting function. This gives a more precise approximation of the evanescent field, being constant only in the lateral direction.

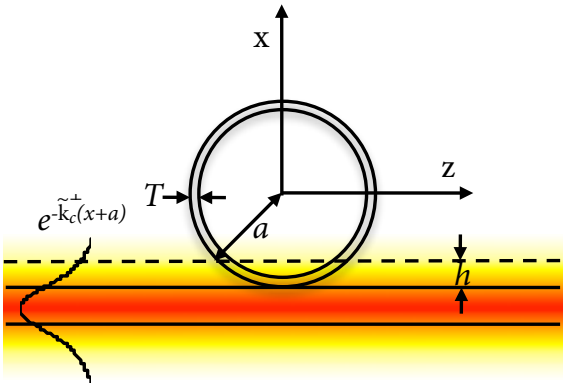


Figure 4.11: Cross section along the waveguide showing a hollow glass sphere with radius $a$ and shell thickness $T$. The two evanescent function approximations are indicated. $h$ denotes the extent of the step weighting function and $e^{-\tilde{k}_c^{\perp}(x+a)}$ is the decaying weighting function. The origin is set in the center of the sphere.

#### Step weighting function

Results from the step weighting function have previously been described by Ahluwalia et al. [2]. The approximation assumes a constant field with height $h$ which only interacts with the bottom cap of the sphere. The height $h$ is defined from the decay length of the field, $e^{-1}$, at the center of the waveguide. From section 2.3.1 in chapter

2, this gives

$$\mathbf{E}(x{=}h, y{=}0, z) = \mathbf{E}(y{=}0, z)e^{-\tilde{\mathrm{k}}_c^{\perp} h} = \mathbf{E}(y{=}0, z)e^{-1}, \tag{4.5}$$

such that

$$h = \frac{1}{\tilde{\mathrm{k}}_c^{\perp}} = \frac{1}{\sqrt{\mathrm{k}^{\|2} - \mathrm{k}_c^2}}. \tag{4.6}$$

The weighted index calculation is similar to the average index calculation, equation (4.4). However, for the weighted index, only the cap region is considered.

The cap of a hollow sphere with radius $a$ and shell thickness $T$ have four distinct weighted refractive index regions, depending on the height of the field $h$. The four different categories are shown in figure 4.12.

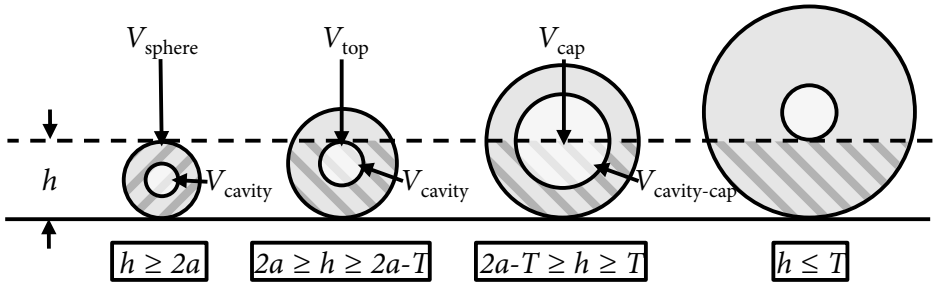


Figure 4.12: The four categories describing the weighted index with a step weighting function, showing the relation between sphere radius $a$, shell thickness $T$ and field height $h$. The refractive index for each case is given in equations (4.7), (4.8), (4.10) and (4.11).

In the first case, the whole sphere is covered by the field ($h \geq 2a$). The weighted index is simply the average refractive index of the whole hollow sphere, described in section 4.2.2,

$$n_{\mathrm{HS}}^{\text{cap (1)}} = \frac{n_{\text{shell}} V_{\text{sphere}} - (n_{\text{cavity}} - n_{\text{shell}}) V_{\text{cavity}}}{V_{\text{sphere}}}, \tag{4.7}$$

where $V_{\text{sphere}}$ and $V_{\text{cavity}}$ are the volumes of the full sphere and the cavity, respectively.

In the second case, the shell is partially covered, and the cavity is fully covered by the field ($2a \geq h \geq 2a - T$). The weighted index is then given by

$$n_{\mathrm{HS}}^{\text{cap (2)}} = \frac{n_{\text{shell}} V_{\text{top}} + (n_{\text{cavity}} - n_{\text{shell}}) V_{\text{cavity}}}{V_{\text{top}}}, \tag{4.8}$$

with $V_{\text{top}}$ is the volume of the sphere covered by the field, shown by both the light and dark diagonally shaded regions in figure 4.12,

$$V_{\text{top}} = \frac{4\pi a^3}{3} - \frac{\pi(2a-h)^2}{3}\left(3a-(2a-h)\right). \tag{4.9}$$

In the third case, both shell and cavity regions are partially covered by the field ($2a - T \geq h \geq T$). The weighted index is given by

$$n_{\text{HS}}^{\text{cap (3)}} = \frac{n_{\text{shell}} V_{\text{cap}} + (n_{\text{cavity}} - n_{\text{shell}}) V_{\text{cavity-cap}}}{V_{\text{cap}}}, \tag{4.10}$$

where $V_{\text{cap}}$ is the sphere region covered by the field, shown by both the light and dark diagonally shaded region in figure 4.12, and $V_{\text{cavity-cap}}$ is the cavity region covered by the field, shown by the light diagonally shaded region in figure 4.12,

$$V_{\text{cap}} = \frac{\pi h^2}{3}(3a-h) \quad \text{and} \quad V_{\text{cavity-cap}} = \frac{\pi(h-T)^2}{3}\left(3(a-T)-(h-T)\right). \tag{4.11}$$

In the fourth case, the cavity does not experience the field, which only covers parts of the shell ($h \leq t$), and the weighted index is the same as the shell index,

$$n_{\text{HS}}^{\text{cap (4)}} = n_{\text{shell}}. \tag{4.12}$$

For a hollow sphere with radius $a$ and shell thickness $T$ in a field with height $h$, the appropriate equation is found by choosing from (4.7), (4.8), (4.10), and (4.11). This will be the weighted refractive index $n_{\text{HS}}^{\text{cap}}$ of the hollow sphere for the step-weighting function.

### Exponentially decaying weighting function

The exponentially decaying weighting function can be used if one assumes the effective index contribution to be proportional to the field strength. The field strength is described by an exponentially decaying field with a decay constant $\tilde{\text{k}}_c^{\perp}$. The principle of the decaying effective index calculation is the same as for the other effective indices, with the exception of representing the outer (radius $a$) and inner (radius $a - t$) weighted volumes with parameters $B$ and $C$.

$$n_{\text{HS}}^{\text{exp}} = \frac{n_{\text{glass}} B + (n_{\text{air}} - n_{\text{glass}}) C}{B}, \tag{4.13}$$

where the weighted volumes are found from the integrals in equations

$$B = \int_{-a}^{a} \mathrm{d}x\, e^{-\tilde{\mathrm{k}}_c^{\perp}(x+a)} \int_0^{\sqrt{a^2-x^2}} r\,\mathrm{d}r \int_0^{2\pi} \mathrm{d}\theta = \pi \int_{-a}^{a} \mathrm{d}x\, e^{-\tilde{\mathrm{k}}_c^{\perp}(x+a)}(a^2 - x^2) \tag{4.14}$$

and

$$C = \int_{-a+T}^{a-T} \mathrm{d}x\, e^{-\tilde{\mathrm{k}}_c^{\perp}(x+a)} \int_0^{\sqrt{(a-T)^2-x^2}} r\,\mathrm{d}r \int_0^{2\pi} \mathrm{d}\theta$$
$$= \pi \int_{-a+T}^{a-T} \mathrm{d}x\, e^{-\tilde{\mathrm{k}}_c^{\perp}(x+a)} \left((a-T)^2 - x^2\right). \tag{4.15}$$

The integrals assume a hollow sphere with radius $a$ and shell thickness $T$, an evanescent field with decay constant $\tilde{\mathrm{k}}_c^{\perp}$, and use cylindrical coordinates with origin in the sphere center, as seen in figure 4.11.

Equations (4.14) and (4.15) are straightforward to solve using integration by parts, resulting in the following expressions,

$$B = \frac{2\pi}{(\tilde{\mathrm{k}}_c^{\perp})^3} \left\{ a\tilde{\mathrm{k}}_c^{\perp} - 1 + e^{-2a\tilde{\mathrm{k}}_c^{\perp}} \left( a\tilde{\mathrm{k}}_c^{\perp} + 1 \right) \right\} \tag{4.16}$$

and

$$C = \frac{2\pi}{(\tilde{\mathrm{k}}_c^{\perp})^3} \left\{ e^{-\tilde{\mathrm{k}}_c^{\perp}(2a-T)} \left( \tilde{\mathrm{k}}_c^{\perp}(a-T) + 1 \right) + e^{-\tilde{\mathrm{k}}_c^{\perp}T} \left( \tilde{\mathrm{k}}_c^{\perp}(a-T) - 1 \right) \right\}. \tag{4.17}$$

Inserting the equations for $B$ and $C$ into equation (4.13) gives an expression for the weighted refractive index. This weighted index only depends on the knowledge of sphere radius, shell thickness, and decay constant. The decay constant can for example be found from a two-dimensional simulation, giving the weighted refractive index presented in section 4.5.2.

### 4.5.2 Transition Between Low and High Index Hollow Spheres

The transition between low- and high-index spheres exists for sphere indices which are equal to the index of the surrounding medium. The boundary determines

whether a sphere is attracted or repelled by an optical gradient, and thus if it can be optically trapped.

The waveguide's evanescent field only interacts with the bottom cap of a sphere. Thus, the weighted function formulas derived in the previous section for refractive indices can be used to give an estimate of the trapping properties of hollow spheres by considering only radius and shell thickness data.

From two-dimensional simulations, the decay constant $\tilde{k}_c^{\perp}$ is found to be[1] 14, and the constant field height $h$ is found to be 150 nm. Assuming glass shells with $n_{\text{shell}}$=$n_{\text{glass}}$=1.5 and air cavities with $n_{\text{cavity}}$=$n_{\text{air}}$=1, the index equations depend the sphere radius and the shell thickness. By setting the index equations equal to the refractive index of water ($n_{\text{water}}$=1.33), equations (4.7), (4.8), (4.10), and (4.13) can be used to find how the transition between high and low indices depends on sphere diameters and shell thicknesses.

Figure 4.13 shows the transition lines for a hollow sphere fully covered in a uniform field (dotted red, $n_{\text{HS}}$), a hollow sphere partially covered by a uniform field (solid black, $n_{\text{HS}}^{\text{cap}}$), and a hollow sphere partially covered by an exponentially decaying field (dash-dotted black, $n_{\text{HS}}^{\text{exp}}$). The regions above the lines indicate high-index spheres, while the regions below the lines indicate low-index spheres. The figure also shows the line of transition between floating and sinking spheres (dashed blue), and the transition points from the three-dimensional FEM simulations (red crosses, obtained from figure 4.7). As expected, hollow spheres with a thin shell (large cavity) tend to be low-index, while spheres with a thicker shell tend to be high-index. Figure 4.14 shows a close-up of the transition lines for small sphere diameters, including more transition points from the FEM simulations.

The calculated transition lines show the weighted index models and the FEM simulations to have similar transition points. This supports the assumption that the average refractive index in the intersection region between a field and an object can be used to explain the boundary between attracted and repelled objects. The FEM simulations consider spheres placed 25 nm above the waveguide surface. This has not been taken into account in the refractive index models. However, the transition point is not expected to vary significantly due to the waveguide–sphere distance.

For large spheres (diameters above 250 nm), the transition value converges to a shell thickness between 60 and 70 nm. This agrees with the aggregation of transi-

[1] The decay is found using intensity ($|\mathbf{E}|^2$) data.

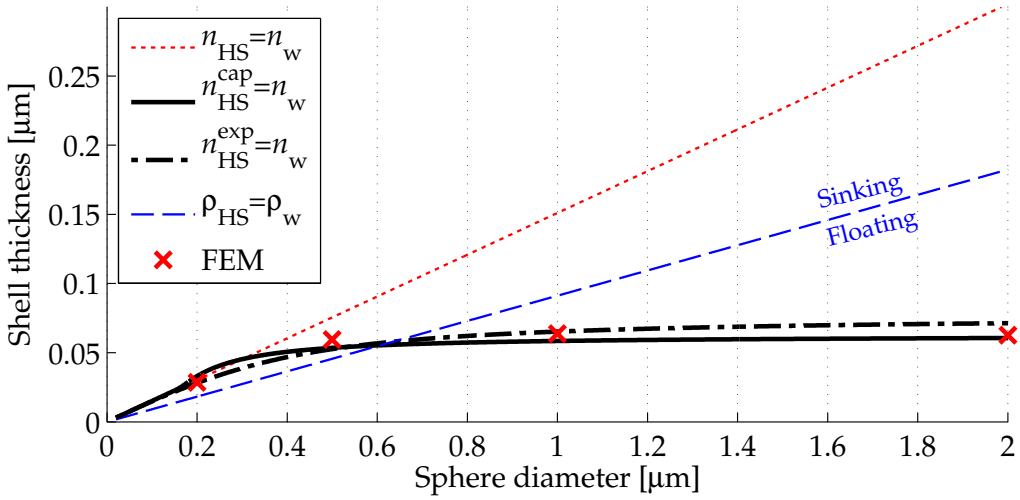


Figure 4.13: Regions of high- and low-index hollow spheres. The solid and dash-dotted black transition lines represent the two weighted index functions (equation (4.13) and equations (4.7), (4.8), (4.10), and (4.11)). The dotted red transition line represents the average index of a hollow sphere fully covered by a constant field (equation (4.7), equal to equation (4.4)). Transition points for the FEM simulations are shown with red crosses. The dashed blue transition line represents the transition between floating and sinking hollow spheres. The values of the weighted index models both agree well with the finite element results. Data from [2].

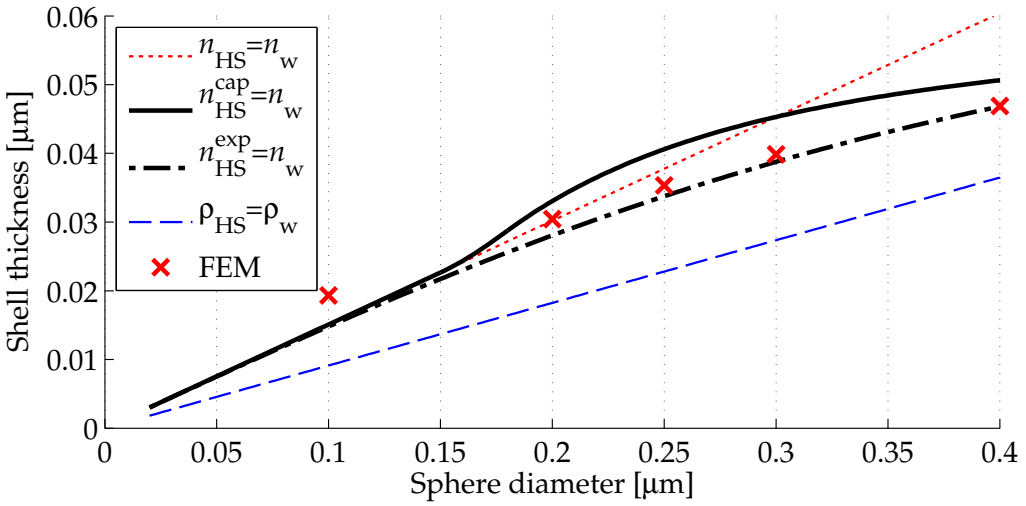


Figure 4.14: Close-up of figure 4.13 showing the transition lines for small hollow spheres. The exponential decaying model is seen to give slightly better agreement with the FEM simulations in this region.

tion points for larger spheres seen in figure 4.14. However, spheres with diameters larger than 0.6 µm have transition points in the region where they would be floating. This would make it difficult to verify these transitions experimentally. Smaller spheres are mostly covered by the evanescent field, which should give good agreement between the FEM and weighted function transition points. However, there is a small discrepancy, suggesting that the average refractive index model do not fully explain the transitions.

The two weighted index models give very similar results. Thus, it is sufficient to use the simpler step weighting function to find the trapping properties of hollow spheres on waveguides. However, both these functions have only been tested on spherical shapes. Findings in chapter 5 suggest that other geometries don't give as precise results with the weighted index methods. This is related to the fact that it is the surfaces, not the volumes, that usually are responsible for the index gradients, and will be discussed further in section 5.3.3.

## 4.6 Comparing Simulations with Experimental Data

### 4.6.1 Calculated Velocities

The horizontal forces on the hollow spheres can be translated into steady state velocities with Stokes' law,

$$F_z = 6\pi\mu a v, \tag{4.18}$$

where $\mu$ is the viscosity of the fluid and $v$ is the velocity of the sphere. However, since the spheres are close to the waveguide surface, wall effects have to be taken into consideration. Depending on the relation between sphere radius and sphere-wall distance, corrections are given by O'Neill [82] and Goldman [83]. Goldman discusses the case of spheres large relative to the distance to the wall, which is relevant to the waveguide simulations. For non-rotating particles very close to the wall, Goldman's correction gives

$$F_z = 6\pi\mu a v \left( \frac{8}{15} \ln\left(\frac{\delta}{a}\right) - 0.9588 \right), \tag{4.19}$$

where $\delta$ is the shortest distance from the waveguide surface to the sphere surface. In the simulations, $\delta$ was chosen to be 25 nm to avoid too high mesh densities. It is difficult to get a measure of the experimental $\delta$, but as long as the sphere is translated forward, and not rolling, the forward thrust will lift the sphere slightly, such that $\delta$ is non-zero, even if the waveguide strongly attracts the sphere.

Figure 4.15 shows the predicted velocities for solid and hollow spheres given by equations (4.18) and (4.19), where the forces are found from the FEM simulations results in figure 4.6. The simulation parameters have been set close to the experimental parameters. Assuming 10 dB coupling losses, the waveguide power is set to 0.15 W.

The velocities of the solid glass spheres in figure 4.15 were calculated from the forces found in figure 4.10. For the hollow spheres, the mean values of the sphere size distribution in figure 4.3 was used to find representative experimental sphere diameters and shell thicknesses. Forward forces corresponding to these sphere parameters were found by linear interpolation of the simulation results in figure 4.6, and these forces were used to find the hollow sphere velocities in figure 4.15. The shell thicknesses used for each diameter are noted in the figure.

The near-wall corrected velocities are smaller than the pure Stokes law velocities for both solid and hollow spheres. The glass spheres show velocity maxima between 1 and 3 μm diameter, and the hollow spheres show a decreasing velocity trend for increasing sphere diameters. The shell thicknesses distribution in figure 4.3 does not give data for spheres smaller than 2.5 μm diameter.

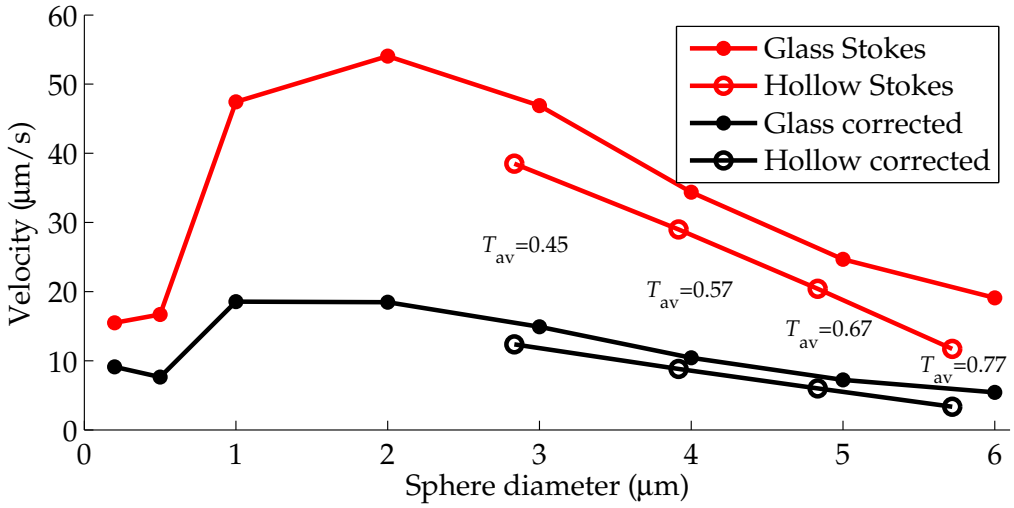


Figure 4.15: Calculated velocities for solid and hollow spheres from the force simulations using Stokes law with (black) and without (red) near-wall correction. The near-wall correction gives smaller velocities, but the general trend is similar for the different calculations.

### 4.6.2 Experimental Velocities

Figure 4.16 combines the experimental velocity data from figure 4.4 with the near-wall corrected simulated velocities from figure 4.15. The magnitude of calculated and observed velocities are found to be similar, but the trend of decreasing velocities for larger spheres is not seen in the experiments. Instead, the highest velocities are found for the 6 μm diameter solid spheres[2] and the velocities are fairly constant for the hollow spheres .

Differences between simulation and experiment could be due to unknown properties of hollow and solid spheres, such as different refractive indices, surface proper-

[2]The experimental velocities decreased for spheres with diameters above 6 μm.

ties or shell thicknesses. For example, a lubricant was added to allow hollow sphere trapping experiments, probably due to surface effects. However, the velocity increase measured for larger spheres is significantly different from the simulation results, as a large force increase would be necessary to overcome the drag forces given by Stokes' law. It is evident that some important parameter is not taken into account by the simulations.

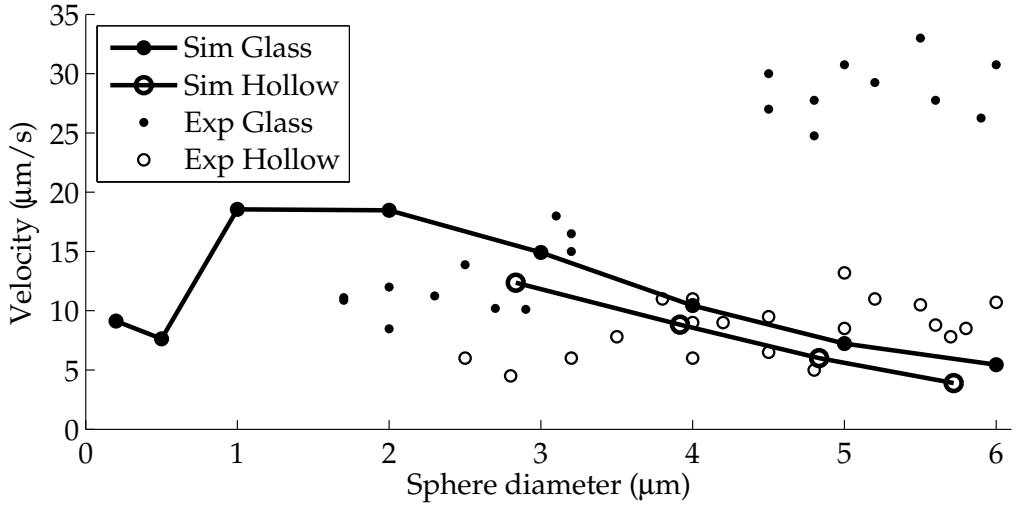


Figure 4.16: Near-wall corrected calculated velocities plotted together with experimental velocities for solid and hollow spheres. The waveguide power is 0.15 W for simulations and experiments, where a 10 dB coupling loss have been assumed.

### 4.6.3 Force Ratio of Solid and Hollow Spheres

A different comparison between the simulations and experiments looks at the relationship between the solid and hollow spheres. For a perfect model, the ratio of the experimental velocity and the ratio of the simulated forces would be equal. This makes the comparison less dependable on unknown parameters like guided power, losses and systematic numerical errors, as well as uncertainties of the velocity calculations. In the comparison, only 3, 5, and 6 μm diameter spheres will be used.

The experimental data in figures 4.3 and 4.4 give mean velocity ratios between solid and hollow spheres of 2.5, 3.2 and 3.2 for 0.51, 0.64 and 0.68 μm shell thicknesses

and 3, 5, and 6 μm diameters, respectively. By comparison, the force simulations in figure 4.6 give force ratios between solid and hollow spheres of 1.1, 1.3 and 1.7 for 0.5 μm shell thickness and 3, 5, and 6 μm diameters, respectively[3]. These ratios confirm that there are differences between the solid and hollow spheres which the simulations do not find. These differences could be due to material properties, as mentioned in section 4.6.2.

## 4.7 Conclusions

Optical trapping of hollow microspheres is challenging, and demands specific optical designs to avoid repelling the low-index cavity inside the sphere. The short reaching evanescent field above an optical waveguide only interact with the outer cap of a sphere, and therefore can be used to trap and propel hollow spheres.

This chapter has shown, with finite element method simulations, how the optical forces from the waveguide field depend on the shell thickness of a hollow sphere. Spheres with very thin shells are repelled from the waveguide, as the evanescent field interacts with the cavity. As the shell thickness increases, the attractive force increases up to shell thicknesses of 0.5 μm, where it becomes stable.

The transition point between repulsive and attractive forces determine whether a sphere can be trapped. For spheres larger than 1 μm diameter, the transition occurs at a shell thickness of 65 nm. However, spheres smaller than 1 μm diameter have transition points for thinner shells. The transition points can be explained with refractive index calculations. A model is presented which looks at the average refractive index in the interaction region of the field and the sphere. For an average index lower than the surrounding medium refractive index, the sphere is considered low-index, and repelled from the waveguide. Conversely, if the average index is higher, it is considered high-index, and will be optically trapped. Approximations for the evanescent field is done with two different weighting functions, which both are found to give results comparable to the full FEM simulations. The models successfully predict the transition points, but some signs suggest that a better model would consider the boundary surfaces interacting with the field instead of the interacting hollow sphere volumes.

A sphere trapped on a waveguide also experiences forces in the horizontal direc-

[3]Note that the 6 μm sphere simulation might be unreliable due to the model's large size.

tion, being pushed along the waveguide surface. These forces are more than one order of magnitude smaller than the vertical forces, and difficult to simulate accurately. The simulations show minimum horizontal force for about the same shell thickness as the vertical force gave a transition point, indicating that for specific shell thicknesses, the field pass almost uninterrupted through the sphere. This trend is found for all the simulated sphere diameters.

The horizontal forces are used to compare the simulations with experimental results. Spheres trapped on a waveguide similar to the one in the numerical model have been propelled, and their velocities registered. Stokes' law with a near-wall correction is used to calculate expected velocities from the force simulations. Experimental and calculated velocities have the same order of magnitude, but show different dependencies on sphere diameter. The deviations could be due to unknown sphere material properties. However, even the trend seen between sphere diameter and velocity was not correctly predicted, suggesting that some other factor influences the spheres in the waveguide experiments.

# Chapter 5

# Modeling Red Blood Cells on a Waveguide

## 5.1 Introduction

Numerical analyses of scattering from red blood cells have been done for a long time [84, 85]. More recent studies include simulations of optical forces on RBC in optical traps [86], but little work has been done on forces from evanescent fields. This chapter presents simulations of a red blood cell on a waveguide surface. Force dependencies on cell refractive index and size have been studied for spherical RBC, and results for spherical and disk shaped cells are compared. The first part of the chapter describes red blood cells and optical studies of red blood cells in section 5.2. Then, section 5.3 presents the numerical model and the results from the simulations, and also compares the results with experimental velocities. Finally, section 5.4 sums up the findings in the chapter.

## 5.2 Red Blood Cells

The red blood cell (RBC, erythrocyte) is the most numerous cell type in human blood. The cells are small, contain hemoglobin, do not have an internal structure, and are used to transport oxygen throughout the body. RBC have a biconcave shape (see figure 5.1) with a diameter of about 8 μm and a thickness that varies between

0.5 and 2.5 μm [87]. RBC absorb light in the green spectral region, and optical studies with RBC are usually done with red or near-infrared light to reduce photodamage.

In RBC studies done outside the body (in vitro), the cells are kept in solution. Osmotic pressure differences between the cell and the solution cause the cells to change shape. In hypotonic solutions, with a low ion concentration, living RBC swell to a spherical shape and eventually burst. In hypertonic solutions, the ion concentration is high, and the RBC shrink. In isotonic solutions, the ion concentration of the solution is similar to that inside the cell, and the cell shape remains unchanged. To study cells in vitro, an isotonic solution is preferable. However, studies are often done in slightly hypotonic solutions, such that the cells are spherical. In vitro studies can also be done with fixed cells. Fixing is a procedure which kills the cell, but prevents cell decay, and stabilize and strengthen the cell structure. Thus, the shape remains constant in such studies.

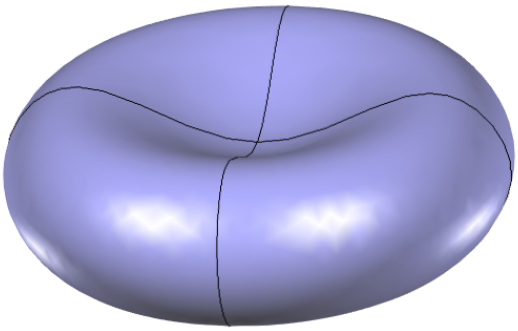

Figure 5.1: A model of the biconcave shape of a red blood cell. The diameter across is around 8 μm and the thickness varies from 0.5 to 2.5 μm.

### 5.2.1 Optical Red Blood Cell Studies

The important medical and biological properties of the RBC make them a popular study object. With the introduction of the optical tweezer, the RBC have also become an important object in optical research. The tweezer is a good fit for the cells, which are small and easily available. Combined with Raman spectroscopy, studies of both mechanical [88–90] and spectral [91–93] properties of single red blood cells have been conducted. The studies have provided insight in both the physical

and chemical properties of the cell, including cell deformability, cell elasticity and cell hemoglobin concentration.

The refractive index $n_{\text{cell}}$ of a RBC is dependent on its hemoglobin content, and thus gives both optical and biochemical information about the cell. In the literature, the value ranges from 1.376 to 1.43, with the most recent studies giving mean values of 1.399 (measured with a wavelength of 514 nm) [94] and 1.418 (measured at 663 nm) [87] for healthy cells.

Early studies of RBC scattering reported that their light scattering properties were strongly affected by small changes in refractive index [84]. In addition, a correlation between the cell's hemoglobin content (osmolarity) and refractive index was found [95]. A range of different optical techniques have since been used to study RBC scattering and refractive index. In recent years, studies have looked at refractive index differences between deoxygenated and oxygenated hemoglobin [96] and between healthy and unhealthy RBC, for example from people with diabetes [97] or malaria [94].

### 5.2.2 Waveguide Trapping of Red Blood Cells

Trapping and propelling red blood cells on waveguides have been done experimentally by Gaugiran et al. [21] and Ahluwalia et al. [98]. Two challenges limit efficient trapping and propulsion of cells on a waveguide. First, the small refractive index difference $\Delta n$ between the cell and the surrounding medium makes the optical forces smaller for cells than for higher-index dielectric objects. Stronger optical gradients are needed to provide comparable forces. This is achieved experimentally by using narrow waveguide cores with high refractive index. Second, live cells tend to stick strongly to surfaces [99]. Thus, only non-adherent cells like RBC have been trapped and propelled on waveguides. But RBC also stick to the waveguide and substrate surfaces in most cell culture media. Ahluwalia [98] reported propulsion of RBC only in hypotonic water and isotonic sucrose solutions. Fixed cells are less prone to sticking, and are often used in experimental studies.

Potential applications for waveguide trapping can be cell transport, cell sorting and cell elasticity studies. The strong dependence of scattering on index differences suggests that small index differences can be revealed with waveguide trapping, either by velocity differences or by trapping force differences (for example combined with microfluidics, as done by Schmidt et al. [100]).

## 5.3 Simulations of a Red Blood Cell on a Waveguide

The simulations presented in this section are similar to the ones presented in chapter 4, and based on the theory described in chapter 3. After a brief introduction of the numerical model in sections 5.3.1 and 5.3.2, the optical force dependency of the cells' refractive index, size and shape is presented in sections 5.3.3 and 5.3.4. Finally, comparisons between simulation results and experiments are discussed in section 5.3.5.

### 5.3.1 Cell model

Figure 5.2 shows the geometries of two numerical models of an RBC on a waveguide. The spherical model (figure 5.2 a)) is used in most simulations since the the mesh density requirements are lower than the disk model (figure 5.2 b)), thus requiring smaller simulations. The spherical shape is a good approximation to cells in a hypotonic solution, and is commonly used in RBC simulations. The spherical model is used to study the optical forces dependency on refractive index. Spherical models with diameters up to 6 μm have been modeled, corresponding to the actual size of RBC in hypotonic solution. An ellipsoidal model was considered, but the disk model was chosen as its shape better resembles the cell shape. However, for studies of incremental changes in the cell shape, the ellipsoid model could be suitable.

The shape of a living RBC (in isotonic solution) trapped on a waveguide is not known. The gradient force from the evanescent waveguide field attracts the cell toward the surface and the cell's biconcave shape is altered. A reasonable assumption is that the cell surface will be pulled close to the waveguide. Thus, a disk shaped cell model (figure 5.2 b)) is used to approximate a RBC trapped on the waveguide. Simulations have been run using a 4 μm diameter and 1 μm thick disk shaped RBC model.

In both the cell models, the cell is set 25 nm above the waveguide surface. This gap is used to avoid extremely many small mesh elements in the region between waveguide and cell, which would strongly increase the model size. For the disk model, the gap region is large, and it will be seen in section 5.3.4 that this makes these simulations susceptible to numerical mesh errors.

The medium surrounding the cells in the trapping experiments was a 0.2 mol/L su-

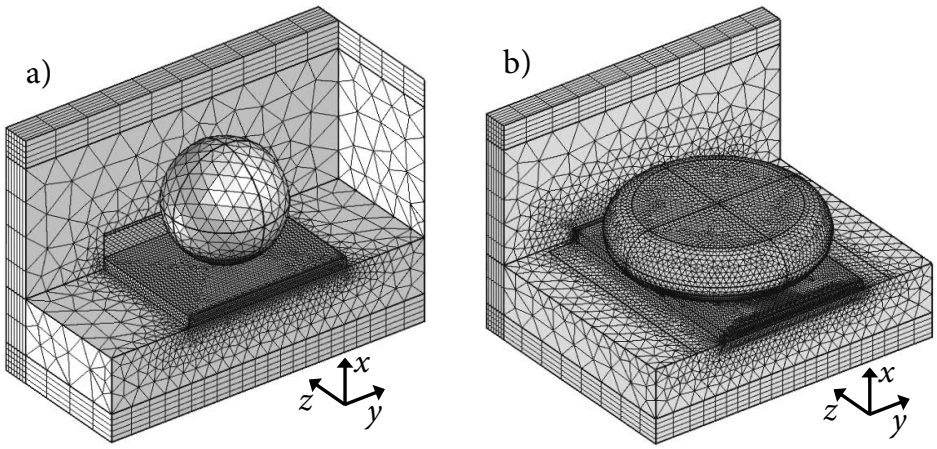


Figure 5.2: Two different cell models are used in the simulations. a) shows the mesh of a 1 μm diameter sphere. b) shows the mesh of a 4 μm diameter disk. Both models use a waveguide that is 3 μm wide and 0.2 μm thick. The mesh density on the disk surface is denser than on the sphere surface. Other mesh parameters are similar in the two models.

crose isotonic solution with a refractive index $n_{\text{sucrose}}$=1.345. This sucrose medium was used in a previous numerical model [3], but the models presented here use a pure water medium with refractive index $n_{\text{water}}$=1.33. By choosing a medium with a lower refractive index, the index contrast is increased, and the calculated optical forces are stronger. This makes it easier to exceed the numerical noise level (increase the resolution) for large models. It should be noted that this choice of medium in some way justifies the use of a spherical model (hypotonic solution), but compared to the experimental results in section 5.3.5, the calculated forces are stronger than what the exact experimental parameters would give.

### 5.3.2 Mesh and Resolution

The precision of the numerical model is strongly dependent on the mesh density. A dense mesh is necessary in regions and on surfaces with strong or changing field values, as was described in section 3.2.2. In the RBC models, the mesh density is set to a minimum of six points per wavelength inside and close to the waveguide. This value varies with the refractive index of the media. The cell surface close to the waveguide is set to have a maximum mesh density of 55 nm to avoid too narrow or too wide mesh element angles (see section 3.2.2).

As described in section 3.4.2, the resolution, or numerical noise level, of the model is found by simulating a model with no refractive index difference between cell and medium. The resolution is mesh-dependent, giving different values for different cell diameters, since the mesh pattern changes when the model geometry changes. When studying refractive index changes without changing the cell size, the mesh is similar for all indices. Thus the resolution is the same for all these simulations. Like the hollow sphere simulations (section 4.4), the force offset given by a specific mesh is subtracted from the force calculated for the models using that specific mesh. For the vertical force, the subtracted force offsets (resolutions) range from 0.7 pN for small cells to 6 pN for big cells. For the horizontal force, the subtracted force offsets range from 0.2 pN for small cells to 1 pN for big cells. The horizontal force resolution of the disk model is very low, and will be discussed in more detail in section 5.3.4.

### 5.3.3 Vertical Forces

Figure 5.3 shows simulated vertical forces ($x$ direction) for an RBC on a waveguide in water medium. For the sphere model, results for diameters up to 6 μm and refractive index differences $\Delta n$ between 0 ($n_{\text{cell}}$=1.33) and 0.17 ($n_{\text{cell}}$=1.5) are given. For the 4 μm diameter disk model, results for refractive index differences $\Delta n$=0.05 ($n_{\text{cell}}$=1.38) and $\Delta n$=0.07 ($n_{\text{cell}}$=1.4) are given. For the $\Delta n$=0.05 results, forces from four different disk meshes are plotted (not distinguishable in the figure).

As expected from the hollow sphere results given in chapter 4, the direction of the force in the plot is negative, meaning that the cells are pulled toward the waveguide. For the sphere model, the forces increase with refractive index difference and sphere size. The disk model results, plotted with rings, show that the disks experience markedly stronger forces than the spheres. For the disks, a refractive index difference of 0.02 increases the force with more than 250 pN[1]. Thus, for the disk model, the force is strongly sensitive to index changes. For the sphere model, this effect is weaker.

The simulation results in chapter 3 suggested that only the part of the sphere surface interacting with the field contributes to the force. This means that the main contribution to the forces is the sphere cap region 150 nm above the waveguide surface. This can be used to explain why the force increases for larger sphere diameters.

[1] Too few data points are found to describe the force as a function of the refractive index.

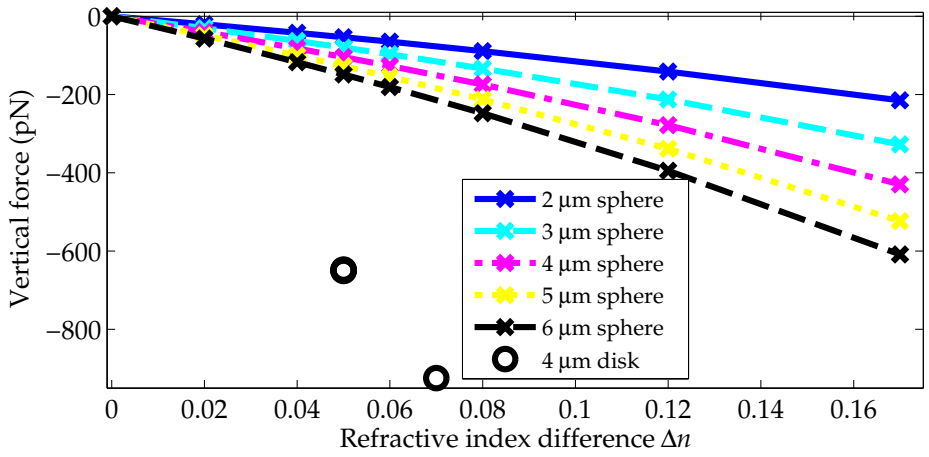


Figure 5.3: Calculated vertical forces on spherical and disk shaped cells as function of refractive index difference between cell and medium. The forces are increasing with refractive index difference and with cell size. The calculated force offset (resolution) have been subtracted from each simulation.

When the diameter increases, the sphere surface area and sphere volume interacting with this field also increases. There is good agreement between the increases in size and vertical force, as shown in figure 5.4. In the figure, the cap surface area[2] is compared to the vertical force for each sphere diameter. The surface area and the force are normalized with respect to their values for the 6 µm diameter sphere. For a thin cap (i.e. a large diameter or a thin evanescent field), the sphere cap volume and sphere cap surface area have the same dependency on sphere diameter, such that the same agreement with the force holds for the cap volume.

For the disk model, the surface area close to the surface is not similar to cell volume close to the waveguide. Comparing the 4 µm diameter disk with the 4 µm diameter sphere, the surface area ratio within 150 nm above the waveguide surface is 5.4, while the the volume ratio is 10.4. The force ratio between the sphere and the disk is 5.8, similar to the surface area ratio. This suggests that it is the surface area interacting with the field that determines the optical forces, not the sphere volume interacting with the field. This result is confirmed by the physical understanding of the force, which states that the index gradient is responsible for the force (see for example equation (2.65)). The only index gradient in the cell model is at the surface. This suggests that the average index calculations in chapter 3 are not ap-

[2]The cap surface area is defined as the sphere surface up to 150 nm above the waveguide.

plicable to geometries with large differences between surface area and volume in the region close to the waveguide.

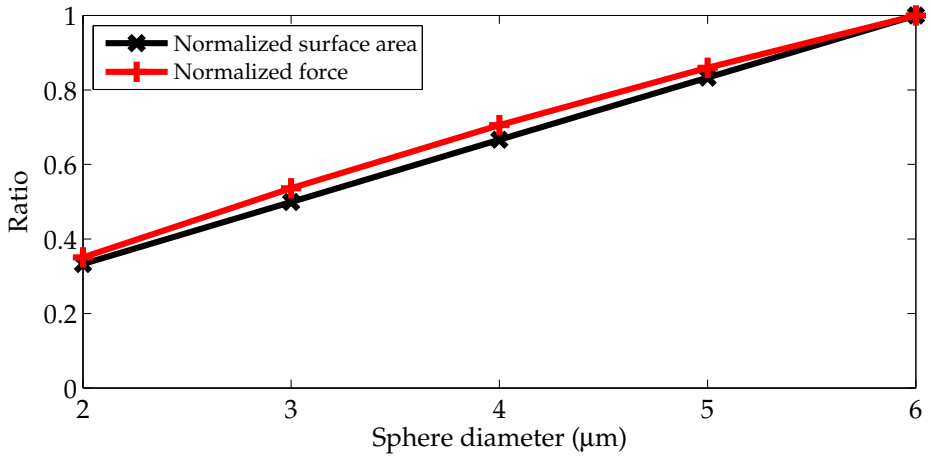


Figure 5.4: Force (red) and sphere cap surface area (black) shows the same trend for the sphere diameters used in the RBC simulations. The data points have been normalized by their respective values for the 6 μm diameter sphere.

### 5.3.4 Horizontal Forces

Figure 5.5 shows the simulated horizontal forces ($z$ direction) of an RBC on a waveguide in water medium. Cell sizes and refractive index differences are the same as presented for the vertical force simulations, with sphere diameters ranging from 2 to 6 μm diameter and refractive index differences ranging from 0 to 0.17 and a 4 μm diameter disk with refractive index differences $\Delta n$=0.05 (four different meshes), and $\Delta n$=0.07. As before, the force offset has been subtracted from the results. The calculated forces on the spherical model are discussed first.

#### Sphere

Similar to the hollow sphere simulation results in chapter 4, the horizontal forces are more than one order of magnitude smaller than the vertical forces, with 3 and 4 μm diameter spheres giving the strongest forces (the pink dash-dotted and cyan dashed lines in figure 5.5). The lens effect argument used for the hollow spheres

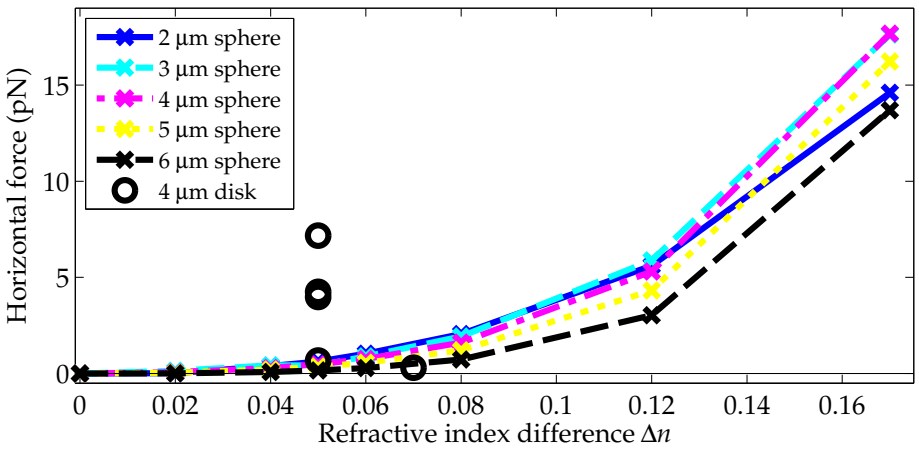


Figure 5.5: Horizontal forces on spherical (crosses) and disk shaped (rings) cells for refractive index differences between 0 ($n_{\text{cell}}$=1.33) and 0.17 ($n_{\text{cell}}$=1.5). Simulations with four different meshes are shown for the disk model at $\Delta n$=0.05. Each simulation series have been normalized such that the force is zero for $\Delta n$=0.

can be used again to explain this maximum, as the strongest gradient occurs when the sphere size matches the width of the waveguide (i.e. the evanescent field).

For small index differences, the forces are very small. Figure 5.6 gives a closer look at the refractive index differences between 0 and 0.08. The two figures show that there is an exponential increase of force with the index difference. A quadratic dependence on small index differences is given for small spheres. This can be seen from the Rayleigh force equation in the evanescent field from chapter 2,

$$\mathbf{F}_{\text{scat}} = \frac{n_{\text{eff}}}{c}\mathfrak{s}I(\mathbf{r}) = \frac{4\pi}{3}n_{\text{eff}}^2\epsilon_0(\mathrm{k}^{\parallel}a)^4a^2\left(\frac{(n_{\text{p}}/n_{\text{c}})^2-1}{(n_{\text{p}}/n_{\text{c}})^2+2}\right)^2|\mathbf{E}(\mathbf{r})|^2\hat{z}, \qquad (2.95)$$

where $n_p$ is set to the cell refractive index $n_{\text{cell}}$ and $n_c$ is set to the medium refractive index $n_{\text{water}}$. For small refractive index differences, the Clausius-Mosotti factor in the equation can be shown to be proportional to to $\Delta n$,

$$\left(\frac{(n_{\text{cell}}/n_{\text{water}})^2-1}{(n_{\text{cell}}/n_{\text{water}})^2+2}\right) = \left(\frac{(1+\Delta n/n_{\text{water}})^2-1}{(1+\Delta n/n_{\text{water}})^2+2}\right) \simeq \left(\frac{2\Delta n/n_{\text{water}}}{3+2\Delta n/n_{\text{water}}}\right) \simeq \left(\frac{2\Delta n}{3n_{\text{water}}}\right), \qquad (5.1)$$

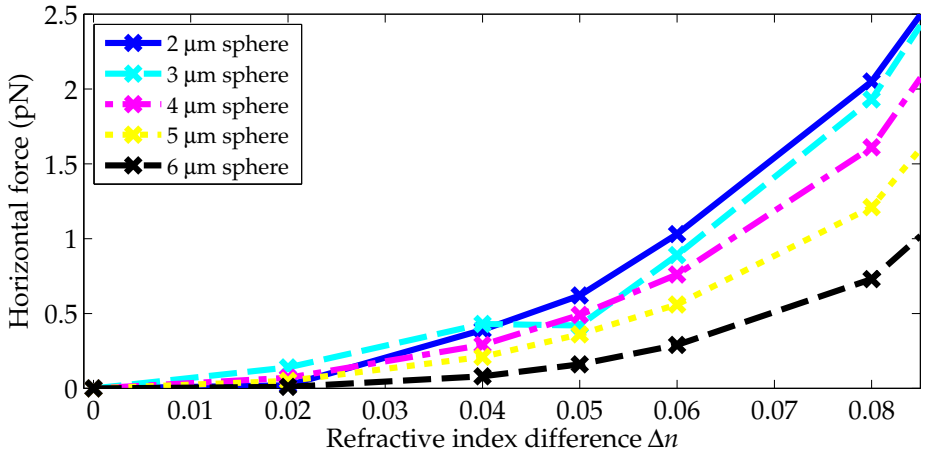


Figure 5.6: Close-up of figure 5.5 for refractive index differences between 0 ($n_{\text{cell}}$=1.33) and 0.08 ($n_{\text{cell}}$=1.41). Each simulation series has been normalized such that the force is zero for $\Delta n$=0.

where quadratic terms in $\Delta n$ were dismissed at the third step, and it is assumed that $\Delta n/n_{\text{water}} \ll 1$ at the last step. In equation (2.95), the Clausius-Mosotti factor represents the polarizability of an isotropic dielectric. Implementing equation (5.1), it can be seen that the force for small spheres has a quadratic dependence on small refractive index differences.

Looking more closely at the plots in figures 5.5 and 5.6, it can be seen that the horizontal force for smaller spheres increases more quickly than for the larger spheres up to an index difference of about 0.09. From that point on, the larger spheres catches up. Specifically, it can be measured (not shown in the figure) that the force for the 2 µm diameter sphere is proportional with $(\Delta n)^{2.7}$, the 4 µm diameter sphere is proportional with $(\Delta n)^3$ and that the 6 µm diameter sphere is proportional with $(\Delta n)^4$. This indicates that the growth increases with sphere size. This is reasonable, as more of the sphere is interacting with the evanescent field when the diameter increases. Thus, the quadratic increase from the refractive index change is combined with an increase in the intersection region of the field and the cell.

To see how much the refractive index influences light scattering, figure 5.7 illustrates the propagating field above the waveguide surface. The field in a cross section along the center of the waveguide structure is plotted for index differences of $\Delta n$=0.05 ($n_{\text{cell}}$=1.38) and $\Delta n$=0.12 ($n_{\text{cell}}$=1.5) for 2 µm and 6 µm diameter spheres. The magnitude of the field is enhanced 100 times to reveal the weak evanescent

field outside the waveguide core. For the larger sphere, the field propagates along almost the full circumference. If the field was coupled all the way, a standing wave could arise inside the sphere. Such resonances are called whispering gallery modes. These modes are the cause of the resonances seen in Mie scattering. As the largest simulated spheres are 6 µm diameter, the figure indicates that no such resonances occur in the size range of the simulations. Jaising's Mie calculations [44] confirm that resonances starts occuring for larger diameters.

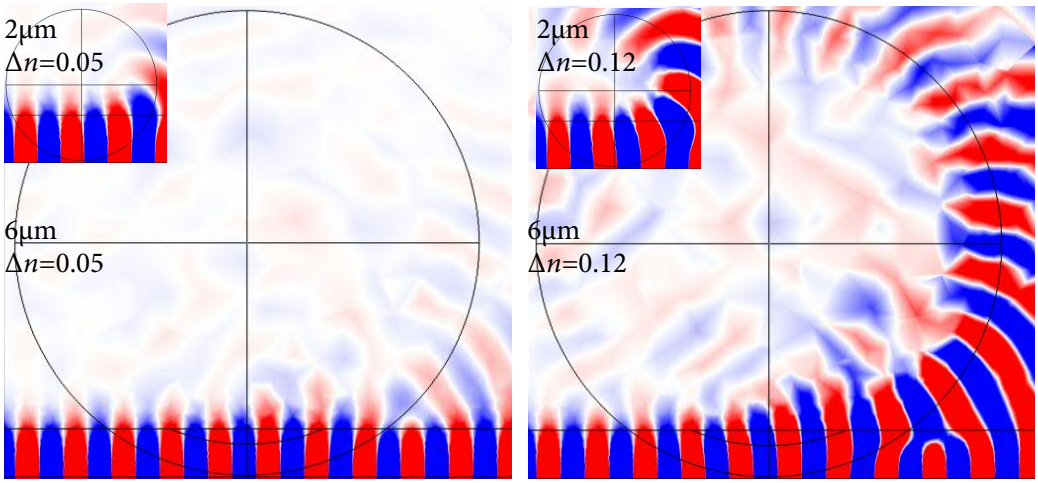


Figure 5.7: The field scattering is much stronger for higher index spheres, giving much stronger forces. 2 and 6 µm diameter spheres with refractive index differences of 0.05 ($n_{\text{cell}}$=1.38) and 0.17 ($n_{\text{cell}}$=1.5) are plotted. The magnitude of the field is enhanced 100 times to reveal the weak scattering.

### Disk

The disk simulation results are plotted with rings in figure 5.5. The four different meshes at $\Delta n$=0.05 were adjusted by increasing the mesh density inside the disk. However, the results did not converge with increased model size. Thus, the numerical resolution of the disk model is presumably too low to calculate accurate horizontal forces within reasonable memory use (up to 40 computer nodes, each with 16GB memory). The reason for the low accuracy is the 25 nm thin layer between the disk and the waveguide, as explained in the following paragraphs.

The forces in on the disk are found by summing up the stress over the whole disk surface. The stress components in each direction (as introduced in section 3.3.2) are plotted for a $n_{\text{cell}}$=1.4 disk in figure 5.8. The stresses are seen on the bottom disk surface in vertical ($\mathbf{T}_x$), lateral ($\mathbf{T}_y$), and horizontal ($\mathbf{T}_z$) directions. The red stress values are positive, and the blue stress values are negative.

By enhancing the values of the stress in the horizontal direction $\mathbf{T}_z$, the reason for non-converging forces becomes apparent. Figure 5.9 plots the stresses enhanced 1000 times, seen from the front, side, bottom and end of the disk. The horizontal force is a sum of large positive and large negative values, and is thus sensitive to the unexpected variations seen at the bottom surface. The region subject to the large variations is the 25 nm thin layer between disk and waveguide. The mesh in this region is not sufficiently dense to describe the field across the region. For the sphere model, this region is very small, and does not contribute to low quality mesh and numerical errors. The vertical force on the disk is also affected by the mesh quality, but is not as sensitive to the noise since the relative error is very small.

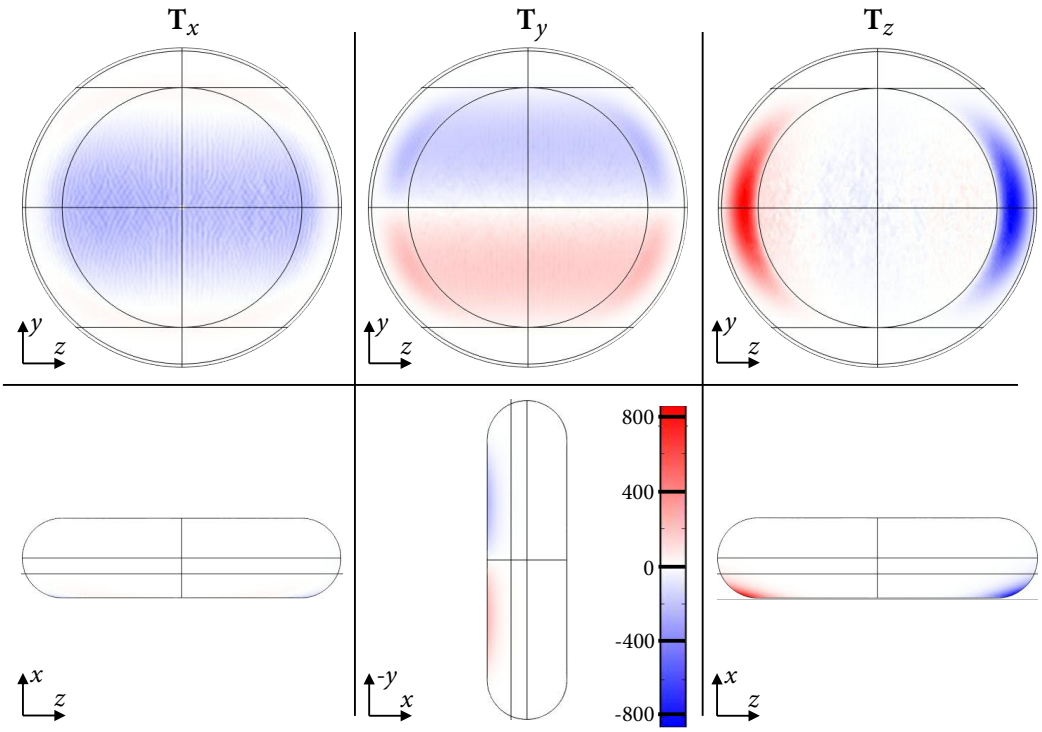


Figure 5.8: Stress distribution on the disk in vertical ($\mathbf{T}_x$), lateral ($\mathbf{T}_y$) and horizontal ($\mathbf{T}_z$) directions. The upper row shows the disk from the bottom, the bottom row shows the disk from the side (left and right figure) and from the front (center figure). The local stress values range from -850 (blue) to +850 (red) N/m$^2$.

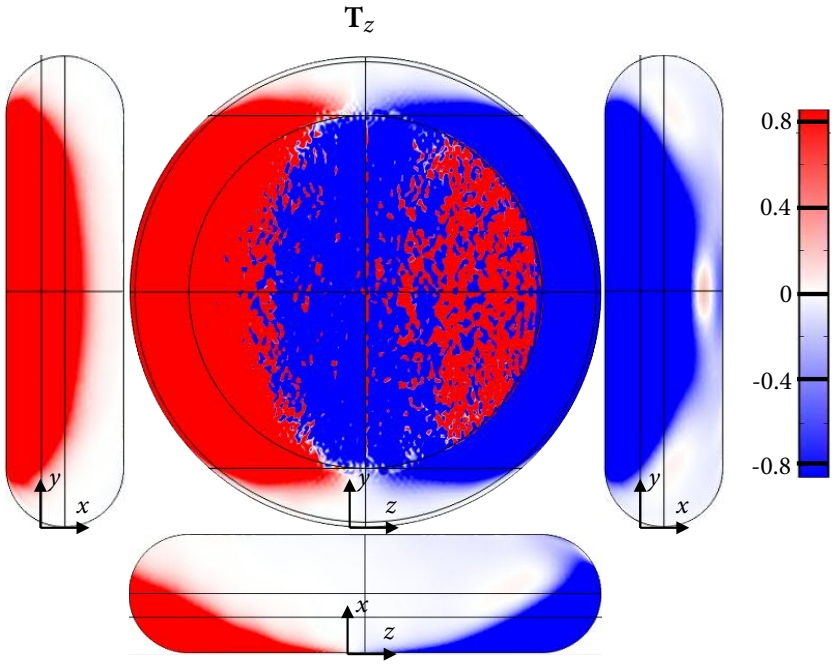


Figure 5.9: Stress distribution on the disk in the horizontal direction seen from the front, bottom, back and side. Low quality mesh elements in the narrow region between the disk and the waveguide lead to incorrect field propagation and numerical noise. The magnitude is enhanced 1000 times compared to figure 5.8 to reveal numerical noise at the bottom surface.

### 5.3.5 Red Blood Cell Trapping Experiments

In their experiments, Ahluwalia et al. [98] describe RBC propagation velocities of between 0.5 and 1 μm/s on 3 μm wide tantalum pentoxide waveguides in sucrose solution with 1000 mW input power. The paper also gives a velocity ratio of 1.38 between cells in water and cells in sucrose solution using 1000 mW input power on 10 μm wide waveguides, and a velocity ratio of 1.33 between cells on 3 μm and 10 μm wide waveguides. A linear extrapolation of these values gives expected velocities for RBC in water on 3 μm wide waveguides of between 0.9 and 1.8 μm/s.

For the 6 μm diameter spherical cell model with refractive index $n$=1.41, the simulated horizontal force of 0.73 pN corresponds to a velocity in water of 4.13 μm/s, using the near-wall correction of Goldman [83] presented in section 4.6. The calculated velocity assumes a waveguide power of 1000 mW, and does not consider any losses. Experiments suggest losses giving about 10 dB power decrease, leading to a velocity of 0.41 μm/s.

The higher experimental velocity may be due to the refractive index of the cell membrane, which may have a higher value than the cell interior. This has not been considered in the simulations. A difference between cell mean refractive index and membrane refractive index have been found in liver cells [101], but such a difference has not been reported for RBC. A better explanation for the velocity discrepancy can be grounded in the cell shape. When the cell is attracted to the waveguide surface, its shape changes. Thus, a larger part of the cell interacts with the evanescent field, leading to a stronger horizontal force. The disk shaped cell model attempted to simulate this situation. As seen in the horizontal force results, such calculations were not successful, and the explanation cannot be confirmed. A last argument for the velocity difference is the unknown distance between the cell and the waveguide. If the RBC were closer to the surface than 25 nm, the cell would interact with a larger, and stronger, evanescent field. The calculations would then give increased horizontal forces. On a last note, the focusing effect seen for the spherical cell would contribute less to the the disk shaped cell. Thus, the maximum seen for the 3 to 4 μm diameter spherical cell would presumably not be seen for the disk shaped cell.

## 5.4 Conclusions

Numerical simulations have been performed on spherical and disk shaped red blood cells interacting with the evanescent field of an optical waveguide. Vertical and horizontal forces were derived as a function of cell refractive index and cell size. The disk cell model is half as long as a real red blood cell. However, since the cell in the simulations fully covers the waveguide width, qualitative results should be similar to those for real cells.

The simulations show that a strong vertical force attracts the cell toward the waveguide. This presumably leads to a deformation of the cell geometry. The vertical force increased with both cell refractive index and size. The size dependency was found to be proportional to the amount of surface area inside the evanescent field since the refractive index changes occur at the surface only. In addition, a disk shaped cell experienced significantly stronger vertical forces and showed high sensitivity to refractive index changes.

The horizontal forces were found to be very weak for small index differences, and more than one order of magnitude smaller than the vertical forces. A power law dependence on refractive index was found for the cell–medium index differences, with a quadratic dependence for Rayleigh particles and higher powers for larger sphere diameters. This relation can be explained with the polarizability dependence (Clausius-Mossotti factor) of forces on Rayleigh particles together with the increasing interaction between sphere surface area and evanescent field for larger spheres.

The modeled geometries are large compared to the wavelength of the field, and thus computationally intensive. In the simulations, up to 640 GB of memory distributed on 40 computer nodes were used. Still, for the disk-shaped cell model, horizontal force calculatioins did not converge. The stress on a modeled disk revealed that this was due to a low quality (too coarse) mesh in the narrow region between the cell and the waveguide. By integrating the stress tensor around the object surface, the horizontal force results from the difference between two very large numbers. Thus, a more precise mesh, outside the available computational power, is required for accurate simulations.

By comparing velocities calculated from the horizontal forces with experimental velocities of cells, it is found that the calculations underestimates the velocity. This can be due to a cell membrane index larger than the average cell index used in the

simulations, but more likely is due to the experimental cell shape being different from the spherical cell model.

# Chapter 6

# Principles of Raman Scattering

## 6.1 Introduction

In a light scattering event, the incident light interacts with the electron distribution in the target molecule. However, this interaction is not an absorption-emission process. When the light scatters, the energy of the field is not high enough to permanently excite electrons to higher energy levels. The field instead interacts with the lower energy vibration and rotation levels in the molecule. This involves the movement and position of the atom nuclei relative to the electrons, a fairly complex system. A basic description of the interaction can explain the process by introducing a temporary energy state and only considering the electrons' energy levels. When light is scattered without any change of energy, it is called elastic or Rayleigh scattering. This is by far the most common scattering event. When the scattering is inelastic, the scattered light gain or lose energy to the molecule. This is called Raman scattering.

In 1878, Lommel [102] calculated inelastic scattering using classical theory. His treatment was based on a wave incident on a vibrating molecule, where the vibration induced sum and difference frequencies in the wave. However, inelastic scattering was not described specifically until the early 1920's by Sir C. V. Raman [103]. Raman then considered this to be an optical analogue to X-ray Compton scattering. Experimental results from his lab were presented in a series of publications in 1928 [104–108]. At this time, Raman acknowledged the need for quantum mechanical principles for a proper description of the phenomenon. Incidentally, in

the period between 1923 and 1928, important works on the quantum theoretical principles of light-matter interaction were published by A. Smekal [109], H. A. Kramers and W. Heisenberg [110], E. Schrödinger [111] and P. A. M. Dirac [112]. A summary of the theoretical developments was given by Breit shortly after [113].

Chapters 7 and 8 present experiments that use Raman scattering for sample analysis. This chapter provides a background on Raman scattering theory. It will not give a complete description of the theory, but presents general results following the semi-classical introductions of G. Glockler [114], and J. Brandmüller et al. [115], which both refer to the full theory given by G. Placzek [116]. The first part of the chapter briefly describes how the scattered light intensity relates to a molecule's dipole moment. Then, a very brief introduction to some quantum mechanical principles is given. The last part of the chapter treats the scattered light intensity in the context of a quantum mechanical dipole moment.

## 6.2 Scattering From a Dipole

### 6.2.1 The Dipole Moment

The charge distribution in a molecule is perturbed by any incident electrical field **E**. When the wavelength of the field is much larger than the molecule, the field can be treated as uniform and static across the molecule[1]. The change of the charge distribution affects both the polarization $\alpha$ and the dipole moment $\mathfrak{p}$ of the molecule, and influences the scattered field[2]. The polarizability relates the dipole moment to the field as

$$\mathfrak{p} = \alpha \mathbf{E} = \alpha \left( \mathbf{E}_0 e^{-\jmath 2\pi \nu_0 t} + \mathbf{E}_0^* e^{\jmath 2\pi \nu_0 t} \right), \tag{6.1}$$

when the incident field is considered to be monochromatic with frequency $\nu_0$. In the case of non-isotropic molecules, $\alpha$ takes the form of a tensor.

For an isolated molecule (gas) without permanent dipole moment, interacting with a monochromic, harmonic field, the scattered dipole radiation is found to have a

[1] As the field energy is much lower than the electron energy, the field frequency is much slower. Thus, the field can be considered constant.

[2] In general, contributions from higher order moments are also involved, but only the dipole moment is considered here.

total intensity (Born & Wolf [10], section 2.3)

$$I = \frac{2}{3c^3}\langle \ddot{\mathfrak{p}} \rangle \tag{6.2}$$

far from the dipole, where $\langle \ddot{\mathfrak{p}} \rangle$ is the time average of the twice time differentiated dipole moment. The theory of field-matter interaction can be used to derive the dipole moment, and thus lead to a description of the scattered radiation. As mentioned previously, quantum mechanics is necessary to further develop the theory.

### 6.2.2 Principles of Quantum Mechanics

Quantum mechanics describe the physics of atoms and molecules using systems with discrete energy levels. Any configuration, or state, of the physical system is then described with a wave function. The wave function is found as a solution of the Schrödinger equation, which describes the energy properties of the system. The condition of the system cannot be known exactly, but is described with a probability distribution. For example, the probability of some parameter $\mathfrak{N}$ to move from discrete state $k$ to discrete state $n$ in a system is described by a distribution given by an integral involving the wave functions $\Psi_k$ and $\Psi_n$ of the two states,

$$\int \Psi_k^* \, \mathfrak{N} \, \Psi_n \, \mathrm{d}\tau, \tag{6.3}$$

where $^*$ implies the adjoint of a function and $\tau$ are the spatial coordinates. The integral in itself represents the probability amplitude of the quantum transition. In the following, a time-dependent wave function is denoted $\Psi$, while a time-independent wave function is denoted $\psi$. The properties of quantum mechanics will not be discussed further.

### 6.2.3 Dipole Perturbations

The incident field's perturbation of the molecule vibration induces a change in the molecule's electric moment. A modified Shrödinger equation can be used to find the new wave function $\Psi'$. If the molecule initially is in state $k$ with energy $E_k$, the electric moment can then be described by [114–116]

$$\int \Psi'_k \mathfrak{p} \Psi'_n \, \mathrm{d}v = \mathfrak{p}^{(0)} + \mathfrak{p}^{(1)} = \mathfrak{p}^{(0)} + \mathfrak{E}_{kn} e^{-\jmath 2\pi(\nu_0 + \nu_{kn})t}, \tag{6.4}$$

when the molecule ends up in state $n$ with energy $E_n$. The term $\mathfrak{p}^{(0)}$ contains the permanent dipole moment and terms for spontaneous emission, and the last term describes the electric moment involved in Raman scattering, with

$$\mathfrak{E}_{kn} = \sum_r \left\{ \frac{\left[|\mathbf{E}_0| \int (\psi_k^* \mathfrak{p} \psi_r)\, \mathrm{d}v\right] \cdot \int (\psi_r^* \mathfrak{p} \psi_n)\, \mathrm{d}v}{h\nu_{rk} - h\nu_0} + \frac{\int (\psi_k^* \mathfrak{p} \psi_r)\, \mathrm{d}v \cdot \left[|\mathbf{E}_0| \int (\psi_r^* \mathfrak{p} \psi_n)\, \mathrm{d}v\right]}{h\nu_{rn} + h\nu_0} \right\}. \quad (6.5)$$

In the expression for $\mathfrak{E}_{kn}$, $r$ represents all quantum states in the molecule different than $k$ and $n$, $|\mathbf{E}_0|$ is the amplitude of the incident field, and $\nu_{kn}$=$(E_k - E_n)/h$ is the frequency shift of the field, where $h$ is Planck's constant. The functions $\psi$ represents the wave function of intermediate, initial and final quantum states $r$, $k$ and $n$.

Equation (6.5) shows that Raman scattering occur when both the initial and final state have a possible transition to a common intermediate state (both $\psi_k^* \mathfrak{p} \psi_r$ and $\psi_r^* \mathfrak{p} \psi_n$ are nonzero). Only then can energy be transferred from the molecular vibration to the incident field. If one of the integrands are zero for all intermediate states $r$, no scattering occur in the transition between $k$ and $n$.

### 6.2.4 Rayleigh Scattering

If the initial and final state are the same ($k$=$n$), the scattered field has the same energy and the same phase as the incident field ($\nu_{kn}$=0). This is the Rayleigh scattering. Rayleigh scattering only requires a possible transition between the original state and an intermediate state, and is thus the most common scattering.

### 6.2.5 Scattered Intensity

By introducing the last term from equation (6.4) into equation (6.2), the intensity of the field scattered from the molecule can be found. This procedure mix classical and quantum mechanical equations, but it can be shown [115] that this is a valid approximation, giving the same results as if the field was quantized. The total

spatially averaged scattered intensity from state $k$ to state $n$ is then [115, 116]

$$I_{kn} = \frac{2^6\pi^4}{3c^4}(\nu_0 + \nu_{kn})^4 \left|\mathfrak{E}_{kn}\right|^2. \tag{6.6}$$

### 6.2.6 Stokes and Anti-Stokes Scattering

If the initial state is at a lower energy level than the final state, the frequency of the scattered field decreases. This is called Stokes scattering. Conversely, if the initial state is at a higher energy level than the final state, the frequency of the scattered field increases. This is called anti-Stokes scattering. Stokes scattering usually dominate the scattering, as most occupied states are at a low energy level. Increasing the temperature of the matter increase the population of higher level states, and thus the amount of anti-Stokes scattering.

### 6.2.7 Uniqueness

As the energy levels are unique for all molecules sharing the same structure, $\mathfrak{E}_{kn}$ and $\nu_{kn}$ are specific to one molecule geometry. Thus, the scattering signature is unique for different molecules. This can be used to recognize molecules and, by looking at the intensity distributions, to study the internal properties of a molecule.

### 6.2.8 Polarizability

Equation 6.5 shows that Raman intensities depend on the interaction between the electric moment and the quantum states. As stated in equation (6.1), the induced electric moment depends on the polarizability of the molecule

$$\int \psi_k \mathfrak{p}^{(1)} \psi_n \,\mathrm{d}\tau = \mathbf{E} \int \psi_k(q) \left(\alpha_{x_i x_j}(q)\right) \psi_n(q) \,\mathrm{d}q, \tag{6.7}$$

where $q$ is the displacement in the vibrating molecule. From equation (6.7), the intensity can be expressed using the polarizability tensor [116, 117]

$$I_{kn} = \frac{2^7\pi^5}{3^2c^4} I_0(\nu_0 + \nu_{kn})^4 \sum_{x_i,x_j} \left|\left(\alpha_{x_i x_j}\right)_{kn}\right|^2, \tag{6.8}$$

where $x_i$ and $x_j$ are spatial dimensions, and the polarizability tensor is expressed as

$$\left(\alpha_{x_i x_j}\right)_{kn} = \sum_r \left\{ \frac{\left[\int (\psi_k^* \mathfrak{p}_{x_i} \psi_r)\, \mathrm{d}v\right] \cdot \int (\psi_r^* \mathfrak{p}_{x_j} \psi_n)\, \mathrm{d}v}{h\nu_{rk} - h\nu_0} + \frac{\int (\psi_k^* \mathfrak{p}_{x_i} \psi_r)\, \mathrm{d}v \cdot \left[\int (\psi_r^* \mathfrak{p}_{x_j} \psi_n)\, \mathrm{d}v\right]}{h\nu_{rn} + h\nu_0} \right\}. \quad (6.9)$$

Describing the Raman scattering is thus dependent on finding the transition probabilities (integrals) in equation (6.9).

### 6.2.9 Molecule Symmetry

Solutions to the Schrödinger equation find that wave functions $\psi$ are Hermitian functions, and that almost all allowed transitions are by only one quantum number ($n$=$k \pm 1$). Hermitian functions are odd for odd numbers and even for even numbers, such that the product of two 'neighboring' functions always is an odd function. For the integral on the right hand side in equation (6.7) to be nonzero, the polarizability component also needs to be an odd, or antisymmetrical, function of $q$. This means that the symmetry properties of a molecule and the molecule's vibrations are fundamental in determining the Raman scattering properties. G. Glockler [114], J. Brandmüller et al. [115] and Ferraro et al. [118] generalize and discuss such properties. For this introduction it is sufficient to mention that when the derivative of the polarizability at the center of the vibration is nonzero, the vibration is Raman active, (i.e. can cause inelastic scattering).

As an example, figure 6.1 shows one Raman-active and one Raman-inactive vibration in the linear $CO_2$ molecule. The polarizability of the two vibrations are shown on the side with a polarizability ellipsoid, which represent the polarizability with $1/\sqrt{\alpha}$ in each spatial direction. The polarizability ellipsoid shows how easily the molecule aligns with a field, with the narrow dimensions corresponding to ease of alignment. In the figure, the bending vibration on the left gives a symmetric polarizability change about the centre position of the vibration, and thus is Raman-inactive. The stretching vibration on the right gives an asymmetric polarizability change about the centre position of the vibration, and thus is Raman-active. All vibrations in a molecule need to be considered when the Raman spectrum is interpreted. For complex molecules, this is difficult, but the process can be somewhat

simplified by classifying the molecular symmetries using group theory. This is described thoroughly in for example the text book of Ferraro et al. [118].

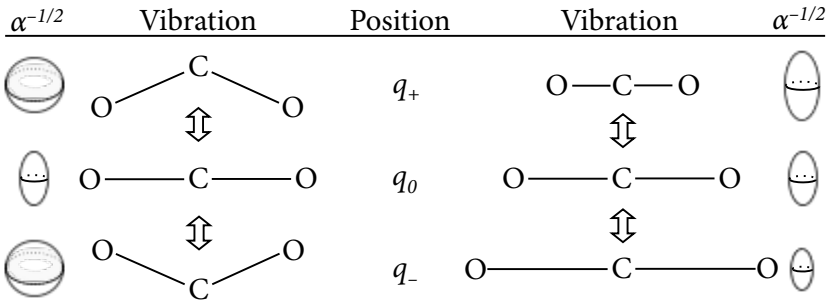


Figure 6.1: Two vibrations in the linear $CO_2$ molecule, with corresponding polarizability ellipsoids.

# Chapter 7

# Quantitative Study of Cell Proliferation Using Raman Probes

## 7.1 Introduction

This chapter describes an experiment that tracks a Raman-active DNA probe as it is incorporated into, and travels from mother to daughter cells in non-adherent cells. The experimental setup combines Raman spectroscopy and optical tweezers, and the results provide data on how fast the cells replicate, or proliferate. Techniques that measures cell proliferation are called proliferation assays, and Yamakoshi et al. [119] were the first to perform this Raman specific assay in 2011. This study looks at quantitative properties of the assay. The experiment was performed at Center for Biophotonics (CBST) at University of California Davis in a collaboration with Thomas Huser, Deanna Thompson and Ana Popovich.

The dedicated Raman tweezers system at CBST achieves much stronger Raman signals than the setup presented in chapter 8. Combining the level of sensitivity achieved at CBST with optical waveguides should enable for example rapid cell sorting experiments based on cell proliferation. The results in these two chapters demonstrate the feasibility of such experiments in the future. However, the combination of waveguide sorting and an optimized Raman setup has not been demonstrated.

The chapter starts out with a section on cell proliferation and measurements of

cell proliferation. Sections 7.3 and 7.4 then describe the experimental properties, procedure and data handling, and the measurement results. Finally, the results are discussed and conclusions are given in sections 7.5 and 7.6.

## 7.2 Cell Proliferation Assays

Cell proliferation is studied to understand basic cell biology, and to see how cells respond to different external influences. One method of measuring cell proliferation is to introduce a label molecule into the DNA and follow the label concentration over time. The results provide information on the proliferation properties of the cell. Such measurement procedures are called proliferation assays.

The label molecule is brought into the DNA by modifying the nucleosides in the growth medium. The cell incorporates the labeled nucleosides in the DNA during DNA replication. Different measurement techniques are used to detect different labels, for example radioactive, fluorescent or Raman active labels.

The following three parts first describe cell replication and cell death and then describe different proliferation assays and their differences. The fist part is central to get an understanding of the results described in section 7.4, while the last part provides a background to the experimental procedure.

### 7.2.1 Cell Replication and Cell Death

Cells replicate by division. Before a cell splits into two new cells, a copy of its DNA molecule is produced. The new DNA is assembled with building blocks called nucleosides which are present in the growth medium surrounding the cell[1]. The division, or mitosis, is the last part of the cell's life cycle. To prepare this process, the cell goes through a growth phase, a DNA replication phase and a new growth phase, after which it is ready to divide. The two new cells then proceed with their own, equivalent cell cycles. The time a cell uses to complete a cell cycle is called the replication time, indicating the rate of replication. In addition to the mentioned phases, the cell can enter a stable phase of rest (a quiescent state). Given the right conditions, a quiescent cell can return to the ordinary cell cycle [120].

[1] Inside the DNA molecule, the nucleosides are connected with phosphate groups. The nucleoside coupled to the phosphate group is called a nucleotide.

When the DNA replicates, the two DNA strands in the mother cell separate and become templates for new DNA strands, as sketched out in figure 7.1. Nucleosides are paired with matching nucleotides on the strands to create two new sets of DNA. Four nucleosides exist in DNA, adenine (A) which matches with thymidine (T), and cytosine (C) which matches with guanine (G). Section 7.2.3 describes a molecule similar to thymidine called EdU (5-ethynyl-2'-deoxyuridine). As these two molecules are similar, both can possibly be matched with the adenine nucleotide on an original DNA strand. The two new DNA strands incorporates an amount of EdU corresponding to the EdU to thymidine ratio in the growth medium. The original DNA strands from the mother cell do not change during the replication.

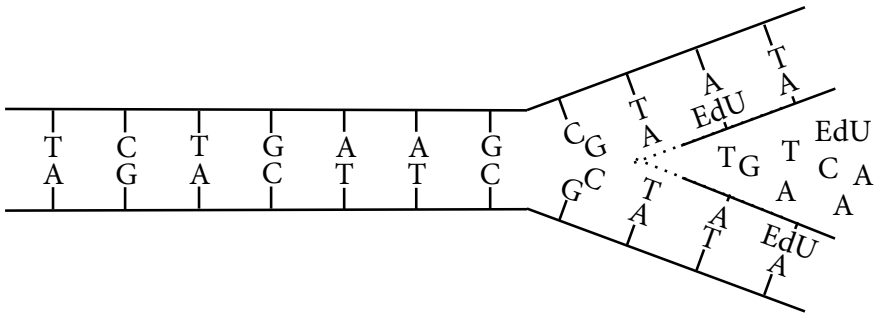


Figure 7.1: DNA replication. The mother cell's two DNA strands (represented by the long straight lines) are connected with pairs of nucleotides. During DNA replication, enzymes in the cell separate the nucleotide pairs (right) and attach matching nucleosides from the growth medium to the each separated strand. Thymidine (T) or EdU match with adenine (A), cytosine (C) match with guanine (G). This process creates two copies of the mother cell DNA, each copy with one old and one new DNA strand.

Cancer cells divide indefinitely when their living conditions allow it. Ideally, the number of cells would double after each replication period, such that $N$ cells become $N \cdot 2^i$ cells after $i$ replications. However, the living conditions influence the cell growth. If nutrient supply is impaired, the proportion of replicating cells can decrease, the replication time can increase, and the proportion of cell death can increase (chapter 7 in [121]).

It is not obvious to point out exactly when a cell is dead. One definition of cell death is that the cell permanently loses all proliferation capacity [121]. This loss can be brought on in one of four different ways, apoptosis, autophagy, necrosis and

senescence. Apoptosis is controlled cell death, were the dying cell is disassembled by other cells. Autophagy is a kind of self-eating, which can occur when the environments are lacking nutrients. Necrosis is death from external influences (strong injuries). Finally, senescence is an age-related death which leads to an inability of the cell to divide. The cell's senescent state can last for a long time.

### 7.2.2 Tritiated Thymidine and BrdU

Traditionally, the label molecule in proliferation assays has been attached to the thymidine nucleoside. This results in a molecule called a thymidine analogue. Figure 7.2 shows the structure of the thymidine molecule. The two most commonly used thymidine analogues have been tritiated thymidine and BrdU (5-bromo-2'-deoxyuridine).

In tritiated thymidine, the hydrogen atoms in the thymidine molecule are replaced with tritium atoms ($^3$H), and the label concentration is measured with autoradiography. The tritiated thymidine was first used in the late 1950's [122] and has been a very common proliferation assay since. However, tritium is radioactive and it is time-consuming to analyze the tritium concentration.

In BrdU, the methyl group in thymidine molecule is replaced with a bromine atom, and the label concentration is measured with fluorescence microscopy after a fluorophore has been attached to the bromine location. As the BrdU assay is quick to analyze and non-radioactive, it has become the more common technique in recent years [123]. Unfortunately, the bromine atoms slightly change the structure of the DNA, changing cell behavior. In fact, both tritiated thymidine and BrdU have been found to be toxic for the cell in vivo [124]. This means that the results found in these proliferation assays are more accurate for DNA replication measurements than for cell division measurements.

### 7.2.3 EdU

The amount of BrdU in the DNA is measured by fluorescence microscopy. To detect fluorescence, it is necessary to fix the cells and attach fluorescent antibodies to the bromine atoms. However, access to the bromine atoms for the antibodies is blocked by the double helix structure of the DNA, and strong chemicals need to be used to reveal the bromine in the DNA structure in the fixed cells. To avoid

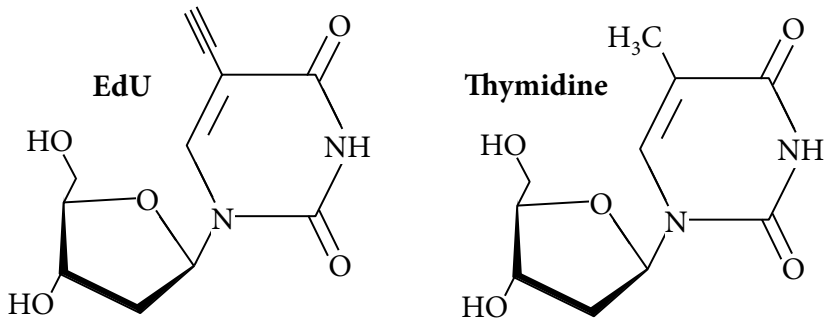


Figure 7.2: EdU (5-Ethynyl-2'-deoxyuridine) and thymidine molecule structures. The methyl group of thymidine is replaced with an alkyne in EdU.

the use of these chemicals, a slightly different assay was developed by Salic and Mitchison [125]. Instead of BrdU, EdU (5-ethynyl-2'-deoxyuridine) is used. This is a thymidine analogue where the methyl group is replaced with an alkyne. Figure 7.2 shows the structure of EdU next to the structure of thymidine.

Similar to the BrdU assay, fluorescent molecules are used to measure the amount of EdU in the DNA. But instead of using antibodies, fluorescent azides[2] are attached to the alkyne labels in a so-called "click" chemistry reaction[3]. This is a sensitive and fast reaction, and since the fluorescent azides are much smaller than the antibodies used in the BrdU assay, they are allowed into the double helix structure, and the use of strong chemicals is prevented.

Recently, Yamakoshi et al. [119] performed an EdU proliferation study where the "click" chemistry step was skipped. Yamakoshi took advantage of the fact that the triple bond in the alkyne is a strong Raman scatterer in a wavenumber region where the cell otherwise is a weak Raman scatterer (a Raman-silent region). By measuring the Raman signal from living HeLa cells[4], the authors showed that the Raman signature from the alkyne could be used to measure cell proliferation.

By using Raman spectroscopy to quantify the EdU signal, there is no need to modify the sample before a measurement. The cell is not affected by the scattering

[2] Azides are molecules containing a negatively charged group of nitrogen atoms that are involved in chemical reactions.

[3] The "click" reaction creates a covalent bonding between the alkyne and an azide, using copper as a catalyst

[4] The HeLa cell line consists of cervical cancer cells.

process, the Raman signal is stable, and does not degrade over time. All these properties are advantageous compared to using a fluorescent label. A fluorophore needs to be attached to the DNA, may be toxic to the cell, and have a limited life span. Thus, the Raman measurements allow different proliferation studies. Unique cell signatures can be tracked over time, cell proliferation can be measured under specific constraints, and it could be possible to study whether the strength of the EdU Raman signal can determine how many times a cell has replicated since the label was introduced.

The remainder of this chapter presents a quantitative study of the EdU Raman proliferation assay using living, non-adherent Jurkat cells. The study shows how EdU in the growth medium accumulate in the cells' DNA and how removal of EdU from the growth medium leads to reduction of the EdU content in the cells' DNA.

## 7.3 Method

The EdU Raman cell proliferation experiment was performed to study how EdU incorporates in the cell DNA. This was done to gain an insight in the cells' proliferation rate and development. In order to study this, two samples of living Jurkat cells was followed over the course of five days, 118 hours. One sample was grown as a control. In the other sample, the growth medium contained a small concentration of EdU molecules for the first 50 hours, after which the growth medium was replaced. From this point in time, the only EdU molecules in the sample were the ones incorporated in the DNA of the cells. Raman signals were acquired from between 20 and 50 cells in the EdU sample every 8 to 10 hours during the whole experiment. In addition, the cell concentration was measured by manual counting in a hemocytometer once every day to control cell health and cell proliferation in the experiment. At the same time, a small cell sample was collected and fixed for later fluorescence measurements. The intent of the fluorescence measurements was to obtain an independent reference of the label uptake seen in the Raman measurements. The fixation of the sample was a necessary step in the "click" chemistry process of attaching a fluorophore to the EdU molecule. Deanna Thompson and Ana Popovich at CBST helped to perform much of the work, including preparation of cell samples, cell counting and fixation, and fluorescence measurements.

The following parts of the Method section describes the cell culture, the setup and the procedure of the measurements, and the analysis of the acquired Raman spec-

tra.

### 7.3.1 Cell Culture

The experiment used cells from the Jurkat cell line. Jurkat cells are lymphocytes, a type of white blood cells. The cells are non-adherent, and between 6 to 15 μm in diameter, well suited for optical trapping experiments. The cells were grown in RPMI growth medium inside a cell culture flask, and kept in an incubator at 37°C and 5% $CO_2$ concentration. Two cell culture flasks were prepared, a control flask without EdU, and a flask with a 10 μmol/L EdU concentration. The initial cell concentrations were $5 \cdot 10^5$ cells/mL. The EdU was provided from Invitrogen's[5] Click-iT® package.

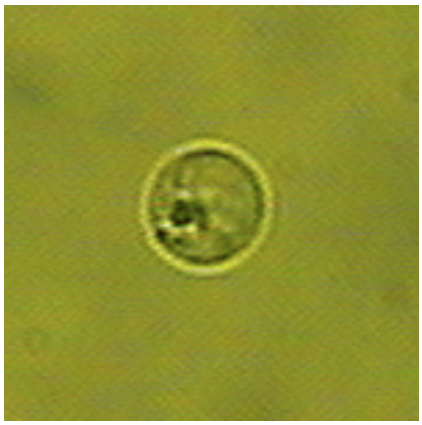

Figure 7.3: White light Image of a single Jurkat T cell, optically trapped in the laser tweezers Raman spectroscopy setup. The image is acquired in a measurement session 83 hours into the experiment.

[5] Life Technologies, Paisley, UK

### 7.3.2 Measurement Setup

#### Micro Raman spectroscopy system

Figure 7.4 shows a sketch of the micro Raman spectroscopy setup. The measurements were done using an inverted microscope from Olympus[6], where the cell sample is kept in a modified cell culture flask. Single cells in the sample were trapped, excited and imaged with a water immersion objective lens (60XW NA1.2, Olympus), and the Raman signal is collected through the same lens. The excitation light was a continuous wave 785 nm laser (CrystaLaser[7]) operated at 80 mW. A telescope modified the diameter of the excitation beam to 6 mm, and the beam is reflected into the objective lens with a long-pass dichroic filter. Single cells are trapped and excited 20 μm above the cover slip surface of the culture flask. The collected Raman signal pass trough the dichroic filter and a 785 nm notch filter to remove excitation light. The background signal is removed with a spatial filter; a 100 μm pinhole confocal with the laser focus. The Raman spectrum is acquired in a spectrometer (PI Acton[8]) with a 600 grooves/mm grating, and registered on a thermoelectrically cooled CCD camera. Spectra were acquired using the Winspec software program (PI Acton), and imported to Matlab[9] for data analysis.

#### Cell culture flasks

The cells were grown in modified cell culture flasks (Sarstedt[10]). A 1 cm diameter hole was drilled in the center of the flask bottom, and a #1.5 cover slip was attached with super glue to cover the hole. Figure 7.5 shows a sketch of the flask. Through the cover slip, a high NA objective lens could image the sample, trap single cells, and excite and collect Raman signal from single cells inside the flask.

The color of the RPMI medium changes from orange to pink when the pH of the medium decreases and to yellow when the pH of the medium increases. This happens because the chemical equilibrium in the blood changes when the outer $CO_2$ concentration decreases. The system of cells and surroundings strives to reach a

[6]Tokyo, Japan
[7]Reno NV, USA
[8]Trenton NJ, USA
[9]MathWorks, Natick MA, USA
[10]Nümbrecht, Germany

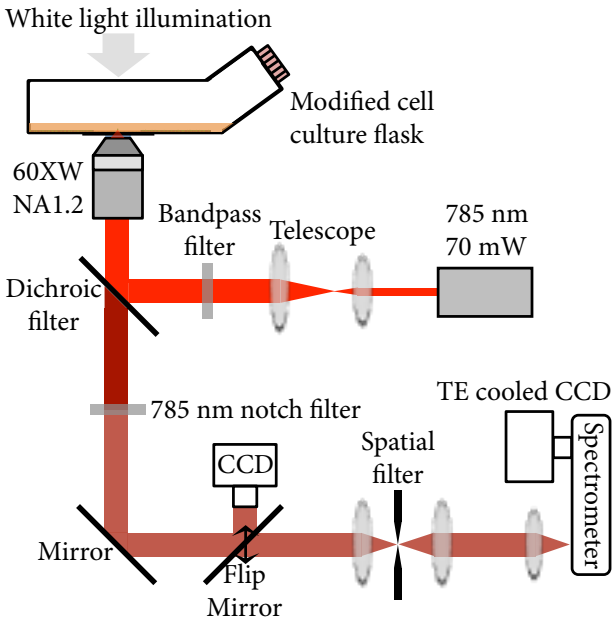


Figure 7.4: Sketch of the micro Raman spectroscopy system. Cells in the culture flask are excited with a 785 nm laser. Raman excitation and collection is done through a water immersion objective lens (60X NA1.2). The collected signal is brought to a spectrometer trough a dichroic filter, a notch filter and a spatial filter to remove excitation light and background signal. Alternatively, white light images of the sample can be acquired with a CCD camera in the collection path.

new chemical equilibrium. This is achieved by the release of $H^+$ ions from the blood cells, increasing the pH in the medium. The color change gives a good indication on cell health. Outside the incubator, the samples changed color after 20 to 30 minutes. Each measurement session lasted approximately 30 minutes. To prevent severe sample degradation, the region around the sample was heated to a temperature between 31 and 33 °C. This was done by covering the microscope with a cardboard hood and heating the sample region with a thermostatic heater (Nevtek) through a hole in the hood. The $CO_2$ levels inside the hood were not controlled.

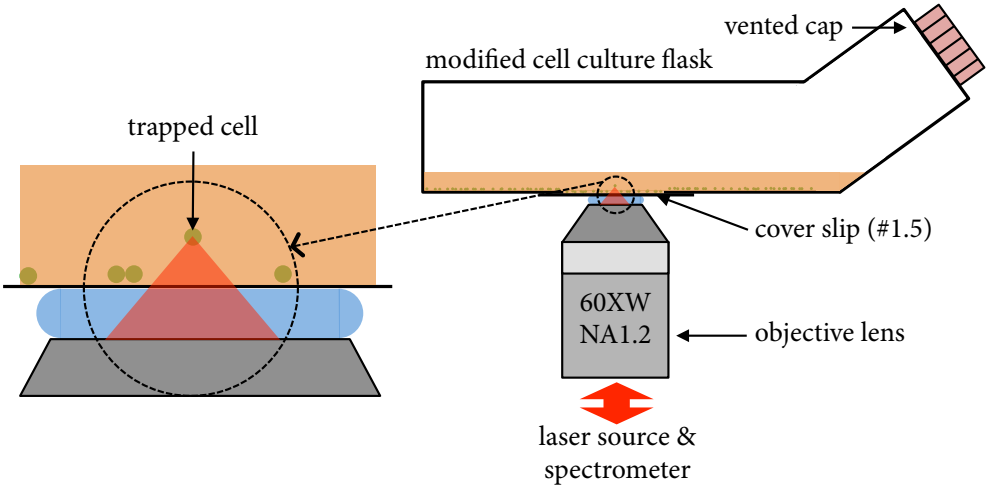


Figure 7.5: Modified cell culture flask with an optically trapped cell. The water immersion objective lens of the inverted microscope excites and collects Raman scattering through the cover slip attached to the cell culture flask. A Jurkat cell is trapped in the focus of the laser, 20 µm above the surface of the cover slip. The figures are not to scale.

### 7.3.3 Experimental Procedure

Five procedures were performed in the experiment; Raman spectrum acquisitions, cell counting, sample fixation, "click" chemistry and fluorescence microscopy. Raman spectra were acquired at intervals of between 8 and 10 hours, while counting and fixation was done once a day. About halfway through the experiment, the growth medium containing EdU was replaced with normal growth medium (the

"washing" process). After the Raman experiment was finished, "Click" chemistry and fluorescence microscopy were performed on the fixed cells.

### Spectrum acquisition

For spectrum acquisitions, the EdU sample flask was taken from the incubation chamber to the laser tweezers Raman setup, and single, living cells were trapped and excited through the cover slip at the bottom of the cell culture flask. No cells were removed from the cell culture flask. Measurement sessions usually lasted around 30 minutes, and gave spectra from 20 to 30 single cells[11]. The cells were trapped with the excitation laser and held 20 μm above the cover slip surface during the 30 seconds acquisition time. After the acquisition, the laser light was blocked to release the cell, and the sample stage of the microscope was translated to trap and excite a new cell. After the measurement session, the flask was returned to the incubator. The sample pH increased during a measurement session, according to changes in the sample medium color. However, the pH had returned to normal levels when the next session began 8 to 10 hours later.

Before each measurement session, the spectrometer was calibrated with a 3 μm diameter polystyrene sphere, and a background spectrum was acquired from the growth medium in the cell culture flask.

### Counting and fixation

For counting and fixation, a 1 mL sample was extracted from the EdU flask. 10 to 15 μL of the sample was counted on a hemocytometer, while the remaining volume was fixed for "click" chemistry and fluorescence imaging. The counting with a hemocytometer is done by applying a small sample of cell solution in many compartments with precisely defined volumes, and counting the number of cells in each compartment using a microscope. This gives a measure of the cell concentration in the sample. To fixate the cells, the sample was centrifuged three times at 3000 rpm for 5 minutes to separate the cells from the medium. After the first centrifuge, the medium was replaced with 4% paraformaldehyde in phosphate-buffered saline

[11] A few sessions were divided in two, where in total 50 spectra were acquired in two 20 to 30 minute long sessions. These shorter sessions were separated by a one hour break in the incubator.

solution (Dulbecco's PBS), and left for 15 minutes. After the second and third centrifuges, the paraformaldehyde was replaced with pure PBS. After the fixation process, the sample was refrigerated at 4°C until the cells were plated for fluorescent imaging.

### Washing

After 52 hours, the growth medium with EdU in the cell culture flask was replaced with unmodified growth medium. After the medium replacement, any remaining EdU molecules in the sample are inside the cells, incorporated in the cell DNA. To exchange the medium, the cell sample was extracted to a test tube and centrifuged at 3000 rpm for 5 minutes. The growth medium containing EdU was then replaced with pure growth medium. The medium replacement process was repeated three times. The sample flask was thoroughly rinsed with pure growth medium before the washed cell sample was returned. Before washing, the cell concentration was counted. The amount of new growth medium in the sample was adjusted such that the cell concentration was $4 \cdot 10^5$ per mL. The control sample concentration was also adjusted to this concentration. Spectrum acquisitions, counting and fixing continued for 67 more hours after washing and concentration adjustments.

### "Click" chemistry

The "click" chemistry reaction was obtained following the instructions in the Click-iT® EdU Imaging Kit from Invitrogen [126]. In the procedure, the fixed cell sample was introduced into a solution of reaction buffer, fluorescent azide and a copper sulphate catalyst. After 30 minutes, the fluorescent molecules were attached to the EdU in the DNA of the cells. The solution was washed out with PBS with 3% bovine serum albumin (BSA) and finally pure PBS.

### Fluorescence microscopy

Fluorescence measurements of the cells that had been treated with "click" chemistry were done to independently check the Raman experiment results. Samples from each day were distributed in sterile silicone holders on poly-l-lysine covered glass slides, where they dried for two hours. The remaining liquid was removed, and

the cells were covered with Prolong Gold (Invitrogen) and a cover slip. After one day, the cover slips were sealed with nail polish. One slide was prepared for each of the five fixed cell samples. Fluorescence imaging of the samples was done on a deconvolution microscope (DeltaVision[12]).

### 7.3.4 Data Treatment

The spectral data were imported to Matlab. A script was written to extract the size of peaks in the spectra in order to reveal the amount of EdU in the DNA. In each measurement session, each cell provides a unique spectrum. The EdU uptake is shown by the Raman peak distribution in a spectrum. Several numerical procedures were performed on each spectrum to give an accurate description of the time development of EdU uptake. The following paragraphs describe how the peak magnitudes were found from the spectral data. As calibration and background acquisitions were done at each measurement session, the series of spectra from each session were treated separately in the calculations.

#### Finding the amount of EdU incorporated in the DNA of the cell

When the Raman signal is acquired, the cell is trapped by the focused laser. As Raman scattering is proportional to the intensity of the incident light, the part of the cell in the focal point scatters most light. The cell nucleus has a slightly larger refractive index than the other parts of the cell, and usually settles in the focal point. However, to be sure that the collected EdU signal originates in the nucleus, its peak value is compared to the peak value of a DNA specific signal. Thus, two peaks are analyzed in each spectrum; the peak from the alkyne group in EdU (at 2120 $cm^{-1}$), and a peak from the phosphate backbone in DNA (at 1093 $cm^{-1}$). The ratio of the EdU and DNA backbone peaks is used as a measure of the amount of EdU incorporated in the DNA of the cell. Figure 7.6 shows spectra from a cell in the control sample (without EdU) and a cell in the EdU sample, pointing out EdU and DNA backbone peaks.

Examples of fit procedures are shown in figure 7.7 for three spectra. All spectra show similar DNA backbone peak amplitudes, while the EdU peak amplitudes varies. The top spectrum shows a large peak, the centre spectrum shows a small

[12] Applied Precision, Issaquah WA, USA

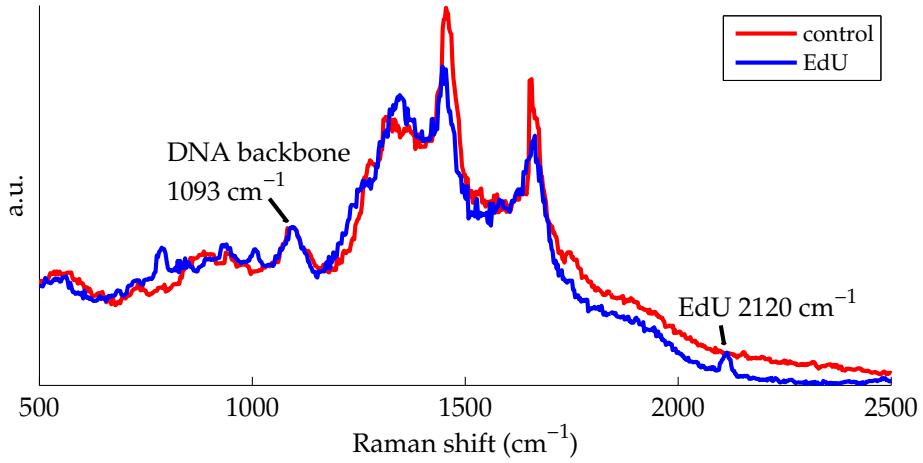


Figure 7.6: Raman spectra from a cell in the control sample (red line) and a cell in the growth medium with 10 µmol/L EdU (blue line) after 52 hours. The signal of the control spectrum is shifted to make the DNA peaks of the two spectra equal. Backgrounds have been subtracted.

peak and the bottom spectrum shows no peak. Since the DNA peaks are similar, the three spectra would give one large, one small and one zero peak amplitude ratio.

### Subtracting backgrounds and filtering

The first step in the data processing is to subtract the spectral backgrounds from the cell spectra. For each session, two to three background spectra were acquired from a region of the sample without cells. These spectra were averaged and filtered with a 5-point median filter and a 3-point boxcar filter. The filters remove contributions from cosmic rays, and smooth out high-frequency noise. After subtracting the filtered background from the cell spectra, the cell spectra themselves were filtered by a 5-point median filter to remove cosmic ray contributions. The resulting spectra (shown with red lines in figure 7.7) provided the base for the remaining numerical analysis.

**Determining the peak amplitude with a curve fitting procedure**

The amplitude of a peak was found by fitting the Cauchy-Lorentz function,

$$f(\bar{\nu}) = \frac{Ib^2}{(\bar{\nu} - a)^2 + b^2}, \tag{7.1}$$

to the spectrum in a wavenumber region close to the peak[13]. The fit was done with Matlab's 'fit' function, which optimizes the fit with a nonlinear least square algorithm. This gave estimates of the peak amplitude $I$, the peak center position $a$ and the peak's full width at half maximum value (FWHM) $2b$ for wavenumbers $\bar{\nu}$.

The Matlab algorithm provides goodness-of-fit statistics. How well the model fits the data can be described by the coefficient of determination $R^2$. The unbiased coefficient of determination $\tilde{R}^2$ was used, together with the calculated peak position $a$, to automatically determine whether the fit represented a real peak or not[14].

The fit parameters were defined to describe a real peak if the fit's $\tilde{R}^2$ value was larger than 0.55 and the peak position was within 2 wavenumbers from the average peak position of that measurement session. The average peak position was defined from the spectra in that session which had $\tilde{R}^2$ values larger than 0.7 and a peak position between 1070 and 1110 $cm^{-1}$ for the DNA backbone peak, and between 2105 and 2130 $cm^{-1}$ for the EdU peak. To prevent faulty spectra to influence the results, spectra without a DNA backbone peak was rejected from the analysis. The chosen limits of $R^2$ and wavenumbers were found by testing reasonable values in several datasets such that the peaks found numerically corresponded to visible peaks in the spectra.

The Raman-silent region above the EdU peak tend to have an linearly increasing or decreasing slope after the background has been subtracted. For some spectra, the fit algorithm fails to recognize the EdU peak because of the slope. To make sure that these peaks are included in the analysis, a linear regression is done in the spectral region above the EdU peak[15]. This regression line is then subtracted

[13] $\bar{\nu}$ from 2080 to 2160 $cm^{-1}$ for the EdU peak, $\bar{\nu}$ from 1030 to 1140 $cm^{-1}$ for the DNA backbone peak.

[14] Strictly speaking, the biased coefficient of determination $R^2$ would have given a more correct measure of the goodness-of-fit, as the fit used all wavenumbers in the region and not a sampling. However, using $\tilde{R}^2$ only lead to slightly lower values than would have been found using $R^2$, and does not influence the results.

[15] $\bar{\nu}$ from 2160 to 2500 $cm^{-1}$.

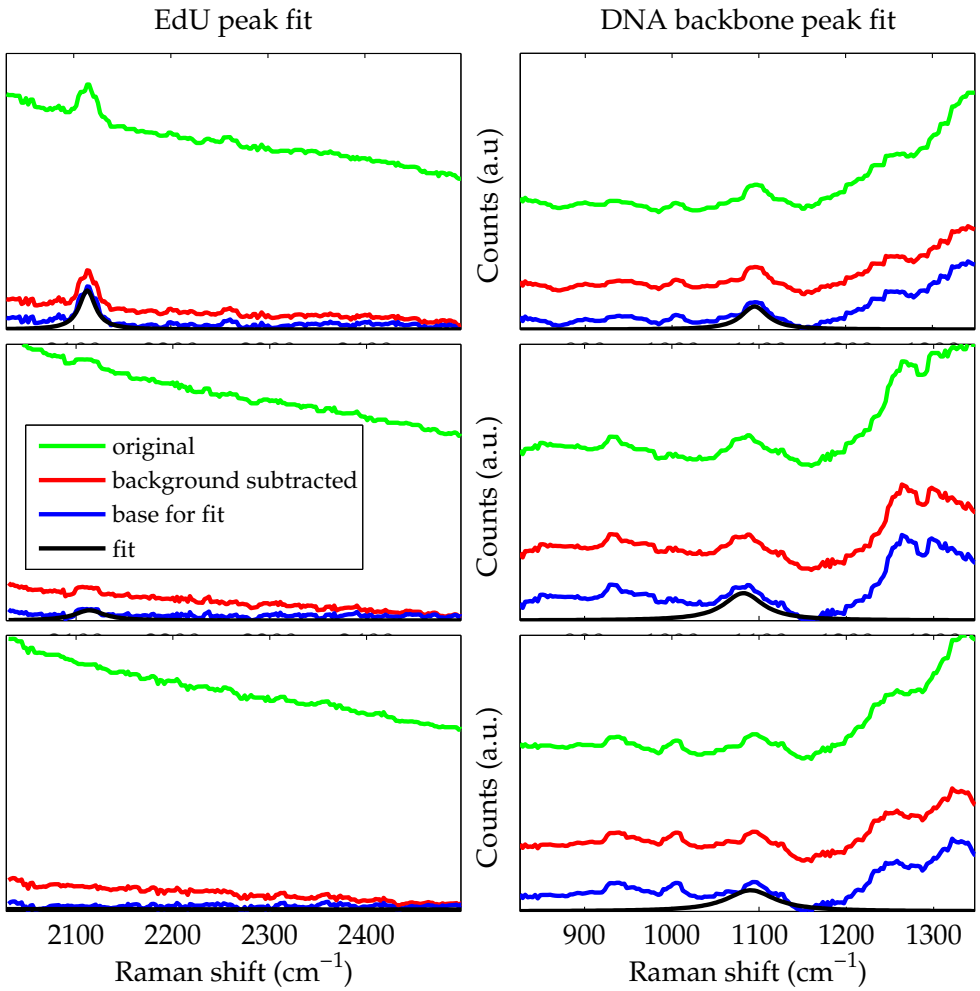


Figure 7.7: The fitting process shown for both EdU and DNA backbone peaks. Spectra from three cells are included, one with a strong EdU signal (top left), one with a weak EdU signal (middle left), and one with no EdU signal (bottom left). The cells have similar DNA backbone peaks, as seen on corresponding plots on the right. By subtracting the background, straightening (for the EdU peak) and setting the minimum value to zero, the optimization algorithm finds a Lorentzian fit. The three EdU peak plots share similar axes, and the three DNA backbone peak plots share similar axes.

from the original spectrum. The amplitude of the EdU peak is not affected by the straightening operation, as the regression line is close to zero at the peak position.

The last step before the peak fitting procedure is to shift the spectrum vertically such that the minimum value in the region above the peak position (the linear regression region) is zero. This provides the basis for the fit, which is shown by the blue lines in figure 7.7.

## 7.4 Results

Interpretation of the experimental results needs special consideration, as the results are connected to each other. Thus, only brief comments are given on the results to allow a more coherent discussion in section 7.5.

### 7.4.1 Raman Measurements of EdU Signal

#### The EdU concentration in DNA

The development of EdU concentration in the cells' DNA over time is shown in figure 7.8. The vertical axis represents the amplitude ratio between the EdU peak around 2120 $cm^{-1}$ and the DNA phosphate backbone peak around 1093 $cm^{-1}$. The figure plots ratios from all spectra (blue crosses), in addition to the mean (black squares) and the standard deviation of each measurement session. Only spectra where an EdU peak has been found are included in the plot. In the figure, the EdU concentration in the DNA increases until the sample is washed. After the EdU is washed out of the growth medium, the EdU concentration in DNA decreases for around 30 hours, before the concentration increases again during the last 34 hours. The exact concentration of EdU in the DNA has not been found, due to problems with dissolving high EdU concentrations in PBS for reference concentration values. Thus only the trends of EdU accumulation and dissipation in the DNA have been found.

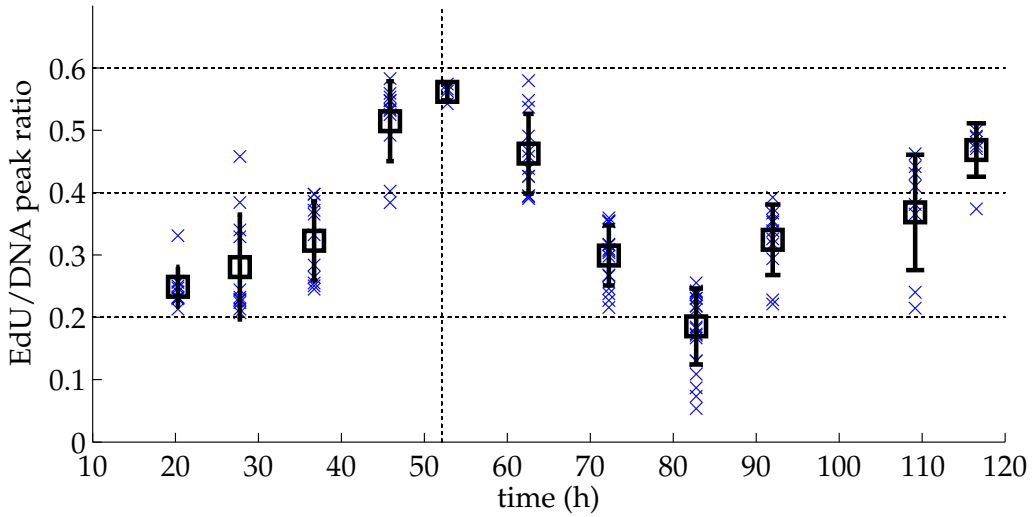


Figure 7.8: Scatter plot of the EdU concentration in the DNA during the experiment. Means and standard deviation bars are superimposed. The concentration increases steadily as long as the growth medium contains EdU. After 52 hours, the EdU is washed out, and the EdU concentration starts decreasing. 30 hours after the washing, the EdU concentration again starts to increase. Only cells showing an EdU peak have been included in the plot (corresponding to the red crosses in figure 7.9).

### The ratio of cells with EdU

A different plot of the same dataset is given in figure 7.9. This figure shows the number of measured cells in each session as well as the number of cells where EdU peaks were found. The ratio of cells with a measurable amount of EdU is fairly constant throughout the experiment.

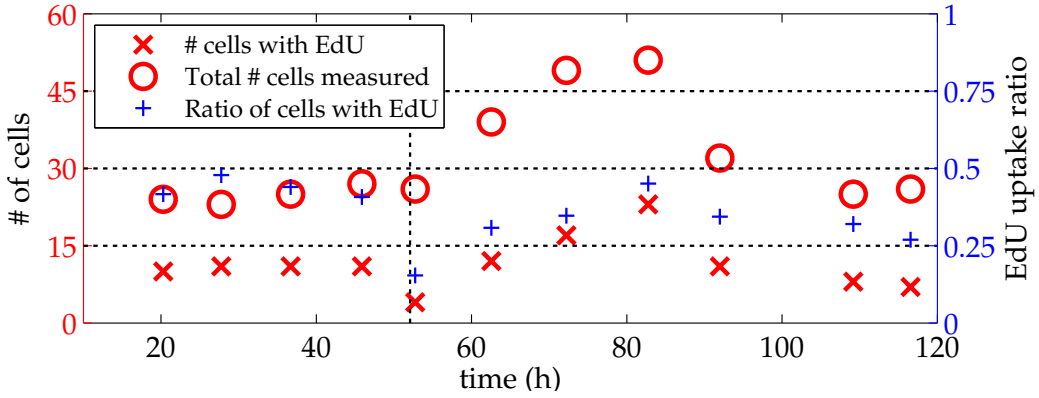


Figure 7.9: The number of cells and ratio of cells where EdU was detected. The ratio is fairly constant throughout the experiment, with a slight decrease after the EdU is washed out of the growth medium at 52 hours.

## 7.4.2 Fluorescence Measurements of EdU Signal

The fixed cell samples extracted at daily intervals were imaged in a microscope after fluorophore staining ("click" chemistry treatment) and plating. Figure 7.10 shows the number of fluorescent cells, similar to the Raman data shown in figure 7.9. Unfortunately, the total number of measured cells is small, due to low cell concentrations in the extracted samples. Since fluorescence provides stronger signals than Raman scattering, the measured number of cells containing EdU was expected to be higher for these measurements. However, the ratio in figure 7.10 does not reveal that trend. This could be due to the small sample size, or it could be due to an unsuccessful "click" chemistry reaction. A separate "click" chemistry fluorescent measurement of 87 cells showed 70% uptake of EdU 20 hours into the experiment. The fluorescent data in the figure suggests that the ratio of cells containing EdU was stable, similar to the Raman measurements.

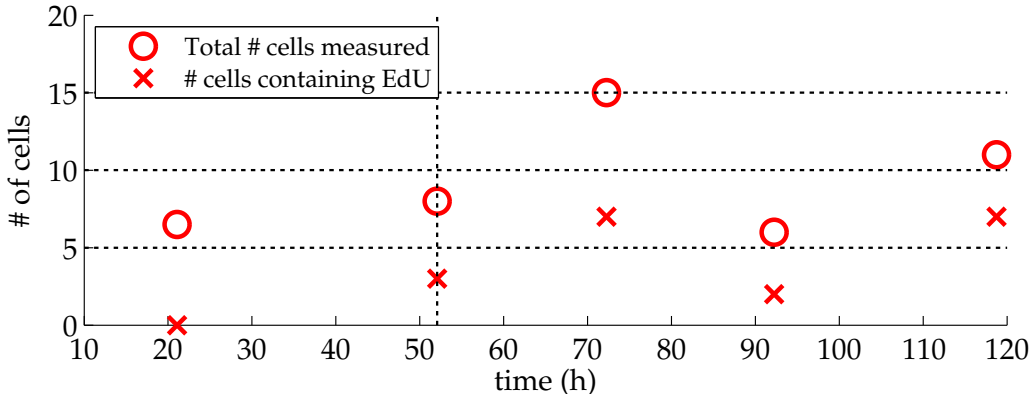


Figure 7.10: Fluorescent signal from plated and "click" chemistry treated cells were measured in a DV microscope. The number of cells containing EdU is lower than the Raman measurements, contrary to what is expected, as the fluorescent signal is much stronger than the Raman signal. This result is probably due to the small number of measured cells.

### 7.4.3 Cell Counting

Figure 7.11 shows the cell count of the the control and EdU samples at daily intervals during the experiment. The cells were counted in a hemocytometer. The start concentration of the samples is $5 \cdot 10^5$ cells per milliliter, and the concentration after the washing is set to $2 \cdot 10^5$ and $3 \cdot 10^5$ cells per milliliter for the control and the EdU sample, respectively. It is evident from the figure that cell proliferation in the EdU sample is severely limited. The control sample data suggest that the number of cells doubles after around 77 hours before the washing and around 36 hours after the washing, giving replication times of 77 and 36 hours, respectively. Earlier experience with the same cell culture indicates a replication time of around 22 hours [127], and Nuñez reports a replication time for Jurkat cells of 32 hours [128]. This suggests that also the control sample proliferation was restricted before the washing.

Previous studies do not report significant decrease in cell proliferation due to EdU [119, 125]. Thus, other factors should be considered to explain the cell death and the slow replication rate found by counting the EdU and control samples, respectively. It is likely that the reason for the observed cell concentration development was the treatment of the cells during measurement sessions. Color change in the growth medium (section 7.3.2) showed that lower temperatures and lower carbon dioxide levels for more than 30 minutes did affect the cells adversely. In the control

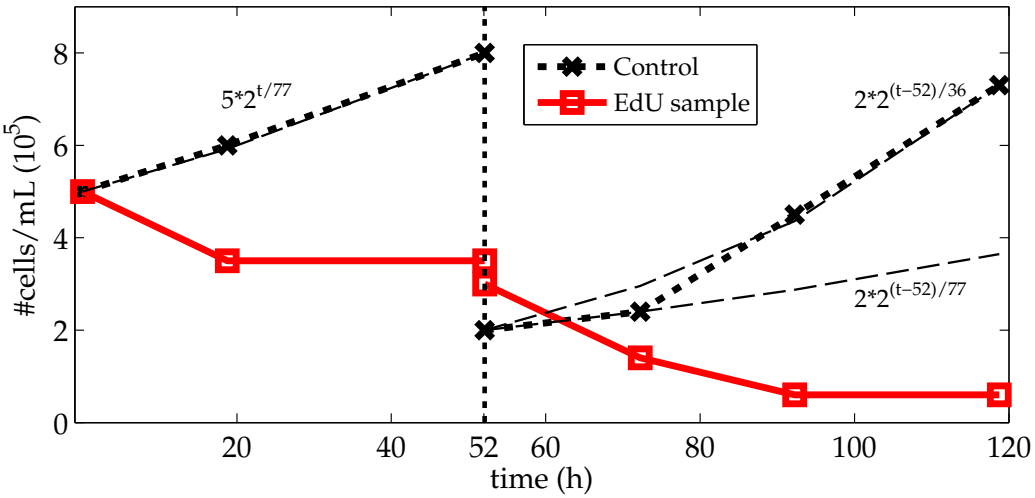


Figure 7.11: Cell concentrations calculated from hemocytometer counts during the experiment. Formulas describing the replication rate of the control sample are superimposed on the plot. When the EdU is washed out, new cell concentrations are set in both samples, adjusted by the amount of new growth medium. The slow replication rate of the control and the decline in the EdU sample suggest that the measurement sessions were stressful for the cells.

sample, shorter measurement sessions lasting around 20 minutes were performed regularly up to the time of washing. After that time, only one brief measurement was done. This could explain the increased cell replication time seen in the figure after the washing, and indicates that the living conditions during the measurement sessions indeed were responsible for cell death and limited the number of cells.

The replication times given by figure 7.11 points to a shortcoming of using cell counting as a proliferation assay. There is no way to know whether a cell in the hemocytometer is actively replicating or not. And as long as a cell has not dissolved, it will be counted. By including non-replicating cells in the count, the measured replication time will be slower than the true replication time. This effect could also have contributed to the slow replication time found for the control sample in the measurement.

Lastly, it should be noted that both the cells that did and did not show EdU signatures looked healthy in the microscope during the Raman measurements. However, a few spectra showed strong lipid peaks (at around 1450 and 1650 $cm^{-1}$), indicating membrane blebbing, which is a sign of apoptosis and autophagy (see section 7.5.1).

## 7.5 Discussion

The developments of the EdU concentration in the DNA, the ratio of cells with EdU, and the cell proliferation that were presented in figures 7.8, 7.9 and 7.11 demand careful analysis. It will be helpful for the analysis of the results to first look at the expected cell proliferation and development of EdU concentration. As such, section 7.5.1 describes how EdU is incorporated into DNA. In the following section, 7.5.2, it is discussed how the results match these expectations and how discrepancies can be explained. Three cases are considered separately: the ratio of cells with EdU, the EdU concentration increase and decrease in the period from EdU is added to it is washed out, and the subsequent period of increasing EdU concentration.

### 7.5.1 Expected Uptake of EdU

#### The ratio of cells with EdU

The phases of the cells in a sample are randomly distributed. When EdU molecules are added to the growth medium, the molecules incorporate in the cells' DNA during the replication phase. Some cells incorporate EdU immediately, while cells which just ended their previous replication will not incorporate EdU until a full cell cycle has passed. Thus, during the first 22 to 36 hours (depending on the actual replication time), the number of cells containing EdU would increase linearly. When the time of one full cell cycle has passed, all replicating cells have incorporated some EdU.

#### The EdU concentration in DNA

The concentration of EdU in the cells' DNA increases for each cell replication until a plateau is reached. This plateau is expected to be given by the EdU to thymidine ratio in the growth medium. The incorporation of EdU and Thymidine molecules is a stochastic process, giving the cells a distribution of EdU concentrations. Each measurement session should include a large number of cells to find a representative mean value of the EdU concentration.

After $i$ replications in a growth medium with an EdU to thymidine ratio[16] of $X_\mathrm{t}$, the average EdU concentration $C_i$ is given by

$$C_i = \frac{2^i - 1}{2^i} X_\mathrm{t}. \tag{7.2}$$

This can be seen by considering the ratio of 'new' to 'original' DNA strands: After one division, all replicating cells contain one original DNA strand without EdU, after two divisions, a fourth of the replicating cells contain one DNA strand without EdU, and so on. Note that any individual cell's DNA would contain EdU in either both strands or only one strand.

After the EdU is washed out, new DNA strands cannot incorporate any EdU. Only EdU molecules already inside the DNA are left in the sample. This means that the

[16] The amount of EdU molecules divided by the sum of EdU and thymidine molecules.

average EdU concentration in the DNA is halved after each new replication. Thus, the average EdU concentration is given by

$$C_i = \frac{1}{2^{i-r_{\text{wash}}}} C_{r_{\text{wash}}}, \tag{7.3}$$

where $r_{\text{wash}}$ ($> i$) is the number of replications before the washing. If the cells were allowed to replicate 5 times before ($r_{\text{wash}}$=5) and 5 times after the washing, the average EdU concentration in the cell sample would then develop as shown in figure 7.12.

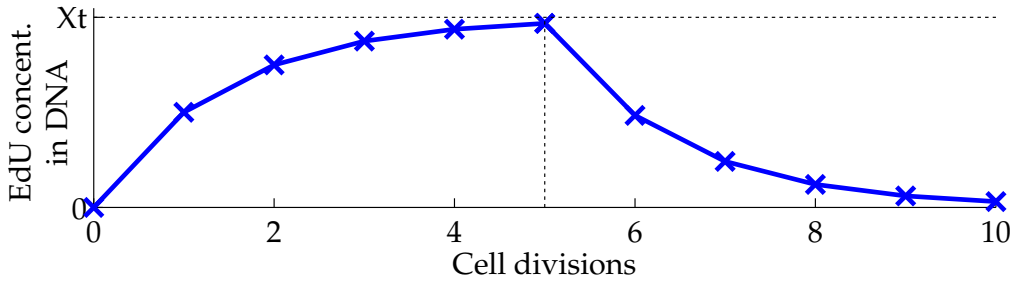


Figure 7.12: Expected development of EdU concentration in the DNA for a cell in a medium with an EdU to thymidine ratio of $X_t$ with 5 full replication cycles before and after the EdU is washed out.

### 7.5.2 Actual Uptake of EdU

#### The ratio of cells containing EdU

The plots in figures 7.9 and 7.10 show the number of cells with a measurable content of EdU from the Raman and fluorescent measurements in absolute numbers and as ratios. Between 40% and 50% of the cells contained an observable amount of EdU before the EdU was washed out. After washing, the average ratio decreased to around 30%. This is contrary to the expected result; that all cells would incorporate EdU before washing, and that the ratio of cells with EdU would decrease rapidly afterwards. In addition, the expected linear increase during the first cell cycle is not seen, but this was probably due to the fact that no measurements were done for the first 20 hours of the experiment.

The reason why the observed trends do not match the expected results can be explained by two hypotheses. First, it is possible that many of the cells, for some unknown reason, do not incorporate EdU in their DNA. This implies that there are some fundamental structural difference between the cells. However, all the cells should be exactly equal, coming from the same cell culture. Second, there is a possibility that many of the measured cells are not actively replicating, but are either dead, but not dissolved, or put on hold, living in a resting state. This looks to be the most reasonable explanation, since the senescent and quiescent states and death may be caused by tough living conditions. However, further experiments are required to confirm this hypothesis.

**Predicted increase and decrease of the EdU concentration**

Figure 7.8 shows that the incorporation of EdU into the cells' DNA matches the expected trends fairly well. This plot differs from the plot in figure 7.9 in two ways. First, only spectra from cells containing EdU are included. As only replicating cells incorporate EdU, measurement errors introduced by non-replicating cells are avoided. In addition, the normalization performed by plotting the ratio between EdU and DNA peaks decreases errors introduced by differences in excitation intensity, signal collection and trapping region in each measurement. This gives a more true picture of the activity of the replicating cells. When the experimental mean values are combined with the expected EdU uptake calculated with equations (7.2) and (7.3), the development of the incorporation can be compared with different replication times.

Plots a) and b) in figure 7.13 show how the EdU concentration in DNA, represented by the average experimental EdU to DNA peak ratios, match the calculated uptake for the shortest and longest replication times given in section 7.4.3, 22 and 36 hours respectively. The values are normalized such that the maximum peak ratio coincides with the calculated concentration at 52 hours, the time of the washing. The EdU to thymidine ratio in the growth medium is indicated by $X_t$ (from equations (7.2) and (7.3)). The cell cycle times are indicated with crosses. A comparison between the two plots in the figure shows that the increase in concentration before the washing best matches the slower replication time, while the decrease in concentration best matches the faster replication time. A numerical fit of the first four peak ratios after the washing to equation (7.3) gives a replication time of 22.6 hours with a 95% confidence interval between 13.7 and 31.6 hours. The peak ratios be-

fore the washing cannot be fitted to equation (7.3). Note that both the experimental and calculated values represent average concentration. The EdU concentration in individual cells would increase stepwise in time with the replication time. The increase in concentration during the last thirty hours is discussed separately on the next page.

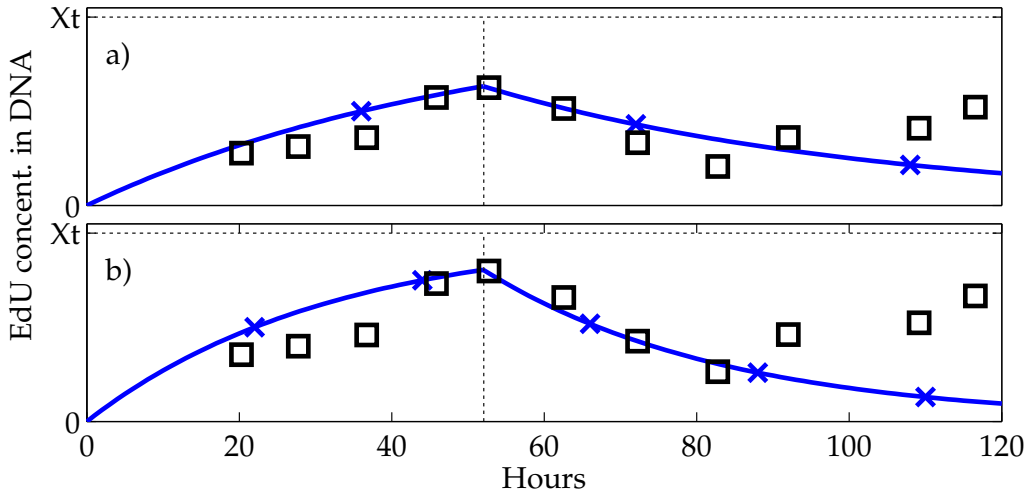


Figure 7.13: The mean values of normalized experimental peak ratios (black squares) are superimposed on plots of the expected time development of EdU concentration. Plot a) shows calculated values for a 36 hour replication time, and plot b) shows calculated values for a 22 hour replication time. In each plot, the experimental data are normalized to the same maximum value of the calculations at the time of the washing.

The steady increase of EdU up to the time of washing indicates that the average EdU content in the DNA still increased at the time the EdU in the growth medium was removed. This is supported by figure 7.12, which suggests that the EdU concentration is not saturated after more than 4 full cell cycles. This would at best take 88 hours with the shortest replication time of 22 hours. Looking closely at the distribution of peak ratios in figure 7.8, it can be seen that the minimum and maximum peak ratios are fairly stable up to the 37 hour measurement session. At the next measurement session in hour 46, the minimum and maximum ratios jump. This suggests that all the cells have replicated (i.e. taken up EdU) two or three times at that time in the experiment. This fits for replication times of approximately 22 hours (third replication) and approximately 36 hours (second replication). In context of the better fit after the washing for a 22 hours replication time, it seems

likely that 22 hours is the best approximation. The result does, however, differ from the 36 hour and 77 hour replication times suggested by the hemocytometer measurements. Due to the fact that only data from replicating cells are included, it is likely that the Raman tweezers method provides better estimates of the active (non-quiescent) cells' replication time. However, more experimental data is necessary to confirm this result, and to provide a more precise value.

### Unpredicted increase in EdU concentration after the washing

The increase in EdU concentration during the last 30 hours of the experiment was not expected. All the extracellular EdU had been removed from the sample 20 hours prior to the increase, and the only possible source of EdU molecules were the cells in the sample[17]. Four hypotheses can explain the cause of the increase, all of which relates to the decreasing number of cells in the sample. First, the EdU could come from dissolved dead cells in the sample, freeing up EdU that were incorporated in the DNA of the remaining replicating cells. Second, the EdU could come from extranuclear parts inside the replicating cell, for example the cytosol[18] or the cell membrane. Third, the observed increase could have been caused by measurements of quiescent or senescent cells with high EdU concentration. Fourth, the EdU could come from pieces of DNA from dissolved dead cells which were attached to the measured cell. The hypotheses are discussed in the following paragraphs, but no final conclusion can be reached without data from further studies.

**1. EdU from dissolved cells** The cell concentration shown in figure 7.11 indicates that the number of cells had been halved 20 hours after washing. This would lead to a large amount of cell fragments in the sample. The existence of dissolved and dissolving cells supports the first hypothesis; that the EdU originates from dead cells. It would take time for the dying cells to dissolve, making it plausible that the EdU increase began 30 hours after the washing (assuming that most dead cells were removed when the sample was washed). However, the EdU from these cells is not freely available, but attached to larger molecules from the dead cells. In addition, the released amount of EdU would give a much lower EdU to thymidine ratio due to the new growth medium added to the sample after the EdU was washed out.

[17] Contamination of the sample is possible, but not plausible, as the sample was contained inside a closed container throughout the experiment.

[18] The cytosol is the intracellular gel/liquid.

**2. EdU from the cell itself** The peak normalization (EdU/DNA ratio) in figure 7.8 was required to see any trend of increasing and decreasing concentrations. The EdU peaks alone did not show any development over time. This suggests that EdU exists in extranuclear regions of the cell and that this EdU contributes to the Raman signal. The existence of such EdU supports the second hypothesis; that EdU in the cytosol or the membrane is incorporated during the DNA replication. The tough living conditions suggested by the decreased cell concentration could have lead to cell autophagy. Autophagy is a process where the cell eats its own internals to survive (section 7.5.1). However, blebbing, which is commonly associated with autophagy, was not found to dominate the measured cells in neither the Raman spectra or visually in the microscope. Also, the 30 hours delay in the increase is not explained by this hypothesis.

**3. Measurements of quiescent and senescent cells** Tough living conditions may have forced cells to stop replicating and turn into a resting (quiescent) or dying (senescent) state. This supports the third hypothesis; that the measured cells containing EdU have stopped replicating and that the observed increase is caused by the random sampling. This is supported by the low number of measured cells containing EdU. The average concentration was calculated from 11, 8 and 7 cells in the last three measurement sessions. There would be far between replicating cells containing EdU (a low probablility of measuring these cells). It is not unlikely that 30% of the cells were in a quiescent state and containing EdU, as the ratio of quiescent cells at the beginning of the experiment was found in figure 7.9 to be around 50 to 60%. This hypothesis implies that all the measurements after the washing contain quiescent cells with EdU, undermining the calculated replication time found from the decrease in EdU concentration after the washing.

**4. DNA from dissolved cells** The fourth hypothesis; that cells incorporate strings of DNA from dissolved cells, combines elements from the first and third hypotheses, explaining the increase with EdU coming from dead cells and the random sampling of measured cells. Pieces of DNA from dissolving cells would be too small to observe in the microscope. If incorporated into or attached to a measured cell, this external DNA could be the source of a Raman signal containing both EdU and DNA peaks. There would be no way to distinguish this signal from that of the cell's own DNA, and the measurement would not represent the measured cell. Similar to the first hypothesis, the delayed increase could be explained be the time it would

take to release the DNA.

**Testing some hypotheses** Figure 7.14 plots the expected increase in EdU concentration if EdU was released in the growth medium 22 hours after washing. Two concentrations are tested: The original EdU to thymidine ratio ($X_t$, red dotted line), and the concentration given by the average EdU to thymidine ratio in the DNA at the time of the washing (read off be $0.81X_t$, blue dotted line). The rings in the plot represent the cell replication time of 22 hours. The time of the reintroduction of EdU is chosen to give time for the dying cells to dissolve and release EdU, for simplicity set one full cell cycle after the washing.

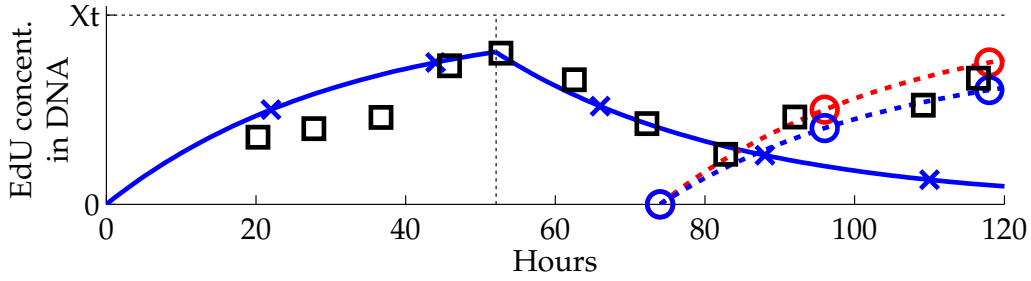


Figure 7.14: The increase of incorporated EdU the last 30 hours can be outlined by the release of an EdU concentration similar to that in the top point at 52 hours (blue) and similar to EdU conc. in medium (red) of EdU, 22 hours after the EdU is washed out.

The plot indicates that the calculated increases fit the shape of the experimental increase after 83 hours fairly well. Since the cells already contain EdU at this time, the calculations slightly underestimate the EdU concentration. However, the existing EdU would also lead to a slower uptake, making the estimations slightly overestimate the concentration. The two errors thus partially cancels out. More importantly, the plot shows that the amount of EdU necessary to give the observed increase in concentration is close to the original concentration. Neither the first nor the second hypothesis would provide sufficient EdU to explain the observed increase. This makes the third and the fourth hypothesis the most plausible explanations for the increase. However, as mentioned previously, further studies are necessary to say anything conclusive about the second increase in EdU concentration.

## 7.6 Conclusions

It has been shown in this chapter that EdU can be used as a Raman probe for proliferation measurements of non-adherent cells. The incorporation and dissipation of EdU in the DNA was followed for 118 hours: The first 52 hours in a growth medium containing EdU, after which the EdU was washed out. A steady increase in EdU concentration up to the time of washing and decrease in concentration up to hour 83 was found. The measured concentrations matched a cell replication time of 22 hours, which agree well with earlier observed replication times in that specific cell culture found under ideal proliferation conditions. In the literature, 32 hours and longer replication times are also reported, and cell counting in a hemocytometer gave a replication time of at least 36 hours. However, hemocytometer count is prone to include non-replicating cells, which are avoided in the first stages of the Raman measurements. (If cells containing EdU become quiescent or senescent, these would also be included in the Raman measurements.)

A Raman based proliferation assay would allow measurements on living cell cultures without the use of radioactive or fluorescent markers. Cells would remain alive after the measurements, and fast results would be provided. The presented results suggest that the Raman measurements could be a solid alternative to the established proliferation assays, but further investigations are required to better understand the proliferation process. First, less than half of the measured cells were found to incorporate EdU, and expected periods of increasing and decreasing ratios were not observed. Second, living conditions during the measurement sessions influenced cell proliferation, making interpretations of the results challenging. Finally, comparative fluorescent measurements were not successful, and could not confirm the results.

The low degree of EdU incorporation may have been due to the low sensitivity of Raman detection. However, the ratios of cells containing EdU were not larger in the fluorescent measurements, even though these measurements were done on very few cells. This indicates that a large portion of the cells were not replicating[19].

The fairly constant ratio of cells containing EdU after the EdU is washed indicates that actively proliferating cells might have become quiescent after the washing. This change in behavior could be caused by the living conditions during measurements.

[19] A single, independent fluorescent measurement session of 72 cells gave EdU uptake ratios of 72% after 20 hours, indicating that the uptake potentially could be larger.

A large decrease in the number of cells in the sample indicates that many cells struggled throughout the experiment. This could prolong the average cell cycle times of the replicating cells. However, based on the assumption that the best adopted cells survive, it is possible that the cells that managed to live in experimental conditions grew at the same rate as before.

If further studies were to be done on EdU incorporation and the use of Raman probes for proliferation assays, it would be recommended to have more frequent, but shorter measurement sessions. This could reveal the expected increase in the ratio of cells containing EdU at the start of the experiment. A second improvement that could be considered would be to extract cells from the cell culture flask for measurements and keep the cell culture in an incubator throughout the experiment. Both these methods would ensure a healthier cell culture and simplify interpretation of the results. An alternative would be to have more control samples, which got the exact same treatment as the EdU cell cultures. A third improvement could be achieved by designing the experiment for more efficient Raman techniques, like stimulated Raman scattering or coherent anti-Stokes Raman spectroscopy. However, such methods would lead to much more complex measurement procedures. Finally, a more thorough comparison between Raman and fluorescent measurements should be implemented to provide information on the efficiency of the Raman assay.

The ability to follow the proliferation of a cell culture over time with a minimum of interventions and with the option to leave the cells in the sample throughout the experiment could lead to a simple way of testing the proliferation of cells in different conditions. Using EdU as a Raman probe looks to be a promising technique to achieve this.

# Chapter 8

# Raman Spectroscopy on Waveguides

## 8.1 Introduction

Optical trapping on waveguides has since the mid-1990's been shown to be a high-precision, low-velocity transportation method for cells and microparticles [13, 98, 129, 130]. The technique uses the evanescent field to propel micrometer-sized particles on top of the waveguide, and thus controls the motion precisely without exposing the particle to high optical intensities. Sorting and assembly line-like transportation have been previously been demonstrated on waveguides, either using Y-branched waveguides or combined with microfluidics. [100, 131]. However, analysis of the trapped particles besides size or refractive index estimates, cannot be done by the waveguide trapping technique alone.

Raman spectroscopy gives detailed information on the identity and structure of objects under study. By combining Raman spectroscopy with waveguide trapping, a tool could be made for highly specific sorting of particles trapped on the waveguide. In addition, Raman analysis could provide information on structural changes caused by the evanescent field, for example deformations, or be used to study the effect waveguide surface coatings would have on trapped objects.

Different waveguide designs allow different trapping experiments. Straight waveguides work as conveyor belts, efficiently transporting several particles on the same path. A 'gap' design which trap particles in one place by the use of counterpropagating beams would be favorable for Raman spectroscopy, where long exposure

times may be necessary to collect enough signal. Both the gap and the straight waveguide designs have been used in this chapter.

This chapter presents methods and results from combined waveguide trapping – Raman spectroscopy setups, and give insight in the advantages, challenges, and limits of the combined techniques. The goal of the implementation has been to acquire Raman signals. However, more work is required to optimize the sensitivity of the setup. Both promising results and major challenges are found, encouraging further studies.

## 8.2 Experimental Setups and Equipment

This section begins with presenting the setups, including the waveguiding, microcope and spectrometer parts. This is followed by descriptions of the specific waveguide designs used in the experiments. The section is concluded with two brief parts on sample preparation and data treatment of the collected spectra.

### 8.2.1 Setups

Two different setups were used to acquire Raman signatures from particles optically trapped on top of the waveguide. One setup uses two different lasers for waveguide trapping and excitation. The experimental method using this setup is referred to as external Raman excitation. The other setup use the same laser for both waveguide trapping and excitation. The experimental method using this setup is referred to as internal Raman excitation. The use of each setup differs in regards to excitation power, acquisition time and waveguide design.

#### Setup for External Raman excitation

The external Raman excitation setup is shown in figure 8.1. The main purpose of this setup is analysis and characterization of microparticles propagating on a waveguide, potentially to be combined with sorting waveguide designs [131]. The setup uses two laser sources. Laser $L_1$ in the figure couples laser light into the waveguide, and laser $L_2$ excites Raman scattering. The use of two lasers gives independent control of microparticle propulsion and Raman excitation. Particularly,

an independent laser for excitation controls both the position of the acquisition and the excitation power. In addition, free-space optical trapping is possible. However, two laser sources comes with the cost of a larger setup and a more demanding setup alignment.

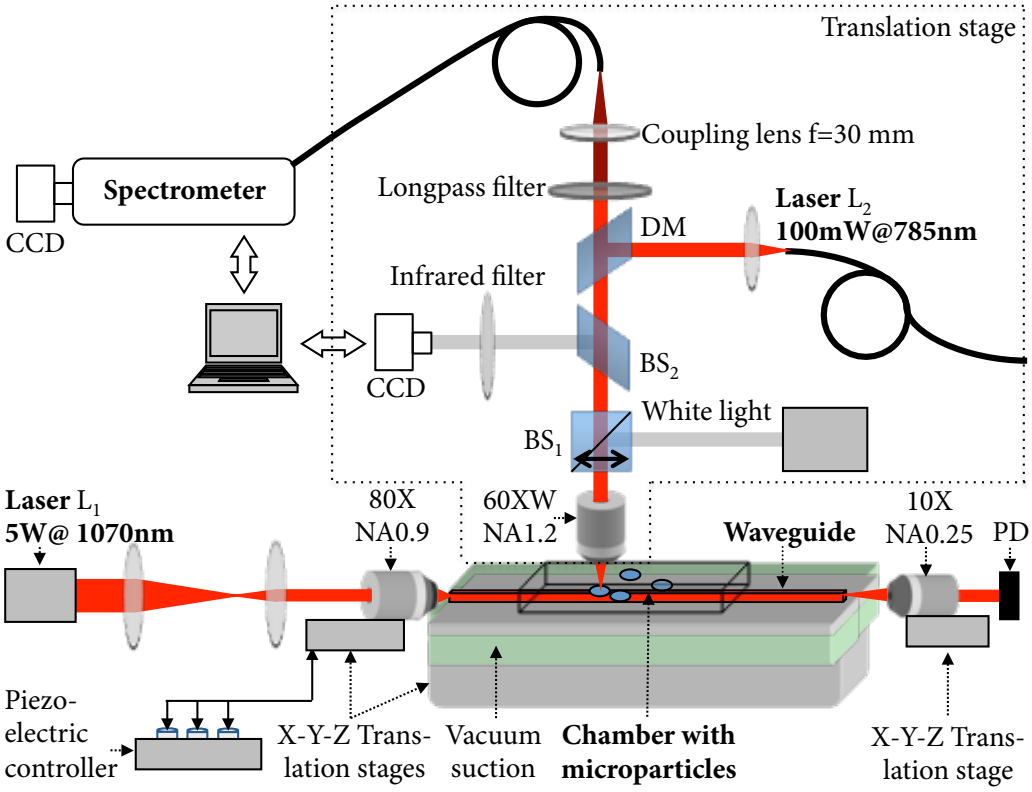


Figure 8.1: Setup for external Raman excitation. 1070 nm laser $L_1$ is coupled into a waveguide with a NA0.9 objective lens. The waveguide is imaged with a modified microscope (inside the dotted line). 785.8 nm laser $L_2$ is focused with a NA1.2 objective lens to excite scattering from particles on the surface. Scattered light is collected by the microscope, filtered, and sent to the spectrometer for analysis. A separate white light source and CCD camera is used to image the waveguide.

The setup consists of three parts, a waveguiding section, a microscope section, and a spectrometer. These parts are described separately in the following paragraphs.

**Waveguiding section** The waveguiding section controls the waveguide trapping and microparticle propagation, and is represented in figure 8.1 as all the elements underneath the 60X objective lens. The section consists of one laser source and three translation stages. The first translation stage after the laser is piezo-electrically controlled to optimize light coupling into the waveguide. The second translation stage holds the waveguide, which is held in place by a vacuum suction. A sample chamber is situated on top of the waveguide. The third translation stage holds an objective lens which collects the output light from the waveguide into a photodetector.

Light passes through the waveguiding section in the following order: The beam from laser $L_1$, a high-power 1070 nm fiber laser (table 8.1), passes a beam expander to match the entrance aperture of an IR coated objective lens (80X NA0.9, Nachet[1]). The lens couples the laser beam into the waveguide. Propagating in the waveguide, the evanescent field of the light interacts with microparticles in the sample chamber. Exiting the waveguide, the light is collected by an objective lens (10X NA0.25, Leitz[2]) for output power measurements. Due to risk of burning the waveguides, no more than 1.3 W of input laser power was used in the experiments.

**Microscope section** The microscope section controls Raman excitation and collection and imaging of the sample. This section is outlined by the dotted line in figure 8.1, and consists of a laser source, a white light source, a CCD camera and different optical elements. It is based on an upright Olympus microscope, modified by standard and custom made parts. The whole microscope section is placed on a computer controlled translation stage to allow movement independent of the waveguiding section and spectrometer.

Light passes through the microscope section in the following order: The beam from laser $L_2$, a fiber coupled 785.8 nm solid state laser (table 8.1), is collimated onto dichroic mirror DM. The mirror reflects the laser beam through beamsplitter $BS_2$ (pellicle 92/8) and beamsplitter cube $BS_1$. The beam is focuses onto the sample with a water immersion objective lens (60X NA1.2, Olympus). During excitation and collection, beamsplitter $BS_1$ is moved out of the beam path to minimize reflections. Light scattering from a particle in the sample is again collected by the water immersion lens. Collimated Stokes-shifted scattered light is allowed to pass through the pellicle beamsplitter, the dichroic mirror (17 dB@785 nm) and a long

[1] Paris, France
[2] Leica, Wetzlar, Germany

pass filter (60 dB>792.9 nm). The remaining light is coupled into a multimode fiber (NA=0.275, Thorlabs[3]) by a NIR coated lens (f=30 mm) and sent to the spectrometer.

The white light source is used for sample illumination. The light enters the sample through a removable beamsplitter cube ($BS_1$). A 92/8 pellicle beamsplitter ($BS_2$) reflects collected light to a CCD camera connected to a computer. The white light source is turned off and the beamsplitter cube $BS_1$ is moved out of the light path during excitation and collection of Raman signals. Thus, no sample images can be acquired at those times.

**Spectrometer** The fiber coupled light is sent to an imaging spectrometer (Triax320, 320 mm focal length[4]). The spectrometer uses a 900 lines/mm grating with 850 nm blaze angle, giving 2 $cm^{-1}$ resolution at 800 nm with a water-cooled, high-resolution CCD camera (Newton DU940N-UV[5]) with quantum efficiency between 0.2 and 0.5.

### Setup for Internal Raman excitation

The internal Raman excitation setup is shown in figure 8.2. The main purpose of this setup is to integrate transportation and analysis in a smaller apparatus with simpler alignment, potentially developing into an on-chip device. This is well suited for analysis of particles propagating on a waveguide with a loop and gap design, as the setup uses the waveguide light for Raman excitation. Alignment of a second laser in not necessary, but signal strength is limited by propagation losses in the waveguide and background signal from the waveguide. The instrumentation is similar to the setup used for external excitation, with the exception of laser source and objective lenses.

**Instrumentation** In the setup, excitation and propagation are both done with a high power tunable laser (table 8.1) set to $\simeq$ 785 nm, combined with a 60 dB laser line filter (3 nm FWHM, Semrock[6]). The beam is sent directly through a coupling

[3]Newton NJ, USA
[4]Jobin Yvon, Horiba, Kyoto, Japan
[5]Andor Technology, Belfast, UK
[6]Rochester NJ, USA

objective lens, and scattered light is collected from an imaging objective lens. Due to risk of waveguide burning damage, no more than 0.5 W of laser power was used in the experiments.

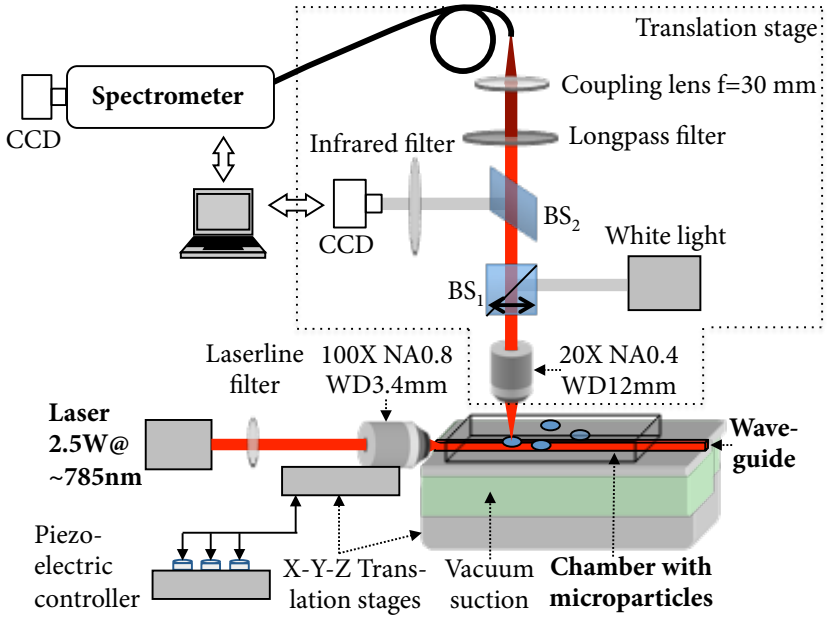


Figure 8.2: Setup for internal Raman excitation. A tunable laser set to 785 nm is coupled into a waveguide with a long working distance objective lens. The guided light is used for Raman excitation. The waveguide is imaged with a modified microscope (inside the dotted line). Scattered light is collected by the microscope, filtered, and sent to the spectrometer for analysis. A separate white light source and CCD camera is used to image the waveguide.

Coupling and propagation losses (see section 2.4.2) in the waveguides make it necessary to collect the scattered light close to the waveguide input. Thus, there is less space for the high NA objective lenses used for waveguide coupling and signal collection. To make room for both lenses, the objective lens for waveguide input coupling is changed to an IR coated long working distance 100X objective lens (NA0.8 WD3.4 mm, Olympus), and the objective lens for signal collection is changed to a long working distance 20X objective lens (NA0.4 WD12 mm, Olympus). The lower NA of the new lenses decrease both coupling efficiency and signal collection compared to the external Raman excitation setup.

Due to lower coupling efficiency and stronger propagation losses (narrower waveguides are used), no output light could be measured for this setup. Thus, in these

experiments, no collection lens was necessary at the waveguide output.

Table 8.1: Lasers used in experiments. Manufacturer data.

| Use | Type | Wavelength (nm) | Power (W) | Line width (nm) | $M^2$ | Manufacturer |
|---|---|---|---|---|---|---|
| Propagation | Ytterbium fiber | 1070 | 0.3-5 | - | <1.1 | IPG Photonics[7] |
| Excitation | Solid state | 785.8 | 0.1 | $<10^{-4}$ | <1.2 | CrystaLaser |
| Propagation & excitation | Diode, tunable (Littman/Metcalf) | 770-798.7 | 0.3-2.5 | $<10^{-4}$ | <1.7 | Sacher Lasertechnik[8] |

### 8.2.2 Waveguide Designs

In the experiments, two waveguide designs are employed, straight waveguides and waveguides ending in a loop. At the far end of the loop design, an opening, or gap, is incorporated, as seen in figure 8.3. Thus, all the light in the waveguide diverges from the ends of the loop into the gap. All waveguides are strip waveguides, with a rectangular core of tantalum pentoxide on a silica substrate. The waveguide dimensions range from 165 to 200 nm in thickness and 1 to 10 μm in width. Some waveguides also have a top cladding of silica. The waveguides were produced as described in chapter 2.

**Straight waveguide** The experiments using straight waveguides use the power of the evanescent field in the cover medium either to propagate microparticles or to excite Raman scattering in microparticles. When the waveguide was used for propagation, a 7 μm wide and 200 nm thick waveguide was used, and an external 785 nm laser was used for excitation. When the waveguide was used for Raman excitation, a 1 μm wide and 185 nm thick waveguide was used, and the microparticles were not propagating, but rested motionless on top of the waveguide.

**Waveguide loop with gap** The waveguides incorporating a loop with gap were used to propel microparticles to the gap. The use of the gap design allows transport

[7] Oxford MA, USA
[8] Marburg, Germany

on top of the waveguide to a predefined and small region with a strong light intensity. At the same time, stable trapping in the gap allow long Raman acquisitions. When the particle reaches the gap from one of the two ends, the two diverging fields stably trap the particle in the gap. At this position, two methods are possible for Raman excitation. Either an external laser can be used, exciting the particle from the collection objective lens. Or the diverging fields can be used, exciting the particle from the waveguide. By using the diverging waveguide light, only one laser source is required for the experiment. When the waveguide light is used for excitation on the straight waveguide, only the evanescent field is contributing to the scattering. Much higher intensities are available when the diverging waveguide light in the gap is used for excitation. As the gap experiments were performed with an objective lens with long working distance and low NA, the results from these experiments should be considered as preliminary, or proofs of concept. A study of waveguide trapping in waveguide loops have been performed by Ahluwalia et al. [1]

In the gap experiments, 1 μm wide and 185 nm thick waveguides were used, with a loop diameter of 100 μm and gap length of 2 or 10 μm. A sketch of the gap design is shown in figure 8.3 and figure 8.4 shows a scanning electron microscope micrograph of a 2 μm long gap. Figure 8.5 shows a plot from [1] where scattering of the field in a 2 μm gap has been simulated. The divergence close to the waveguide ends is very strong, as expected.

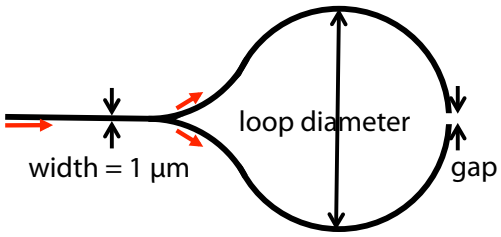


Figure 8.3: Illustration of gap design.

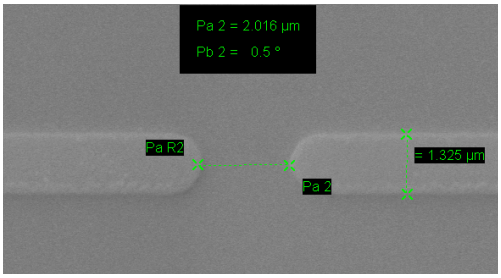


Figure 8.4: Scanning Electron Microscope micrograph of 2 μm gap.

The exact origin of the trapping force in the gap is not obvious. Three explanations can be given. Either the gradient force from the diverging fields is stronger than the scattering force (see chapter 2 for an introduction to optical forces), trapping the particle at one of the waveguide ends. Or the particle is trapped at the center of the gap, held in place by the two diverging fields' equal and opposite scattering forces, similar to the counter-propagating beam optical trap [132]. Or the opposite

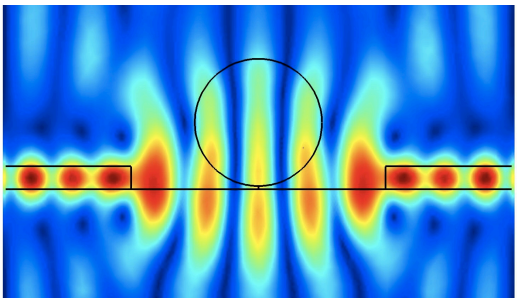

Figure 8.5: Cross section across a 2 μm gap showing simulation results of a 1070 nm wavelength optical field propagating and scattering on a 1 μm polystyrene sphere. Plot from Ahluwalia et al. [1].

fields in the gap region interfere, creating an intensity pattern with several optical gradients which may trap particles. In the experiments, trapping occurs either at the end of a waveguide or centered in the gap, supporting the two first explanations. The simulations of Ahluwalia et al. [1] support the last explanation for 2 μm wide gaps, showing interference patterns in the gap at positions supported by experimental observations.

#### Cladded waveguides

Cladded waveguides were used for some internal excitation experiments. These waveguides are covered with a 0.5 to 1 μm thick layer of silica to decrease the waveguide-surface index contrast, and thereby also the propagation losses (by confining the field more inside the waveguide) and scattering losses (by decreasing the refractive index contrast and by preventing dirt from aggregating on the waveguide surface). No evanescent field reaches above the cladding. This means than the waveguide trapping must be done in uncladded regions of the waveguide. In the waveguide gap designs, the cladding is removed in a small region close to the gap (see figure 8.15 in section 8.3.2).

### 8.2.3 Sample Preparation

For both internal and external excitations, Raman spectra were acquired from microspheres trapped or placed on top of the waveguides or in the gaps. The micro-

spheres were polystyrene particles (n=1.59) from Duke Scientific[9] [133] and Bangs Laboratories[10] [134]), and borosilicate glass[11] particles (n=1.56) from Duke Scientific.

The waveguide trapping experiments were performed in a dilute solution of microspheres in water. Two different sample chambers were used, a Gene Frame well (25 μL, 250 μm thick, ABGene[12]), and a PDMS well (1 to 2 mm thick). The wells were completely filled and covered with a cover slip. The thin Gene Frame well was used for experiments with the 60X water immersion objective lens, while the PDMS wells were used for experiments with the 20X long working distance objective lens.

Experiments that did not involve optical trapping were done with dry microspheres (no solution) or without microspheres (acquiring signal from the liquid in the well). The microspheres were placed on the waveguide either by applying a solution with quickly evaporating ethanol, or by moving the spheres manually to the desired position with a cotton swab. None of these methods gave precise control of the microsphere placement, but the large number of waveguides on a slab and the large number of particles gave sufficient positioning to allow experiments on a few waveguides on the chip.

## 8.3 Experimental Procedures and Results

Using the two setups and the two waveguide designs, five different experiments were conducted. Excitation power and background contribution determined the specific experimental method used in each experiment. The experiments demonstrated particle characterization on the waveguide, and signals were acquired for all configurations. The signal strengths differ strongly between the experimental methods, but are in general weak. For the case of a polystyrene sphere internally excited in the gap, the signal is close to nonexistent. The results from all configurations are presented to give an idea of the sensitivity limits of the current setups.

[9] Thermo Fisher Scientific, Waltham MA, USA

[10] Bangs Laboratories, Fishers IN, USA

[11] Duke Scientific specifies the typical composition of these to be 52.5% silica, 22.5% calcium oxide, 14.5% aluminum oxide, 8.6% boron oxide, 0.3% sodium oxide, 0.2% potassium oxide, and 0.2% iron oxide.

[12] Thermo Fisher Scientific, Waltham MA, USA

After a brief paragraph describing the numerical procedures performed on the spectra, the experimental procedures and acquired spectra are presented in sections 8.3.1 and 8.3.2. Section 8.3.1 covers the experiments done using an external laser for Raman excitation on straight and loop waveguides. Section 8.3.2 covers the experiments done using guided light for Raman excitation on straight and loop waveguides. Unless otherwise stated, all images of the experiments are acquired through a 60X magnification objective lens.

**Data treatment** All the spectral data presented in this chapter have been digitally smoothed with a 2-point median filter and a 3-point average filter. Spectra from the internal excitation experiments needed more elaborate optimization due to strong background signal from the waveguide and the cladding. As such, they are shown as averages of several spectra, where a smoothed and scaled background has been subtracted. Since the backgrounds strongly dominate these spectra, the scaling of the background was done such that the areas of the background and target spectra within some spectral region were equal before subtraction.

### 8.3.1 External Raman Excitation

The strongest Raman signatures were acquired in the experiments using an external laser for excitation. Efficient particle characterization were demonstrated on both straight waveguides and waveguides with a loop and gap design.

**Spectra from particles propagating on a straight waveguide** The first experiments were done with straight waveguides, where Raman spectra were acquired from microspheres on the waveguide surface. The procedure was as follows: The 1070 nm laser was used to propel 7 μm diameter polystyrene spheres and 8 μm diameter borosilicate glass spheres on top of a 7 μm wide waveguide, as shown in figures 8.6. The 785 nm laser was focused with the high NA objective lens on a point a few micrometers above the waveguide surface. When a sphere propelling on the waveguide reaches the position of the focus, it is optically trapped and held in place by the focus, as shown in figure 8.7. Scattered light was collected from the trapped sphere for 1 second and sent to the spectrometer. After a spectrum was acquired, the external laser was blocked to release the sphere. The sphere continued to propel along the waveguide, and a new sphere was trapped and analyzed. Figure

8.8 shows a time series of the two polystyrene and one borosilicate glass spheres from figure 8.6 being trapped, analyzed, and released.

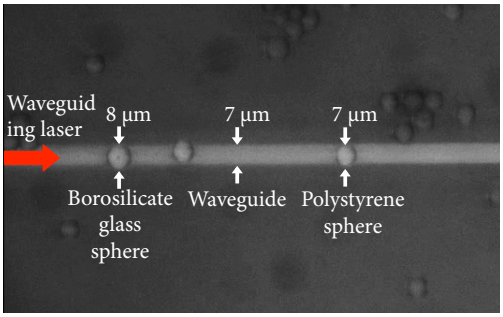


Figure 8.6: Overview of the straight waveguide experiment. Different microspheres are being propelled along the waveguide by the evanescent field toward the external laser focus spot.

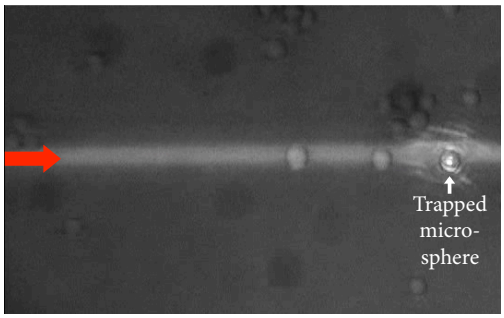


Figure 8.7: External laser trapping. When a microsphere reaches the laser focus spot, it is trapped in place, and spectral data can be collected. The external laser excites the scattering.

The spectra acquired from spheres $P_1$ and $B$ in figure 8.8 are shown in figure 8.9. Plot a) represent the 7 µm diameter polystyrene sphere and plot b) represents the 8 µm diameter borosilicate glass sphere. Three Raman peaks can be distinguished in the polystyrene sphere spectrum; 621 $cm^{-1}$ (benzene ring deformation), 1001 $cm^{-1}$ (benzene ring breathing), and 1031 $cm^{-1}$ (CH in-plane bending). The strong peak in the spectra at 520 $cm^{-1}$ comes from silicon, the substrate base material. Other spectral background contribution comes from the waveguide substrate, vitreous silica ($SiO_2$) and the waveguide, Tantalum pentoxide ($Ta_2O_5$).

To be able to visually distinguish borosilicate glass spheres from polystyrene spheres, the chosen glass spheres were slightly larger. This makes it possible to single out glass spheres by their size and propagation velocity. The spectrum in b) confirms the visual observation, with no visible peaks in the Raman active region of polystyrene.

**Spectra from particles trapped in a waveguide gap** The second set of experiments was done on waveguides with a loop and gap design, where Raman spectra were acquired from microspheres optically trapped in the gap. The procedure was as follows: A 2 µm diameter polystyrene sphere was propelled by the 1070 nm laser along the 1 µm wide loop waveguide into the gap. In the gap, the sphere was trapped by the light diverging from the waveguide ends. The 785 nm laser was

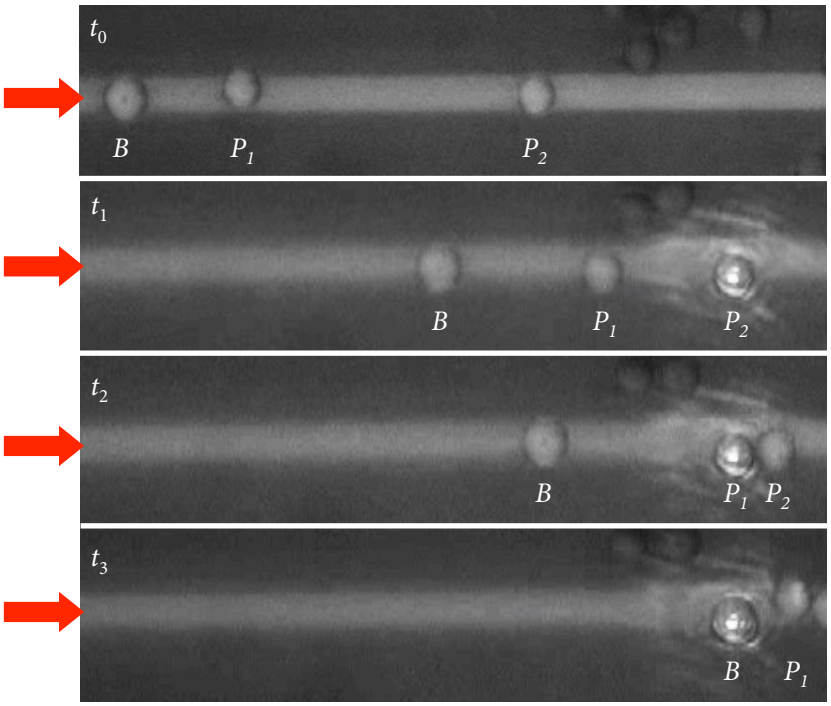


Figure 8.8: Using the Gaussian beam to trap and release microspheres propagating on the waveguide. Micrographs of the borosilicate glass sphere $B$ and polystyrene spheres $P_1$ and $P_2$ are acquired at four points in time, separated by between three and five seconds. In the first picture ($t_0$) (the same as in figure 8.6), the external laser is blocked, and the spheres are being propelled to the right. In the second picture ($t_1$) (the same as in figure 8.7), the $P_2$ sphere is trapped by the external laser while spheres $B$ and $P_1$ still are propagating. The two last pictures ($t_2$ and $t_3$) similarly show the trapping of spheres $B$ and $P_1$. A one second Raman spectrum was collected from each of the trapped spheres.

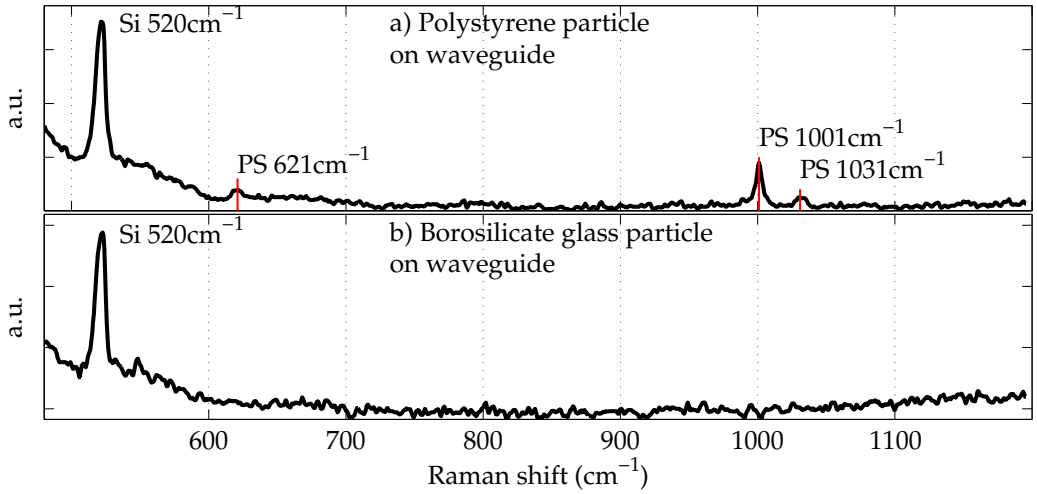


Figure 8.9: Spectra from external excitation, 1 second acquisition. Experiments are done on a straight waveguide with a) a 7 μm diameter polystyrene microsphere. b) an 8 μm diameter borosilicate glass microsphere.

then focused with the high NA objective lens at the trapped sphere to excite Raman scattering[13]. During excitation, the 785 nm laser traps the sphere, as its trapping power is much stronger than the diverging light's. Figures 8.10 and 8.11 show an overview of the gap region and the scattering from a trapped sphere, respectively. Scattered light was collected from the trapped sphere for 2 seconds and sent to the spectrometer. After a spectrum was acquired, both the external laser and guided laser were blocked, letting the microsphere diffuse away. When the guided light was turned on again, a new microsphere is propelled into the gap for new analysis. Spheres larger than 2 μm could not be successfully trapped and propelled along the waveguide, due to the power of the guided light being too low close to the gap.

Figure 8.12 shows a spectrum acquired from a 2 μm diameter polystyrene particle trapped in a 2 μm gap. The spectrum have been smoothed with a 2-point median filter. Plot a) shows the spectrum at full scale, while plot b) shows the same spectrum using the axes from figure 8.9 a) for signal strength comparisons. Three dotted lines are drawn at equal heights in a) and b) to show the range of the scaling.

[13]The1070 nm laser also scatters light, but the sensitivity of the CCD camera in the spectrometer is very small in this wavelength range, and no light in this wavelength range contributes to the spectrum.

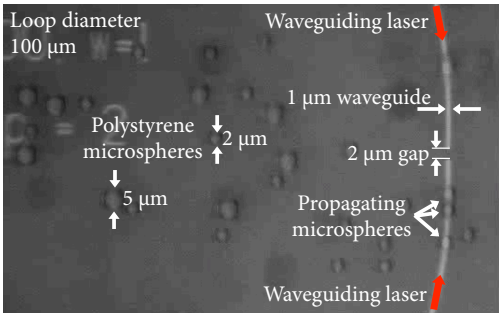


Figure 8.10: Overview of the waveguide gap experiment. 2 µm diameter microspheres are trapped and propelled along the waveguide into the gap. 5 µm diameter microspheres could not be propelled on the waveguide.

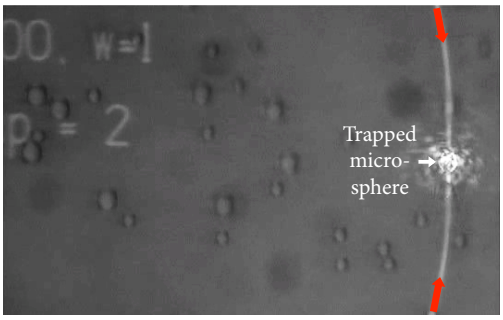


Figure 8.11: Excitation in the gap. When the 2 µm diameter microsphere is trapped in the gap, an external laser is focused on the sphere to excite Raman scattering.

The Raman signal from the 2 µm sphere decrease compared with the 7 µm sphere in the straight waveguide experiment. Increasing signal by increasing the acquisition time to 2 seconds also increase the background levels in the spectrum. In addition, more scattered light is collected from regions outside the polystyrene sphere, due to the sphere's smaller size.

### 8.3.2 Internal Raman Excitation

The light propagating in the waveguide was used to excite Raman scattering from microspheres in the setup for internal Raman excitation. To collect signals in the wavelength region where the spectrometer CCD camera is sensitive, the wavelength in the waveguide was changed from 1070 nm to 785 nm. Two means of excitation are possible, exciting with the evanescent field on the waveguide surface and exciting with the guided light from the gap.

Compared to the 1070 nm laser, the tunable 785 nm laser has lower available power, higher coupling losses, and a mode distribution with a slightly smaller evanescent field for the same waveguide dimensions. This prevented efficient trapping both on the waveguide and in the gap, and also decreased the intensity of the excitation light. As mentioned in section 8.2.1, the higher losses meant that Raman excitation had to be done closer to the input facet of the waveguide. This again meant that

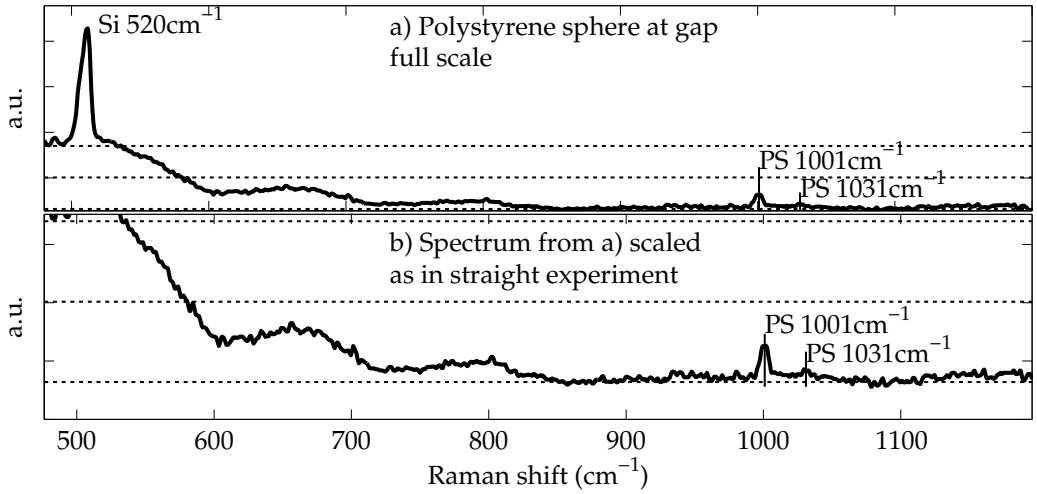


Figure 8.12: Spectrum from external excitation, 2 seconds acquisition. Experiments are done with the waveguide gap design with a 2 μm diameter polystyrene microsphere. a) shows the spectrum at full scale. b) shows the same spectrum with similar axes as figure 8.9 a). The three dotted lines in each figure are inserted for comparison of signal level in a) and b).

a long working objective lens had to be used. This lens' NA of 0.4 decreased the collection efficiency of the microscope. The procedures of the external excitation experiments thus had to be modified. The following sections describe the experimental changes and the reason for the changes. They also present the acquired spectra, such that the results from the two setups easily can be compared.

**Evanescent field excitation** Strong scattering from microspheres on 1 μm wide waveguides suggested that Raman signal could be acquired by collecting the scattered evanescent field. The low power of the evanescent field intensity meant that long acquisition times were required. Thus, the scattering particles needed to stay still, and not be propelled by the waveguide. This was achieved by not exciting microspheres in solution, but instead use dry microspheres.

Exciting with the evanescent field yields very low intensities, requiring as large as possible evanescent field strength. As the waveguides used for waveguide trapping are developed to maximize the evanescent field, they are clearly the most suitable waveguides also for this purpose. To optimize the intensity from the evanescent

field, narrow, 1 μm wide waveguides were used.

Low scattering intensity from the evanescent field and lower NA objective lens in the microscope decreased the acquired Raman signal. This was compensated by implementing three changes to the sample. First, a cluster of 3 μm diameter polystyrene was used instead of single particles to increase the excitation and collection volume of the Raman scattering from polystyrene. Second, a 1 μm wide waveguide was used instead of the 7 μm wide waveguide to maximize scattering from the evanescent field. Third, the cluster was placed close ($\simeq$2 mm) to the input facet to minimize propagation losses in the waveguide. In addition, the particles were at rest, so much longer acquisition times could be used. Figure 8.14 shows scattering of the evanescent field from a cluster of polystyrene spheres.

Light scattered from a small group of spheres was collected for 60 seconds using an excitation wavelength of 784.2 nm. Spectra from two slightly different positions are shown in figure 8.13. The total amount of scattered light is different at the two positions, probably due to the random topology of the cluster. Plot a) shows the strong background contribution. Plot b) is found by subtracting a separate and normalized background spectrum from the average of the two spectra in a). A pure polystyrene spectrum, scaled to the evanescent spectrum peak at 1001 $cm^{-1}$, is included in b), making a good fit with the spectrum from the evanescent field excitation. The experiment was repeated with waveguides wider than 1 μm without showing any improvement in signal strength. This was probably due to the smaller power of the evanescent field for larger waveguide cores.

**Gap excitation** The guided light diverging into the gap should be more powerful than the evanescent field, and should be able to excite Raman scattering from an object situated in the gap. However, Raman scattering from the core, substrate and cladding would accumulate throughout the waveguide before reaching the gap, thus yielding a strong background signal.

The strong propagation losses in the 1 μm wide waveguides and the available power from the tunable 785 nm meant no microspheres could be propelled further than 5 mm from the input facet of the waveguides by the evanescent field. However, the smallest distances from the input facet to a gap for the available waveguides were between 6 and 10 mm. Thus, no microspheres could be propelled into the gap. This meant excitation had to be done on a substance already present in the gap. Two options were possible. Either a microsphere could be brought to the

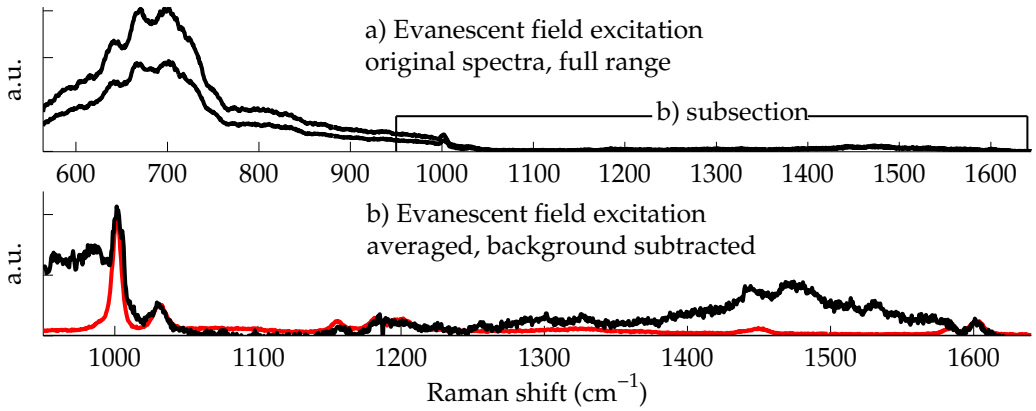


Figure 8.13: Spectra acquired from evanescent field excitation of a 3 µm diameter polystyrene particle cluster. a) Two original spectra b) A subsection of the averaged spectra from a) with background subtracted and a scaled pure polystyrene spectrum laid over.

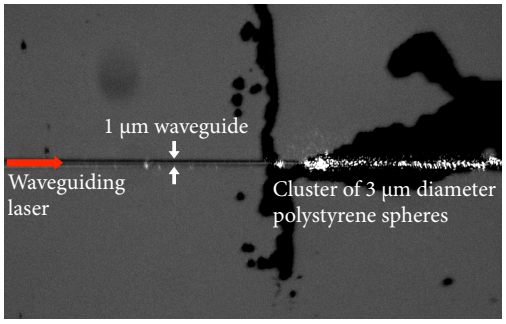


Figure 8.14: Overview of evanescent field excitation. A cluster of 3 µm diameter polystyrene spheres are placed on the waveguide close to the input. Imaged with a 20X objective lens.

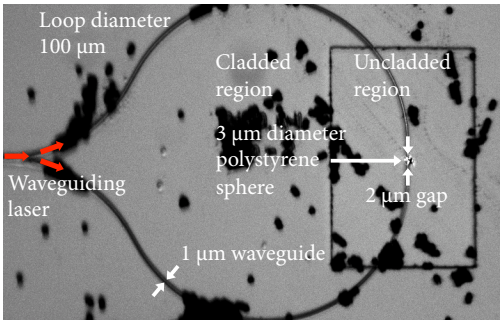


Figure 8.15: Overview of gap excitation. A 3 µm diameter polystyrene sphere is placed in the 2 µm gap in an uncladded region of the waveguide. Imaged with a 20X objective lens.

gap position manually, or a Raman active liquid in the gap could be excited. Both options were tested.

***Liquid ethanol*** Ethanol is a strong Raman scatterer. By covering a 10 μm wide gap with ethanol, all of the diverging light excited Raman scattering, and the the objective lens collected Raman scattering from the whole focal spot volume ('collection volume'). However, the scattering cross section in the direction of the objective lens' NA was small. To reduce propagation losses, a cladded waveguide with an uncladded region near the gap, similar to the waveguide seen in figure 8.15, was used.

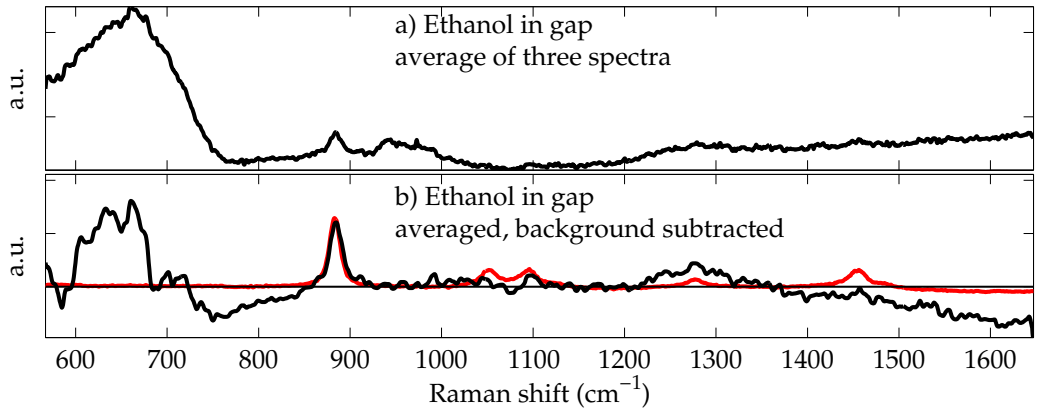


Figure 8.16: Spectra from ethanol excited at a 10 μm long gap. a) Average of spectra from three 60 seconds acquisitions. b) The average spectrum from a) where the background is subtracted. Superimposed is a scaled pure ethanol spectrum (red).

Light diverging into the gap with an excitation wavelength of 784.2 nm was acquired for 60 seconds for each spectrum. Figure 8.16 a) shows an average of three spectra collected from a liquid ethanol sample at the gap. 8.16 b) shows the spectrum from plot a) where a background acquired with a liquid water sample has been subtracted. A pure ethanol spectrum, scaled to fit the peak height at 890 cm$^{-1}$, is superimposed on the graph. The ethanol Raman signature from the experiment is recognizable from the strong peak at 890 cm$^{-1}$.

***Polystyrene particle*** A cotton swab was used to manually place a 3 μm diameter polystyrene sphere in a 2 μm gap, as seen in figure 8.15. To reduce propagation

losses, a cladded waveguide with an uncladded region near the gap was used. Since no trapping takes place, the sphere is not pulled to the highest-intensity region of the field. Thus, the scattering is weaker than it would be for a trapped sphere.

Figure 8.17 shows several spectra collected from the sphere with acquisition times of 30 seconds using an excitation wavelength of 784.5 nm. Plot a) shows the spectra to be completely dominated by the background signal. In plot b), all the spectra have been normalized in a subsection between 800 and 1300 $cm^{-1}$. The resulting spectra shows a slight bump in the ridge close to 1000 $cm^{-1}$, hinting of a polystyrene signal. 8.17 c) shows the resulting spectrum when a background signal, scaled to the level of a normalized subspectrum, has been subtracted from the average of several spectra. A peak at 1001 $cm^{-1}$ can be seen with a peak comparable to the standard deviation of the noise. Thus, no firm conclusion can be made regarding the validity of a polystyrene peak.

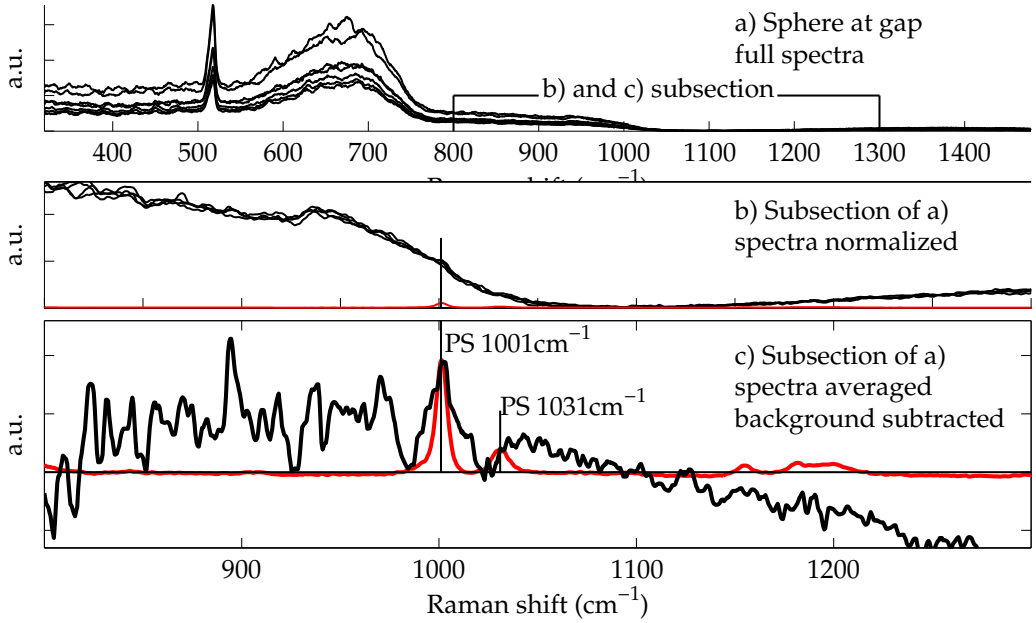


Figure 8.17: Spectra from a 3 μm diameter polystyrene particle excited in a 2 μm gap. a) Original spectra are dominated by background. b) A subsection of plot a) with normalized spectra. c) By averaging the spectra from plot b) and subtracting the background, a small peak at noise level shows up. A red, pure polystyrene spectrum, scaled to fit the peak at 1001 $cm^{-1}$ in plot c) is superimposed in plots b) and c).

## 8.4 Discussion

The experiments described in the previous section show Raman spectroscopy to be a possible technique for characterization of microparticles trapped on and propelling along an optical waveguide. Waveguide trapping and Raman spectroscopy work well in combination, as both techniques are highly specific, handling the microparticles one at a time. Also, since the long acquisition times of Raman scattering match the slow speed of the particles on the waveguide, none of the techniques are slowed down by the other.

Compared to pure Raman acquisition setups, the collection efficiency of the presented setups can potentially be increased substantially. Due to this, strong Raman scatterers with clearly distinguishable peaks have been used in the experiments. For weaker Raman scatterers, like red blood cells, more efficient Raman collection and reduction of background signal are necessary for proper characterization. This would also be the case for faster characterization of the strong scatterers.

In the following sections, the acquired spectra and the setups' influence on the spectra are discussed. First, this is considered in light of how the waveguide affect the results. Then, the results from each experimental configuration are examined. Finally, improvements of the setups are suggested.

### 8.4.1 Waveguide Considerations

Raman spectra are preferably acquired in regions with minimal background signal. By acquiring spectra from particles on a waveguide surface, the influence of the waveguide should be considered. This is of course even more important when Raman scattering is excited with guided light. Some considerations are described in the following paragraphs.

#### Spectral background

Exciting and collecting spectra close to the waveguide surface increases the background levels and reduces the signal-to-noise ratio of the desired Raman signal. The spectral contribution from the waveguide and the substrate contribute to varying extent to all the acquired spectra.

When the acquisition time increases due to low Raman scattering from the target, the spectral signature of the waveguide begins to dominate. Figure 8.18 shows the average of two spectra collected from the output of a 1.8 cm long tantalum pentoxide waveguide with a 40X objective lens and an acquisition time of 120 seconds.

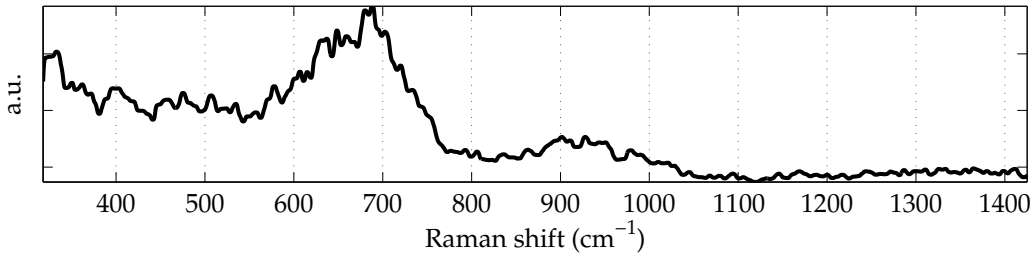


Figure 8.18: Raman spectrum collected from the output of a $Ta_2O_5$ waveguide. Average of two signals with 120 s acquisition times. and a 40X objective lens used for collection.

The wide peak between 600 and 700 cm$^{-1}$ and the small ridge between 800 and 1000 cm$^{-1}$ in the background spectrum can be recognized in all the acquired spectra. The silicon peak at 520 cm$^{-1}$, which is prominent in the experimental spectra, cannot be seen. The signal was collected directly from the waveguide and not from the substrate. This suggests that the substrate and the waveguide contribute independently to the spectral background, and that much of the collected light originate from the substrate. This should be especially prominent for external excitations. It is possible that trapped microspheres act as a lens, focusing light in the waveguide and substrate regions, generating strong Raman scattering there.

The waveguide contribution from figure 8.18 is least in the external excitation setup spectra (figures 8.9 and 8.12), as the acquisition times are short and the excitation light is focused on the polystyrene sphere. The spectral waveguide contribution is stronger in the spectra which are internally excited from the gap (figures 8.16 and 8.17). This is to be expected, as the acquisition times are long and Raman signal has accumulated throughout the waveguide. A strong contribution is also found when the evanescent field is used for excitation (figure 8.13). This either suggests that the evanescent field accumulates Raman signal from the waveguide core, or it suggests that the excitation is done by light from the waveguide core due to scattering. Further studies are required to reach any conclusion as to whether the evanescent field accumulate Raman signal from the core or not.

By acquiring background spectra, much of the spectral contribution from these regions can be subtracted from the microsphere spectrum. As the scattering properties change when a particle is introduced, it is necessary to normalize the background before subtraction. Normalizations are based on a unique Raman peak in the background spectrum to make the subtraction process less dependent on the increased scattering from the sphere.

#### Interface reflections

There is one small advantage of collecting spectral data close to the waveguide: Reflection from the waveguide and substrate surfaces. Some of the downward-scattered excitation light reflect into the microscope, and increase the collection efficiency in the experiment. At 785 nm, the reflectivities at normal incidence are 19% for silicon-silica[14], 0.5% for silica-water, 5.04% for water-tantalum pentoxide, and 3.78% for tantalum pentoxide-silica. This suggests that a noticeable part of the downward-scattered light is reflected back from the silicon-silica surface.

### 8.4.2 External Raman Excitation

The experiments where an external laser is used for Raman excitation gave stronger Raman signatures. This is mostly due to stronger excitation intensity (around 50 mW of the laser light is focused by the objective lens), but may also be caused by the larger polystyrene microspheres, which leads to a higher signal-to-background ratio and allows shorter spectrum acquisition times. Power and position of the excitation laser are well controlled in these experiments, all in all being the most successful way of combining waveguide trapping with Raman spectroscopy.

#### Straight waveguide

Spectral characterization and differentiation of the borosilicate glass and polystyrene microspheres propelling along the waveguide was shown in the straight waveguide experiment. Short acquisition times were used such that interruption of the flow of the propelling particles was avoided. The propulsion speed on the waveguide can be adjusted with the input guided light power. This means the characterization

[14]Reflectivity for silicon found from [10], page 757, using $n_{\mathrm{Si}}$=3.691+0.005$j$.

procedure can be timed such that the acquisition times match the particle velocities. As the gradient forces are stronger than the propulsion forces, the particles do not diffuse away at lower input powers. Thus, also longer acquisition times would be possible. Also, if the sensitivity of the setup was increased, shorter acquisition times would allow faster particle propulsion, speeding up the characterization process.

Differentiation of microspheres can also be possible by comparing propulsion velocities. For the same sphere size, higher index spheres would travel faster along the waveguide. However, particle accumulation and waveguide losses would make this an unreliable characterization method.

#### Waveguide with loop and gap

Much weaker Raman signals were collected from the 2 μm diameter polystyrene microspheres trapped in the gap. If the waveguide width was increased to 2 or 3 μm, larger particles, with larger scattering cross sections, could probably have been propelled into the gap. This would allow external excitation with the same efficiency as the straight waveguide experiment. The advantage of the gap is the possibility to keep the microsphere at rest, allowing longer acquisition times. In this sense, the gap design is probably better fitted for internal excitation experiments.

### 8.4.3 Internal Raman Excitation

Recognizable Raman signatures were acquired with evanescent field excitation and waveguide gap excitation. However, lower light intensity, lower collection efficiency, and smaller microspheres decreased signal-to-background ratios significantly compared to the experiments with a focused external excitation beam.

High coupling and propagation losses were the underlying reasons for the weak Raman signals. Propagation losses would decrease significantly, perhaps by more than 20 dB, by using waveguides wider than 1 μm (confer table 2.2 in chapter 2). Wider waveguides would both allow waveguide trapping on the loop design with a 785 nm laser, and increase the light intensity in the gap. In addition, improving the quality of the mode of the 785 nm laser could increase waveguide coupling by up to 10 dB comparing to the 1070 nm laser according to table 2.2. The mentioned changes would increase trapping ability, and possibly make room for the NA1.2

water immersion lens, which collects around 7 times more light than the NA0.4 long working distance objective lens.

The signal-to-background ratio could also be improved by reducing the background contribution. The background could be reduced or spectrally shifted by changing waveguide materials. However, the materials used in these waveguides are not especially strong Raman scatterer, so the gain would not be significant. Increasing excitation intensity or collection efficiency would be a more efficient improvement.

### Evanescent field excitation

A distinct polystyrene Raman signature was acquired from the cluster of particles excited by the evanescent field when the background signal had been subtracted. The long acquisition time and need of a group of scatterers limit practical applications of this technique. It is however interesting to see that the evanescent field can be used for Raman excitation. As an extension of this experiment, it is intriguing to see whether gold or silver colloids applied on a small section of the waveguide can act as localized plasmons excited by the waveguide field. If this was possible, surface enhanced Raman spectroscopy (SERS) which increase Raman signal manyfold, could be an option.

### Waveguide gap

The low intensity of the light diverging into the gap made Raman excitation in the gap challenging. The acquired liquid ethanol signature shows that Raman signal from microparticles is possible if the excitation and collection is optimized. Unfortunately, all waveguides with loops and gaps available for the experiments were 1 μm wide, so experiments with larger intensities (less losses) could not be performed. As the light scattering onto a sphere is diverging, the intensity decrease with the sphere's distance from the gap. This means that the positioning of the sphere is essential for Raman signal optimization. For further investigations of waveguide gap Raman excitation, waveguides with different dimensions are necessary. Ideally, a tapered waveguide should be used, 8 μm wide at the input to decrease coupling losses, and 2-3 μm wide throughout the loop to decrease propagation losses while not decreasing the mode intensity too much.

Further investigations of the gap design could introduce specific geometry adjustments or surface treatments. For example, barriers could be introduced, to allow particles entry the gap only from one direction. Or substances could be attached on the surface close to the gap to study for example localized surface chemistry reactions.

### 8.4.4 Improving the Setup

The presented setups do not have the sensitivity of single-purpose Raman spectrometers. Signal collection efficiency would need to be improved to establish a useful combination of waveguide trapping and Raman spectroscopy. This section suggests two different setup designs that would simplify alignment and increase the collection efficiency of the microscope section.

At each beamsplitter, between 8% and 10% of the incident light is reflected away. By shifting beamsplitter $BS_2$ from figure 8.1 to the white light illumination path, a measurable improvement of signal strength can be achieved. Shifting the beamsplitter also decrease the path length of the collected light. A shorter path would be easier to screen off from stray light, and would give a more stable setup, less sensitive to vibrations. Increased stability would allow alignment of a single mode fibre to the spectrometer providing stronger spatial filtering of the signal. Figure 8.19 suggests how such a configuration would look. The excitation and imaging paths are now introduced by dichroic mirror DM, minimizing interruption with the light collection path. In the white light illumination path, the excitation laser is introduced through notch filter NF, and light is sent to the imaging CCD camera by pellicle beamsplitter BS. Filtering the white light illumination with a shortpass filter prevents white light from passing the dichroic mirror, and could make it possible to image the sample and acquire Raman signal at the same time. With this design, it is easy to switch between the external and internal excitation setups, as the collection light path is the same in the two cases. A mirror is proposed for fibre coupling to the spectrometer, but an achromatic lens could also be used. Lenses for CCD imaging and Köhler illumination are not shown in the figure.

The setup in figure 8.19, optimized for collection efficiency, aligns both excitation laser and fibre coupling inside the microscope. This is challenging if the path lengths are short. A setup optimized for alignment is suggested in figure 8.20. By coupling both excitation and collection light into the same optical fibre, the excitation and collection are automatically aligned to the same focal spot. This means

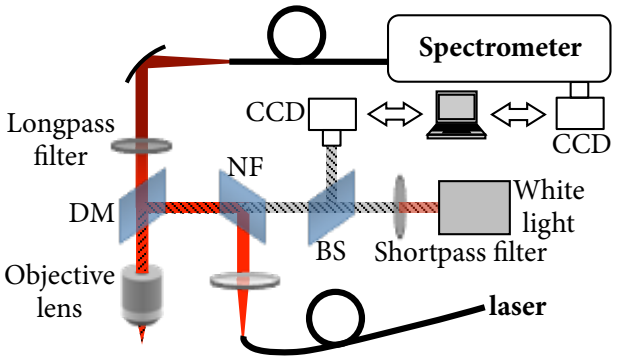


Figure 8.19: Suggested redesign of the imaging and excitation section of the setup. The design is adapted for both external and internal Raman excitation and optimized for light collection. The collected Raman scattered light only pass through dichroic mirror DM and a longpass filter before it is coupled to the spectrometer. The external laser is introduced by notch filter NF. Beamsplitter BS sends light to the imaging CCD camera. The white light is sent through a short pass filter to enable imaging while acquiring spectra.

that the microscope can be moved independently of the fiber coupling and makes adjustments much easier. Introducing a removable beamsplitter in the imaging path reduce reflections in the optical path during spectrum acquisitions. Compared to the setup optimized for collection, coupling into and collimation out of the fiber in this setup give slightly higher losses. The setup optimized for alignment would be less prone to drift, and is probably preferable in daily use.

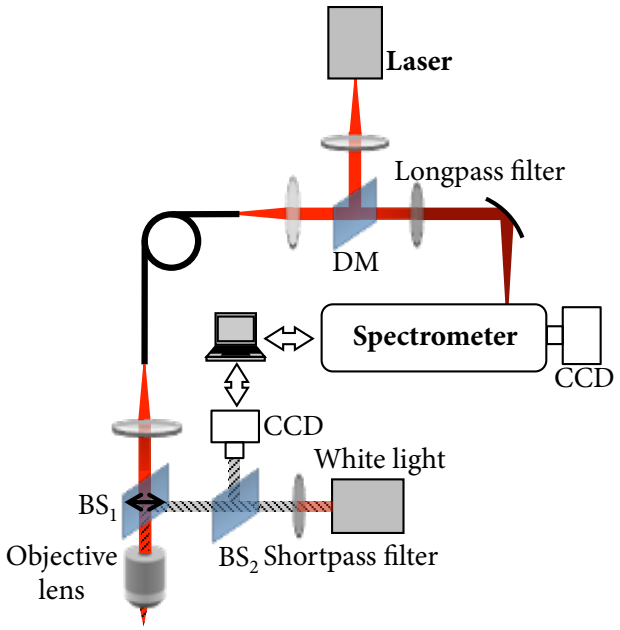


Figure 8.20: Suggested redesign of the imaging and excitation section of the setup. The design is adapted for both external and internal Raman excitation and optimized for easy alignment. The excitation laser and the scattered light are coupled into the same fiber, and share light path through the microscope. This ensures consistent positioning for collection of the excited Raman scattered light. Imaging is possible through removable beamsplitter BS.

## 8.5 Conclusions

Two setups for exciting Raman spectra from microspheres trapped on an optical waveguide have been tested, one using an external excitation laser at 785 nm, and one using guided light at 785 nm for excitation. When the external excitation laser was used, waveguide trapping was done with a high power 1070 nm laser. Collection of Raman signatures of objects close to the waveguide leads to spectral contributions from the waveguide materials. These background signals can be subtracted, but will influence the results, especially for objects that are weak Raman scatterers.

The external excitation laser setup gave the strongest microsphere Raman signatures. Raman signatures of polystyrene and borosilicate glass microspheres propelling on a straight waveguide were clearly distinguishable with one second acquisition times. Two seconds Raman acquisitions of polystyrene microspheres trapped using a loop-gap waveguide design were weaker, but still clearly recognizable. Strong losses in the narrow loop waveguides limited the size of spheres trapped in the gap to 2 μm diameter. Increasing the waveguide width in the gap design, would allow trapping of larger spheres. The high reflectivity of the silicon base under the waveguide leads to a higher light intensity near the microspheres. This increases the object's Raman signal, but also increases the signal contribution from the waveguide.

The internal excitation laser setup used guided light to excite Raman scattering. Recognizable Raman signatures were acquired with evanescent field excitation and with excitation by the field diverging into the waveguide gap. Due to weak excitation intensities, the spectra had low signal-to-background ratios. This lead to increased acquisition times and stronger background signal compared to the external excitation laser configuration. Background subtraction was necessary to achieve recognizable spectral signatures. To improve the strength of the Raman signal, increasing the width of the waveguide with gap, or improving mode quality or power of the tunable 785 nm laser propagating in the waveguide would be necessary.

The ability to characterize microparticles propelled along the waveguide without interrupting the flow of particles could lead to automated sorting and characterization applications. By using a narrow sample chamber around the waveguide, the ratio of characterized particles in a sample would increase. The waveguide would act like a conveyor belt, propelling particles into and out of the characterization region, analyzing each particle only once. This would give a precise, but time con-

suming, characterization of a full sample. Microfluidic transport would give faster, but less precise characterization. If strong Raman signatures were achieved with internal excitation, true lab-on-a-chip characterization would be possible.

Improvements of the imaging and excitation section of the setups would improve the quality of collected Raman signatures. The suggested redesign in figure 8.19 would give higher mechanical stability, simpler alignment, and higher transmission of both excitation light and collected Raman signal. An implementation of this is recommended for further Raman waveguide studies, especially if weaker Raman scatterers are to be analyzed. A different approach for signal improvement could be to utilize the proximity of the waveguide surface to the object. By attaching metal colloids on the waveguide surface for surface plasmon excitation (surface-enhanced Raman spectroscopy), the intensity of the light would significantly increase, enhancing the Raman signal by several orders of magnitude.

# Chapter 9

# Concluding Remarks

## 9.1 Overview

As mentioned in the introduction, waveguide trapping and Raman spectroscopy became the topics of the thesis based on the goal of characterizing objects trapped and propelled on top of a waveguide.

To provide a background to the topics presented in the thesis, basic properties of optical forces, waveguides, waveguide trapping, finite element method simulations, and Raman scattering were presented in chapters 2, 3 and 6. These are all well established topics, and the theory was presented to give a unified, short and physically intuitive introduction to the fields.

The remaining chapters of the thesis presented procedures and results from simulations and experiments. The simulations in chapters 4 and 5 were performed to find the forces exerted on various objects in the evanescent field on top of an optical waveguide. The experiments in chapters 7 and 8 studied applications of Raman spectroscopy, both as a measure of cell proliferation and for characterization of microparticles trapped on a waveguide. The following sections will sum up the results presented in these chapters.

## 9.2 Waveguide Simulations

The evanescent field outside the core of a waveguide can be used to propel micro- and nanoparticles on top of the waveguide structure. This makes it possible to create a narrow and highly specific conveyor belt for particles of this scale. Such structures are similar to optical tweezers in the sense that no mechanical contact is required to control the particle position. There are three major differences between the tweezers and the waveguide techniques. The first difference is the interaction volume of the particle and the field, which is much smaller for the waveguide trapping. The second difference is the position control of the trapping. For the tweezers, the control is three dimensional, only depending on the position of the focusing lens, while the waveguide only controls the particle on top of the waveguide surface. The third difference is the surrounding media. The waveguide trapping takes place along the surface of a dielectric, while the optical tweezers traps particles in free space. A fourth, more minor difference, is the intensity of the trapping light, which is much weaker in waveguide trapping.

In chapters 4 and 5, results from three dimensional finite element method simulations of optical forces were presented to study the advantages of the unique waveguide trap abilities. Simulations of trapped objects up to six micrometer in diameter were performed.

### 9.2.1 Hollow Spheres

The small interaction volume of the trap was found to be advantageous for the trapping of hollow spheres. Within the field, the thin shell of the sphere experienced an attractive force toward the waveguide, while the enclosed gas cavity of the sphere experienced a repulsive force away from the waveguide. Thus, for a specific shell thickness, no vertical attraction force is experienced by the hollow sphere. This can make it possible to levitate hollow spheres above the waveguide. However, special consideration must be given to buoyant and gravitational forces to achieve this. In the same way, the hollow sphere experiences a minimum propulsive force in the horizontal direction for similar shell thicknesses. It was found that the force on hollow spheres can be described in a simple way by looking at the average refractive index in the region interacting with the evanescent field. A closer investigation revealed that a more precise model would be based on the refractive index differences of the hollow sphere surfaces within the evanescent field.

### 9.2.2 Red Blood Cells

Trapping of cells is difficult as the cell and its surrounding medium are very similar. This leads to a small refractive index difference and small forces. The simulations found the horizontal propagation force of spherical cell models to have a quadratic dependence on small changes in refractive index. However, the magnitudes found were below the accuracy of the numerical model for typical cell refractive indices. The vertical forces were found to be more than one order of magnitude larger than the horizontal forces, and increased slowly with the size of the spherical cell models. The increase is due to the larger interaction volume of the sphere and the evanescent field when the diameter increases. To approach the shape of biconcave red blood cells, a four micrometer diameter disk shaped model was constructed. Due to the large narrow region between the disk and the waveguide, no horizontal forces could be accurately simulated with the available computer power. However, the attractive force increased significantly compared to the spherical cell models, and also increased markedly with the refractive index of the cell.

## 9.3 Raman Scattering Experiments

Raman experiments were performed on two different setups, one specifically designed for optical tweezer Raman studies, and one specifically designed for Raman studies of particles on waveguides. The optical tweezer setup had a much higher sensitivity, and was used to study the proliferation of weakly scattering cells. The waveguide setup was much less sensitive, and was used to study signals from strongly scattering polystyrene spheres. Both experiments showed promising results, but the results could be significantly improved by optimizations of experimental procedures and setup designs. Such improvements would probably lead to efficient analysis and characterization techniques for routine analysis.

### 9.3.1 Cell Proliferation

Cell growth is commonly measured by studying the uptake in DNA of labeled molecules incorporated during DNA replication. Previous methods were cumbersome to work with, and required removal of the measured cells. In chapter 7, a newly proposed proliferation assay was tested and quantified on non-adherent

cells. EdU, a thymidine analogue which contain a highly specific ethyne Raman peak, was incorporated into Jurkat white blood cells. With a setup combining optical tweezers and micro Raman spectroscopy, the incorporation and dissipation of EdU in the DNA was followed in a sample of living cells over a period of 118 hours. In spite of decreasing cell numbers, a clear increase and decrease in EdU concentration in the DNA was found when EdU was present in the growth medium and after EdU was washed away, respectively. The results matched the expected development fairly well, and suggested a cell proliferation time of 22 hours. However, a sudden increase in concentration of EdU for the last 30 hours of the experiment could not be explained satisfactorily.

Due to the heterogeneity of cell cultures, uptake ratio and replication time can vary strongly from cell to cell. Combined with an unknown ratio of non-replicating cells, this makes proliferation studies difficult to analyze. Raman based EdU assays would give simultaneous data on uptake ratio and uptake concentration, and allow rapid and exact proliferation data from cell cultures and single cells.

### 9.3.2 Characterization of Objects on Waveguides

An automated differentiation process could give accurate and fast sorting of different microparticles. Since Raman spectroscopy gives highly specific characterization based on the target's molecular structure, precise and real time characterization for sorting purposes can be achieved by collecting Raman scattered light from objects trapped on the waveguide. Special waveguide designs could then be used to sort different particles to different regions of the waveguide.

Chapter 8 presents results from characterization experiments of particles on waveguides using Raman spectroscopy. It is found that by using an external laser for excitation, Raman signatures of polystyrene microspheres can be acquired in 1 to 2 seconds, depending on the sphere diameter. On a straight waveguide, an external laser is used to trap and excite the target particle when it reaches the laser's focus spot. On a waveguide with a loop and gap design, the target particle is trapped in the gap incorporated in the loop. The stationary particle is then trapped and excited by an external laser. Potentially, the particle could be excited by the diverging guided light in the gap. It is shown that the Raman signature of liquid ethanol can be acquired with guided light excitation, but high losses in the 1 micrometer wide loop waveguide prevents proper characterization (and trapping) of polystyrene microspheres in the gap. Finally, it is shown that microspheres on the

waveguide surface can be characterized by the scattering of the evanescent field. However, this requires a large, stationary scatterer. In all the experiments, background signal from the waveguide and waveguide substrate contribute to the signal, and in some experiments it is required to subtract the background to see the Raman peak signatures. Low light collection efficiency limited the quality of the acquired Raman signatures. Thus, improvements of the microscope setups were suggested for simpler alignment and increased signal throughput.

## 9.4 Summary

The results presented in the thesis show that there are diverse applications for both waveguides and Raman spectroscopy. Different waveguide designs and microparticle properties can trap moving and stationary microparticles, among them non-adherent cells, and could even allow particle levitation for hollow spheres. Combined with the precise characterization of Raman spectroscopy, efficient microparticle sorting could be achieved. The thesis also show promising properties of a Raman tweezer based cell proliferation assay using non-adherent cells.

All the presented results have potential for improvements. For the simulations, the mesh density was a limiting factor for accurate horizontal forces, and could be improved by increasing computer memory. For the Raman proliferation assay, a more thorough comparison with fluorescent measurements, as well as improving measurement conditions of the Raman measurements would further improve the validity of the results. For the microsphere Raman characterization, the sensitivity of the Raman setup could be increased by simplifying the microscope design.

# List of Figures

# List of Tables

# Bibliography


[1] Balpreet Singh Ahluwalia, Olav Gaute Hellesø, Pål Løvhaugen, Ananth Z. Subramanian, and James S. Wilkinson. Surface transport and stable trapping of particles and cells by an optical waveguide loop. *Lab on a Chip*, 2012.

[2] Balpreet Singh Ahluwalia, Pål Løvhaugen, and Olav Gaute Hellesø. Waveguide trapping of hollow glass spheres. *Optics Letters*, 36(17), 2011.

[3] Pål Løvhaugen, Balpreet Singh Ahluwalia, Thomas R. Huser, Peter McCourt, and Olav Gaute Hellesø. Optical trapping forces on biological cells on a waveguide surface. In *Proceedings of SPIE*, volume 7902, 2011.

[4] Pål Løvhaugen, Balpreet Singh Ahluwalia, and Olav Gaute Hellesø. Optical waveguide trapping forces on hollow glass spheres. In *Proceedings of SPIE*, volume 7950, 2011.

[5] Satish Rao, Štefan Bálint, Pål Løvhaugen, Mark Kreuzer, and Dmitri Petrov. Measurement of mechanical forces acting on optically trapped dielectric spheres induced by surface-enhanced raman scattering. *Physical Review Letters*, 102:087401, 2009.

[6] Kay Gastinger, Pål Løvhaugen, and Ola Hunderi. Numerical simulations of interferometrical deformation measurements in multi-layered objects. In *Proceedings of SPIE*, volume 6995, 2008.

[7] John David Jackson. *Classical Electrodynamics*. John Wiley & Sons, third edition, 1999.

[8] Donald L. Lee. *Electromagnetic Principles of Integrated Optics*. John Wiley & Sons, 1986.

[9] David J. Griffiths. *Introduction to Electrodynamics*. Prentice Hall, 1999.

[10] Max Born and Emil Wolf. *Principles of Optics*. Cambridge University Press, seventh edition, 2001.

[11] Ping Hua, B. Jonathan Luff, Geoffrey R. Quigley, James S. Wilkinson, and Kenji Kawaguchi. Integrated optical dual mach–zehnder interferometer sensor. *Sensors and Actuators B*, 87:250–257, 2002.

[12] Katrin Schmitt, Bernd Schirmer, Christian Hoffmann, Albrecht Brandenburga, and Patrick Meyrueis. Interferometric biosensor based on planar optical waveguide sensor chips for label-free detection of surface bound bioreactions. *Biosensors and Bioelectronics*, 22:2591–2597, 2007.

[13] Satoshi Kawata and T. Tani. Optically driven Mie particles in an evanescent field along a channeled waveguide. *Optics Letters*, 21(21), 1996.

[14] Allen H. J. Yang, Sean D. Moore, Bradley S. Schmidt, Matthew Klug, Michal Lipson, and David Erickson. Optical manipulation of nanoparticles and biomolecules in sub-wavelength slot waveguides. *Nature*, 457:71–75, 2009.

[15] Julius Adams Stratton. *Electromagnetic Theory*. McGraw-Hill, 1941.

[16] S. Iraj Najafi, editor. *Introduction to Glass Integrated Optics*. Artech House, 1992.

[17] Philip Russell. Photonic crystal fibers. *Science*, 299:358–362, 2003.

[18] Balpreet Singh Ahluwalia, Ananth Z. Subramanian, Olav Gaute Hellesø, Nicolas M. B. Perney, Neil P. Sessions, and James S. Wilkinson. Fabrication of submicrometer high refractive index tantalum pentoxide waveguides for optical propulsion of microparticles. *Photonics Technology Letters*, 21(19), 2009.

[19] R. Derek Arnell and Peter J. Kelly. Recent advances in magnetron sputtering. *Surface and Coatings Technology*, 112:170–176, 1999.

[20] Balpreet Singh Ahluwalia, Olav Gaute Hellesø, Ananth Z. Subramanian, Nicolas M. B. Perney, Neil P. Sessions, and James S. Wilkinson. Fabrication and optimization of tantalum pentoxide waveguides for optical micropropulsion. In *Proceedings of SPIE*, volume 7604, 2010.

[21] Stephanie Gaugiran, Stéphane Gétin, Jean-Marc Fedeli, Guillaume Colas, Alexandra Fuchs, François Chatelain, and Jacques Dérouard. Optical ma-

nipulation of micro-particles and cells on silicon nitride waveguides. *Optics Express*, 13(18), 2005.

[22] Firehun Tsige Dullo. Trapping of nanoparticles with optical waveguides. Master's thesis, University of Tromsø, 2011.

[23] Iver Brevik. Experiments in phenomenological electrodynamics and the electromagnetic energy-momentum tensor. *Physics Reports*, 52(3), 1979.

[24] David J. Griffiths. Resource letter em-1: Electromagnetic momentum. *American Journal of Physics*, 80(1):7–18, 2012.

[25] Stig Stenholm. The semiclassical theory of laser cooling. *Reviews of Modern Physics*, 58(3), 1986.

[26] Karel Svoboda and Steven M. Block. Biological applications of optical forces. *Annual Revew of Biophysics and Biomolecular Structures*, 23:247–285, 1994.

[27] Yasuhiro Harada and Toshimitsu Asakura. Radiation forces on a dielectric sphere in the rayleigh scattering regime. *Optics Communications*, 124:529–541, 1996.

[28] Arthur Ashkin. Forces of a single-beam gradient laser trap on a dielectric sphere in the ray optics regime. *Biophysical Journal*, 61:569–582, 1992.

[29] R. Gussgard, Tore Lindmo, and Iver Brevik. Calculation of the trapping force in a strongly focused laser beam. *Journal of the Optical Society of America B*, 9(10), 1992.

[30] Gérard Gouesbet, B. Maheu, and Gérard Gréhan. Light scattering from a sphere arbitrarily located in a gaussian beam, using a bromwich formulation. *Journal of the Optical Society of America A*, 5(9), 1988.

[31] Feng Xu, Kuanfang Ren, Gérard Gouesbet, Gérard Gréhan, and Xiaoshu Cai. Generalized Lorenz–Mie theory for an arbitrarily oriented, located, and shaped beam scattered by a homogeneous spheroid. *Journal of the Optical Society of America A*, 24(1), 2007.

[32] John Paul Barton, Dennis R. Alexander, and Scott A. Schaub. Theoretical determination of net radiation force and torque for a spherical particle illuminated by a focused laser beam. *Journal of Applied Physics*, 66(10), 1989.

[33] James A. Lock. Calculation of the radiation trapping force for laser tweezers by use of generalized Lorenz–Mie theory. I. localized model description of

an on-axis tightly focused laser beam with spherical aberration. *Applied Optics*, 43(12), 2004.

[34] James A. Lock. Calculation of the radiation trapping force for laser tweezers by use of generalized Lorenz–Mie theory. II. on-axis trapping force. *Applied Optics*, 43(12), 2004.

[35] K. F. Ren, Gérard Gouesbet, and Gérard Gréhan. Radiation pressure forces exerted on a particle arbitrarily located in a gaussian beam by using the generalized Lorenz-Mie theory, and associated resonance effects. *Optics Communications*, 108:343–354, 1994.

[36] Li Na Ng, B. Jonathan Luff, Michalis N. Zervas, and James S. Wilkinson. Forces on a Rayleigh particle in the cover region of a planar waveguide. *Journal of Lightwave Technology*, 18(3), 2000.

[37] Dennis C. Prieve and John Y. Walz. Scattering of an evanescent surface wave by a microscopic dielectric sphere. *Applied Optics*, 32(9), 1993.

[38] John Y. Walz. Ray optics calculation of the radiation forces exerted on a dielectric sphere in an evanescent field. *Applied Optics*, 38(25), 1999.

[39] Satoshi Kawata and Tadao Sugiura. Movement of micrometer-sized particles in the evanescent field of a laser beam. *Optics Letters*, 17(11), 1992.

[40] Hitesh Y. Jaising, Katarina Grujić, and Olav Gaute Hellesø. Simulations and velocity measurements for a microparticle in an evanescent field. *Optical Review*, 12(1), 2004.

[41] Hitesh Y. Jaising and Olav Gaute Hellesø. Radiation forces on a Mie particle in the evanescent field of an optical waveguide. *Optics Communications*, 246:373–383, 2005.

[42] Eivind Almaas and Iver Brevik. Radiation forces on a micrometer-sized sphere in an evanescent field. *Journal of the Optical Society of America B*, 12(12), 1995.

[43] Iver Brevik, T. A. Iversen, and Eivind Almaas. Radiation forces on an absorbing micrometer- sized sphere in an evanescent field. *Journal of the Optical Society of America B*, 20(8), 2003.

[44] Hitesh Y. Jaising. *Manipulation of Dielectric Particles with Optical Evanescent Fields*. PhD thesis, University of Tromsø, 2004.

[45] B. M. Azizur Rahman and J. Brian Davies. Finite-element analysis of optical and microwave waveguide problems. *IEEE Transactions on Microwave Theory and Techniques*, 32(1), 1984.

[46] John L. Volakis, Abhijit Chatterjee, and Leo C. Kempel. Review of the finite-element method for three-dimensional electromagnetic scattering. *Journal of the Optical Society of America A*, 11(4), 1994.

[47] Delphine Néel, Stéphane Gétin, Pierre Ferret, Milan Rosina, Jean-Marc Fedeli, and Olav Gaute Hellesø. Optical transport of semiconductor nanowires on silicon nitride waveguides. *Applied Physics Letters*, 94(25):253115, 2009.

[48] Allen H. J. Yang and David Erickson. Stability analysis of optofluidic transport on solid-core waveguiding structures. *Nanotechnology*, 19:045704, 2008.

[49] Jianming Jin. *The Finite Element Method in Electromagnetics*. John Wiley & Sons, 1993.

[50] Ivo Milan Babuška and A. Kadir Aziz. On the angle condition in the finite element method. *SIAM Journal on Numerical Analysis*, 13(2), 1976.

[51] Jonathan Richard Shewchuk. What is a good linear finite element interpolation, conditioning, anisotropy, and quality measures. `http://www.cs.cmu.edu/~jrs/jrspapers.html`, December 2002.

[52] Alain Bossavit and Isaak Mayergoyz. Edge-elements for scattering problems. *IEEE Transactions on Magnetics*, 25(4), 1989.

[53] Salvatore Caorsi, Paolo Fernandes, and Mirco Raffetto. On the convergence of galerkin finite element approximations of electromagnetic eigenproblems. *SIAM Journal on Numerical Analysis*, 38(2), 2000.

[54] Jin-Fa Lee, Din-Kow Sun, and Zoltan J. Cendes. Full-wave analysis of dielectric waveguides using tangential vector finite elements. *IEEE Transactions on Microwave Theory and Techniques*, 39(8), 1991.

[55] Jean-Pierre Berenger. A perfectly matched layer for the absorption of electromagnetic waves. *Journal of Computational Physics*, 114(2), 1994.

[56] Weng Cho Chew and William H. Weedon. A 3-D perfectly matched medium from modified maxwell's equations with stretched coordinates. *Microwave and Optical Technology Letters*, 7(13), 1994.

[57] Iain S. Duff. Matrix methods. *Rutherford Appleton Laboratory Technical Reports*, 076, 1998.

[58] Iain S. Duff. Sparse numerical linear algebra: direct methods and preconditioning. In I. S. Duff and G. A. Watson, editors, *The state of the art in numerical analysis*, pages 27–62. Oxford University Press, 1997.

[59] Iain S. Duff. Direct methods. *Rutherford Appleton Laboratory Technical Reports*, 054, 1998.

[60] Patrick Amestoy, Alfredo Buttari, Abdou Guermouche, Jean-Yves L'Excellent, and Bora Ucar. MUMPS: a multifrontal massively parallel sparse direct solver. `http://graal.ens-lyon.fr/MUMPS/`, September 2011.

[61] Cleve Ashcraft and Roger G. Grimes. SPOOLES: An object-oriented sparse matrix library. In *Proceedings of the Ninth SIAM Conference on Parallel Processing for Scientific Computing*, 1999.

[62] Olaf Schenk and Klaus Gärtner. Solving unsymmetric sparse systems of linear equations with PARDISO. *Journal of Future Generation Computer Systems*, 20:475–487, 2004.

[63] Gene H. Golub and Henk A. van der Horst. Closer to the solution: Iterative linear solvers. In I. S. Duff and G. A. Watson, editors, *The state of the art in numerical analysis*, pages 63–92. Oxford University Press, 1997.

[64] Youcef Saad. Overview of krylov subspace methods with applications to control problems. In M. A. Kaashoek, J. H. van Schuppen, and A. C. M. Ran, editors, *Signal Processing, Scattering and Operator Theory, and Numerical Methods: Proceedings of the International Symposium MTNS-89 v.3*, Progress in Systems and Control Theory, pages 401–410. Birkhäuser Verlag, 1990.

[65] Magnus Hestenes and Eduard Stiefel. Methods of conjugate gradients for solving linear systems. *Journal of Research of the National Bureau of Standards*, 49:409–436, 1952.

[66] Youcef Saad and Martin H. Schultz. GMRES: a generalized minimal residual algorithm for solving nonsymmetric linear systems. *SIAM Journal on Scientific and Statistical Computing*, 7:856–869, 1986.

[67] William F. Ames. *Numerical Methods for Partial Differential Equations*. Nelson, 1969.

[68] Comsol. *RF Module User's Guide*, 4.2a edition, October 2011.

[69] The Norwegian Metacenter for Computational Science Notur. Stallo compute cluster. `http://www.notur.no/hardware/stallo/`, September 2011.

[70] Carmel M. Moran. *Clinical Ultrasound*, chapter Ultrasonic contrast agents, pages 77–89. Elsevier, 2011.

[71] Yoshiaki Kawashima, Toshiyuki Niwa, Hirofumi Takeuchi, Tomoaki Hino, and Yoji Itoh. Hollow microspheres for use as a floating controlled drug delivery system in the stomach. *Journal of Pharmaceutical Sciences*, 81(2), 2006.

[72] Marcus Lankers, Elsayed Esam M. Khaled, Jürgen Popp, Georg Rössling, Harald Stahl, and Wolfgang Kiefer. Determination of size changes of optically trapped gas bubbles by elastic light backscattering. *Applied Optics*, 36(7), 1997.

[73] Kevin Thomas Gahagan and Grover A. Swartzlander Jr. Optical vortex trapping of particles. *Optics Letters*, 21(11), 1996.

[74] Kevin Thomas Gahagan and Grover A. Swartzlander Jr. Trapping of low-index microparticles in an optical vortex. *Journal of the Optical Society of America B*, 15(2), 1998.

[75] Kevin Thomas Gahagan and Grover A. Swartzlander Jr. Simulatanious trapping of low-index and high-index microparticles observed with an optical-vortex trap. *Journal of the Optical Society of America B*, 16(4), 1999.

[76] Veneranda Garcés-Chávez, Karen Volke-Sepulveda, Sabino Chávez-Cerda, Wilson Sibbett, and Kishan Dholakia. Transfer of orbital angular momentum to an optically trapped low-index particles. *Physical Review A*, 66:063402, 2002.

[77] Khyati S. Mohanty, Carlo Liberale, Samarendra Kumar Mohanty, and Vittorio Degiorgio. In depth fiber optic trapping of low-index microscopic objects. *Applied Physics Letters*, 92:151113, 2008.

[78] Balpreet Singh Ahluwalia, Xiaocong Yuan, Shaohua Tao, Wai Chye Cheong, Lesheng Zhang, and Hong Wang. Micromanipulation of high and low indices miroparticles using a microfabricated double axicon. *Journal of Applied Physics*, 99:113104, 2006.

[79] Keiji Sasaki, Masanori Koshioka, Hiroaki Misawa, Noboru Kitamura, and Hiroshi Masuhara. Optical trapping of a metal particle and a water droplet by a scanning laser beam. *Applied Physics Letters*, 60:807, 1992.

[80] Philip H. Jones, Eleanor Stride, and Nader Saffari. Trapping and manipulation of microscopic bubbles with a scanning optical tweezer. *Applied Physics Letters*, 89:081113, 2006.

[81] Michael Peter MacDonald, Lynn Paterson, Wilson Sibbett, Kishan Dholakia, and Peter E. Bryant. Trapping and manipulation of low-index particles in a two-dimensional interferometric optical trap. *Optics Letters*, 26(12), 2001.

[82] Michael E. O'Neill. A slow motion of viscous liquid caused by a slowly moving solid sphere. *Mathematika*, 11:67–74, 1964.

[83] Arthur Joseph Goldman, Raymond G. Cox, and Howard Brenner. Slow viscous motion of a sphere parallel to a plane wall – I motion through a quiescent fluid. *Chemical Engineering Science*, 22:637–651, 1967.

[84] Paul F. Mullaney and Phillip N. Dean. The small angle light scattering of biological cells. *Biophysical Journal*, 10:764–772, 1970.

[85] Geert J. Streekstra, Alfons G. Hoekstra, Evert-Jan Nijhof, and Robert M. Heethaar. Light scattering by red blood cells in ektacytometry: Fraunhofer versus anomalous diffraction. *Applied Optics*, 32(13):2266–2272, 1993.

[86] Sebastien Rancourt-Grenier, Ming-Tzo Wei, Jar-Jin Bai, Arthur Chiou, Paul P. Bareil, Pierre-Luc Duval, and Yunlong Sheng. Mechanics of the human red blood cell deformed by optical tweezers. *Optics Express*, 18(10):10462–10472, 2010.

[87] Benjamin Rappaz, Alexander Barbul, Yves Emery, Rafi Korenstein, Christian Depeursinge, Pierre J. Magistretti, and Pierre Marquet. Comparative study of human erythrocytes by digital holographic microscopy, confocal

microscopy, and impedance volume analyzer. *Cytometry A*, 73A:895–903, 2008.

[88] Jochen Guck, Revathi Ananthakrishnan, Tess .J. Moon, C. Casey Cunningham, and Josef Käs. The optical stretcher: A novel laser tool to micromanipulate cells. *Biophysical Journal*, 81(2), 2001.

[89] Ming Dao, Chwee Teck Lim, and Subra Suresh. Mechanics of the human red blood cell deformed by optical tweezers. *Journal of the Mechanics and Physics of Solids*, 51:2259–2280, 2003.

[90] John P. Mills, Lan Qie, Ming Dao, Chwee Teck Lim, and Subra Suresh. Nonlinear elastic and viscoelastic deformation of the human red blood cell with optical tweezers. *Molecular and Cellular Biology*, 1(3), 2004.

[91] Dmitri V. Petrov. Raman spectroscopy of optically trapped particles. *Journal of Optics A: Pure and Applied Optics*, 9:139–156, 2007.

[92] Kerstin Ramser, Jonas Enger, Mattias Goksör, Dag Hanstorp, Katarina Logg, and Mikael Käll. A microfluidic system enabling Raman measurements of the oxygenation cycle in single optically trapped red blood cells. *Lab on a chip*, 5:431–436, 2005.

[93] Aseefhali Bankapur, Elsa Zachariah, Santhosh Chidangil, Manna Valiathan, and Deepak Mathur. Raman tweezers spectroscopy of live, single red and white blood cells. *PLoS ONE*, 5(4):10427, 2010.

[94] YongKeun Park, Monica Diez-Silva, Gabriel Popescu, George Lykotrafitis, Wonshik Choi, Michael S. Feld, and Subra Suresh. Refractive index maps and membrane dynamics of human red blood cells parasitized by Plasmodium falciparum. *PNAS*, 105(37), 2008.

[95] Evan Evans and Yuan-Cheng Fung. Improved measurements of the erythrocyte geometry. *Microvascular Research*, 4:335–347, 1972.

[96] Dirk J. Faber, Maurice C. G. Aalders, Egbert G. Mik, Brett A. Hooper, Martin J. C. van Gemert, , and Ton G. van Leeuwen. Oxygen saturation-dependent absorption and scattering of blood. *Physical Review Letters*, 93(2), 2004.

[97] Gunta Mazarevica and Talivaldis Freivalds Antra Jurka. Properties of erythrocyte light refraction in diabetic patients. *Journal of Biomedical Optics*, 7(2), 2002.

[98] Balpreet Singh Ahluwalia, Peter McCourt, Thomas Huser, and Olav Gaute Hellesø. Optical trapping and propulsion of red blood cells on waveguide surfaces. *Optics Express*, 18(20):21053, 2010.

[99] G. Sagvolden, I. Giaever, E. O. Pettersen, and J. Feder. Cell adhesion force microscopy. *Proceedings of the National Academy of Sciences in the USA*, 96:471–476, 1999.

[100] Bradley S. Schmidt, Allen H. J. Yang, David Erickson, and Michal Lipson. Optofluidic trapping and transport on solid core waveguides within a microfluidic device. *Optics Express*, 15(22):14322, 2007.

[101] Jürgen Beuthan, Olaf Minet, Jürgen Helfmann, Matthias Herrig, and Gerhard Müller. The spatial variation of the refractive index in biological cells. *Physics in Medicine and Biology*, 41:369–382, 1996.

[102] Eugen von Lommel. Theorie der normalen und anomalen Dispersion. *Annalen der Physik*, 239(3):339–356, 1878.

[103] Chandrasekhara Venkata Raman. On the molecular scattering of light in water and the colour of the sea. *Proceedings of the Royal Society A*, 101:64–80, 1922.

[104] Chandrasekhara Venkata Raman. Investigations of the scattering of light. *Nature*, 123:50, 1928.

[105] Chandrasekhara Venkata Raman and Kariamanickam Srinivasa Krishnan. A new type of secondary radiation. *Nature*, 121:501–502, 1928.

[106] Chandrasekhara Venkata Raman. A change of wavelength in light scattering. *Nature*, 121:619, 1928.

[107] Chandrasekhara Venkata Raman and Kariamanickam Srinivasa Krishnan. The optical analogue of the Compton effect. *Nature*, 121:711, 1928.

[108] Chandrasekhara Venkata Raman and Kariamanickam Srinivasa Krishnan. The negative absorption of radiation. *Nature*, 122:711, 1928.

[109] Adolf Smekal. Zur Quantentheorie der Dispersion. *Naturwissenschaften*, 11(43):873–875, 1923.

[110] Hendrik Anthony Kramers and Werner Heisenberg. Über die Streuung von Strahlung durch Atome. *Zeitchfrift für Physik A*, 31(1):681–708, 1925.

[111] Erwin Schrödinger. An undulatory theory of the mechanics of atoms and molecules. *Physical Review*, 28(6):1049–1070, 1926.

[112] Paul A. M. Dirac. The quantum theory of the emission and absorption of radiation. *Proceedings of the Royal Society A*, 114:243–265, 1927.

[113] Gregory Breit. Quantum theory of dispersion. *Reviews of Modern Physics*, 4(3):504–576, 1932.

[114] George Glockler. The Raman effect. *Reviews of Modern Physics*, 15(2):111–173, 1943.

[115] Josef Brandmüller and Heribert Moser. *Einführung in die Ramanspektroskopie*. D. Steinkopff Verlag, 1962.

[116] George Placzek. Rayleigh Streuung und Raman Effekt. In *Handbuch der Radiologie*. Akademische Verlagsgesellschaft, Leipzig, second edition, 1934.

[117] Andreas C. Albrecht. On the theory of Raman intensities. *The Journal of Chemical Physics*, 34(5):1476–1484, 1961.

[118] John R. Ferraro, Kazuo Nakamoto, and Chris W. Brown. *Introductory Raman Spectroscopy*. Academic Press, second edition, 2003.

[119] Hiroyuki Yamakoshi, Kosuke Dodo, Masaya Okada, Jun Ando, Almar Palonpon, Katsumasa Fujita, Satoshi Kawata, and Mikiko Sodeoka. Imaging of EdU, an alkyne-tagged cell proliferation probe, by Raman microscopy. *Journal of the Americal Chemical Society*, 133:6102–6105, 2011.

[120] Marcos Malumbres and Mariano Barbacid. To cycle or not to cycle: A critical decision in cancer. *Nature Reviews Cancer*, 1(3):222–231, 2001.

[121] Michael Joiner and Albert van der Kogel, editors. *Basic Clinical Radiobiology*. Hodder Arnold, 2009.

[122] Richard L. Sidman, Irene L. Mieale, and Ned Feder. Cell proliferation and migration in the primitive ependymal zone; an autoradiographic study of histogenesis in the nervous system. *Experimental Neurology*, 1:322–333, 1959.

[123] Howard G. Gratzner. Monoclonal antibody to 5-bromo- and 5-iododeoxyuridine: A new reagent for detection of DNA replication. *Science*, 218(4571):474–475, 1982.

[124] Alvaro Duque and Pasko Rakic. Different effects of bromodeoxyuridine and [$^3$H]thymidine incorporation into DNA on cell proliferation, position, and fate. *The Journal of Neuroscience*, 31(42):15205–15217, 2011.

[125] Adrian Salic and Timothy J. Mitchison. A chemical method for fast and sensitive detection of DNA synthesis in vivo. *Proceedings of the National Academy of Sciences in the USA*, 105(7):2415–2420, 2008.

[126] Life Technologies Corporation. Click-iT® EdU cell proliferation assays. `http://www.invitrogen.com/`, August 2012.

[127] Deanna Thompson. private communication, 2012.

[128] Lucía Nuñez, Ruth A. Valero, Laura Senovilla, Sara Sanz-Blasco, Javier García-Sancho, and Carlos Villalobos. Cell proliferation depends on mitochondrial $Ca^{2+}$ uptake: inhibition by salicylate. *Journal of Physiology*, 571(1):57–73, 2006.

[129] Takuo Tanaka and Sadahiko Yamamoto. Optically induced propulsion of small particles in an evanescent field of higher propagation mode in a multimode, channeled waveguide. *Applied Physics Letters*, 77(20), 2000.

[130] Katarina Grujić, Olav Gaute Hellesø, James S. Wilkinson, and John Patrick Hole. Optical propulsion of microspheres along a channel waveguide produced by $Cs^+$ ion-exchange in glass. *Optics Communications*, 239:227–235, 2004.

[131] Katarina Grujić, Olav Gaute Hellesø, John Patrick Hole, and James S. Wilkinson. Sorting of polystyrene microspheres using a y-branched optical waveguide. *Optics Express*, 13(1), 2005.

[132] Arthur Ashkin. Acceleration and trapping of particles by radiation pressure. *Physical Review Letters*, 24(4), 1970.

[133] Duke Scientific. NIST traceable particle size standards. `www.thermoscientific.com/`, September 2011.

[134] Bangs Laboratories. NIST traceable particle size standards. `www.bangslabs.com/`, September 2011.

*Hopefully, my process will not end with this, but continue to meander through life.*